CHEMISTRY OF MATERIALS

pubs.acs.org/cm

Review

Boosting Photocatalytic Activity Using Carbon Nitride Based 2D/2D van der Waals Heterojunctions

Pawan Kumar,* Devika Laishram, Rakesh K. Sharma, Ajayan Vinu,* Jinguang Hu,* and Md. Golam Kibria*

Cite This: *Chem. Mater.* 2021, 33, 9012−9092

Read Online

ACCESS | Metrics & More | Article Recommendations

ABSTRACT: The surging demand for energy and staggering pollutants in the environment have geared the scientific community to explore sustainable pathways that are economically feasible and environmentally compelling. In this context, harnessing solar energy using semiconductor materials to generate charge pairs to drive photoredox reactions has been envisioned as a futuristic approach. Numerous inorganic crystals with promising nanoregime properties investigated in the past decade have yet to demonstrate practical application due to limited photon absorption and sluggish charge separation kinetics. Two-dimensional semiconductors with tunable optical and electronic properties and quasi-resistance-free lateral charge transfer mechanisms have shown great promise in photocatalysis. Polymeric graphitic carbon nitride ($g\text{-}C_3N_4$) is among the most promising candidates due to fine-tuned band edges and the feasibility of optimizing the optical properties via materials genomics. Constructing a two-dimensional (2D)/2D van der Waals (vdW) heterojunction by allies of 2D carbon nitride sheets and other 2D semiconductors has demonstrated enhanced charge separation with improved visible photon absorption, and the performance is not restricted by the lattice matching of constituting materials. With the advent of new 2D semiconductors over the recent past, the 2D/2D heterojunction assemblies are gaining momentum to design high performance photocatalysts for numerous applications. This review aims to highlight recent advancements and key understanding in carbon nitride based 2D/2D heterojunctions and their applications in photocatalysis, including small molecules activation, conversion, and degradations. We conclude with a forward-looking perspective discussing the key challenges and opportunity areas for future research.

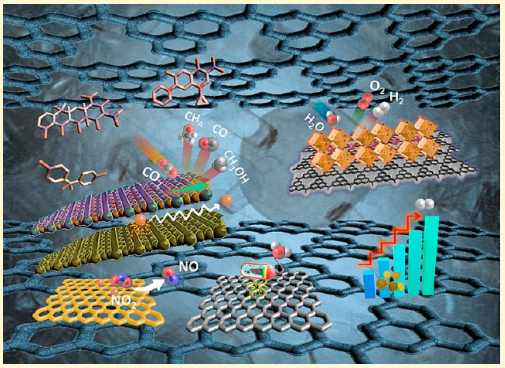

1. INTRODUCTION

The access to clean energy and per capita energy consumption is an archetype of societal and scientific progress and directly related to human living standards and economic prosperity.[1,2] In the year 2019, the total world energy consumption has been estimated to be ≈14 500 Mtoe.[3] Unfortunately, a significant fraction of world energy is exploited from fossil fuels that have skyrocketed global CO_2 concentration to a catastrophic level of 420 ppm (May 2021), a significantly higher number than the preindustrial era.[4] High per capita energy consumption is also responsible for the deteriorating environment and climate change.[5] The United States alone, which has only 5% of the world population, consumes 20% of the world energy and emits 6.5 billion metric tons of CO_{2e} greenhouse gases.[6,7] Irresponsible industrializations, rapid urbanization, and abusive exploitation of natural resources have adversely affected earth conditions of which water pollution is most severe. Almost 80% of the world's wastewater (34 billion gallons of wastewater per day) is dumped in water bodies without any treatment.[8] According to the United Nations' World Water Development Report 2018, the demand for clean water is expected to increase by nearly one-third by 2050.[9] In addition to recalcitrant pollutants such as pesticides, herbicides, fungicides, insecticides, antibiotics, heavy metals, etc., colored dye from textile industries is plaguing the water bodies due to shrinking penetration depth, leading to eutrophication and death of aquatic flora and fauna.[10,11] The impact of climate change and pollution is discernible from the global warming and extreme weather events such as unusual melting of icecaps, excessive rain, etc.[12−14] To limit the global temperature rise to below 1.5 °C, as suggested in the Paris agreement, at least a 7% emission reduction per year is needed.[15] To foster alternative energy usage, governments are adopting policies and subsidizing

Received: September 14, 2021
Revised: November 2, 2021
Published: November 24, 2021

https://doi.org/10.1021/acs.chemmater.1c03166
Chem. Mater. 2021, 33, 9012−9092

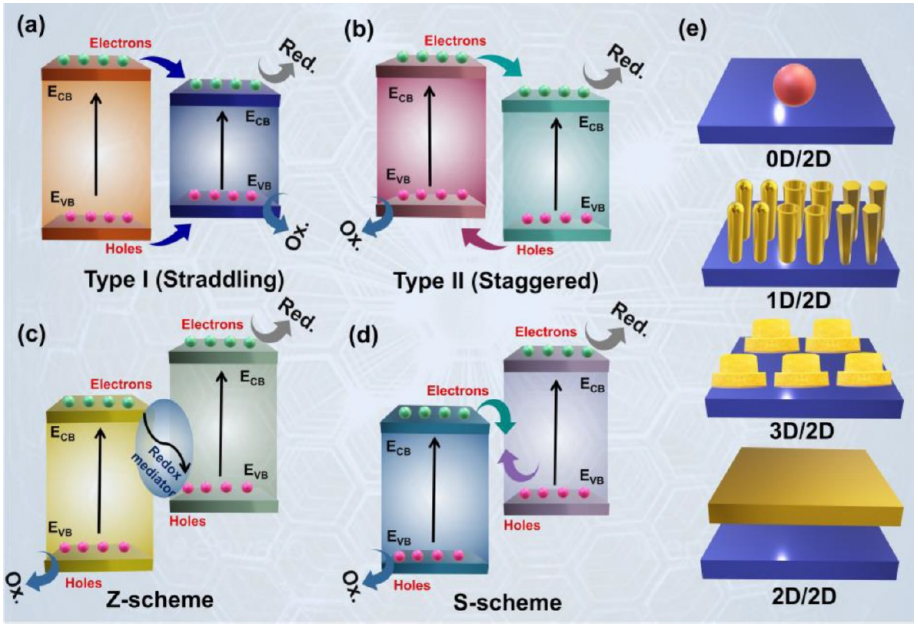

Figure 1. Types of heterojunctions: (a) Type I (Straddling), (b) Type II (Staggered), (c) Z-scheme, (d) S-scheme, and (e) 0D/2D, 1D/2D, 3D/2D, and 2D/2D.

technologies that make a minimum adverse impact on the environment.[16,17]

Among various energy sources, inexhaustible and clean solar energy is the most abundant, fulfilling all our future energy demands (1.7×10^{22} J energy is being dissipated on the earth's surface in 1.5 days, which is equivalent to 3 trillion barrels of total oil resources found on Earth).[18] Solar energy is expected to contribute significantly and is projected to reach up to 1200 GW by the end of 2024.[19] Among various solar energy harvesting technologies, photovoltaic cells are at the forefront, which can transform solar energy into electrical energy at an efficiency of ∼22.5% (47.1% in multijunction PV cells under concentrated solar light) and is significantly higher than natural photosynthesis (0.5−1% in most plants and up to 5% in some algae).[18,20−22] However, intermittency, unequal insolation in a different part of the world, associated energy storage and transportation issues, and longer payback time are some challenges for widespread implementation.[23]

Artificial photosynthesis using sunlight to energize electrons (and holes) in photocatalysts and their subsequent storage in the chemicals bonds to convert CO_2 into hydrocarbons and water into hydrogen is a preeminent way to capture and utilize sunlight.[24,25] Conventional thermochemical conversions of CO_2 into hydrocarbons (Fischer−Tropsch) and value-added chemicals such as ethylene glycol and ethylene carbonates relies on expensive catalysts and an energy carrier (usually hydrogen) and requires elevated temperature and pressure.[26,27] Photocatalysis provides a low energy route using photocatalysts and sunlight to transform extremely stable CO_2 (Δ_{Hf} −394 kJ/mol) into useful chemicals.[28] H_2 is an attractive clean energy fuel due to its high energy density (120 kJ/g), used as a fuel for fuel cells to produce electricity, and water is the sole byproduct. Additionally, hydrogen works as a high-energy carrier that can transform CO_2/CO into hydrocarbons addressing challenges associated with voluminous storage and explosion hazards and avails easy transportation.[29−31]

Research efforts in past decades on semiconductors were mostly focused on the heterogeneous inorganic crystalline materials and homogeneous catalysts, which led to activity only up to the micromole to millimole regime due to the lack of sufficient photon absorption in the visible region, fast charge recombination, and nonresiliency.[32−36] Even though a catalyst can harvest visible photons, a major fraction of generated charge carriers get recombined before any fruitful reactions. The estimated time for a photon to absorb on a nanocrystal under solar irradiation with a flux density of 2000 μmol s^{-1} m^{-2} is approximately 4 ms while the time taken in recombination is on the order of microseconds. Therefore, driving reactions that involve multiple electrons, such as water splitting and CO_2 reduction (4 for H_2 and 8 for CH_4), becomes challenging.[37,38] Various strategies such as surface modification with cocatalysts, increasing performance by plasmonic materials, organic 0D−2D sensitizers, quantum dots, and heterojunctions formation have been suggested to improve the visible light absorption and charge separations.[39−42] The formation of a heterojunction of carbon nitride with other semiconductor materials provides an opportunity to synchronize the wide fraction of the solar spectrum and charge separation requirement.[43]

Various types of heterojunctions can be realized, such as type-I (straddling), type-II (staggered or direct scheme), type-III (broken), Z-scheme, and S-scheme, based on the band position type of electron flow and nature of conductivity (n- or p-type) (Figure 1).[44−46] In a type-I heterojunction, the conduction and valence band of one semiconductor are straddled between the conduction and valence band of the second semiconductor, resulting in the flow of electrons and holes from the high band gap semiconductor to low band gap semiconductor (Figure 1a). The type-II heterojunction facilitates better charge separation and maximum utilization of absorbing photons; however, this configuration relies on a wide band gap semiconductor to meet the criteria of the redox reaction (E_{CB} > 0.00 V and E_{VB} > 1.23 eV), and the opposite flow of electrons and holes further reduces the potential gap (Figure 1b).[47] In type-III heterojunctions, the valence and conduction bands of two semiconductors have a significant

https://doi.org/10.1021/acs.chemmater.1c03166
Chem. Mater. 2021, 33, 9012−9092

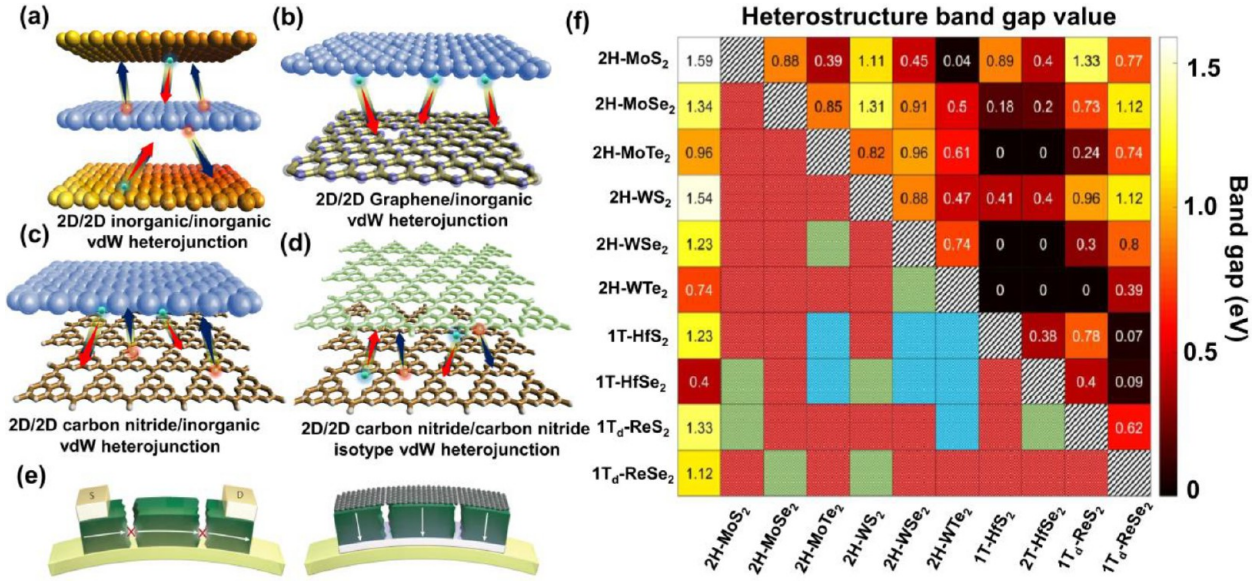

Figure 2. Face-to-face interaction and vertical charge transport mechanism in the 2D/2D vdW heterostructure. (a) 2D/2D vdW heterojunction between two inorganic heterostructures. (b) Unidirectional charge flow in inorganic/graphene-based 2D/2D vdW heterojunctions. (c) 2D/2D carbon nitride/inorganic semiconductors vdW heterostructure. (d) 2D/2D interfacial vdW heterojunction between carbon nitrides. (e) Comparison between conventional and flexible vertical FET on a flexible plastic substrate. Reprinted with permission from ref 105. Copyright 2016 Macmillan Publishers Limited (Springer Nature). Reprinted with permission from ref 121. Copyright 2014 American Chemical Society. (f) Quasi-particle band gap values and types for various 2D vertical heterostructures composed of TMDC, obtained using DFT−PBE calculations and displayed as a heatmap. Reprinted with permission from ref 122 by Chaves et al. under the terms of the Creative Commons Attribution 4.0 International License (CC BY) (https://creativecommons.org/licenses/by/4.0/). Copyright 2020 Chaves et al.

energy difference and so are not aligned together and scarcely reported. In contrast, Z-scheme and S-scheme photocatalysts are constituted of two tandem structured photosystems that can meet the requirement of higher wavelength absorption and wideband energy gap of conduction and valence bands; however, the two-photon excitation mechanism reduces half of the efficiency of the system (Figure 1c,d).[48,49] The physicochemical/photophysical properties and charge separation mechanism in the semiconductor heterojunction and their advantage over conventional modification approaches such as using electron and hole capturing agents have already been discussed before in other pioneering reviews.[40,43,48,50]

Theoretically, heterojunction formation seems to solve the problem of light absorption and charge separation; however, practically, these problems persist due to the enormous recombination of charge carriers at the interface of the two semiconductors and long migration distance in the heterojunction to reach another semiconductor.[51] Two-dimensional materials have emerged as a promising material platform that can overcome these issues due to excellent charge carrier mobility, confinement of electrons in a few angstrom thick layers, short diffusion distance, and better absorption even at a low flux density.[37] Graphene is the most influential member of the 2D family due to its excellent electron mobility (>50 000 $cm^2/(V\ s)$ at room temperature).[52] Contrary to inorganic nanocrystals, the charge transport along the 2D graphene sheets is almost resistant-free, which provides excellent charge carrier mobility.[53,54] However, due to the absence of a band gap, its photocatalytic application is limited to charge capturing agents, macromolecular sensitizers, and redox mediators in heterojunction structures.[55] Heteroatom doping such as N, P, and S opens up the band gap in graphene and influences the charge distribution of neighboring carbon atoms, resulting in shifting of the Fermi level above the Dirac point, and graphene behaves as a semiconductor.[56,57] However, due to the low doping level and multitudinous nature of doping (pyridinic, pyrrolic, quaternary N's, etc.), the band gap of graphene is restricted below 1.0 eV, which cannot meet the theoretical band gap requirement of water splitting (1.23 eV) or CO_2 reduction (over 1.0 eV).[58]

Other 2D semiconductors, such as 2D hexagonal boron nitride (hBN), are lagging because of their wide band gap (~6 eV).[59] Beyond hexagonal sp^2 carbon-containing graphene, 2D transition metal dichalcogenides (TMDCs) of Group V and VI metals (V, Nb, Ta, Cr, Mo, and W) and chalcogens (i.e., S, Se, and Te) with a layered structure and trigonal prismatic 1H, 1T, and 1T′ phases have shown great promise in the photocatalysis.[60−62] Though the most investigated members such as MoS_2 and WS_2 possess a low band gap, their inability to catalyze both sides of redox reactions limits their applicability.[63−65] Again, fast charge recombination coupled with the instability of some chalcogenides remains an evident problem.

Recently, metal-free graphitic carbon nitride (g-C_3N_4, CN, melon) composed of tertiary nitrogen linked tris-*s*-triazine (heptazine; C_6N_7) units arranged in a 2D sheets structure has galvanized the photocatalysis field due to its attractive optical and electronic properties.[66,67] The graphene-like 2D structure, moderate band gap (2.6−2.7 eV), compelling band positions (E_{CB}: −1.1 and E_{VB}: + 1.6 eV vs NHE) to facilitate oxidation and reduction at their valence and conduction bands (water splitting, CO_2 reduction, pollutant oxidation) make them a superlative photocatalyst.[68] Unfortunately, bare absorption after the blue region (450 nm), fast charge recombination, hydrogen-bonded sheets, and intricate film formation are major obstacles.[69] A plethora of articles reported metal/nonmetal doping,[70,71] insertion of N/C rich units,[72] changing of the coordination/bridging pattern,[73] self-doping, surface chemical modification using metal complexes,[74,75] quantum

https://doi.org/10.1021/acs.chemmater.1c03166
Chem. Mater. 2021, 33, 9012−9092

dots, heterojunction formations,[76] etc. to improve the visible absorption of the carbon nitride in longer wavelengths.[68,77] During the synthesis of bulk carbon nitride from its precursor, several uncondensed fragments with terminated NH/NH_2 promote intersheet hydrogen bonding, leading to low crystallinity.[78] Further, these regions also act as localized charge recombination centers. Transformation of bulk g-C_3N_4 into single to few-layered sheets by breaking hydrogen bonding has been suggested as a viable approach to alleviating these problems.[79,80] Many approaches such as solvent assisted exfoliation (in water, IPA, butanol, DMF, NMP),[81] thermal exfoliation, chemical exfoliation using harsh chemicals such as LiCl,[82] HNO_3,[83−85] H_2SO_4,[86] KOH,[87] $KMnO_4$+H_2SO_4/H_3PO_4,[88] and even altering/adding precursors during synthesis[89,90] have been reported to yield few/monolayered carbon nitride sheets.[84,91] However, these processes lead to poor crystallinity (periodicity), interfering with charge migration distance.[92−94] Further, due to the confinement effect in monolayered sheets, visible photon absorption is compromised, which further intensifies the problem of charge recombination. The crystallinity of both triazine and heptazine-based carbon nitride can be improved by molten salt-assisted synthesis using KCl and LiCl. Many other approaches such as breaking of hydrogen bonding, improving polymerization degree, using hydrogen-bonded precursors with planar structure, etc. have also been investigated to improve the performance of heptazine/triazine-based networks.[95]

Depending upon the morphology and interfacial interaction between various semiconductors and 2D materials, mainly four types of heterojunctions can be realized, namely, 0D/2D, 1D/2D, 2D/2D, and 3D/2D (Figure 1e).[96−99] Since 0D spherical morphology has a low surface area, point interaction with the 2D materials makes the effective interaction poor to achieve facile charge migration. On the other hand, the 1D configuration provides the advantage of high surface, directional charge transport, and reduced recombination losses due to a less populated bulk phenomenon; however, the interfacial contact between the 1D and the 2D structure remains confined to the stem diameter of the 1D structure.[100] Though 3D morphology provides relatively improved interaction, the bulk recombination in the 3D structure remains prevalent.[101] In recent years, 2D/2D heterojunctions constituted via the face-to-face interaction of two semiconductors are gaining popularity due to maximum charge separation between two semiconductors interfaces (Figure 1e).[102−104] Additionally, a distinct interfacial charge separation mechanism prevents recombination due to short diffusion length (few Å ≈ equal to interplanar distance).[37] In lateral/bulk 3D heterojunctions, a significant fraction of carriers get recombined at the materials heterointerface. The vertical charge transport mechanism in the 2D/2D heterojunction ensures minimum migration length for the majority and minority charge carriers for efficient collection of photogenerated charge by the second semiconductor before the annihilation (Figure 2).[105−107] The constitution of the 2D/2D heterostructure also provides maximum accessibility to active sites for reactant molecules to adsorb and react on the semiconductor surface.[108] Several 2D/2D heterojunctions designed from inorganic 2D semiconductors have been reported previously for various applications, including photocatalysis.[109−115] For the inorganic 2D/2D heterojunction, epitaxial matching is an indispensable criterion for efficient charge transfer between two semiconducting materials (Figure 2a). The lattice mismatch limits the choice of available materials (lattice mismatch < 10%) and compromises the quantum efficiency due to populated recombination at the interface.[116,117] Several approaches such as chemical vapor deposition (CVD), molecular beam epitaxy (MBE), and pulsed laser deposition (PLD) have been devised for layer-by-layer growth of the 2D/2D heterojunction; however, such processes are slow/energy intensive and require sophisticated tools.[118,119] Furthermore, stiff strenuous nanoarchitecture impedes their applications in flexible devices. In contrast, the 2D/2D heterojunction of layered carbonaceous materials (especially graphene and carbon nitride) and inorganic 2D semiconductors does not require lattice matching and can remain in contact due to van der Waals interaction (Figure 2b−d).[76,103,120] When two 2D materials are in close contact with weak van der Waal forces, they are generally referred to as 2D/2D vdW heterostructure. Graphene based 2D/2D vdW heterostructures have been widely investigated for electronics/optoelectronics such as FETs. Due to the flexible and conductive nature of graphene, it can overcome the issues of broken junction in conventional inorganic semiconductor-based devices to fabricate foldable devices on a plastic substrate (Figure 2e).[105] Although zero-band gap and graphene enhanced photocatalytic activity due to better charge collection on conductive sheets, it however does not contribute further because of their inability to produce electron−hole pairs. On the other hand, carbon nitride due to moderated band gap, conjugated nature, and analogous graphenic structure is an ideal candidate for making 2D/2D heterojunctions.

The 2D/2D heterojunction of 2D carbon nitrides with inorganic/organic 2D semiconductors demonstrated excellent potential for photocatalytic and electronic applications. The weak van der Waals interactions between carbon nitride sheets and 2D semiconductors overcome the conventional lattice matching constraint.[105,123−125] Beyond the advantage of 2D/2D vdW heterojunctions in better charge separation, the 2D/2D architecture also influences the charge distribution on two semiconductor sheets resulting in band gap modulation. As depicted in Figure 2f, by choosing an appropriate combination of semiconductors and controlling the number of layers, the band gap can be tuned to get the desired products.[122,126,127] The ability of carbon nitride to form a strain-free heterojunction with other 2D semiconductors allows vast permutation to fabricate many 2D/2D heterostructures.[54,128] Layered double hydroxides (LDHs), 2D oxides, oxynitrides, sulfides, and mixed oxides including perovskite oxides have been explored to form a 2D/2D heterojunction assembly with carbon nitrides for various applications such as photocatalytic hydrogen evolution, CO_2 reduction, pollutants, antibiotics, NO_2 degradations, etc.[129,130] The formation of a p−n type heterojunction by coupling of n-type carbon nitride with p-type semiconductors such as bismuth oxyhalides (BiOX: X = Cl, Br, I), perovskite oxides, phosphorene, etc. is particularly appealing because of the dual advantage of better face to face interaction and innate charge separation in the built-in electric field.[131] In recent years, new 2D materials with promising properties are emerging such as conductive/semiconductor MXenes, low band gap phosphorene (P), borophene (B), stanene (Sn), tellurene (Te), silicene (Si), bismuthine (Bi), arsenene (As), antimonene (Sb), etc. which further ameliorate the scope of carbon nitride-based 2D/2D heterojunctions.[132−137] The possibility of chemical structure manipulation and decoration with single atoms (single atom catalysts,

https://doi.org/10.1021/acs.chemmater.1c03166
Chem. Mater. 2021, 33, 9012−9092

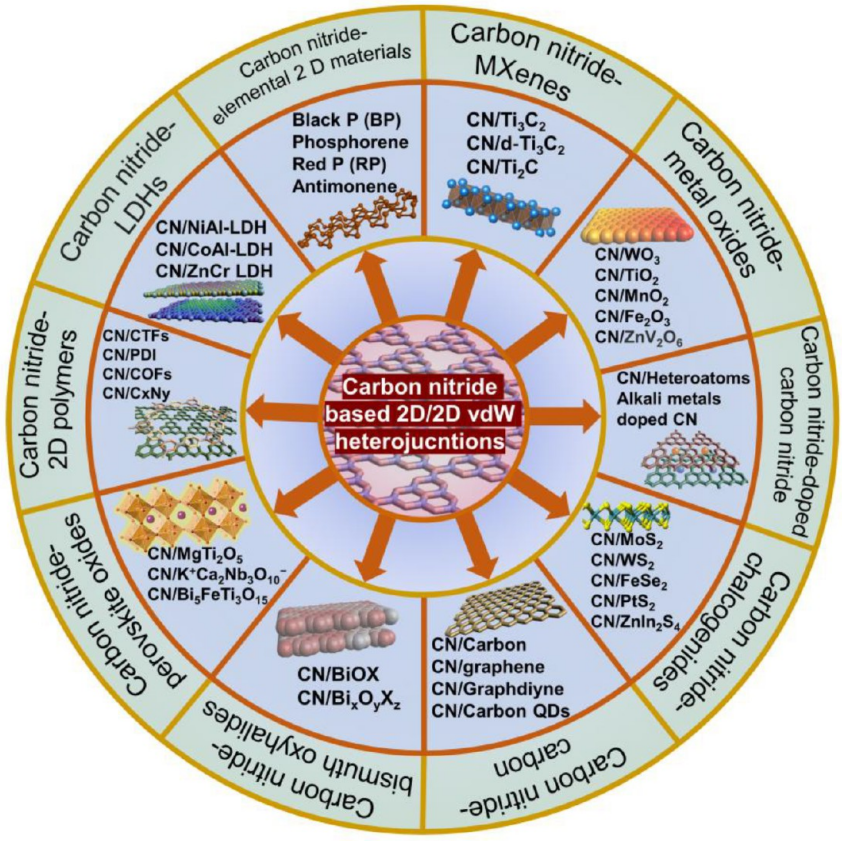

Figure 3. Schematic illustration of carbon nitride-based 2D/2D vdW heterojunctions with various 2D materials.

SACs) of carbon nitride sheets provide an opportunity to facilitate selective adsorption of a specific substrate on the surface to achieve excellent product selectivity.[138−143] The chemically modified carbon nitrides with a differential band gap can make a metal free n−n isotype heterojunction. The doping of carbon nitride with electron deficient elements/units (such as boron) can shift the Fermi level to transform n-type carbon nitride to p-type carbon nitride, suitable to fabricate a p−n isotype heterojunction.

The research on 2D/2D carbon nitride-based vdW heterojunction materials is gaining momentum. Several reports have emerged in recent years demonstrating excellent photocatalytic performance over conventional heterojunction photocatalysts and other applications. This review article focuses on photocatalytic processes for clean energy production and pollutants degradation using 2D/2D carbon nitride vdW heterostructures (Figure 3). As of today, no comprehensive review has been reported explicitly focusing on the carbon nitride-based 2D/2D vdW heterostructure. This review compiles the research work done in the field in the past four years and emphasizes various synthetic protocols such as solvent and chemical exfoliation, in situ approach, and electrostatic interaction. The 2D/2D vdW heterojunction of g-C_3N_4 with 2D materials such as elemental 2D materials (black P, red P, antimonene), MXenes, metal oxides (TiO_2, MnO_2, WO_3, ZnV_2O_6), transition and noble metal chalcogenides (MoS_2, WS_2, $FeSe_2$, $ZnIn_2S_4$, PtS_2), bismuth oxyhalides, perovskite oxides, LDHs, etc. has been thoroughly investigated. Additionally, a broad section dedicated to isotropic heterojunctions has been added, which are rarely discussed in any report. An implanted carbon-containing heterostructure is a new subdiscipline of the field. Additionally, a section demonstrating various 2D polymer semiconductors which can be used for the 2D/2D interfacial junctions has also been canvassed. Finally, a comparison between vdW and lateral 2D/2D heterostructures has been made. Among photocatalytic applications, we have thoroughly revisited hydrogen evolution, CO_2 reduction, and pollutant degradations. The present review bridges the gap as it highlights the recent research work done in the field of the 2D/2D carbon nitride-based heterojunction. In the following sections, we have focused our discussion on carbon nitride-based 2D/2D heterojunction with a wide variety of inorganic and allotropic 2D semiconductors. The photophysical properties of each material amalgamating with carbon nitride on the 2D/2D heterojunction are also discussed in detail. We conclude with forward-looking perspectives and rational design of 2D/2D configuration to develop a universal catalyst with complete visible photon absorption and efficient charge separation.

2. CARBON NITRIDE−ELEMENTAL 2D MATERIAL vdW STRUCTURES

2.1. Carbon Nitride−Black Phosphorus (BP)/Phosphorene. Black phosphorus (BP), a stable elemental allotrope of phosphorus (compared to red and white phosphorus), has attracted significant interest in the materials science community due to its low direct band gap (0.3 eV) with tunability depending on numbers of layers, 2D graphite type layered structure, and excellent field-effect mobility (~1000 $cm^2/(V\ s)$ at room temperature).[144] The high-temperature synthesis at 873 K (in the presence of gold, tin, and tin(IV) iodide)[145,146] usually led to rhombohedral forms with

https://doi.org/10.1021/acs.chemmater.1c03166
Chem. Mater. 2021, 33, 9012−9092

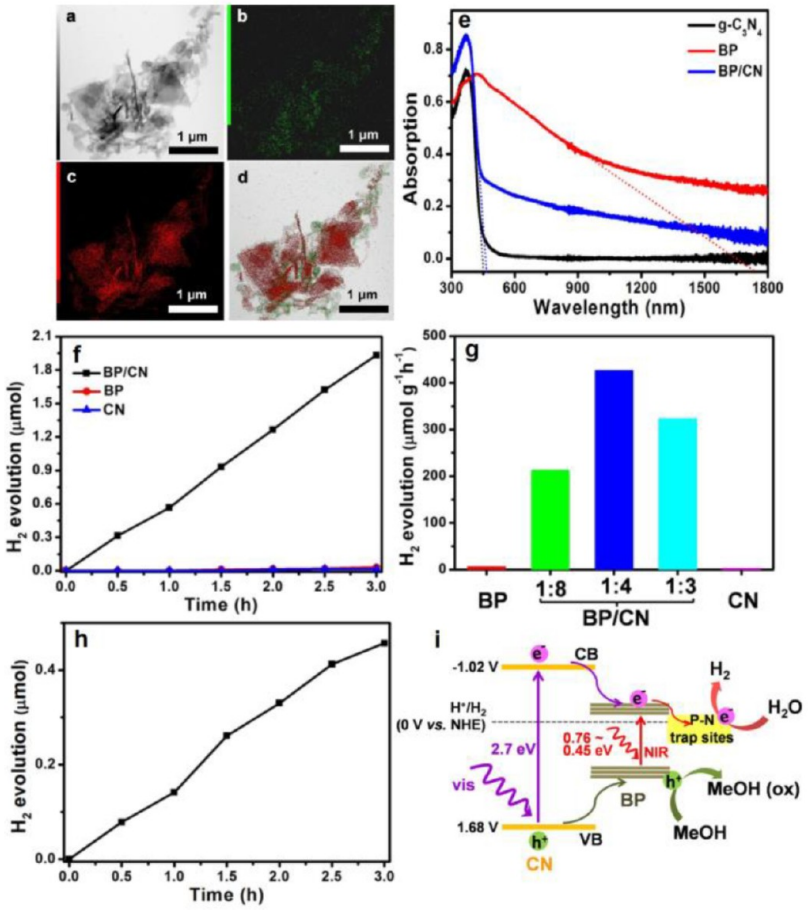

Figure 4. (a) HAADF-STEM image. EDX elemental mapping of (b) N and (c) P and (d) overlay of HAADF-STEM of N (green) and P (red) elements of BP/CN. (e) UV−vis diffuse reflectance spectra of CN, BP, and BP/CN. (f) Photocatalytic H_2 evolution from water containing methanol (20 vol %) on different catalysts under visible light (>420 nm) irradiation. (g) Effect of BP:CN ratio in BP/CN on photocatalytic H_2 evolution rate under visible light irradiation for 3 h. (h) Photocatalytic H_2 evolution from BP/CN with >780 nm light irradiation. (i) Proposed mechanism for the visible and NIR light-activated photocatalytic H_2 evolution using BP/CN in the presence of methanol. Reprinted with permission from ref 178. Copyright 2017 American Chemical Society.

directional ductility along with the sheet and large in-plane anisotropy due to its puckered atomic structure (dichroism).[147] The exfoliation of black phosphorus in aprotic and polar solvents such as acetone,[148] chloroform,[149] ethanol,[150] isopropyl alcohol (IPA),[150] dimethylformamide (DMF),[151] dimethyl sulfoxide (DMSO),[152] *N*-methyl 2-pyrrolidone (NMP),[153] and *N*-cyclohexyl 2-pyrrolidone (CHP)[154] offers single-layered sp^3 hybridized 2D sheets of phosphorene with a band gap of ∼2.1 eV and theoretical electron mobility of 10 000−26 000 $cm^2\ V^{-1}\ s^{-1}$.[155] Unlike MoS_2 and WS_2, the transition of bulk BP into phosphorene does not lead to indirect-to-direct band gap transition while going from bulk to monolayer, which provides flexibility to use band gap tuned fragments (depending on the numbers of layers) for photocatalysis.[156] Due to its wide absorption profile extended up to the NIR region and *p*-type conductivity with high hole mobility ($10^5\ cm^2/(V{\cdot}s)$),[157] BP is an excellent material for making a heterojunction with *n*-type materials.[147] Unfortunately, under air and moisture phosphorene forms strong P−O and P═O dangling bonds with oxygens to form indirect band gap nonstoichiometric oxides PO_x, which ultimately degrades via the formation of phosphoric acid.

Since the first few reports on the potential of BP to enhance dye degradation and water splitting in black−red phosphorus heterostructure[158] and Ag/BP nanohybrids,[159] numerous reports on BP have emerged.[160−163] DFT calculations reveal the valence band position (0.21 eV) of phosphorene does not meet the criteria of water oxidation (H_2O/O_2; +1.23 eV vs NHE at pH 0) while the conduction band (−0.56 eV) is well suited for the proton reduction to hydrogen (H^+/H_2; 0.0 eV vs NHE at pH 0), making it a good hydrogen evolution catalyst in the presence of a sacrificial donor.[164] However, switching the pH of the solution to 8.0 was found to shift the valence band toward the positive side, facilitating both an oxidation and a reduction reaction for overall water splitting.[165] Additionally, it was predicted that the edge decoration of BP with pseudohalogens such as nitrile (CN) and cyanate (OCN) can also tune the band position to facilitate water splitting.[166] To sustain the water-splitting process and prevent fast oxidation, the use of alkali and tedious chemical functionalization is undesirable.

To overcome the stability and band alignment issues without compromising the visible absorption, heterostructures of BP with a wide variety of materials such as graphene, TiO_2, WS_2, $BiVO_4$, MoS_2, and ZIF-8 and plasmonic metals such as Ag and Au have been fabicated.[167,168] However, carbon nitride remains one of the best candidates to make a heterostructure with BP due to its appropriate band structure and 2D

https://doi.org/10.1021/acs.chemmater.1c03166
Chem. Mater. 2021, 33, 9012−9092

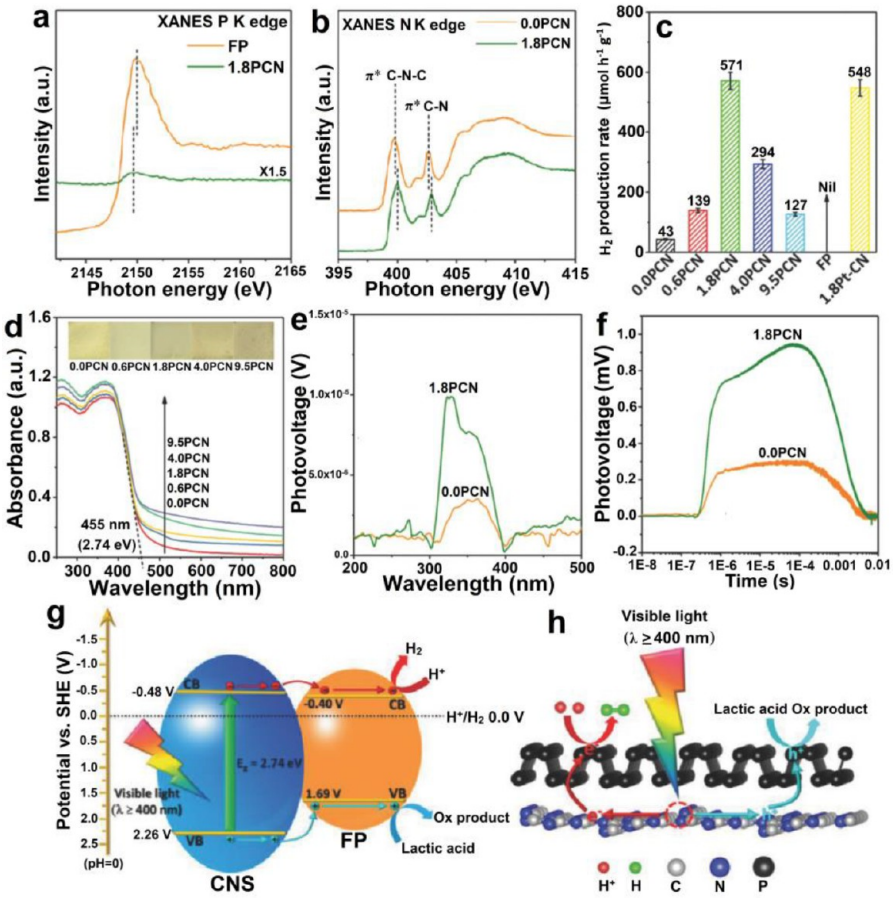

Figure 5. (a) XANES P K-edge of FP and 1.8PCN. (b) XANES N K-edge of 0.0PCN and 1.8PCN. (c) Photocatalytic H_2-production activities of 0.0PCN, 0.6PCN, 1.8PCN, 4.0PCN, 9.5PCN, and 1.8Pt-CN in 18 vol % lactic acid aqueous solution under visible-light irradiation (λ > 400 nm). (d) UV−vis diffuse reflectance spectra of 0.0PCN, 0.6PCN, 1.8PCN, 4.0PCN, and 9.5PCN. The insets show the colors of these samples, (e) Steady-state SPV spectra of 0.0PCN and 1.8PCN. (f) Transient-state SPV spectra of 0.0PCN and 1.8PCN. (g) Charge separation and transfer in the FP/CNS system under visible-light irradiation (λ > 400 nm). (h) Schematic illustration of photocatalytic H_2 production in the FP/CNS system under visible-light irradiation (λ > 400 nm). The red, green, gray, blue, and black spheres denote H^+, H, C, N, and P atoms, respectively. Reprinted with permission from ref 180. Copyright 2018 Wiley-VCH.

nature.[169] Many reports demonstrate the harsh sonication of BP in NMP/aprotic solvents/deoxygenated water to form BP quantum dots followed by mixing with carbon nitride to form 0D/1D hybrids.[170−174] Transformation of BP in quantum dots reduces the absorption profile and compromises the potential of BP to harvest NIR photons.[175] Though quantum dots are still visiblly active, the processability, leaching, and presence of plenty of oxygen functionality (e.g., P−O, P═O) presents stability and resiliency-related challenges.[176] Zheng et al. demonstrated that in situ exfoliation of bulk BP and g-C_3N_4 powders in NMP is a compelling approach to produce BP sheets supported on carbon nitride sheets.[177] The developed catalyst with 10% BP (10%BP/CN; average thickness of 4.2 ± 1.0 nm) displayed the maximum visible light degradation efficiency toward the rhodamine B (RhB) and H_2O_2 production. Although the material displayed absorption as far as up to 800 nm, only visible light from the solar simulator (λ > 420 nm) was employed that can achieve a 98% RhB degradation efficiency within 15 min and 540 μmol g^{-1} H_2O_2 generation after 1 h. The mechanism evaluation using radical scavengers such as 1,4-benzoquinone (BQ as a $^{\bullet}O_2^-$ scavenger), KI (h^+ and $^{\bullet}$OH radical scavenger), and isopropanol (IPA as a $^{\bullet}$OH radical scavenger) followed by radical trapping using 5,5-dimethyl-1-pyrroline *N*-oxide (DMPO) and measuring EPR demonstrate that superoxide radicals (quartet for DMPO−$^{\bullet}O_2^-$ adduct 1:1:1:1) were the main reactive oxygen species.

To further explore the potential of BP and g-C_3N_4 (CN) hybrid to harvest NIR light, Zhu and co-workers synthesized BP/CN hybrid via sonication and stirring of bulk BP and CN in NMP.[178] HR-TEM and HAADF-STEM images display amalgamated BP and CN sheets in the hybrid (Figure 4a−d). DFT calculations on the BP/CN structure suggested that P atoms are situated in the interstitial sites of CN through P−N coordinate bond and connected to two adjacent pyridinic-N atoms from two separate triazine units to form a P−N_3C_2 ring. FTIR spectra of BP/CN exhibited a signature peak at around 960 cm^{-1} due to P−N stretch and further demonstrates a strong interfacial interaction between BP and CN. Usually, the formation of a heterojunction proceeds through charge migration and Fermi level alignment, which can be observed via a change in binding energy and shifting of valence band positions. The P 2p XPS spectra of BP/CN displaying a downshifting of the binding energy by a factor of 0.1 eV relative to pristine BP along with observation of a new peak at 133.2 eV (due to P−N of P_3N_5) further validate the formation of the chemically stable BP/CN hybrid. A similar pattern was also observed in UPS spectra, where the onset potential of BP/

https://doi.org/10.1021/acs.chemmater.1c03166
Chem. Mater. 2021, 33, 9012−9092

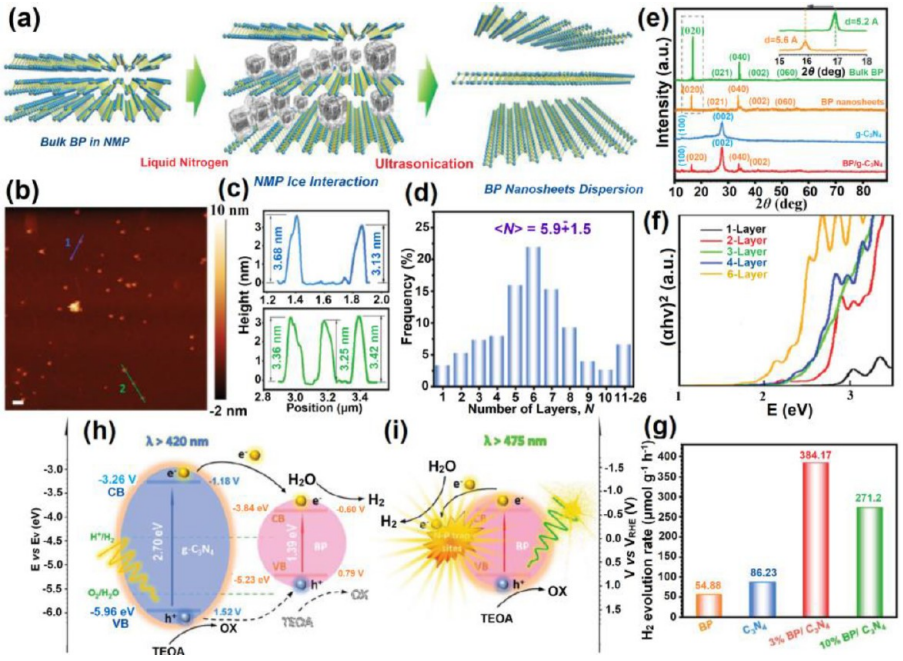

Figure 6. (a) Schematic illustration of the preparation of BP nanosheets with the NMP ice-assisted exfoliation method. (b) Tapping mode AFM topographical image of few-layer of BP nanosheets. (c) Height profiles of BP nanosheets along the blue line 1 and green line 2 in part (b). (d) Distribution of BP layers calculated from the height profiles of 150 BP nanosheets in AFM images. (e) XRD patterns of bulk BP, BP nanosheets, g-C_3N_4, and BP/g-C_3N_4 samples. The inset shows the amplification of XRD patterns of bulk BP and BP nanosheets in the lower-angle range, which is marked by the dashed rectangle (f). Theoretical Tauc-plot curves of BP with different layer numbers (1−4 and 6 layers). (h) Photocatalytic H_2 evolution rate achieved in the presence of BP (orange), g-C_3N_4 (blue), 3 wt % BP/g-C_3N_4 (red), 10 wt % BP/g-C_3N_4 (green), and 15 wt % BP/g-C_3N_4 (purple) photocatalysts under $\lambda > 420$ nm light irradiations. Schematic energy diagram of BP/g-C_3N_4 photocatalyst and proposed possible mechanism for the photocatalytic H_2 evolution under (h) $\lambda > 420$ nm and (i) $\lambda > 475$ nm light irradiation. Reprinted with permission from ref 182. Copyright 2019 Wiley-VCH.

CN was slightly shifted. The solid evidence of a P−N coordinate bond between two 2D heterostructures comes from solid-state ^{31}P NMR, which displayed the main peak at 17.1 ppm for P atoms in a BP sheet scaffold and showed two additional signals at −0.2 and 5.4 ppm due to P−N coordination. The UV−vis profile of BP showed absorption up to NIR (absorption edge at 1740 nm) (Figure 4e). The UV−vis of BP/CN after subtracting the absorbance of CN and BP evidenced NIR absorption of the materials. When tested for the hydrogen evolution in the presence of methanol as a sacrificial donor, the BP/CN in 1:4 weight ratio demonstrated a hydrogen evolution rate of 427 μmol g^{-1} h^{-1} under visible light irradiation ($\lambda > 420$ nm), while under identical conditions CN and BP show negligible hydrogen evolution (Figure 4f,g). Interestingly, under NIR illumination (>780 nm, 780−1800 nm, and 808 nm laser), a fair hydrogen evolution rate was maintained for BP/CN only, and no product was observed for pristine BP and CN (Figure 4h). Time-resolved diffuse reflectance (TDR) spectroscopy using 780 nm laser revealed that BP/CN heterostructure displayed a much longer lifetime (44 ps) compared to pristine BP (0.8 ps), suggesting the P−N coordinate bond at the interface acts as the trap site to facilitate hydrogen generation. Under visible irradiation, most of the charge is generated from the CN, and a small band gap of BP established a straddling gap (type-I heterojunction) with carbon nitride (Figure 4i). Mechanochemical synthesis using ball milling of red phosphorus (RP) to form BP followed by ball milling with carbon nitride was also found to form 2D−2D BP/CN heterostructure.[179] The assembled BP/CN hybrid demonstrated a hydrogen evolution rate (786 μmol h^{-1} g^{-1}) and RhB degradation (complete degradation within 25 min) even under the weak intensity of LED (440−445 nm) and was comparable to BP/CN hybrid realized using a solvent assisted exfoliation. This synthetic approach provides an opportunity for scalable and low-cost production of photocatalysts.

The solvent exfoliation of bulk BP under strong sonication and air leads to oxidation and nonuniform fragmentation of BP sheets, resulting in the formation of quantum dots with low photocatalytic performance. Ran et al. devised a method to exfoliate bulk BP in ethanol under intermittent low sonication power, inert atmosphere, and low temperature.[180] The 2D/2D vdW heterojunction of few-layered phosphorene (FP; thickness ≈ 5−6 nm, lateral sizes ≈ 100−450 nm) and g-C_3N_4 nanosheet (CNS; prepared by thermal annealing of bulk g-C_3N_4 powder at 500 °C) denoted as PCN were realized by mixing both components in a mortar under an inert environment. The shifting of P 2p XPS signals (≈0.8 eV) and XANES P K-edge of PCN toward a lower binding energy value suggest electron migration from CNS to FP to form a p−n type heterojunction (Figure 5a). At the same time, the C K-edge and N K-edge exhibited a positive shift due to the *n*-type conductivity of g-C_3N_4, which concomitantly transfers electrons to electron deficient FP in the heterojunction (Figure 5b). This assumption was confirmed by DFT calculations which reveal the work functions (Φ) of g-C_3N_4 and phosphorene were 4.69 and 5.01 eV, respectively. Due to the higher Fermi level (E_{vac}- Φ) of g-C_3N_4, the electrons are expected to migrate from g-C_3N_4 to FP. The 2D/2D FP/CNS vdW heterojunction with 1.8 wt % of FP displayed an H_2 evolution rate of 571 μmol h^{-1} g^{-1}, which was higher than 1.8

https://doi.org/10.1021/acs.chemmater.1c03166
Chem. Mater. 2021, 33, 9012−9092

wt % Pt loaded CNS (1.8 Pt-CN, 548 μmol h^{-1} g^{-1}) and the highest among metal-free catalysts (Figure 5c). Even though with the addition of FP the visible light absorption gradually increased, the photoactivity decreased beyond 1.8 wt % due to occupancy of active sites and shielded light absorption by the phosphorene (Figure 5d). Steady-state surface photovoltage (SPV) spectra and transient-state SPV (TSSPV) spectra of 0.0PCN and 1.8PCN demonstrated a higher photovoltage on the surface of 1.8PCN, corroborating the fact that the presence of FP can efficiently promote the dissociation of photoinduced charge carriers in CNS (Figure 5e,f). The effective interfacial contact and straddled type-I heterojunction in 2D/2D PCN vdW heterostructure offered better charge separation to accelerate catalytic performance (Figure 5g,h).

The conventional approach for phosphorene synthesis from BP using solvent-assisted exfoliations is challenging due to long hours of synthesis of poor-quality sheets. As van der Waals interaction between P atoms in BP is much stronger than graphene and other 2D structures, a strong sonication power and longer hours are usually needed, which break the sheets and reduce their lateral size as well.[181] Zhang et al. present an intelligent idea of ice-assisted exfoliation to reduce the processing time and increase phosphorene yield.[182] In this synthesis, a dispersion of bulk BP in NMP was frozen using liquid N_2 (Figure 6a). Due to the growth of NMP crystals in between BP sheets, the van der Waals interaction gradually weakens, and mild sonication in the next step can easily exfoliate the BP sheets. By employing this approach, the total time required for the sonication can be reduced up to 2 h at 70 W sonication power with a significantly high 75% yield. The obtained BP sheets have excellent uniformity with a thickness distribution of 93% (mean numbers of layer = 5.9 ± 1.5) and a lateral size of 50 nm to 3 μm (Figure 6b−d). When coupled with g-C_3N_4 in IPA, a well-designed 2D/2D heterojunction was established, evident from TEM and STEM images. Interestingly, no XPS peak corresponding to oxidized P_XO_y species was detected in pristine BP or BP/g-C_3N_4 ascribed to nonoxidative exfoliation of BP. However, the P 2p XPS signal was shifted to lower binding energy due to charge transfer from g-C_3N_4 to BP. After ice-assisted exfoliation, the XRD peak at 16.95° for bulk BP was downshifted to 15.89°, corresponding to interplanar distances of 5.2 and 5.6 Å, respectively, substantiating that intercalation of NMP molecules assists exfoliation of BP (Figure 6e). Due to the formation of few-layered sheets, the BP displayed a band gap of ≈1.39 eV also verified with DFT while the composite still has excellent visible (band edge at 474 nm) to NIR absorption (band tail) (Figure 6f). Using 3% BP/g-C_3N_4 as a photocatalyst under visible light (λ>420 nm), the H_2 generation rate was found to be 384.17 μmol g^{-1} h^{-1}, almost 7 and 4.5 times those obtained from pristine BP (54.88 μmol g^{-1} h^{-1}) and g-C_3N_4 (86.23 μmol g^{-1} h^{-1}) (Figure 6g). The introduction of g-C_3N_4 in the BP/g-C_3N_4 heterostructure not only improves the photocatalytic performance but also strengthens the stability of the material. This was evident from P 2p XPS spectra of BP and BP/g-C_3N_4 after a long reaction time, showing that 21.6 and 7.5 atm % of P transformed to P_XO_y, respectively. The excitation wavelength above 475 nm does not yield any product for pristine BP, g-C_3N_4, and 3% BP/g-C_3N_4 while the 10% BP/g-C_3N_4 vdW heterojunction still affords significant hydrogen (143.47 μmol g^{-1} h^{-1}), demonstrating that at high wavelength excitation and optimum phosphorus contents only BP contributes to the water reduction reaction while CN facilitates charge separation. The small semicircle in the Nyquist plot quenched PL intensity and shorter average PL lifetime (486 ± 5 ns) of BP/g-C_3N_4 compared to its constituting components validates better charge separation in the vdW heterostructure. Valence band edge calculation by UPS followed by determination of CB using optical band gap demonstrates that the CB of BP is more positive (−0.60 V) than that of g-C_3N_4 (−1.18 V). So, electrons can be easily transferred from CB of g-C_3N4 to BP and reducing protons (H^+/H_2; 0.00 eV vs RHE at pH 0) (Figure 6h,i).

2.2. Carbon Nitride−Red Phosphorus (RP). Another stable allotrope of phosphorus named red phosphorus (RP) is emerging as a new photocatalytic material due to its metal-free earth-abundant nature and well-tuned band positions with visible absorption onset extended to 700 nm.[183−187] Among four electronic structures (amorphous, Hittorf, fibrous, tubular), Hittorf's and fibrous phosphorus are important, consisting of polymeric tubular repeating units with a pentagonal cross-section. Due to its more reductive CB for water reduction and sufficient positive VB, RP is a winning candidate among the phosphorus family. Fibrous red P (1.7 eV) demonstrated the optimum photocatalytic performance with the highest reported H_2 evolution record among the elemental photocatalysts such as silicon, boron, and sulfur.[184,188] However, in the viewpoint of 2D structure, Hittorf's phosphorus in which double tube layers are stacked in the *c* direction and held together via vdW forces is important, can attain a layered structure, and can be exfoliated in few layers to monolayers.[189−191] The binding energy to exfoliate bulk Hittorf's phosphorus to single layer Hittorf's phosphorene is 0.35 J m^{-2}, which is significantly lower than that of BP (0.40 J m^{-2}).[192] Regrettably, Hittorf's phosphorene has a theoretical direct band gap (2.52 eV) while Hittorf's phosphorus exhibits an indirect band gap (2.17 eV) which makes exfoliation or fabrication of single to few layers a desirable step. Although the theoretical mobility of Hittorf's phosphorene is 3000−7000 cm^2 V^{-1} s^{-1}, which is comparable to that of black phosphorene (10000 cm^2 V^{-1} s^{-1}), the experimental performance is far too low due to prodigious stacking.[144,192−194]

Recently, research has been intensified to develop RP based photocatalytic materials using various approaches such as hydrothermal, high-temperature vapor deposition, ball milling, etc.[195] Though RP alone is an excellent photocatalytic material, its performance is confined due to sluggish charge mobility both in few-layered and in the bulk form. Heterojunction formation with other semiconductors such as TiO_2, graphene oxide, MOF, CdS, ZnO, etc. has been identified as a promising approach to enhance photocatalytic performance.[196−203] For example, RP was deposited on the TiO_2 nanofibers by the vapor deposition method and displayed excellent performance for H_2 evolution from pure water.[204] The heterojunction of 2D BP with 2D RP in Z scheme or type-I configuration is an emerging approach to make an all-inorganic heterojunction.[158,205] Liu et al. demonstrated that BP/RP 2D/2D Z-scheme catalyst can self-sustain the water splitting performance without any sacrificial donor.[206] However, the reaction rate and the product yield remain low in these approaches.

Coupling of RP with g-C_3N_4 has been found to increase the photocatalytic performance due to synergistic absorption, trap passivation, increased mobility, and better charge separation.[207−209] Jing et al. demonstrated that the introduction of ultrasmall RP particles in the g-C_3N_4 scaffold can minimize the number of defects in the g-C_3N_4 structure due to the formation

https://doi.org/10.1021/acs.chemmater.1c03166
Chem. Mater. 2021, 33, 9012−9092

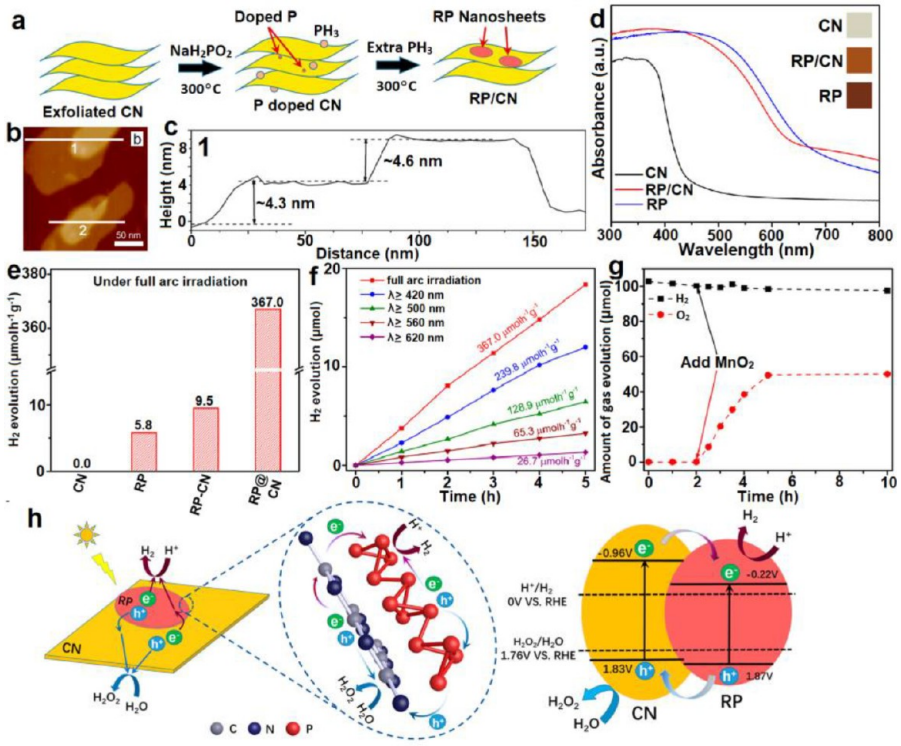

Figure 7. (a) Schematic diagram for fabricating the 2D/2D RP/CN heterostructure. (b) AFM image of RP/CN. (c) Corresponding height profiles along the denoted lines. (d) UV−vis spectra for CN nanosheets, RP/CN, and commercial RP (inset, the digital photographs). (e) H_2 evolution rates of as-prepared samples under full arc irradiation. (f) H_2 evolution rates of RP/CN under the incident light with varied wavelength ranges. (g) H_2 and O_2 production over time after the light was turned off (MnO_2 added into the reaction suspension after the first 2 h). (h) Schematic diagram of a photocatalytic process for RP/CN. Reprinted with permission from ref 212. Copyright 2020 American Chemical Society.

of P−C and P−N bonds, resulting in record hydrogen evolution performance than previously reported for carbon nitride−phosphorus based systems (2565 μmol g^{-1} h^{-1}).[210] In another report, [001]-oriented Hittorf's phosphorus (HP) nanorods were fabricated on g-C_3N_4 using vapor deposition approach reaching a H_2 evolution rate (HER) of 33.2 μmol h^{-1} from pure water.[211]

The 2D/2D vdW heterojunction of RP and g-C_3N_4 is particularly important as it can overcome the shortcomings of other dimensionalities due to intimate electronic contact between two semiconductor surfaces. Wang and coauthors synthesized 2D/2D RP/CN vdW catalysts via low temperature (300 °C) in situ phosphorizations on CN sheets (prepared via hydrothermal exfoliation of bulk CN in NH_4OH) (Figure 7a).[212] The thermal decomposition of NaH_2PO_2 followed by doping and deposition leads to deposition of a uniformly thick RP layer (~4.6 nm) on CN (Figure 7b,c). The HR-TEM and corresponding EDX elemental mapping display the presence of RP nanosheet fragments on the surface of CN. The XRD peak of CN was significantly suppressed and slightly shifted after the formation of the heterostructure, suggesting dense surface coverage via RP. The RP/CN vdW showed a broad visible absorption extended up to NIR while XPS peaks in the C 1s and N 1s region were shifted toward a positive value, suggesting better intimate contact and charge transfer (Figure 7d). The conduction and the valence band positions of CN and RP determined using the Mott−Schottky plot were −0.96 and 1.83 vs RHE and −0.22 and 1.87 V, respectively. In comparison to constituting elements and physical mixture of RP and CN, the RP/CN vdW heterostructure displayed an exception with the enhancement of H_2 evolution, reaching a value of 367.0 μmol g^{-1} h^{-1} (Figure 7e). Further, the RP/CN displayed activity in all visible light ranges up to 620 nm with long hour stability (Figure 7f). However, the stability of the catalyst was reduced after a long run at high temperatures due to the formation of H_2O_2 instead of O_2, oxidizing the RP surface. To validate this hypothesis, when MnO_2 was introduced into the reaction system, the O_2 evolution rate was increased due to the decomposition of H_2O_2 in the presence of MnO_2 (Figure 7g). A significant PL quenching and decreased charge transfer resistance suggest a better charge separation in the RP/CN vdW heterostructure. Due to more negative CB and VB of CN, a type II (staggered) heterojunction was formed where the electron flows from CB of CN to RP, and the holes move in the opposite direction, leading to better carriers separation (Figure 7h).

2.3. Carbon Nitride−Antimonene. Antimonene (Sb) is a relatively newly discovered 2D elemental semiconductor that gained significant attention due to its remarkable electronic and optical properties.[213,214] The 2D structure of antimonene was first predicted theoretically in 2015 by Zhang et al. along with arsenene (As).[215] However, the experimental synthesis of Sb was only realized in 2016 by Gibaja et al. by liquid-phase exfoliation of Sb crystal in a water/ethanol mixture.[216] After that, several procedures to exfoliate Sb have been developed, including mechanochemical and sonochemical methods.[217,218] Additionally, high-quality Sb up to a single atom thickness can be synthesized using epitaxial growth, which includes van der Waals epitaxy and molecular beam epitaxy (MBE).[219] Employing harsh sonication conditions, using NMP, polyols such as PEG, and surfactants, well stabilized antimonene quantum dots can be isolated.[220−222] Van der Waals epitaxial

https://doi.org/10.1021/acs.chemmater.1c03166
Chem. Mater. 2021, 33, 9012−9092

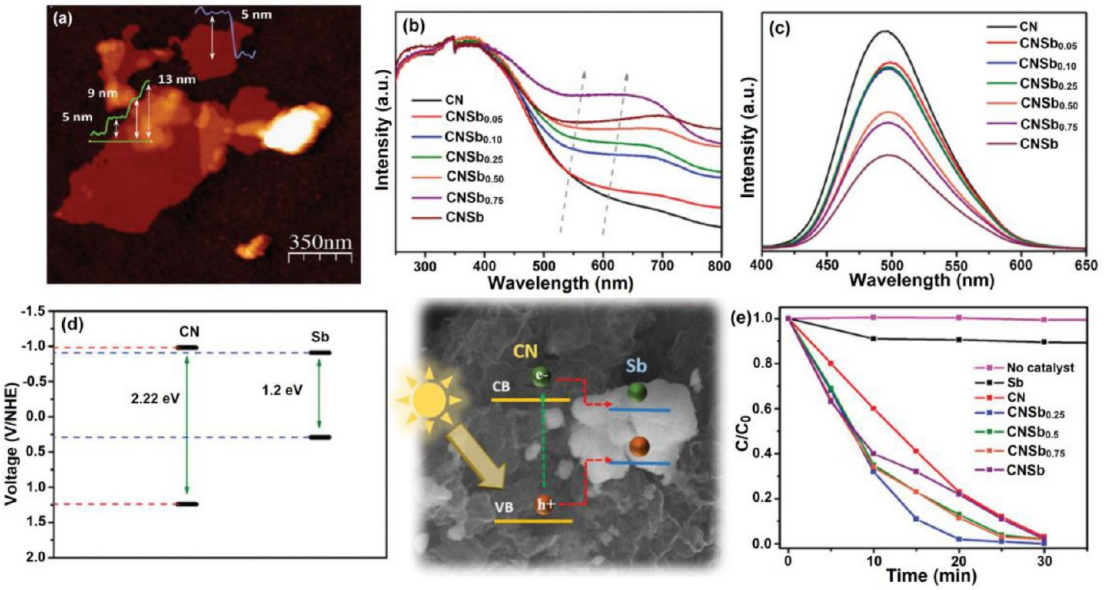

Figure 8. (a) AFM image of two flakes of the CNSb heterostructure with their topographic profiles. (b) UV−vis absorbance spectra. (c) Photoluminescence spectra of $CNSb_x$ heterostructures. (d) Derived band structure of the $CNSb_x$ heterostructure. (e) RhB degradation curves for $CNSb_x$ heterostructures. Reprinted with permission from ref 229. Copyright 2018 Wiley-VCH.

growth, which involves the heating of the substrate in one zone and Ar/H_2 assisted deposition to the relatively cooler substrate, is particularly important due to easy fabrication, easy deposition on any substrate, etc.

Belonging from the same phosphorus VA group, Sb possesses the same allotropic structure as BP with a theoretically predicted band gap of 1.2 eV. Contrary to BP, the Sb is relatively stable under oxygen and atmospheric conditions, making them a suitable candidate for several applications. As it exhibits a small tunable band gap (0 to 2.28 eV) and high carrier mobility, it is complementing graphene for optoelectronic applications, including the hole transport layer in solar cells, thermophotovoltaic devices, electrocatalysis (CO_2 reduction reaction to formates), energy storage devices, photodetectors, etc.[218,223−226] However, due to the small band gap, the reports on the experimental photocatalytic application of antimonene are sparse and limited.[227] Ji et al. synthesized an Sb and BP hybrid nanosheet (HNSs) based Z-scheme artificial photosynthetic system for the reduction of CO_2.[228] In this system Cp*Rh(phen)Cl was used as an electron shuttle with PEI-PEG-C18-M as a "double-side tap" in the presence of $NAD(H^+)$ and enzymes.

Until now, only one report by Barrio et al. had existed on the heterojunction of Sb and g-C_3N_4.[229] In this work, the authors used 2D sheets of g-C_3N_4 and few-layered flakes of Sb ($CNSb_x$) to fabricate a 2D/2D vdW heterojunction (Figure 8, Table 1). The AFM images of CNSbx displayed average lateral dimensions of ≈1 μm and an average thickness of ≈5 nm (Figure 8a). Characteristic XRD peaks of g-C_3N_4 were gradually decreased after the formation of a heterojunction while absorbance of CNSb was increased, extending up to 800 nm (Figure 8b). At the same time the PL intensity was quenched for the CNSbx composites, demonstrating reduced radiative recombination (Figure 8c). The calculation of band energies using the Mott−Schottky measurement confirmed that the CB of CN was situated at −0.98 V while for Sb it was at −0.91 V vs NHE. Thus, the electron can move to Sb without any applied field (Figure 8d and schematic illustration). Photocatalytic testing of $CNSb_{0.25}$ catalysts using RhB as a model pollutant offered a complete degradation within 20 min (Figure 8e). The improved activity was due to better charge injection from CN to Sb, which forms a type-I heterojunction with CN. Elucidation of the reaction mechanism using triethanolamine (TEOA) as a hole scavenger and $AgNO_3$ as an electron scavenger demonstrates that N-deethylation of RhB to the N-deethylated noncolored compound is catalyzed via photogenerated holes in the CB of g-C_3N_4.

3. CARBON NITRIDE-MXENES

MXene is a family of transition metal carbides, nitrides, and carbo-nitrides having layered 2D structures and the general formula $M_{n+1}X_nT_x$, where n is 1−3, M is a transition metal (Ti, Cr, Nb, Sc, Mo, etc.), X is carbon/nitrogen, T_x is a surface-oriented functional group (−OH, −O, and −F), their numbers per empirical units. In 2011, Gogotsi et al. discovered $Ti_3C_2T_x$ MXenes with attractive properties such as high chemical stability, hydrophilicity, and good electrical conductivity.[230] MXenes are 2D materials prepared by etching the A (aluminum) layers from the MAX phase, where M is a transition metal, A is an A-group element such as Al, and X is the C or N element. Since then, they have been of great interest for many applications such as energy storage, catalysis, and biomedicine.[231−234] Additionally, theoretical studies have shown that MXenes have near-zero Gibb's free energy with a low Fermi energy, which is excellent for application as an electrocatalyst in HER and OER reactions.[235] The broad absorption of MXenes until the NIR region and the ability to promote charge transfer by accepting electrons make them a very promising material. Despite all the remarkable properties, MXene has a few shortcomings such as low work function, limited thermal stability, and highly exposed metal atoms on the surface.[236]

The conductive nature of MXene prevented its exploration in photocatalysis until 2014, when the first report appeared, displaying $Ti_3C_2T_x$ has superb MB adsorption and degradation

https://doi.org/10.1021/acs.chemmater.1c03166
Chem. Mater. 2021, 33, 9012−9092

Table 1. 2D/2D Carbon Nitride-Phosphorous/Antimonene Based Heterojunction Photocatalysts

photocatalyst	synthesis	application	light source	AQY/STH	remarks	ref
		Black Phosphorus				
Ni_2P@BP/C_3N_4	Ni_2P@BP NSs were prepared via a solvothermal method: $NiCl_2 \cdot 6H_2O$, BP NSs dispersed in DMF were hydrothermally treated at 160 °C for 3 h.	Photocatalytic H_2 evolution	300 W Xe lamp ($\lambda \geq 420$ nm)	2.8% (420 nm)	H_2—858.2 μmol g^{-1} h^{-1} (Ni_2P@BP/CN) ~50.5 times of CN (17.2 μmol g^{-1} h^{-1})	169
Black phosphorus/graphitic carbon nitride (BP/CN)	CN and BP in NMP were sonicated together.	Photocatalytic H_2 evolution		STH—1.51% AQE—3.18% (420 nm) 1.1% (780 nm)	H_2—427 μmol g^{-1} h^{-1} (BP/CN) 101 μmol g^{-1} h^{-1}—>780 nm for 3 h	178
BP/CN	BP was synthesized by high-energy ball milling. BP/CN was synthesized by ball milling BP and CN together at 500 rpm for 5 h.	Photocatalytic H_2 evolution and RhB degradation	Blue LED lamp (λ = 440−445 nm)	-	H_2—786 μmol g^{-1} h^{-1} (10% BP/CN) CN—negligible 5% BP/CN—complete RhB degradation in 25 min CN—negligible	179
Phosphorene/g-C_3N_4 (PCN)	Mechanical mixing of phosphorene and g-C_3N_4 in an agate mortar in the glovebox.	Photocatalytic H_2 evolution	300 W Xe arc lamp (λ > 400 nm)	1.2% (420 nm)	H_2—571 μmol g^{-1} h^{-1}, 1330% times of CNS, better than 1.8 wt % Pt-CNS (548 μmol g^{-1} h^{-1})	180
Black phosphorus/graphitic carbon nitride (BP-CN)	BP and CN nanosheet dispersion in NMP was ultrasonicated for 4 h.	Photocatalytic inactivation of *E. coli*	300 W Xe lamp (λ > 400 nm)	N.A.	~7 times better log inactivation efficiency of *E. coli* compared to pure CN	181
Black phosphorus (BP)/graphitic carbon nitride (g-C_3N_4) BP/g-C_3N_4	g-C_3N_4 powder and BP nanosheet mixed in IPA.	Photocatalytic H_2 evolution	300 W Xe lamp ($\lambda \geq 420$ nm)	-	H_2—384.17 μmol g^{-1} h^{-1} (BP/g-C_3N_4) ~4.5 times higher than g-C_3N_4 (86.23 μmol g^{-1} h^{-1})	182
		Red Phosphorus/Antimonene				
Carbon nitride/red phosphorus/molybdenum disulfide g-C_3N_4/RP/MoS_2	The RP loaded g-C_3N_4 was prepared by thermal decomposition of monohydrate sodium hypophosphite in the presence of g-C_3N_4 in an Ar gas atmosphere.	Photocatalytic H_2 evolution	300 W Xe lamp ($\lambda \geq 420$ nm)	-	H_2—515.8 μmol g^{-1} after 2 h ~4.4 times of g-C_3N_4/RP (3.18 μmol g^{-1})	209
RP/CN	In situ phosphorization: 2D CN and NaH_2PO_2 were mixed, ground, and heated at 300 °C for 2 h.	Photocatalytic H_2 evolution	300 W Hg lamp ($\lambda \geq 420$ nm)	-	H_2—367.0 μmol g^{-1} h^{-1} (RP/CN) CN—0 RP—5.8 μmol g^{-1} h^{-1}	212
Carbon nitride/antimonene ($CNSb_x$)	g-C_3N_4 and ball-milled Sb were mixed and ultrasonicated.	Photocatalytic degradation of RhB and *p*-nitrophenol (*p*-NP)	White light	-	$CNSb_{0.25}$—complete degradation of RhB in 20 min $CNSb_{0.10}$—complete degradation of p-NP in 120 min	229

https://doi.org/10.1021/acs.chemmater.1c03166
Chem. Mater. 2021, 33, 9012−9092

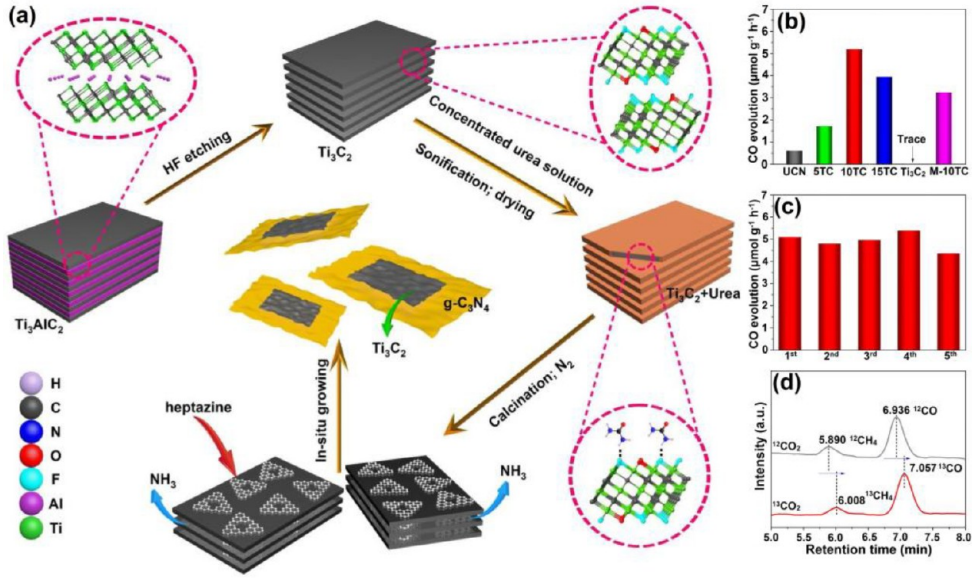

Figure 9. Schematic illustration for the fabrication process of the ultrathin 2D/2D Ti_3C_2/g-C_3N_4 nanosheets heterojunction. (b) Photocatalytic CO_2 reduction performance of as-prepared samples. (c) Cycling tests over the 10TC sample. (d) GC−MS analysis of products from photoreduction of CO_2 over 10TC using labeled $^{12}CO_2$ and $^{13}CO_2$ as the carbon sources. Reprinted with permission from ref 260. Copyright 2020 Elsevier.

ability.[237] The photocatalytic effect was assumed due to the presence of titanium hydroxide and/or TiO_2. Since then, a plethora of reports has been published using MXene as charge transporters, cocatalysts, or modified MXenes to generate photoactive centers.[238−241] Further, the formation of the MXene nanostructure with other semiconductors has been widely explored for all sorts of photocatalytic reactions such as water splitting, volatile organic chemicals degradation, CO_2 reduction, N_2 reduction reactions, etc.[238,242−244] Several variants of MXene have been discovered in the past few years such as Mo_2CT_x, Zr_3C_2, Hf_3C_2, and double-M MXenes ($Mo_2Ti_2C_3T_x$, $Cr_2TiC_2T_x$, and $Mo_2TiC_2T_x$), showing advanced physicochemical properties.[245−247] The introduction of semiconductive properties in MXenes and the possibility of fabrication of single-atom catalysts (SACs) open the gate to developing profoundly active and product selective catalysts.[248−254]

The formation of a heterostructure by coupling of 2D MXene with another 2D material such as g-C_3N_4 widens the possibility of further enhancing the activity and efficiency as a photocatalyst.[255−257] The presence of plenty of surface functional groups such as −OH, −O, and −F provides a growing/interacting platform for other semiconductors without compromising electronic mobility.[258] Due to its inherent architecture, this layered heterostructure will ensure intimate interfacial contact, promote fast separation, and prolong the lifetime of the induced charge carriers and greater exposed active sites. For example, Lin et al. used Ti_3C_2 MXene as an electron acceptor and O-doped g-C_3N_4 as a visible absorbing semiconductor to design a 2D/2D Schottky junction and observed improved H_2 production.[259] Yang et al. synthesized an ultrathin Ti_3C_2 MXene and g-$C_3N_4$2D/2D heterojunction via calcination of an MXene and g-C_3N_4 mixture, as shown in Figure 9a.[260] The urea molecules are well adsorbed on the surface of the exfoliated Ti_3C_2, which, after calcination at high temperature, forms ultrathin nanosheets of g-C_3N_4 over MXene. The photoactivity was estimated by subjecting the synthesized material to photoreduction of CO_2 and OER (Figure 9b). Interestingly, both MXene and pure g-C_3N_4 showed almost no activity for the former but indicated an improved activity with increasing MXene content to an optimum level.

Additionally, the optimized 10TC indicated stability up to 5 cycles when subjected to OER (Figure 9c). Furthermore, using isotopes of carbon (^{13}C and ^{12}C) and gas chromatography−mass spectrometry (GC−MS), it was confirmed that the produced products were originated from the photoreduction of CO_2 (Figure 9d). The electronic band structure revealed that due to intimate contact between g-C_3N_4 and Ti_3C_2 MXene, E_f was organized to equilibrium with $E_{f,equ}$ = −0.95 V. The final equilibrium was brought about by a positive shifting of g-C_3N_4 and a negative shifting of Ti_3C_2 MXene. Thus, the remarkable photoactivity shown can be due to fast transfer and extraordinary capture of the photogenerated electrons to reduce CO_2. Various other modifications on MXene or the g-C_3N_4 were carried out for more enhancement. For example, g-C_3N_4 was functionalized by protonation. This results in protonated g-C_3N_4 that is positively charged with a hyped ionic conductivity and electronic band gap shift.[261,262] Other modifications include growing metal oxides such as TiO_2 with g-C_3N_4 and then integrating with MXene via an electrostatic interaction, creating a 2D/2D vdW heterostructure for convenient electron transfer and good interfacial contact. Besides, black phosphorus quantum dots (BQs) with high absorption coefficients, tunable band gap, high hole mobility, and excellent quantum confinement effects have also been employed alongside g-C_3N_4 nanosheets.[263,264] However, MXene is used as an intermediate to fast track transmission of photogenerated charges and also to overcome the shortcomings of BQ/g-C_3N_4 such as low interfacial contact and low charge carrier mobility.[265] Modifications in MXene such as creating 3-D hollow morphological structure and oxygen vacancies (OV) are also done for superior performance.[266,267] For example, Tahir et al. not only observed that the

https://doi.org/10.1021/acs.chemmater.1c03166
Chem. Mater. 2021, 33, 9012−9092

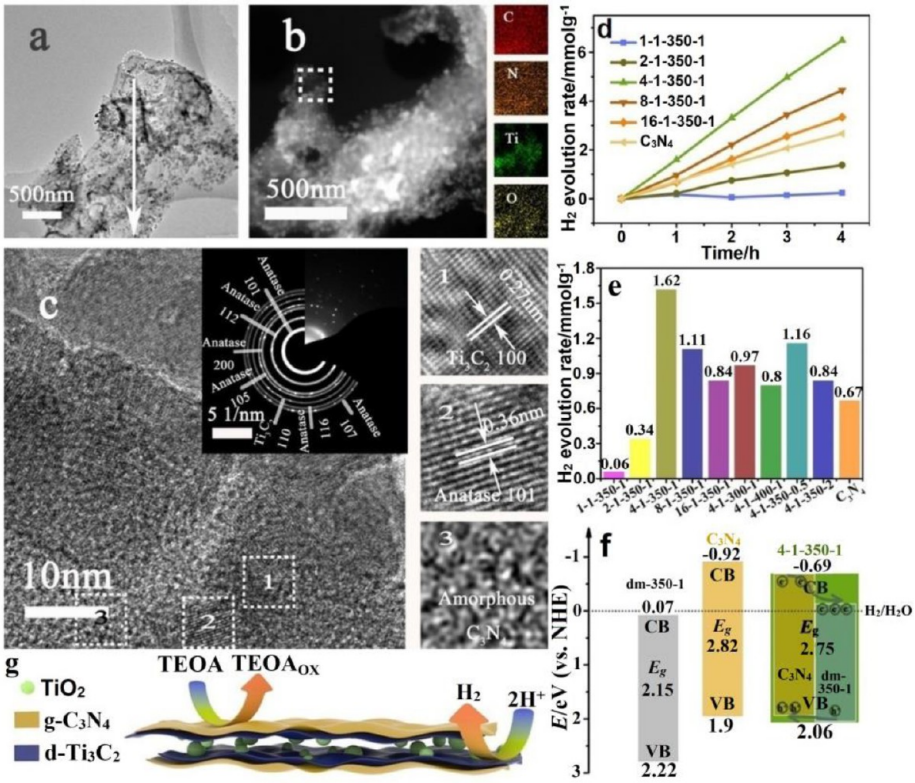

Figure 10. (a) TEM image. (b) Drift-corrected spectrum and elemental mapping. (c) HR-TEM and SAED images of 4-1-350-1. (d) Photocatalytic H_2 evolution rate of the samples with different g-C_3N_4/d-Ti_3C_2 mass ratio. (e) Comparison of the photocatalytic H_2 evolution rate of all the samples. (f) Band structure alignments of partially oxidized Ti_3C_2, pristine g-C_3N_4, and composite 4-1-350-1. (g) Simulated microstructure of the composite sample 4-1-350-1. Reprinted with permission from ref 268. Copyright 2018 Wiley-VCH.

creation of oxygen vacant sites in MXene enhances the optical absorption and charge transportation but also found that, due to high electron conductivity, the synthesized material showed promising results for selective CO_2 methanation.[267]

Other variations in MXene such as delamination (d-Ti_3C_2) are performed to provide a homogeneous and uniform distribution while making composites with g-C_3N_4.[268] The thermal treatment of d-Ti_3C_2 and g-C_3N_4 generates ternary Ti_3C_2/TiO_2/g-C_3N_4 nanocomposites where Ti_3C_2 and g-C_3N_4 were glued together with TiO_2 nanoparticles derived from partial degradation of MXene. The introduction of nanoparticles in between 2D/2D interfaces ensures better electron−hole separation and physicochemical stability. As can be seen in Figure 10a (Table 2), the TEM image of d-Ti_3C_2 and TiO_2/g-C_3N_4 mixed in a 4:1 ratio and calcined at 350 °C for 1 h (4-1-350-1) has an ultrathin layer which acts as a support and also facilitates fast charge transfer. The elemental composition, SAED pattern, and *d*-spacings projected intimate contact between TiO_2 and d-Ti_3C_2 and g-C_3N_4 (Figure 10b,c). The increased visible absorption and photocurrent density justify the excellent charge generation and subsequent separation. Photocatalytic water splitting reaction revealed that the sample 4-1-350-1, prepared by using g-C_3N_4/d-Ti_3C_2 in a mass ratio of 4:1 and calcined at 350 °C for 1 h, gave a maximum H_2 evolution (324.2 μmol) after 4 h (1.62 mmol h^{-1} g^{-1}) with an AQE of 4.16% at 420 nm (Figure 10d,e). The cyclic run using the optimized 4-1-350-1 sample demonstrated high stability up to 12 h with maximum H_2 evolution (302.7 μmol). This significant enhancement of photosplitting of water can be ascribed to an appropriate band alignment between partially oxidized *d*-Ti_3C_2 and g-C_3N_4, forming a type-II heterojunction whereby an excellent system of charge transfer occurs along as a partially oxidized *d*-Ti_3C_2 electron trap, preventing the charge recombination (Figure 10f,g).

4. CARBON NITRIDE−METAL OXIDE 2D/2D vdW STRUCTURES

Metal oxides showcase strong photocatalytic activities and have been exhaustively investigated in the past few decades.[35,270,271] This results from the ability to grow and develop nanomaterials with a certain type of structure, orientation, and morphology that can improve catalytic performance.[272] Metal oxides such as TiO_2, CeO_2, ZnO, WO_3, and Fe_2O_3 exhibit properties such as wide band gaps enabling photon absorption, the formation of charge carriers that have the potential to oxidize and/or reduce on the surface, and the ability to perform charge separation.[273−275] Additionally, these metal oxides are extensively used due to their stability, wide abundance, and biocompatibility.[276] Some of these transition metal oxides such as TiO_2 and ZnO have electronic structures that are either completely occupied d^{10} or empty d^0 orbitals. Electronic excitation of charges after absorbing photons occurs from the valence band to the conduction band, formed from metal 3d or 4s and oxygen 2p. Consequently, these metal oxides show potential for photocatalytic applications due to this excitation and separation of charges.[277]

However, these materials suffer from low efficiency due to high recombination and absorption only in the UV region of the solar spectrum.[50] Moreover, using only a single component restricts its application due to difficulties in simultaneously

https://doi.org/10.1021/acs.chemmater.1c03166
Chem. Mater. 2021, 33, 9012−9092

Table 2. 2D/2D Carbon Nitride–MXene Based Heterojunction Photocatalysts

photocatalyst	synthesis	application	light source	AQY/STH	remarks	ref
		MXenes				
Ti_3C_2/g-C_3N_4	Electrostatic self-assembly approach: monolayer Ti_3C_2 solution and protonated g-C_3N_4 suspension were mixed for 0.5 h.	Photocatalytic H_2 evolution	200 W Hg lamp ($\lambda \geq$ 400 nm)	AQY—0.81% (400 nm)	H_2—25.8 μmol g^{-1} h^{-1} (1-TC/CN) Pristine g-C_3N_4—7.1 μmol g^{-1} h^{-1}	235
Ti_3C_2/porous g-C_3N_4	The suspension of the Ti_3C_2 nanolayer was mixed with the PCN nanolayer aqueous suspension.	Photocatalytic degradation of phenol	500 W Xe lamp ($\lambda \geq$ 420 nm)	-	Ti_3C_2/PCN-1/5—98.0% phenol degradation after 180 min BCN—25.0% phenol degradation after 180 min	256
2D/2D/0D TiO_2/C_3N_4/Ti_3C_2 S-scheme photocatalyst	TiO_2 nanosheets and urea were calcined at 520 °C for 1.5 h.	Photocatalytic CO_2 reduction	350 W Xe lamp	-	CO—4.39 μmol g^{-1} h^{-1} (T–CN–TC) CH_4—1.20 μmol g^{-1} h^{-1} (T–CN–TC) ~ 8 times of TiO_2	269
Ti_2C/g-C_3N_4	The g-C_3N_4 loaded with 2D Ti_2C was prepared by adding a specific amount of melamine into aqueous ethanol containing Ti_2C followed by calcining at 550 °C for 4 h.	Photocatalytic H_2 evolution	AM 1.5 light	4.3% (420 nm)	H_2—47.5 μmol h^{-1} (TiCN-0.4) 14.4 times as high as that of pure g-C_3N_4 (3.3 μmol h^{-1})	258
Ti_3C_2 MXene/O-doped g-C_3N_4	Electrostatic self-assembly: protonated O-doped g-C_3N_4 nanosheets and Ti_3C_2 MXene nanosheets were stirred together for 12 h.	Photocatalytic H_2 evolution	300 W Xe lamp	17.59% (405 nm); 6.53% (420 nm)	H_2—24 900 μmol g^{-1} h^{-1} (MX3/HCN) ~3 times of CN (5366 μmol g^{-1} h^{-1})	259
Ti_3C_2 MXene/g-C_3N_4	Urea and Ti_3C_2 mixture was calcined at 550 °C for 2 h.	Photocatalytic CO_2 reduction	3 W LED (420 nm)	-	CO—0.62 μmol g^{-1} h^{-1} (UCN) CH_4—0.021 μmol g^{-1} h^{-1} (UCN) CO—5.19 μmol g^{-1} h^{-1} (10TC) CH_4—0.044 μmol g^{-1} h^{-1} (10TC)	260
Accordion-like CS@g-C_3N_4/MX	Deacetylated chitosan and g-C_3N_4 were added with MXene solution, followed by the addition of glutaraldehyde as a binding agent.	Photocatalytic degradation of MB and RhB	250 W Xe lamp (400–800 nm)	-	~99% and 98.5% MB and RhB degradation in 40 min	262
Ti_3AlC_2 MAX cocatalyst with proton-rich C_3N_4	Ultrasonication method: f-C_3N_4 and OV-Ti_3AlC_2 were dispersed in methanol and were exfoliated and mixed via ultrasonication.	Photocatalytic CO_2 reduction	35 W high-intensity discharge (HID) lamp	10.84 (420 nm)	CH_4—786 μmol gcat^{-1} h^{-1} (OV-Ti_3AlC_2/f-C_3N_4) ~15.1-fold of g-C_3N_4 CO—145 μmol gcat^{-1} h^{-1} (OV-Ti_3AlC_2/f-C_3N_4)	267
d-Ti_3C_2/TiO_2/g-C_3N_4	d-Ti_3C_2 colloidal solution and g-C_3N_4 powder were mixed, freeze-dried, calcined at 350 °C for 1 h.	Photocatalytic H_2 evolution	300 W Xe lamp ($\lambda \geq$ 420 nm)	4.16% (420 nm)	H_2—324.2 μmol after 4 h pure g-C_3N_4—133.3 μmol after 4 h	268

https://doi.org/10.1021/acs.chemmater.1c03166
Chem. Mater. 2021, 33, 9012–9092

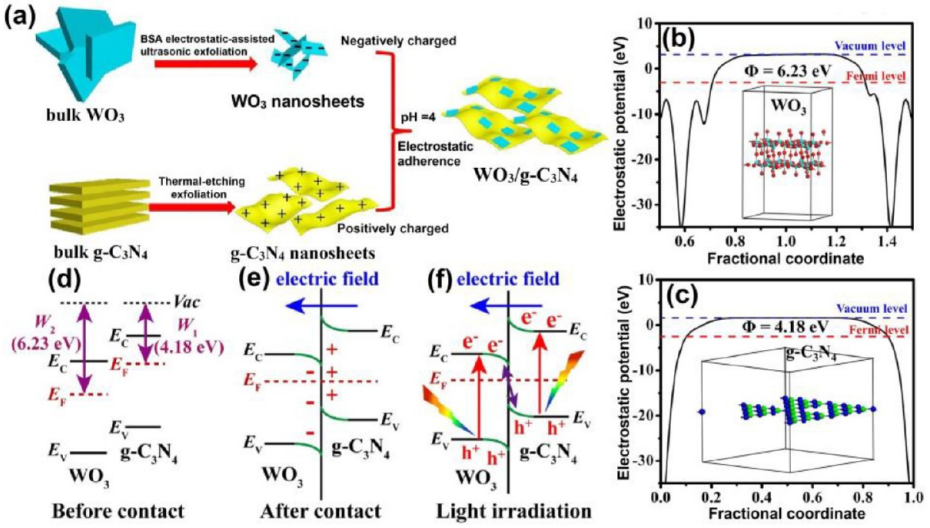

Figure 11. (a) Formation schematic diagram of 2D/2D WO_3/g-C_3N_4 heterojunctions by Coulomb electrostatic interaction. Electrostatic potentials of (b) WO_3 (001) surface and (c) g-C_3N_4 (001) surface. Insets show the structural models of the materials for DFT calculation. (d) Work functions of g-C_3N_4 and WO_3 before contact. (e) Internal electric field and band edge bending at the interface of WO_3/g-C_3N_4 after contact. (f) S-scheme charge transfer mechanism between WO_3 and g-C_3N_4 under light irradiation. Reprinted with permission from ref 294. Copyright 2019 Elsevier.

obtaining a strong visible light response and good redox property. g-C_3N_4 due to sp^2 hybridized C and N content forms conjugated planes, increasing the electrical conductivity, stability, and small band gap (2.7 eV).[278] However, g-C_3N_4 individually is moderately performing, and therefore, the use of metal oxides and g-C_3N_4 provides a favorable connection. The 2D/2D structure displays strong redox potential with active oxidation and reduction sites with well-separated charge carriers.[279] Furthermore, fabrication of such a 2D/2D vdW heterostructure is effective and advantageous compared to other hybrid features. It eliminates complications such as defects arising from point-to-point or point-to-face contact, light-shielding due to thick material, and long charge-transfer distance. For example, the construction of Z-scheme and S-scheme type band structure improves the efficiency of a catalyst by providing a seamless contact, unique morphological features, and proper band alignment, favoring the reaction mechanism.[81,280] Therefore, it can be inferred that the construction of a 2D/2D heterojunction is a smart way to improve photocatalytic performance by matching the band energies of different semiconductors.[281−283] Some of the 2D/2D heterojunctions of various metal oxides and carbon nitride are discussed in this section.

4.1. Carbon Nitride-WO_3. Tungsten trioxide (WO_3) has a narrow band gap of 2.4 eV and possesses suitable band edge potentials with a deep valence band. It is interesting because of its low cost, facile synthesis, resistance to photocorrosion, and strong stability in an aqueous solution. Therefore, it is one of the many important photocatalysts, especially for O_2 evolution reaction and wastewater treatment.[284,285] Despite its interesting properties, because of the high recombination of photoexcited charge carriers, the use of WO_3 is limited. There are various reports on the structural and surface modifications of WO_3 for enhancing the photocatalytic activity, such as smaller grain size that improves the charge carrier transport efficiency from the bulk to the surface.[286,287] Wicaksana et al. synthesized the crystalline nanostructure of WO_3 by a hydrothermal method to improve photoactivity.[288] However, intrinsic drawbacks of these metal oxides such as low quantum yield and poorly visible light harvesting still prevail.

The deep VB of WO_3 restricts its application in the reduction process, while for self-sustained photocatalysis, both oxidation and reduction are required. In this regard, hybrid semiconductor nanocomposites like g-C_3N_4 with negative CB forming heterojunctions such as S-scheme and Z-schemes are highly attractive due to the ease of transfer of light-induced charge carriers and fulfillment of the wide potential requirement.[40,280,289−291] Yang et al. constructed an ultrathin WO_3.H_2O/g-C_3N_4 nanosheets are based on direct Z scheme vdW heterojunctions for efficient water splitting.[292] The conduction band minimum (CBM) of WO_3 in the designed 2D/2D system is 0.5 eV higher than the valence band maximum (VBM) of g-C_3N_4, resulting in fast recombination of electrons from CBM of WO_3 with holes from the VBM of g-C_3N_4. Consequently, more holes in WO_3 VBM and more electrons in g-C_3N_4 are retained, leading to higher photocatalytic activity. Additionally, there is accelerated transportation of visible-light-induced charge carriers and strong absorption in the visible region. Liu et al. adopted a similar direct Z scheme of 2D/2D WO_3/g-C_3N_4 for H_2 production via additional modifications such as loading Pt in g-C_3N_4 and WO_3 nanosheets for hydrogen generation.[293] The synergistic and strong affinity between the coupled nanosheets exhibited a higher number of coordinated surface atoms boosting the H_2 production (862 μmol h^{-1}).[280]

For a similar application of photosplitting of water to H_2, Fu et al. synthesized a WO_3/g-C_3N_4 heterostructure.[294] A high and opposite zeta potential is observed, which is indicative of the strong Coulombic electrostatic attraction between 2D/2D WO_3 and g-C_3N_4 nanosheets. The formation of the 2D/2D nanosheets is shown in the schematic representation in Figure 11a. Theoretical DFT calculation of the designed system showed a higher work function (WF) of WO_3, which is indicative of charge transfer between the nanosheets (Figure 11b,c). Such a phenomenon results in a built-in electric field on the interface that significantly boosts the charge transfer

https://doi.org/10.1021/acs.chemmater.1c03166
Chem. Mater. 2021, 33, 9012−9092

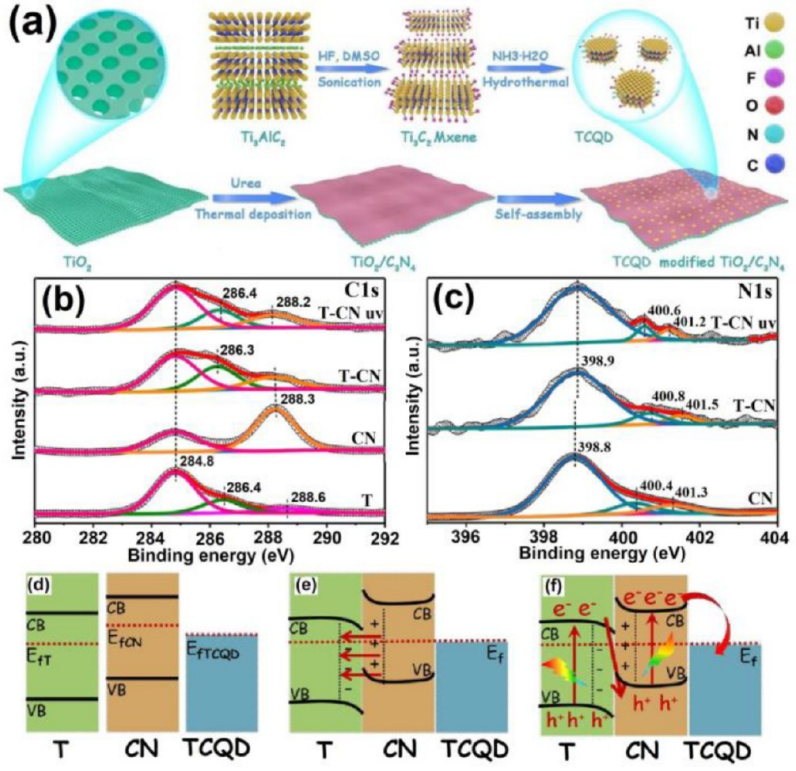

Figure 12. (a) Schematic of the synthesis of ultrathin TCQD anchored TiO_2/C_3N_4 core−shell nanosheets. Comparison of (b) C 1s and (c) N 1s XPS spectra for T, CN, T−CN, and T−CN−TC in the dark or under 365 nm LED irradiation. The S-scheme heterojunction of $TiO_2/C_3N_4/Ti_3C_2$ quantum dots: (d) before contact, (e) after contact, and (f) after contact upon irradiation and charge migration and separation. Reprinted with permission from ref 269. Copyright 2020 Elsevier.

efficiency. The close vicinity of WO_3 with higher WF (6.23 eV) and g-C_3N_4 with smaller WF (4.18 eV) creates a spontaneous transfer of electrons from the former to the latter until a Fermi-level equilibrium was reached. This results in band bending due to the gain and loss of electrons in WO_3 (downward) and g-C_3N_4 (upward), respectively (Figure 11d,e). Due to the S-scheme heterojunction, "useless" electrons and holes from the CB of WO_3 and VB of g-C_3N_4 get eliminated through recombination holding "useful" electrons (CB of g-C_3N_4) and holes (VB of WO_3) (Figure 11f). When employed as a photocatalyst for H_2 production, the constructed S-scheme 2D/2D WO_3/g-C_3N_4 heterojunction showed a remarkable performance 1.7 times higher than pristine g-C_3N_4. This enhanced efficiency can be attributed to the construction of a close contact step-scheme designed to remove "useless" charge carriers via a recombination process, leaving behind the "useful" electrons and holes for an excellent oxidation/reduction system.

4.2. Carbon Nitride-TiO_2. TiO_2 is an extensively and exhaustively used wide band gap semiconductor in photocatalytic and photoelectrochemical applications due to its excellent chemical stability, nontoxicity, wide abundance, and low cost.[295−297] However, the device's efficiency is limited because of its wide band gap nature, leading to underutilization of light resources and a high recombination rate. Various strategies have been adopted to overcome these issues, such as metal/nonmetal doping (Ag, Au, Ru, Cu, N, P, S, F, etc.), surface area modification, sensitization with organic and inorganic molecules, and fabrication of 1D, 2D, and 3D nanostructures.[298−302]

Building the heterojunction of two nanomaterials is one of the most pragmatic approaches for overcoming these drawbacks as it integrates the merits of the individual component.[303,304] For instance, He et al. designed a 2D/2D vdW heterojunction core−shell of TiO_2/C_3N_4 and electrostatically integrated MXene quantum dots (TCQD) for photoreduction of CO_2 (Figure 12a).[269] The XPS spectra elucidate the change in the concentration of electrons with a shift in C 1s and N 1s binding energies toward lower energy after UV illumination indicating an accumulation of electrons in CN and depletion in TiO_2(T) (Figure 12b,c). The designed S-scheme heterojunction between the TiO_2 and C_3N_4 provided strong redox capacity and an efficient transport channel for light-induced charges, whereas a Schottky heterojunction of C_3N_4 with TCQD provided a pathway for electron transport, thereby creating a spatial separation of charge carriers. The state of the electronic bands before the formation of the heterojunction revealed higher Fermi-level energy for CN compared to T and TCQD, which upon contact forms an equilibrium state due to spontaneous transfer of charges from CN to T and TCQD (Figure 12d,e). This phenomenon is accompanied by band bending and the creation of an internal electric field (IEF) at the interfaces. However, under solar irradiation, the light-induced separation of charges occurs in both T and CN (Figure 12f). The electrons at the CB of T combined with holes from VB of CN leave behind electrons in the CB of CN, which migrates to the TCQD to reduce CO_2 to useful hydrocarbon fuels. The multijunction system enhanced the photocatalytic activity through an efficient system of charge separation and transfer, and also an intimate contact of C_3N_4 with TCQD having

https://doi.org/10.1021/acs.chemmater.1c03166
Chem. Mater. 2021, 33, 9012−9092

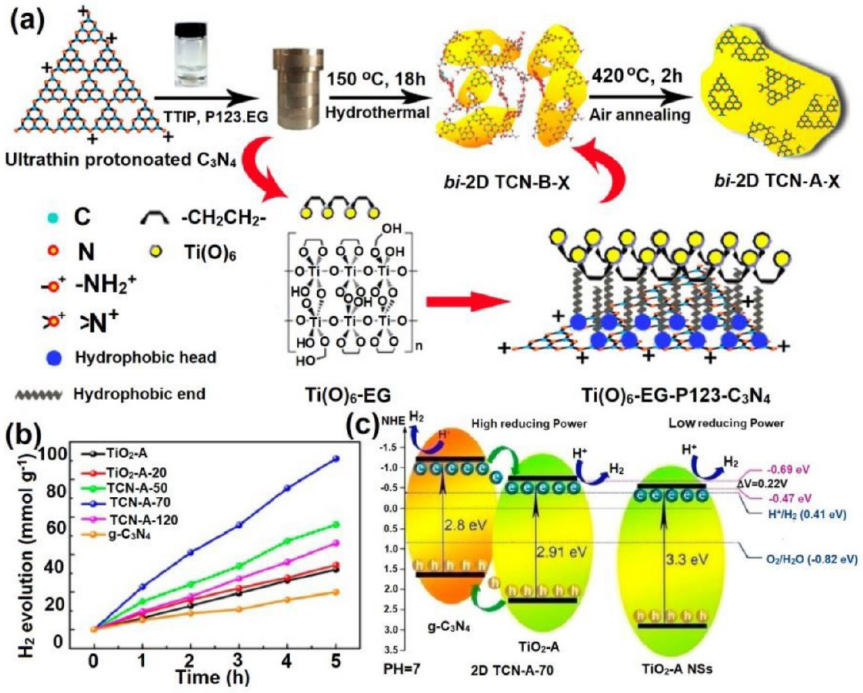

Figure 13. Schematic illustration of the preparation process of (a) 2D TCN-A-*x* nanosheets. TCN-B-*x* containing bronze-type TiO_2 was attained after hydrothermal sandwich assembly and was converted to TCN-A-*x* containing anatase-type TiO_2 through a controlled air-annealing (O_2-insertion) treatment. (b) Photocatalytic H_2 evolution activity of TCN-A nanosheets, g-C_3N_4 nanosheets, and TCN-A-*x* samples with various g-C_3N_4 contents. Proposed band gap structure and photocatalytic mechanism for (c) photogeneration of H_2 over 2D TCN-A-70 nanosheets and TiO_2-A nanosheet photocatalysts under UV−vis light irradiation. Reprinted with permission from ref 305. Copyright 2017 American Chemical Society.

$-NH_2$ terminal groups acts as an active site for better catalytic reactions.

A similar study demonstrates ultrathin g-C_3N_4 in a face-to-face interfacial sandwiched with anatase TiO_2 nanosheets. Bronze type phase TiO_2 (TCN-B-*x*) containing excessive electron trapping Ti^{3+} sites demonstrate a low photocatalytic performance. Optimizing to a favorable amount of Ti^{3+} content is beneficial as it helps in electron hopping. This attracted Gu et al. to perform an air annealing process to remove the vacant oxygen sites.[305] This heterojunction with high energy (010) facet exposed to TiO_2 with g-C_3N_4 was able to increase visible light absorption and curb electron−hole recombination by promoting better charge separation. Figure 13a gives insight into the synthetic process, whereby positively charged g-C_3N_4 and TiO_2 precursors were hydrothermally treated to form initially TCN-B-*x*, which on further annealing in the air gives TCN-A-*x* following a phase conversion to anatase. Annealing in the air provided required oxygen to vacant oxygen sites and perhaps inhibited the aggregation to form ultrathin nanosheets. An inverse micelle is formed by the ethylene glycol (EG) and another surfactant where the hydrophilic part traps the protonated g-C_3N_4 forming a sandwich-like structure. The AFM image confirmed the formation of ultrathin nanosheets of 1.4 nm attached to larger 3 nm nanosheets corresponding to g-C_3N_4. The photocatalytic activity was evaluated in a dye degradation experiment using methyl orange (MO) as a model compound.

The designed heterojunction of TCN-A-*x* performed exceedingly well, degrading 98% of MO in 15 min compared to using a single component such as TiO_2 and g-C_3N_4. Further, the material was subjected to photocatalytic H_2 production with an observed higher yield reaching up to 91 060 μmol/g in 5 h, as shown (Figure 13b). The role of each of TiO_2 and g-C_3N_4 nanosheet during the process of wavelength-dependent H_2 production was also investigated. The quantum yields at 365 and 380 nm were found to be 5.1% and 5.3%, respectively, which is lower than the individual nanosheets, strongly indicating the upsides of forming a heterojunction. The band gap and reaction mechanism is shown in Figure 13c with favorable thermodynamics and potentials for dye degradation and H_2 production. In TCN-A, photoexcited electrons get injected from the CB of g-C_3N_4 to the CB of TiO_2-A, forming superoxide radicals with high oxidizing power on the surface. Similarly, holes migrate from the VB of TiO_2-A to the VB of g-C_3N_4 to oxidize organic pollutants into degradation by-products. The system of charge transfer is efficient in the bicomponent face-to-face heterojunction, reducing the travel path for electrons, thereby increasing the electron lifetime. Comparable work in building the heterojunction of TiO_2 and g-C_3N_4 has been reported for photocatalytic applications under LED illumination and photoelectrochemical application.[306,307308]

4.3. Carbon Nitride−MnO_2. Wide band gap transition metal oxides (TMOs) with completely filled and empty *d*-orbitals such as ZnO and TiO_2 are preferably used as a photocatalyst. These materials have certain shortcomings as they are active mostly to UV irradiation which thus reduces their practical usage. For this reason, partially filled *d*-level TMOs such as MnO_2 are attractive due to the possibility of light absorption following a *d*−*d* transition.[277,309,310] Unfortunately, the *d*-electrons do not migrate to the interface/surface as it stays confined in the metal ion resulting in recombination. As a result, such metal oxides showed the inability to sufficiently generate electron−hole pairs and therefore are

https://doi.org/10.1021/acs.chemmater.1c03166
Chem. Mater. 2021, 33, 9012−9092

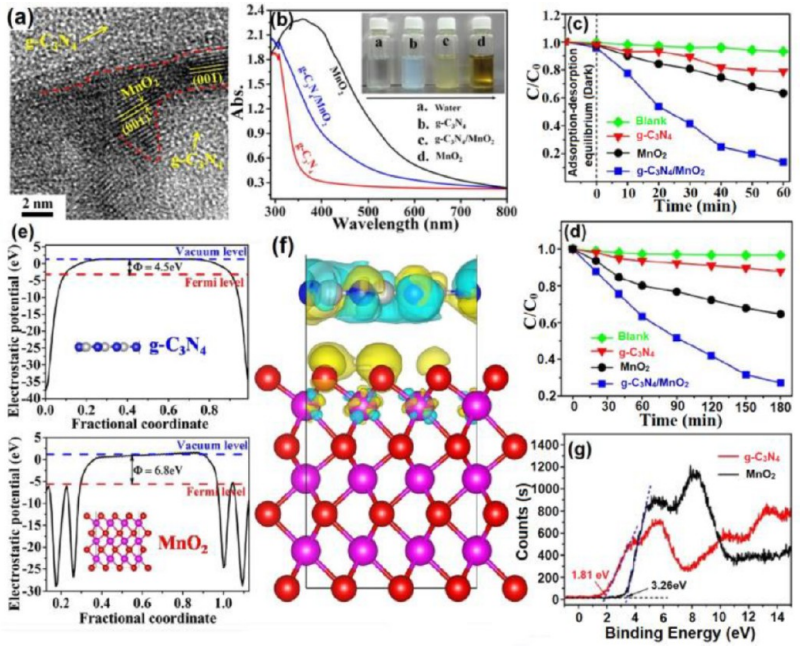

Figure 14. (a) TEM image of the g-C_3N_4/MnO_2 nanocomposite. (b) UV−vis spectra of g-C_3N_4, MnO_2, and g-C_3N_4/MnO_2 samples. Photocatalytic degradation rate of (c) RhB, (d) phenol over g-C_3N_4, MnO_2, and the g-C_3N_4/MnO_2 nanocomposite. (e) Calculated electrostatic potentials for g-C_3N_4 and MnO_2 nanosheets, respectively. (f) Charge density difference model of the g-C_3N_4/MnO_2 nanocomposite. The isosurface is 0.0004 eV $Å^{-3}$. (g) XPS valence band spectra of MnO_2 and g-C_3N_4 nanosheets. Reprinted with permission from ref 314. Copyright 2018 American Chemical Society.

infrequently used. To overcome these shortcomings, certain modifications to its crystal structure are required.[311] MnO_2 with partially filled d^5 configuration and other attractive properties such as narrow band gap, stability, low cost, wide abundance, and environmental friendliness makes it promising for use in photocatalytic applications.[312] Of the many crystal structures, layered δ-MnO_2 with multiple oxygen vacancies shows higher catalytic activity. Additionally, it utilizes the visible spectrum for better absorption due to its narrow band gap.

However, to improve the efficiency of photocatalytic devices, the construction of a 2D/2D architecture can create the possibility for aligning suitably the band structures for proper channeling of charge carriers.[313] Xia et al. synthesized 2D/2D nanocomposite of g-C_3N_4/MnO_2 by in situ depositing MnO_2 on exfoliated g-C_3N_4 in a solution.[314] The TEM images of g-C_3N_4/MnO_2 display a close integration of the nanosheets, which revealed the formation of a heterojunction with the observed lattice fringes corresponding to δ-MnO_2 in (Figure 14a). The UV−vis spectra further substantiate the formation of a heterojunction by an observed optical absorption well beyond the UV region, extending to the visible region (Figure 14b). The photocatalytic activity of the heterojunction nanocomposite was tested against the single-component material for degradation of rhodamine B (RhB) and phenol in an aqueous solution, as shown in Figure 14c,d. RhB was efficiently degraded up to 91.3% within 60 min by the nanocomposite of g-C_3N_4/MnO_2 with a higher apparent reaction rate compared to individual MnO_2 and g-C_3N_4. The photocatalytic efficiency of phenol removal was significantly higher for g-C_3N_4/MnO_2, reaching 73.6% at 180 min of illumination compared to 12.3% and 35.4% using g-C_3N_4 and MnO_2, respectively. Work functions relative to the vacuum level were calculated to be 6.8 and 4.5 eV for MnO_2 (001) and g-C_3N_4 (001), respectively (Figure 14e). Therefore, at the heterojunction near the interface, the g-C_3N_4 from where the electrons flow is more positively charged with respect to MnO_2, which is slightly negatively charged.

The charge deficiency model of the nanocomposite in Figure 14f depicts the different regions of electronic charge accumulation and depletion represented in cyan and yellow, respectively, showing the flow of electrons due to the formation of the g-C_3N_4/MnO_2 heterojunction. Based on the Mott−Schottky results and the valence band XPS spectra in Figure 14g, a band structure showing the mechanism of photocatalysis is proposed. The Mott−Schottky analysis revealed positive slopes for both g-C_3N_4 and MnO_2, indicating an *n*-type semiconductor behavior. The observed flat band potential in such a case can be assumed to be the levels of conduction bands with −1.61 and 1.22 V correspondingly for g-C_3N_4 and MnO_2. Subsequently, the valence band positions were measured from the XPS valence band spectra as 1.81 and 3.26 V for g-C_3N_4 and MnO_2. The assimilated results revealed a Z-scheme type of heterostructure formed between the two nanosheets, showing better utilization of the charge carriers and significantly improving the photocatalytic efficiency. Similar 2D/2D heterojunction synthesis of MnO_2/g-C_3N_4 has been reported by the in situ redox reaction of Mn precursors on the surface of g-C_3N_4 for CO_2 photoreduction.[315] Other modifications such as CNT comodified g-C_3N_4 have been used with MnO_2 for water splitting application.[316] In such a case, CNTs with higher electron capture capacity are expected to increase the electron transfer to a higher activity surface.

4.4. Carbon Nitride−Fe_2O_3. Hematite (α-Fe_2O_3) is an iron oxide semiconductor material having band gap energy in the range 1.9−2.2 eV, absorbing a broad range of the solar spectrum, and, therefore, is favorable for various photocatalytic

https://doi.org/10.1021/acs.chemmater.1c03166
Chem. Mater. 2021, 33, 9012−9092

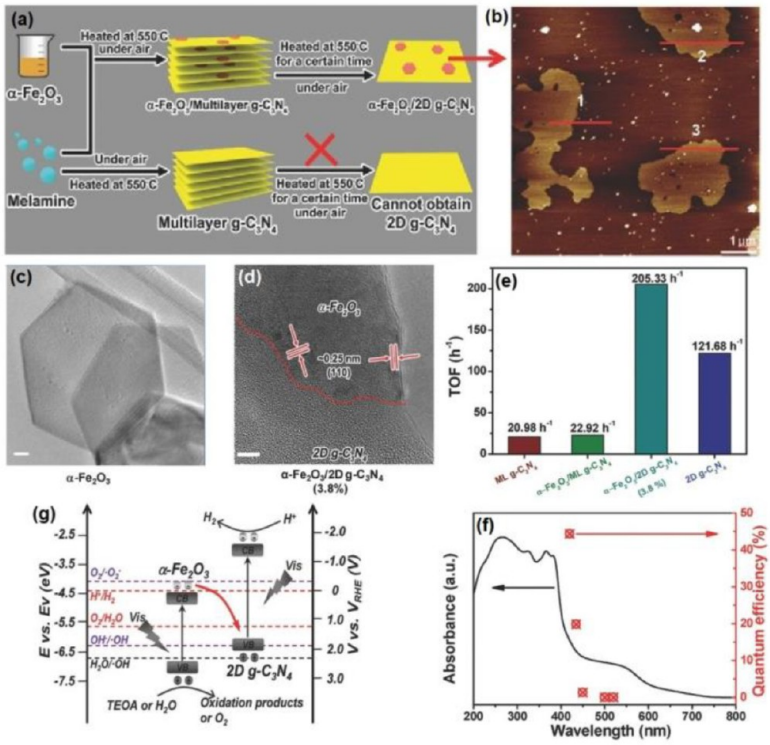

Figure 15. (a) Scheme of the proposed synthetic route to produce the α-Fe_2O_3/2D g-C_3N_4 hybrids. The presence of iron oxide is essential to originate 2D structures. (b) AFM of pure 2D g-C_3N_4, obtained after etching away α-Fe_2O_3 using HCl. Scale bar: 1 μm. (c) TEM image of an α-Fe_2O_3 nanosheet. Scale bar: 20 nm. (d) HRTEM image of α-Fe_2O_3/2D g-C_3N_4 (3.8%) hybrid. Scale bar: 5 nm. (e) Turnover frequency of different materials. (f) Wavelength dependence of external quantum efficiency for α-Fe_2O_3/2D g-C_3N_4 hybrid. (g) Energy band diagram of the Z-scheme mechanism in α-Fe_2O_3/2D g-C_3N_4 hybrids at pH = 0. Reprinted with permission from ref 330. Copyright 2017 Wiley VCH.

reactions.[317,318] It is one of the most abundantly found materials and has been considerably explored due to its excellent chemical stability, low cost, and abundance. It is used in a variety of applications, including solar cells,[319] batteries,[320] photoelectrochemical water splitting, etc. Unfortunately, Fe_2O_3 is an indirect band gap semiconductor and has a low absorption coefficient, small hole diffusion length (2 to 4 nm), unfavorable CB position for reduction of water to hydrogen, and short excitation lifetime (1 ps).[321,322] These dictate modification in pure hematite to remove the inefficiencies and reduce other intrinsic limitations to improve the material and device performance. Morphological and structural nanoarchitectures such as 1D, 2D, and 3D have been explored for enhanced photoactivity by exposing the reactive facets.[323−326]

Other modifications in the form of doping with various elements in the Fe_2O_3 lattice have been reported.[327,328] For example, Cesar et al. doped Si on Fe_2O_3 to get (001) oriented nanoleaflets grown normal to the substrate for an enhanced solar to chemical conversion.[329] She et al. constructed a Z-scheme heterojunction of Fe_2O_3 and ultrathin 2D nanosheets of the g-C_3N_4 photocatalyst for the H_2 evolution reaction.[330] They used a simple one-step method to mix colloidal α-Fe_2O_3 with melamine and annealing at 550 °C to form a hybrid composite α-Fe_2O_3/g-C_3N_4 followed by subsequent calcination to transform multilayer to ultrathin g-C_3N_4 (Figure 15a). The formation of ultrathin mono- and bilayers of g-C_3N_4 was confirmed through AFM measurements (Figure 15b). Additionally, hexagonal morphological Fe_2O_3 nanostructures with a lateral size around 210 nm and thickness of 15 nm were observed in the TEM image (Figure 15c). A sharp interface observed in the HRTEM suggests a successful formation of the Fe_2O_3/2D g-C_3N_4 heterojunction (Figure 15d). α-Fe_2O_3/2D g-C_3N_4 showed 8.95 times higher H_2 production than α-Fe_2O_3/ML g-C_3N_4 hybrids. Additionally, it also showed a better turnover frequency (TOF) compared to an individual component such as monolayer (ML) g-C_3N_4 and 2D g-C_3N_4 (Figure 15e). Furthermore, the external quantum efficiency (EQE) at λ = 420 nm was calculated to be 44.35% higher than others previously reported for g-C_3N_4 based photocatalytic systems (Figure 15f). The proposed band energy diagram in Figure 15g depicts the charge transfer and migration in the constructed hybrid α-Fe_2O_3/2D g-C_3N_4 system.

The compact and intimate interface between the composites easily transports the electrons created from photoexcited α-Fe_2O_3 combined with VB holes in the g-C_3N_4. This leaves the electrons jumping to the CB of g-C_3N_4, which can migrate onto the surface for participating in reactions. Similarly, holes in the valence band of α-Fe_2O_3 are actively available for oxidation reactions. The process trails a Z scheme and subdues the electron−hole recombination in both α-Fe_2O_3 and 2D g-C_3N_4, maximizing the utility of the charge carriers in both the contributing composites. The direct and tight contact Z-scheme formation of the composites result in eliminating the shuttle-mediator redox reactions that showed improved quantum efficiency superior to previously reported single component g-C_3N_4 and metal oxides.

Similar work has been reported with variations. For example, Xu et al. reported the construction of 2D/2D α-Fe_2O_3/g-C_3N_4 by adopting an electrostatic self-assembly process exploiting the strong interaction between the participating materials.[331] Furthermore, other approaches such as ultrasonic-assisted

https://doi.org/10.1021/acs.chemmater.1c03166
Chem. Mater. 2021, 33, 9012−9092

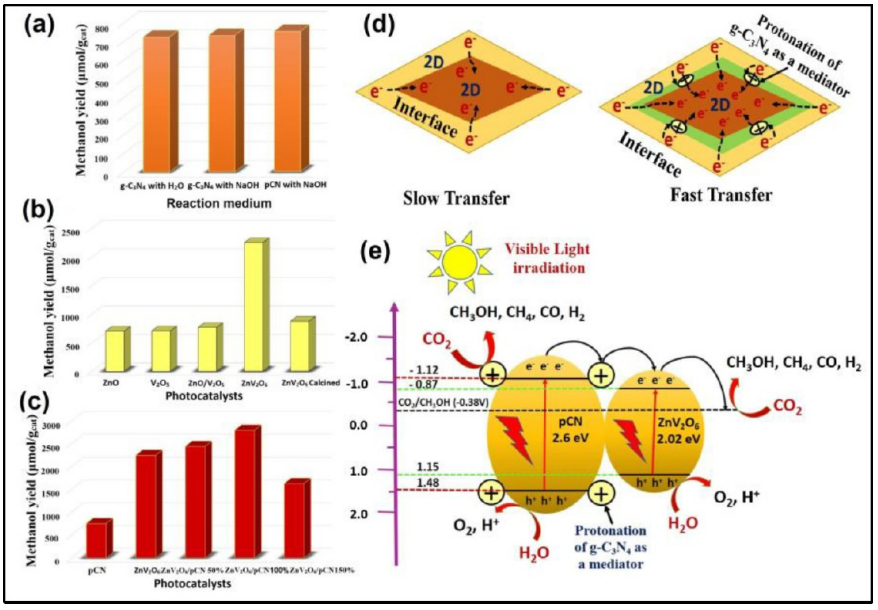

Figure 16. (a) Yield of methanol for different reaction mediums. (b) Effect of types of photocatalysts on the yield of methanol. (c) Yield of methanol over various photocatalysts: reaction parameters (room temperature, atmospheric pressure, feed flow rate 20 mL/min and irradiation time 2 h). Schematic illustration of contact interfaces for (d) 2D/2D heterojunction and (g) 2D/2D heterojunction with protonation (HNO_3) as a mediator. (e) Schematic diagram of the separation and transfer of photogenerated charges in ZnV_2O_6/pCN composite under visible light irradiation. Reprinted with permission from ref 353. Copyright 2019 Elsevier.

preparation methods have been used to synthesize a similar configuration of 2D α-Fe_2O_3/g-C_3N_4.[332]

4.5. Carbon Nitride–ZnV_2O_6. Zinc oxide ZnO, an excellent photocatalyst, is restricted from functional application due to its wide band gap (3.3. eV), fast recombination rate, and photocorrosion.[333,334] Another important oxide semiconductor material, vanadium oxide (V_2O_5), with a band gap of ~2.4 eV has also been explored for many photocatalytic applications; however, its performance is tormented by easy dissolution in aqueous solution and causes secondary pollution.[335,336] Coupling of ZnO and V_2O_5 has been found to show synergistic benefits due to stabilization of V_2O_5, and the less negative CB of ZnO can accept electrons from V_2O_5, leading better charge separation.[337−339] Unfortunately, interfacial recombination, charge carrier energy loss in a type-I heterojunction due to opposite migration, and limited hole mobility are still challenging issues. Using mixed metal oxides such as binary metal vanadates is more appealing to amalgamate the properties of two catalytic components to reach a narrow band gap, resilient chemical nature, better charge mobilities, etc.[340−342]

Zinc vanadium oxide ZnV_2O_4 is an emerging photocatalytic material because of its low band gap, photostable nature, and intriguing structural change at low temperatures. This allowed the fabrication of ZnV_2O_4 with various morphological structures such as hollow spheres, nanosheets, clawlike hollow structures, etc.[343−348] Interestingly, DFT calculations revealed that, compared to electron migration in the CB, the hole transfer to the VB is faster, removing the bottleneck of the low oxidation rate at the valence band.[344] ZnV_2O_4 either in a standalone[349] form or as a heterojunction composite has been widely investigated for various photoredox reactions. The intriguing structural flexibility of ZnV_2O_4 can be harvested to design new more efficient light-harvesting systems. The 2D ZnV_2O_4 nanosheet structure with high specific surface area and active centers has been effectively exploited to form a 2D/2D heterojunction such as ZnV_2O_4/rGO,[350,351] ZnV_2O_4/V_2O_5,[352] etc. 2D/2D vdW heterostructures of ZnV_2O_6 with g-C_3N_4 have shown encouraging performance, which is worth further investigations.

The workgroup of Tahir et al. constructed a 2D/2D ZnV_2O_6/pCN vdW heterostructure for the reduction of CO_2 to CH_3OH, CO, and CH_4 (Figure 16, Table 3).[353] For the fabrication of heterojunctions, g-C_3N_4 nanosheets were first protonated with nitric acid, and then ZnV_2O_6 nanosheets were hydrothermally grown on protonated g-C_3N_4 (pCN) sheets. In the process, the positive charge on protonated pCN provides reaction sites to form self-assembled 2D/2D ZnV_2O_6/pCN architecture. ZnV_2O_6/pCN exhibited excellent visible absorption up to 800 nm. ZnV_2O_6 displayed a selective CH_3OH yield in liquid phase reaction compared to g-C_3N_4 and pCN which was almost doubled for the ZnV_2O_6/pCN vdW heterostructure reaching a maximum value of 776 μmol g-cat^{-1} h^{-1} after 4 h with a quantum yield of 0.081 (Figure 16a−c). Further, when the reaction was pursued in the gas phase, CO was the main reaction product along with a small amount of CH_3OH and CH_4. The improved performance of 2D/2D ZnV_2O_6/pCN was originated from the better face-to-face interaction, and protonated sites provide high-speed charge transfer nanochannels for effective charge separation (Figure 16d). Further, pCN in the established heterojunction can transfer electrons to the CB of ZnV_2O_6 due to the presence of proton centers which serve as a trap center to facilitate charge transportation (Figure 16e). The same group has reported that when reduced graphene oxide is introduced in the system, the charge transfer mechanism was changed from type-I to Z-scheme. In the ternary ZnV_2O_6/RGO/g-C_3N_4 Z-scheme heterojunction, graphene served as an electron mediator and facilitated the efficient transfer of photogenerated electrons on the CB of ZnV_2O_6 to the VB of pCN.[354] Interestingly, the ZnV_2O_6/RGO/g-C_3N_4 heterostructure displayed a quantum

https://doi.org/10.1021/acs.chemmater.1c03166
Chem. Mater. 2021, 33, 9012−9092

Table 3. 2D/2D carbon nitride-metal oxides-based heterojunction photocatalysts

photocatalyst	synthesis	application	light source	AQY/STH	remarks	ref
		Metal Oxides				
N-doped ZnO-graphitic carbon nitride nanosheets (NZCN)	Hydrothermal method: g-C_3N_4, zinc acetate dihydrate, urea, PVP, and aqueous ammonia solution were mixed with continuous stirring. The resultant solution was moved to a Teflon autoclave and treated at 120 °C for 8 h. The obtained product was calcined at 450 °C for 2 h.	Photocatalytic H_2 evolution	300 W Xe lamp	-	H_2—18 836 μmol g^{-1} h^{-1}(NZCN30) heterojunction exhibits high g-C_3N_4—9836 μmol g^{-1} h^{-1}	281
MoO_2 nanosheets and graphene-like C_3N_4 (MoO_2/GL-C_3N_4)	Hydrothermal method: MoO_2 and GL-C_3N_4 dispersed in EG using ultrasonication and hydrothermally treated at 180 °C for 12 h.	Photocatalytic degradation of RhB	300 W Xe lamp ($\lambda \geq$ 420 nm)	-	MoO_2/GL-C_3N_4—97.5% RhB degradation in 120 min pure GL-C_3N_4—38% RhB degradation in 120 min	282
Co_3O_4/2D g-C_3N_4	2D g-C_3N_4 and β-$Co(OH)_2$ were frozen in liquid nitrogen and heated at 573 K for 2 h.	Photocatalytic CO_2 reduction	300 W Xe lamp	-	CO—419 μmol g^{-1} h^{-1} and 89.4% selectivity (Co_3O_4/2D g-C_3N_4) CO—31 μmol g^{-1} h^{-1} with CH_4 and H_2 by-products (2D g-C_3N_4)	283
Ultrathin g-C_3N_4 and WO_3 nanosheets	Grinding: Pt-CN NSs and HWO NSs were ground in an agate mortar, and the obtained solid was calcined at 400 °C under Ar atmosphere for 1 h.	Photocatalytic H_2 evolution	300 W Xe lamp ($\lambda \geq$ 420 nm)	9.4 (420 nm)	H_2—862 μmol h^{-1} (Pt-CN/HWO-40) ~6.2 times of Pt-CN/WO	293
WO_3/g-C_3N_4	Electrostatic self-assembly: WO_3 nanosheets and g-C_3N_4 were stirred together.	Photocatalytic H_2 evolution	350 W Xe lamp	-	H_2—982 μmol g^{-1} h^{-1} (15%WO_3/g-C_3N_4) ~1.7 times of pure g-C_3N_4	294
O-g-C_3N_4/TiO_2	Bottom-up synthetic strategy: to a pretreated g-C_3N_4 dispersion in EG, titanium isopropoxide, concentrated HCl, and P123 solubilized in ethanol was added and hydrothermally treated at 150 °C for 20 h. C_3N_4—180.5 μmol g^{-1} h^{-1}	Photocatalytic H_2 evolution	300 W Xe lamp ($\lambda \geq$ 400 nm)	-	H_2—587.1 μmol g^{-1} h^{-1} (C_3N_4/TiO_2 1:1) g-	304
TiO_2-g-C_3N_4 (TCN-A-x)	Hydrothermal treatment and air annealing: ultrathin g-C_3N_4 nanosheet dispersed EG and precursor solution of TiO_2-B was hydrothermally treated at 150 °C for 18 h.	Photocatalytic H_2 evolution and degradation of MO, MB, and RhB	300 W Xe lamp	5.3% (380 nm)	H_2—18.200 mmol g^{-1} h^{-1} (TCN-A-70) g-C_3N_4—~4.8 mmol g^{-1} h^{-1} TCN-A—70–98% degradation efficiency in 15 min g-C_3N_4—30% degradation efficiency	305
g-C_3N_4/MnO_2	g-C_3N_4 nanosheet $MnCl_2 \cdot 4H_2O$ tetramethylammonium hydroxide (TMA·OH) mixed for 1 h. Subsequently, H_2O_2 (30 vol %) was added dropwise into the mixed suspension under rapid stirring and kept for 30 min.	Photocatalytic degradation of RhB and phenol	Xe lamp	-	g-C_3N_4/MnO_2—91.3% RhB degradation after 60 min g-C_3N_4—19.6%	314
MnO_2/g-C_3N_4	Redox reaction between $KMnO_4$ and $MnSO_4 \cdot H_2O$: g-C_3N_4 adsorbed $MnSO_4 \cdot H_2O$ was treated with $KMnO_4$ at 40 °C for 12 h.	Photocatalytic CO_2 reduction	300 W Xe lamp	-	CO—20.4 μmol g^{-1} (MnO_2-100CN) for 6 h ~4 times higher than pure g-C_3N_4	315
2D α-Fe_2O_3/g-C_3N_4	In situ method: melamine and α-Fe_2O_3 were mixed in a crucible and heated at 550 °C for 4 h. The obtained sample was ground into powder for further use.	Photocatalytic H_2 evolution	300 W Xe lamp ($\lambda \geq$ 400 nm)	44.35% (420 nm)	H_2—31 400 μmol g^{-1} h^{-1}(α-Fe_2O_3/2D g-C_3N_4)	330

https://doi.org/10.1021/acs.chemmater.1c03166
Chem. Mater. 2021, 33, 9012−9092

Table 3. continued

photocatalyst	synthesis	application	light source	AQY/STH	remarks	ref
		Metal Oxides				
					ML g-C_3N_4 3200 μmol g^{-1} h^{-1}	
Fe_2O_3/g-C_3N_4 direct Z-scheme	Electrostatic self-assembly of g-C_3N_4 nanosheet and Fe_2O_3.	Photocatalytic H_2 evolution	350 W Xe lamp ($\lambda \geq$ 420 nm)	-	H_2—398.0 μmol g^{-1} h^{-1} (Fe_2O_3/g-C_3N_4) ~13-fold that of pure g-C_3N_4 (30.1 μmol g^{-1} h^{-1})	331
2D α-Fe_2O_3@g-C_3N_4	Ultrasonic assisted self-assembly method: 2D g-C_3N_4 and 2D α-Fe_2O_3 nanosheets and Nafion solution as stabilizing agents were mixed ultrasonically.	Photocatalytic degradation RhB	500 W halogen lamp ($\lambda \geq$ 420 nm)	-	α-Fe_2O_3@g-C_3N_4—90% RhB degradation after 120 min g-C_3N_4—26% RhB degradation after 120 min	332
g-C_3N_4/{010} facets $BiVO_4$	$BiVO_4$ and g-C_3N_4 were stirred together.	Photocatalytic degradation of RhB	500 W Xe lamp	-	g-C_3N_4/{010} $BiVO_4$—88.3% RhB degradation in 30 min $BiVO_4$—22.66% RhB degradation in 30 min	340
g-C_3N_4/$BiVO_4$ Z-scheme	$BiCl_3$ and CTAB solution in EG were mixed with Na_3VO_4·12H_2O followed by the addition of g-C_3N_4 ultrathin nanosheets, and finally the mixture was hydrothermally treated at 160 °C for 3 h.	Photocatalytic CO_2 reduction	300 W Xe lamp ($\lambda \geq$ 420 nm)	-	CH_4—27.43 μmol g^{-1} (g-C_3N_4/$BiVO_4$) ~4.8 times of g-C_3N_4 (5.76 μmol g^{-1}) (CH_4) CO—31.15 μmol g^{-1}(g-C_3N_4/$BiVO_4$) ~4.4 times of g-C_3N_4—(7.14 μmol g^{-1}) (CO)	341
Porous g-C_3N_4/Ag_3VO_4 (Pg-C_3N_4/Ag_3VO_4)	Pg-C_3N_4 and $AgNO_3$ were stirred for 30 min followed by the addition of Na_3VO_4 and stirring for 6 h; the mixture was freeze-dried after aging for 4.5 h.	Photocatalytic degradation of MB	50 W 410 nm LED	-	40% Pg-C_3N_4/Ag_3VO_4—99.3% MB degradation in 8 min Pg-$C_3N_4$5% MB degradation in 8 min	342
ZnV_2O_6/g-C_3N_4	[NH_4VO_3], [$Zn(O_2CCH_3)_2$], and DMF were mixed, followed by the addition of [$H_2C_2O_4$·2H_2O] in a ratio of oxalic acid to NH_4VO_3 of 1:3. Later, protonated g-C_3N_4 (pCN) was added and hydrothermally treated at 200 °C for 24 h.	Photocatalytic CO_2 reduction	35 WHID Xe lamp	CH_3OH—0.0021; CO—0.028; H_2—0.0029 (450 nm)	3742.19 μmol gcat^{-1} (ZnV_2O_6/100% pCN)	353

https://doi.org/10.1021/acs.chemmater.1c03166
Chem. Mater. 2021, 33, 9012−9092

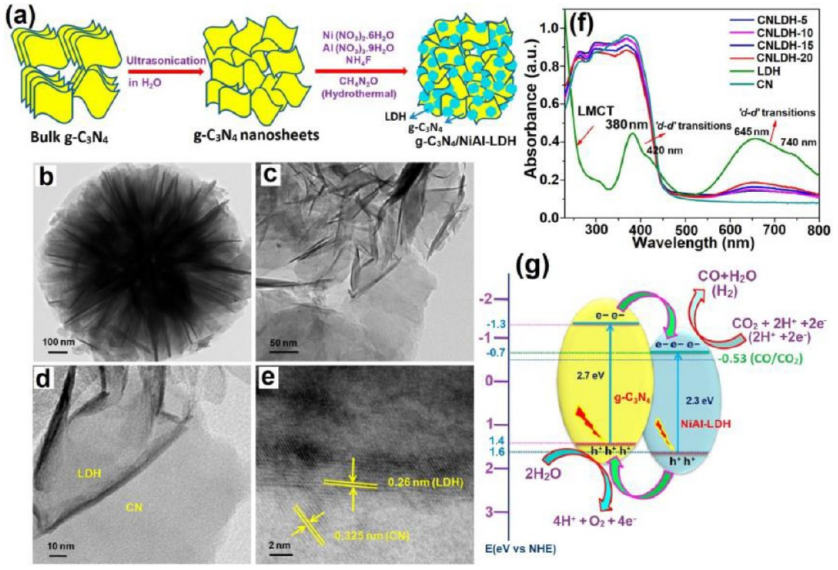

Figure 17. (a) Schematic illustration of the synthesis process of g-C_3N_4/NiAl-LDH hybrid heterojunctions. TEM images of (b) NiAl-LDH, (c, d) CNLDH-10, and (e) HRTEM image of the CNLDH-10 heterojunction. (f) UV−vis DRS of g-C_3N_4, NiAl-LDH, and g-C_3N_4/NiAl-LDH heterojunction samples. (g) Schematic illustration of the proposed mechanism for CO_2 photoreduction in the g-C_3N_4/NiAl-LDH heterojunctions. Reprinted with permission from ref 396. Copyright 2018 American Chemical Society.

yield of 0.2830, which was 3.5 times higher than that of the binary ZnV_2O_6/pCN system (0.081).

5. CARBON NITRIDE−LAYERED DOUBLE HYDROXIDES (LDHS) 2D/2D vdW STRUCTURES

Layered double hydroxides (LDHs), also called hydrotalcite-like materials (structural similarity with $[Mg_6Al_2(OH)_{16}]CO_3 \cdot 4H_2O$), or anionic clays is a class of layered materials with a chemical formula $[M_{1-x}^{2+}M_x^{3+}(OH)_2]^{2x+}(A^{n-})_{x/n} \cdot yH_2O$, where M^{2+} is divalent metal cations (Mg^{2+}, Zn^{2+}, Co^{2+}, Mn^{2+}, Ni^{2+}, or Ca^{2+}) and M^{3+} is trivalent metal cations (Fe^{3+}, Cr^{3+}, and Al^{3+}, etc.) occupying octahedral positions within the hydroxide layers, A^{n-} is the nonframework exchangeable interlayer n-valent anions with highly chemical reactivity (Cl^-, ClO_4^-, NO_3^-, CO_3^{2-}, SO_4^{2-}, etc.), and x is the molar ratio of $M^{2+}/(M^{2+} + M^{3+})$.[355−358] Due to its layered structure, several guest molecules have been intercalated in between galleries of LDHs for various applications. The presence of a basic site on LDHs makes them suitable catalysts to promote base-catalyzed reactions without using harsh alkaline conditions.[359,360] For example, La-doped Ca−Mg−Al layered double hydroxide (La-CaMgAl-LDH) can catalyze base-free aerobic oxidation of HMF to FDCA in water.[361] In another example, cobalt phthalocyanine-assisted oxidation of thiols to disulfide usually takes place under alkaline conditions. However, when a magnetically recyclable MgAl-LDHs tethered phthalocyanine was used, oxidation can occur without using an alkali.[362]

Interestingly, in the recent years, several visible light active LDHs have been synthesized by changing the metal combination (Zn/Cr, Mg/Cr, Zn/Fe, Mg/Fe, Cu/Cr, Co/Cr), doping (Cu, Ni, Zn), and intercalated ions in between brucite layers. The simplicity of LDH synthesis by coprecipitation provides an opportunity to play with compositions, and many fractional composition LDHs have been reported for the photocatalytic applications, especially CO_2 reduction due to the weak acidic nature of CO_2.[363,364] Izumi and co-workers have reported several novel LDHs such as $[Zn_3Ga(OH)_8]^+_2[Cu(OH)_4]^{2-} \cdot mH_2O$, $[Zn_{1.5}Cu_{1.5}Ga(OH)_8]_2^+[Cu(OH)_4]^{2-} \cdot mH_2O$, Zn−Al LDH, etc. for photoconversion of CO_2 to value-added chemicals.[365−368]

In LDHs, brucite layers remain together due to attraction between the positively charged brucite layers and the negatively charged interlayers of H-bonded metal hydroxide and the oxygen atoms of the intercalated anions. Through strong force between the LDH layer, methods such as intercalation with small molecules (formamide, glycine) followed by sonication, anion exchange, plasma-induced exfoliation, etc. have been developed to convert the LDHs into 2D sheets through delamination.[369−372] These 2D sheets, due to high surface area, rich active sites, and excellent visible absorption, can induce various photochemical reactions. The face-to-face interaction of LDHs with carbon nitride to make the vdW heterojunction has been found to boost photocatalytic performance.[373−375] The potential of such a combination has already been traversed by Song et al.[129] Within a short span, a few more reports have emerged on the 2D/2D heterojunction/close contact of carbon nitrides and LDHs.[376−387]

Among various LDHs, bimetallic NiAl-LDH has been proven as the most efficient catalyst due to its excellent visible absorption profile originating from ligand-to-metal charge transfer (LMCT)($O \rightarrow Ni^{2+}$).[388,389] However, $d-d$ transitions of the Ni^{2+} interelectronic excitation pathway hinder the photocatalytic performance due to reduced carrier efficiency.[390,391] The charge carrier separation can be improved by making heterojunctions, i.e., the coupling of n-type NiAl-LDHs with p-type $CuFe_2O_4$ can achieve an excellent charge separation and produce H_2 (345.76 μmol h^{-1}) almost 7 times the values of pristine NiAl-LDHs.[392] Similarly, the coupling of NiAl-LDHs with β-In_2S_3 leads to an increment of CO_2 reduction performance. Interestingly, g-C_3N_4 can make a 2D/2D interface with sharp edges even without converting LDHs into single-layered sheets.[379,393−395]

To crop the tunability of carbon nitride to make a heterojunction, Tonda et al. synthesized a g-C_3N_4/NiAl-LDH nanocomposite via in situ hydrothermal depositions of

https://doi.org/10.1021/acs.chemmater.1c03166
Chem. Mater. 2021, 33, 9012−9092

Table 4. 2D/2D Carbon Nitride-Layered Double Hydroxides Based Heterojunction Photocatalysts

photocatalyst	synthesis	application	light source	AQY/STH	remarks	ref
		Layered Double Hydroxides (LDHs)				
ZnCr-LDH/g-C_3N_4 composite	g-C_3N_4 nanosheets, $Zn(NO_3)_2{\cdot}6H_2O$, and $Cr(NO_3)_3{\cdot}9H_2O$ were dissolved together, followed by titration with NaOH and Na_2CO_3 and finally treated solvothermally at 120 °C for 24 h.	Photoelectrocatalytic water dissociation	300 W Xe lamp	-	The experiment time lasts for 1 h, and the pH decreased to 1.52 from 7 in compartment 2 and simultaneously increased to 13.11 from 7 in compartment 4 by using ZnCr-LDH/g-C_3N_4 catalyst.	373
ZnCr-LDH/N-doped graphitic carbon-incorporated g-C_3N_4 ZnCr-CLDH/g-C_3N_4-C(N)	Coprecipitation method: $Zn(NO_3)_2{\cdot}6H_2O$ and $Cr(NO_3)_3{\cdot}9H_2O$ in 2:1 molar ratio in distilled water and CN-25 with Na_2CO_3 were mixed followed by addition of NaOH and stirred at 60 °C by keeping pH at 9.0. The obtained ZnCr-CLDH/CN-25 powder was calcined at 350 °C for 1 h.	Photocatalytic degradation of Congo Red (CR)	500 W Xe lamp which includes 4% UV (λ < 400 nm) and visible light (400 nm < λ < 700 nm)	-	ZnCr-CLDH/CN-25—70% CR degradation 60 min CN—14% CR degradation 60 min	374
ZnCr LDH nanosheet modified graphitic carbon nitride (CNLDHs)	Dripping exfoliated ZnCr LDH formamide suspension into bulk g-C_3N_4 water suspension under vigorous stirring followed by aging for 24 h.	Photocatalytic H_2 evolution	300 W Xe lamp ($\lambda \geq 420$ nm)	-	H_2—186.97 μmol g^{-1} h^{-1} (CNLDH1) pure CN—65.23 μmol g^{-1} h^{-1}	375
g-C_3N_4/CoAl-LDH	CNNS dispersed in DI water and were added with $Co(NO_3)_2{\cdot}6H_2O$ and $Al(NO_3)_3{\cdot}6H_2O$ (1:1) followed by the addition of 1 M NaOH. The obtained mixture was hydrothermally treated at 100 °C for 24 h.	Photocatalytic H_2 evolution	300 W Xe lamp (AM 1.5)	-	H_2—680.13 μmol g^{-1} h^{-1} (CoAl-LDH/CNNS) CNNS ~ negligible CoAl-LDH—32.91 μmol g^{-1} h^{-1}	379
Plasmonic Ag nanoparticle decorated NiAl-layered double hydroxide/graphitic carbon nitride nanocomposites (Ag/LDH/g-C_3N_4)	In situ hydrothermal treatment: CN nanosheet, $Ni(NO_3)_2{\cdot}6H_2O$, $Al(NO_3)_3{\cdot}9H_2O$, and NH_4F were treated at 120 °C for 24 h followed by photodeposition of 1 wt % Ag under a 400 W mercury lamp.	Photocatalytic degradation of RhB and 4-chlorophenol	300 W Xe lamp	-	Ag/LDH/CN with 15 wt % LDH shows ~99% RhB degradation g-C_3N_4—~28% RhB degradation	394
g-C_3N_4@NiAl layered double hydroxide nanocomposite (g-C_3N_4@NiAl-LDH NCPs)	In situ coprecipitation: g-C_3N_4, $Ni(NO_3)_2{\cdot}6H_2O$, and $Al(NO_3)_3{\cdot}9H_2O$ were mixed, followed by the addition of urea, and hydrothermally treated at 120 °C for 48 h.	Photocatalytic degradation of RhB and MO	500 W Hg lamp	-	g-C_3N_4@NiAl-LDH NCPs—56% RhB degradation after 240 min	395
g-C_3N_4/NiAl-LDH	In situ hydrothermal method: g-C_3N_4 nanosheets, $Ni(NO_3)_2{\cdot}6H_2O$, $Al(NO_3)_3{\cdot}9H_2O$, NH_4F, and urea were treated at 120 °C for 24 h.	Photocatalytic CO_2 reduction	300 W Xe lamp ($\lambda \geq 420$ nm)	0.21% (420 nm)	H_2—8.2 μmol g^{-1} h^{-1} (CNLDH-10) ~5 times of pure g-C_3N_4 (1.56 μmol g^{-1} h^{-1})	396
Graphitic carbon nitride intercalated ZnO\Mg−Al layered double hydroxide	A g-C_3N_4 dispersion in water, zinc chloride, urea, and Mg−Al LDH precursor were mixed and heated at 180 °C for 24 h.	Photocatalytic degradation of MB	250 W Hg lamp	-	g-C_3N_4\ZnO\Mg−Al LDH—96.5% degradation g-C_3N_4—49% MB degradation	397
Oxygen-doped carbon nitride/CoAl-layered double hydroxide (OCN/CoAl-LDH)	Hydrothermal: $Co(NO_3)_2{\cdot}6H_2O$, $(Al(NO_3)_3{\cdot}9H_2O)$, urea, NH_4F, and OCN powder were hydrothermally treated at 110 °C for 24 h.	Photocatalytic degradation of MO and bisphenol A (BPA)	300 W Xe lamp ($\lambda \geq 420$ nm)	-	OCAL-5—~99.7% MO removal efficiency pure OCN—14.2% OCAL-5—51.4% BPA removal efficiency within 95 min	400
CoAl-LDH/g-C_3N_4/RGO	Hydrothermal method: CN, GO, $Co(NO_3)_2{\cdot}6H_2O$, and $Al(NO_3)_3{\cdot}9H_2O$ were mixed followed by the addition of urea and NH_4F and hydrothermal digestion at 120 °C for 24 h.	Photocatalytic degradation CR and tetracycline (TC)	300 W Xe lamp	-	LCR-15−99% degradation of TC after 60 min CN—27% degradation of TC after 60 min	401

https://doi.org/10.1021/acs.chemmater.1c03166
Chem. Mater. 2021, 33, 9012−9092

NiAl-LDHs on g-C_3N_4 sheets (Figure 17a, Table 4). Without using any g-C_3N_4, the pristine NiAl-LDHs displayed flower-like morphology with sharp edges (Figure 17b).[396] However, this morphology was disappeared when g-C_3N_4 was used during synthesis and 2D sheets of LDHs were grown on the surface of g-C_3N_4, which suggests a strong interaction between g-C_3N_4 and NiAl-LDHs (Figure 17c−e). The UV−vis bands of LDHs were slightly blue-shifted in the 2D/2D g-C_3N_4/NiAl-LDHs, while the materials still have a strong visible absorption profile up to 800 nm (Figure 17f). The photocatalytic application in CO_2 reduction using the CNLDH-10 sample with 10% LDH was found to be optimum and afforded 8.2 μmol g^{-1} h^{-1} of CO, which was more than 5 times compared to g-C_3N_4 (1.56 μmol g^{-1} h^{-1}) (Figure 17g).

In the overall water splitting reaction, the kinetics of water oxidation remains a rate-determining step due to the requirement of multiple electron transfer steps followed by O−H bond cleavage and O−O bond formation. Since carbon nitride has a poor oxidizing valence band, the amalgamation of CN with water oxidation catalysts is an appropriate approach to enhance reaction kinetics.[397] Cobalt-based catalysts have demonstrated promising oxygen evolution performance, which makes them an ideal candidate for the formation of 2D/2D heterojunctions with carbon nitride.[398−401] Interestingly, the growth of cobalt hydroxide ($Co(OH)_2$) in the presence of carbon nitride sheets can lead to the formation of a layered structure. For example, Zhang et al. have fabricated a $Co(OH)_2$/g-C_3N_4 heterojunction by using a cobalt nitrate precursor in the presence of NH_3, which demonstrated enhanced visible absorption.[402] The close contact of $Co(OH)_2$ and g-C_3N_4 in 2D/2D fashion led to better charge migration that was evident from the reduced semicircle diameter in the EIS Nyquist plot and PL quenching. Under optimized conditions of 3 wt % $Co(OH)_2$ loading and $AgNO_3$ as an electron acceptor, the oxygen evolution rate was 27.4 μmol h^{-1} using 300 W solar simulated light. The cobalt-based LDHs with Ni counterparts were also found to be good water oxidation catalysts (WOCs).[403,404] Zhang et al. synthesized a 2D/2D heterostructure of Ni−Co LDHs (Ni_xCo_{3-x} LDHs; Ni^{2+}/Co^{2+} = 0, 1, 1.5, 2) and carbon nitride nanosheets (CNU) by a simple ultrasonication approach while keeping the ratio of Ni−Co LDHs in the range of 1−5 wt %.[405] The diminished PL intensity and enhanced photocurrent density in PEC measurement suggest better charge separation in the Ni−Co LDHs/CNU heterojunction. When used as a water oxidation photocatalyst, the $NiCo_2$ LDHS/CN catalysts with 1:2 Ni/Co stoichiometric composition and 3 wt % concentration demonstrated the highest O_2 evolution rate (26.7 μmol h^{-1}), which was 6.5 times higher than pure carbon nitride sheets.

6. CARBON NITRIDE−PEROVSKITE OXIDE 2D/2D vdW STRUCTURES

Perovskite materials with a general formula ABX_3 or A_2BX_4 are constituted of A and B cations coordinated to an X anion. In this structure, A and B cations have 6- and 12-fold coordination, surrounded by an octahedron of the X anions (usually oxygen).[406,407] Due to the stable structure of the perovskite lattice (except halide perovskites), more than 90% of metal elements have been successfully introduced into the perovskite lattice.[408] When X is a halogen (F, Cl, Br, or I) with a monovalent (Cs^+, $CH_3NH_3^+$, formamidinium($HC(NH_2)_2^+$)) and a divalent cation (Pb^{2+}, Ge^{2+}, Sn^{2+}) present in the A and B sites, it is referred to as a halide perovskite.[409] Lead halide-based perovskites have been widely explored for photovoltaics reaching an ∼25.2% efficiency in a monolithic cell nearing the Shockley-Queisser limit of 31.4% due to their excellent visible absorption, long carrier migration length, easy processability, etc.[410] Halide perovskites have also been used as the photocatalysts for the various photocatalytic applications such as CO_2 reduction, organic synthesis, photoelectrochemical synthesis, etc.[411−413] Unfortunately, halide perovskites suffer from a trap assisted recombination and structural stability issue under the ambient conditions such as air and moisture which further deepen becaise of the toxicity of lead.[414,415] Some lead-free perovskites such as $Cs_2AgBiBr_6$ have been recently reported with enhanced stability and photocatalytic performance, but still, the stability is not satisfactory under operating reaction conditions.[412] Several attempts to stabilize halide perovskites such as surface passivation, elemental doping, and alloying have been employed; however, the problem of stability persists. Recently, perovskite nanocrystal encasing inside of the inorganic shell such as silica, metal oxides, or wrapping with various types of 2D material such as graphene, g-C_3N_4, has been identified to prevent degradation.[416−418] However, such approaches inevitably reduce visible absorption and enhance surface recombination.

On the other hand, perovskite oxides with a general formula ABO_3, due to their extreme stability, excellent visible absorption (narrow band gap), and the possibility of multitudinous elemental combinations are gaining popularity in electrocatalysis, catalysis, solid oxides fuel cells (SOFCs), and photocatalysis.[34,419−423] Several bi/trimetallic perovskite materials possessing BO_6 type octahedron, such as $SrTiO_3$, $BaTi_4O_9$, $Ca_xTi_yO_3$, $CoTiO_3$, $LaMnO_3$, $LaCoO_3$, $K_3Ta_3Si_2O_{13}$, $LaNiO_3$, $SrVO_3$, $PbZrO_3$, $Na_2Ti_6O_{13}$, $SrNbO_3$, $K_2Ti_4O_9$, $K_4Nb_6O_{17}$, and $K_2La_2Ti_3O_{10}$, have been explored in recent years for photocatalysis.[424−432] Double perovskites ($A_2B'B''O_6$) are another subclass of perovskites that have shown great promise for photocatalytic applications, especially fuel cells and water splitting.[433−435] Several double perovskite oxides with stoichiometric and nonstoichiometric compositions such as Sr_2NiWO_6, $Sr_2Sc_{0.125}Ti_{0.875}O_4Ba_{0.5}Sr_{0.5}Co_{0.8}Fe_{0.2}O_{3-\delta}$ (BSCF), etc. have been successfully employed in such applications.[436,437] Though an excellent visible absorber, the main challenge associated with perovskite oxides is their low charge migration distance which makes bulk recombination very prominent. The use of reduction and oxidation cocatalysts such as Pt and RuO_2 has been employed to reduce surface recombination.

Layered perovskites oxides of (110), (100), and (111) families with formulas of ($A_{n+1}B_nO_{3n+3}$) and ($A_nB_nO_{3n+2}$), (Bi_2O_2)($A_{n-1}B_nO_{3n+1}$) (Aurivillius phase, AL), $A_{n+1}B_nO_{3n+1}$, or $A'_2A_{n-1}B_nO_{3n+1}$ (Ruddlesden−Popper phase, RP) and $A'[A_{n-1}B_nO_{3n+1}]$ (Dion−Jacobson phase, DJ), where n represents the number of BO_6 octahedra, arranged perpendicular to the layers provide better surface area, interlayer space as reaction sites, and charge carrier mobility, which make them promising candidates for photocatalysis.[438−440] Ruddlesden−Popper type perovskite phases and layered Dion−Jacobson type perovskite phases are the most promising perovskite oxides for photocatalysis. For example, $Sr_{2.7-x}Ca_xLn_{0.3}Fe_2O_{7-\delta}$ with x = 0 and 0.3 and Ln = La and Nd has demonstrated excellent visible light assisted MB degradation.[441] Enticingly, due to the possibility of exfoliation of 2D sheets, layered perovskites can be used for making a 2D/2D heterojunc-

https://doi.org/10.1021/acs.chemmater.1c03166
Chem. Mater. 2021, 33, 9012−9092

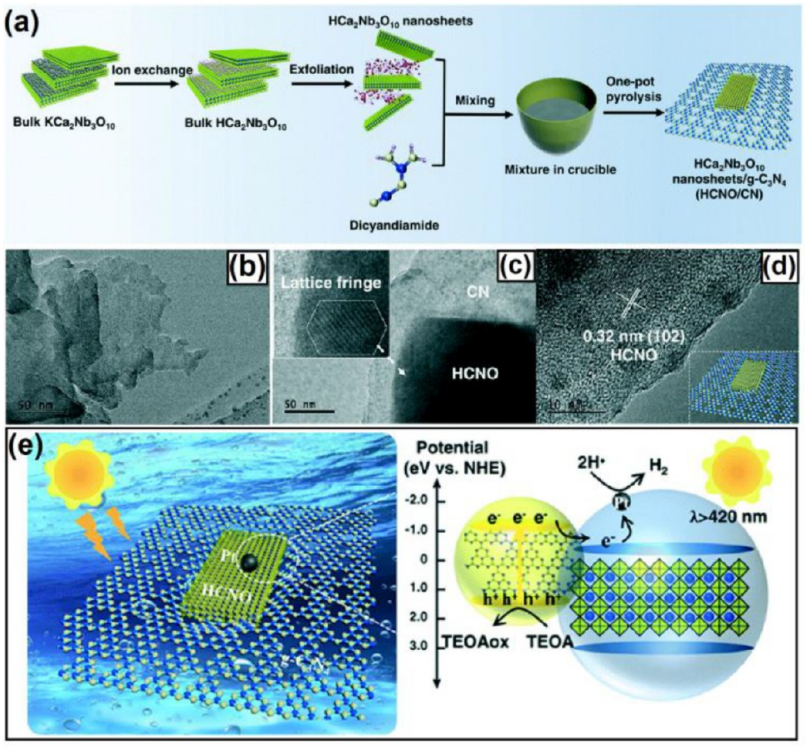

Figure 18. (a) Illustration of the preparation process of HCNO/CN composites. (b) TEM image of CN. (c, d) HRTEM images of 1.0-HCNO/CN. (e) Schematic diagram of photocatalytic H_2 evolution over HCNO/CN under visible-light irradiation (λ > 420 nm). Reprinted with permission from ref 453. Copyright 2020 Royal Society of Chemistry.

tion.[442,443] Various 2D/2D heterojunctions of layered perovskite oxides such as BiOCl/$K^+Ca_2Nb_3O_{10}^-$ Z-scheme heterostructure (tetracycline TC; degradation),[444] WO_3/$K^+Ca_2Nb_3O_{10}^-$ (TC degradation),[445] $Bi_6Fe_2Ti_3O_{18}$−BiOBr (oxygen evolution),[446] $HSr_2Nb_3O_{10}$/CdS (H_2 evolution),[447] and $HSr_2Nb_3O_{10}$/WO_3 (methyl orange degradation)[448] were developed. Heterojunctions with a 2D/2D contact of perovskite oxides and g-C_3N_4 were demonstrated to improve performance significantly due to accommodating interactions.[449] When 2D nanosheets of Bi_4NbO_8Cl were prepared by a molten-salt method coupled with g-C_3N_4 nanosheets using ball milling and thermal annealing, an improved TC degradation and CO_2 reduction were observed.[450] Type-II heterojunctions were established between two systems and photodeposition of Pt and MnO_x facilitating better charge separation. Recently, Kumar et al. demonstrated a p−n heterojunction of $Ba_2Ca_{0.66}Nb_{0.68}Fe_{0.33}Co_{0.33}O_{6-\delta}$ (BCNFCo) and carbon nitride (BCNFCo/CN) exfoliated in a dichlorobenzene and glycerol mixture (10/1, v/v) that can achieve a photocurrent density as high as 1.5 mA cm^{-2} under solar simulated light.[451] The low band gap of BCNFCo coupled with intimate contact with exfoliated carbon nitride sheets was attributed for better visible absorption and concomitant capture via carbon nitride.

In another work, $KCa_2Nb_3O_{10}$ (KCNO), a member of the Dion−Jacobson phases layered perovskite, was exfoliated using HCNO and TBAOH (tetrabutylammonium hydroxide) to form ultrathin $K^+Ca_2Nb_3O_{10}^-$ nanosheets followed by fabrication of a 2D/2D hybrid structure with g-C_3N_4 via a hydrothermal approach.[452] The afforded g-C_3N_4/$K^+Ca_2Nb_3O_{10}^-$ nanojunction displayed improved amperometric photocurrent density and TC degradation (81% in 90 min) due to better charge separation. In a recent report, $HCa_2Nb_3O_{10}$ nanosheets synthesized by ion exchange and solvent exfoliation methods were in situ grown on g-C_3N_4 using a dicyandiamide precursor at high temperature to make a 2D/2D $HCa_2Nb_3O_{10}$/g-C_3N_4 heterojunction (HCNO/CN) (Figure 18a, Table 5).[453] The HR-TEM images of g-C_3N_4 sheets displayed graphene sheet-like morphology while HCNO/CN displayed an imminent contact between two materials along with a visible lattice fringe of HCNO in the TEM images (Figure 18b−d). The absorption spectra show visible to NIR absorption of the materials with excellent charge separation evident from PL spectra. When tested for the hydrogen evolution in the presence of Pt and TEOA as cocatalyst and hole scavengers, respectively, a H_2 evolution rate of 794 μmol g^{-1} h^{-1} was obtained. The obtained activity was almost 4.5 times that of pristine g-C_3N_4. It was suggested that in a type-II heterojunction electrons were transferred to $HCa_2Nb_3O_{10}$ and subsequently to Pt where hydrogen evolution takes place (Figure 18e).

7. CARBON NITRIDE−CHALCOGENIDE 2D/2D vdW STRUCTURES

Transition metal dichalcogenides (TMDCs) constituted of hexagonal layers of metal atoms (M) sandwiched between two chalcogen layers due to their small tunable band gap, crystal structure, and excellent electronic properties have been widely explored for photocatalytic and other applications that rely on small band gap semiconductors. Depending upon the nature of the metal and chalcogens, the properties of TMDCs vary from insulator (HfS_2), semiconductor (MoS_2, WSe_2), and semimetallic (WTe_2) to metallic (TiS_2). Additionally, composition and crystalline structure also govern the conductivity (*n*- or *p*-type), band gap, and metallic transition. For example, MoS_2 is a *p*-type semiconductor and exists in two forms: (1) prismatic

https://doi.org/10.1021/acs.chemmater.1c03166
Chem. Mater. 2021, 33, 9012−9092

Table 5. 2D/2D Carbon Nitride-Perovskite Based Heterojunction Photocatalysts

photocatalyst	synthesis	application	AQY/STH	light source	remarks	ref
		Perovskite/Perovskite Type Structure				
g-C_3N_4/Au/Bi_2WO_6 Z-scheme	Hydrothermal synthesis: $Bi(NO_3)\cdot 5H_2O$ solution was added to $Na_2WO_4\cdot 2H_2O$, CTAB, and Au/CN mixture followed by stirring 30 min and heating at 120 °C for 24 h	Photocatalytic decompositions of RhB	-	300 W Xe lamp ($\lambda \geq 400$ nm)	CN/Au/BWO—88.7% in 30 min CN—59.7% RhB degradation	421
Bi_2WO_6/porous-g-C_3N_4 (W/PCN-X)	PCN and Bi_2WO_6 were mixed by ultrasonication for 48 h.	Photocatalytic degradation of RhB	-	500 W Xe lamp ($\lambda \geq 420$ nm)	The apparent rate constants (k) are for BW/PCN-15 0.043 min^{-1} and pure PCN 0.0294 min^{-1}	422
g-C_3N_4/Bi_2WO_6	Bottom-up approach: ultrathin g-C_3N_4 nanosheets, CTAB, $Na_2WO_4\cdot 2H_2O$, and $Bi(NO_3)_3\cdot 5H_2O$ were mixed and treated hydrothermally at 120 °C for 24 h.	Photocatalytic degradation of ibuprofen (IBF)	-	300 W Xe lamp ($\lambda \geq 420$ nm)	UTCB-25—~96.1% IBF degradation ug-CN—38.2% IBF degradation	423
$MgTi_2O_5$/g-C_3N_4	Hydrothermal treatment of g-C_3N_4, $Mg(CH_3COO)_2\cdot 4H_2O$, and $Ti(OC_4H_9)_4$ at 80 °C for 24 h.	Photocatalytic bacterial inactivation	-	300 W Xe arc lamp ($\lambda >$ 400 nm)	Complete inactivation of 7 log10 cfu/mL of cell reduction within 3 h; pristine g-C_3N_4 and $MgTi_2O_5$ showed almost no cell reduction	429
Bi_2MoO_6/g-C_3N_4	Hydrothermal method: g-C_3N_4, $(NH_4)_2MoO_4$, and $Bi(NO_3)_5\cdot 5H_2O$ in EG and DI water were treated hydrothermally at 443 K for 3 h.	Photocatalytic degradation of MB	-	35 W Xe lamp	BG-3—92.71% MB degradation within 150 min g-C_3N_4—51.55% MB degradation after 150 min	430
Bi_2MoO_6 on ultrathin g-C_3N_4 (UBN)	Few layers or monolayer ultrathin BMO (UBMO) and UCN were separately added and were mixed via sonication.	Photocatalytic degradation of ciprofloxacin (CIP)	-	Visible light illumination	The photocatalytic efficiency of CIP for pure UBMO and UCN is 35.62% and 39.52% within 120 min. UBN ~ 76.5%	431
Graphitic carbon nitride/carbon nanotube/Bi_2WO_6CN/CNT/BWO	Hydrothermal method: CN powder and CNT dispersion and $Bi(NO_3)_3\cdot 5H_2O$ and $Na_2WO_4\cdot 2H_2O$ dispersion were mixed, followed by hydrothermal treatment at 160 °C for 15 h.	Photocatalytic degradation of TC	-	500 W tungsten lamp	CNT/CN/BWO—87.65% TC degradation after 90 min CN—45.63% TC degradation after 90 min	432
$Bi_5FeTi_3O_{15}$/g-C_3N_4	Ultrathin g-C_3N_4 nanosheets and $Bi_5FeTi_3O_{15}$ dispersed in ethanol were ultrasonicated for 6 h and dried, followed by photodeposition of Ag using $AgNO_3$ and a 300 W Xe lamp.	Photocatalytic degradation of TC	-	300 W Xe lamp ($\lambda \geq 420$ nm)	BFTO/2% Ag/10% UCN—86% TC degradation within 20 min ~3.4 times of UCN	442
$Ba_5Nb_4O_{15}$/g-C_3N_4	$Ba_5Nb_4O_{15}$ nanosheets were dispersed into urea aqueous and calcined at 500 °C for 2 h.	Photocatalytic H_2 evolution	6.1% (420 nm)	420 nm LEDs	H_2—1138 μmol g^{-1} h^{-1}($Ba_5Nb_4O_{15}$/g-C_3N_4 (1:20)) ~2.35 times of bare g-C_3N_4 (56.9 μmol g^{-1} h^{-1})	443
g-C_3N_4/$K^+Ca_2Nb_3O_{10}^-$	One-step hydrothermal approach: K^+CNO^- nanosheets and as-prepared CN were sonicated in DI water, followed by hydrothermal treatment at 140 °C for 12 h.	Photocatalytic degradation of tetracycline hydrochloride (TC)	-	500 W tungsten lamp	20-CN/K^+CNO^-—81% of TC in 90 min CN nanosheets—45.9% TC degradation in 90 min	452

https://doi.org/10.1021/acs.chemmater.1c03166
Chem. Mater. 2021, 33, 9012−9092

trigonal 2H phase with semiconducting properties and (1) octahedral 1T phase with metallic properties. Additionally, the transformation of bulk indirect band gap 2H-MoS_2 into a monolayer 1T phase switches the electronic band structure into a direct band gap. Layered transition metal with high effective surface area, numerous exposed active sites, available surface for vdW interaction, manipulatable band structure, and ease of synthesis by numerous chemical and physical methods are considered efficient photocatalytic materials. A typical example is monolayer SnS_2, which yielded a photocurrent density of 2.75 mA cm^{-2} at 1.0 V, nearly 72 times larger than that of bulk SnS_2, proven in theory and experiment.[454]

TMDC 2D sheets have been widely used in photocatalysis as a standalone catalyst, heterojunctions, or cocatalyst to improve the performance of wide band gap semiconductors.[455] TMDCs of groups IV−VI in 0D, 1D, 2D, and 3D morphology such as MoS_2, WS_2, TiS_2, $MoSe_2$, and WSe_2 have been extensively explored due to their excellent optical, electronic, and catalytic activities (unusual catalytic activity at the edges), crystalline structure, layer dependent metal to insulator transition, etc. Cadmium sulfide (CdS), the most investigated chalcogenide with a low band gap (∼2.42 eV) and excellent electronic mobility, suffers from the drawback of extreme photocorrosion.[456−458] To stabilize and modify the optical properties, a solid solution and homojunction of CdS with ZnS with a fractional composition ($Cd_{(1-x)}Zn_xS$) have been reported.[459,460] Ternary and multinary chalcogenides such as I-III-VI_2, I_2-II-IV-VI_4, Cu_2MoS_4, Cu_2MoSe_4, Cu_2WS_4, $AgGaS_2$, $LiAlS_2$, $LiGaSe_2$, Cu_2FeSnS_4, Cu_2NiSnS_4, Cu_2ZnSnS_4, and $Dy_4S_4Te_3$ prevail upon binary TMDCs because of their tunability, choice of several atomic combinations, suitable band gap, and easy fabrication via solution processing/hydrothermal/solid-state synthesis in the 2D structures.[461−465]

Further, heterojunction formation with numerous low and high band gap semiconductors in different morphological structures has been utilized. Astonishingly high numbers of 2D/2D heterojunction are reported using metal chalcogenides as they can easily attain epitaxial or nonepitaxial 2D growth on the different 2D materials.[466−471] Interestingly, small 2D conjugated dye molecules, aromatics, and polymers such as phthalocyanine and pentacene are also found to make a 2D/2D structure with TMDCs.[468,472,473] New 2D organic semiconductors with long-range ordering such as C_2N, C_3N, and C_4N_3 are the potential candidates to make a 2D/2D vdW heterostructure as they possess exceptional optical and chemical properties with an electron-rich conjugated surface to interact effectively with TMDCs.[474−476] C_2N with a graphene-like hexagonal framework with a small cavity constituted of carbons and nitrogens provides faster transport of the charge carrier but behaves like a semiconductor and has plenty of sites for the reactions.[477,478] In 2D/2D C_2N/TMDCs, heterojunctions such as C_2N/MoS_2 and C_2N/WS_2, the deep valence band of C_2N was usually exploited for oxidation while coupled TMDCs with negative CB were used for reduction reactions.[479−483] These 2D organic semiconductors are usually synthesized in milligram scale using sophisticated chemicals and possess only reductive or oxidative bands, so they do not fulfill the criteria of scalable photocatalysis. In contrast, 2D g-C_3N_4 and their conjugates with certain doping can be produced at a large scale to make cheap and resilient photocatalysts for real applications. In the next sections, the 2D/2D vdW heterostructure constituted of binary, ternary, and noble metal-based chalcogenides will be discussed with a few representative examples.

7.1. Carbon Nitride−MoS_2. Natural MoS_2 is an indirect band gap (1.29 eV) semiconductor that exists as hexagonal form 2H-MoS_2 (H—hexagonal symmetry) and has been the most studied chalcogenide due to an earth-abundant nature and unique electronic, optical, and magnetic properties.[63,484,485] Due to its excellent properties, MoS_2 has potential applications in electronics, optoelectronics, and energy applications, including water splitting. The catalytic activity of MoS_2 arises from sharp edges constituted of S atoms and defects while the basal plane is catalytically inert.[486] However, the surface energy at the basal plane is almost two times lower than that at the edge, which allows MoS_2 growth along the basal plane and also provides a platform for epitaxial and nonepitaxial growth of other semiconductors to make heterojunctions.[487] The edges are usually transformed into an unstable sulfide state (Mo−S−O links) during photocatalytic reactions and reducing the photocatalytic performance.[488] The activity of MoS_2 can be increased by the transformation of the 2H crystal phase into more conductive 1T-MoS_2 (T stands for trigonal symmetry with octahedral Mo−S coordination and zigzag $(Mo)_n$ chains)) phase, which has a high electron conductivity to the active sites.[489,490] Due to their extreme metallic nature, 1T-MoS_2 has been used as a cocatalyst in photocatalytic applications.[491,492] Unfortunately, metallic 1T-MoS_2 remain stable only in the presence of excess negative charge on the MoS_2 sheets. An intercalated alkali metal such as Li, Na, etc. has been used to provide electrons; however, the afforded structures are extremely air-sensitive, and removal of alkali atoms leads to phase reversal under mild conditions.[493,494] Use of organic cations such as alkylammonium cations, imidazolium, etc. has been used to stabilize the 1T-MoS_2 sheets.[495−497]

Recently, some reports demonstrate the stabilization of 1T-MoS_2 sheets on the surface of g-C_3N_4 to form 2D/2D heterostructures.[498] For example, the 2D 1T-MoS_2 heterojunction with 2D sheets of oxygen doped carbon nitride (O-g-C_3N_4) was prepared via a hydrothermal approach and demonstrated improved photocurrent generation and H_2 evolution rate in the presence of a triethanolamine sacrificial donor.[499] The metallic component in heterojunctions contributes only to charge separation, while their negligible contribution in absorbance and photocarrier generation coupled with the inappropriate band structure of the single semiconductor are some undesirable attributes. So, the semiconductive form 2H-MoS_2 is more appropriate to fabricate 2D/2D heterostructures. Several 2D/2D heterostructures using the 2H-MoS_2 phase and g-C_3N_4 (modified/unmodified) have been realized for the photocatalytic performance enhancement.[500−504]

MoS_2 demonstrated excellent HER activity due to S terminated edge and S−Mo−S layered structure analogous to carbon nitride that minimizes lattice mismatch in the 2D/2D heterostructure resulting in improved charge separation.[505,506] The pioneering work by Hou et al. demonstrated lateral growth of MoS_2 sheets on g-C_3N_4 using a $(NH_4)_2MoS_4$ precursor followed by sulfidation with H_2S gas at 350 °C.[507] The TEM images demonstrated 2−3 layered thick MoS_2 grown on the surface of carbon nitride, while XPS spectra confirm the presence of populated Mo^{4+} and S^{2-} in a well-constituted MoS_2 structure. The electrochemical HER polarization curve in Na_2SO_4 displayed an enhanced current density

https://doi.org/10.1021/acs.chemmater.1c03166
Chem. Mater. 2021, 33, 9012−9092

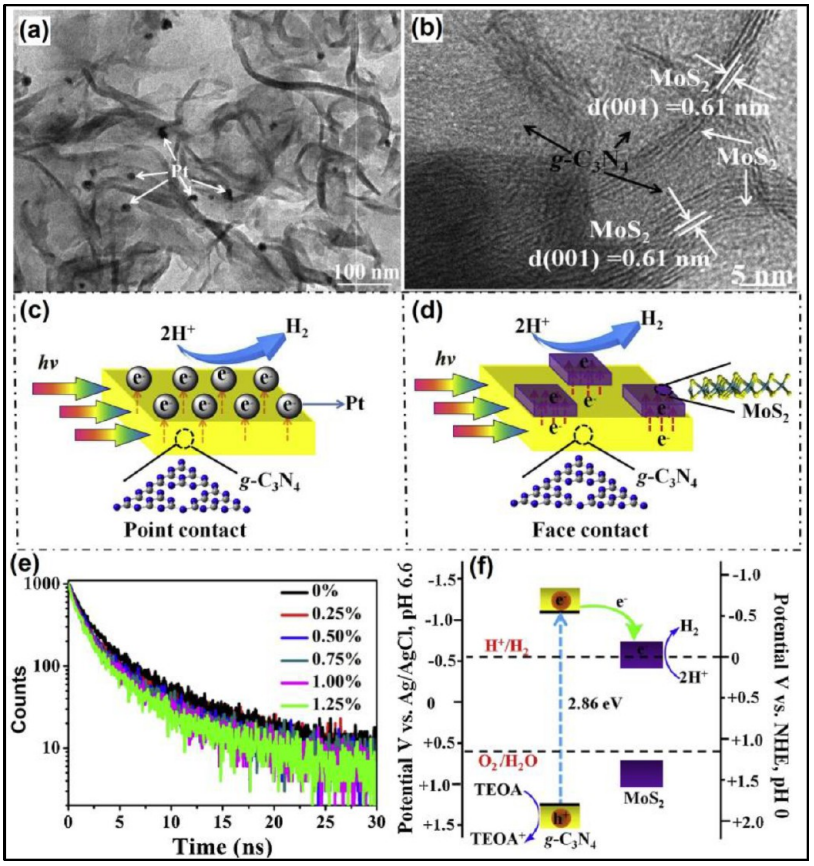

Figure 19. (a) TEM images of the 3% Pt/g-C_3N_4 nanosheets photocatalyst. (b) HRTEM image of 0.75% MoS_2/g-C_3N_4 nanosheets composite. (c and d) Schematic diagrams of 0D-2D Pt/g-C_3N_4 nanosheets photocatalysts and 2D-2D MoS_2/g-C_3N_4 nanosheets photocatalysts. (e) Time-resolved fluorescence spectra of different MoS_2/g-C_3N_4 nanosheets photocatalysts loading with various amounts of MoS_2. (f) Schematic energy-level diagrams of MoS_2 and g-C_3N_4 in comparison with the H^+/H_2 and O_2/H_2O redox potentials. Reprinted with permission from ref 508. Copyright 2019 Elsevier.

for the MoS_2/mpg-CN heterojunction and decreased charge transfer resistance compared to mpg-CN. As a photocatalytic material for HER, 0.5 wt % MoS_2/mpg-CN vdW hybrid (20.6 μmol h^{-1}) outperforms over 0.5 wt % Pt/mpg-CN (4.8 μmol H_2 h^{-1}), suggesting the possibility of exclusion of expensive noble metal catalysts. In a study by Yuan et al., g-C_3N_4 exfoliated in NMP was hydrothermally reacted with ammonium tetrathiomolybdate [$(NH_4)_2MoS_4$] that resulted in the formation of a 2D/2D MoS_2/g-C_3N_4 heterojunction (Figure 19).[508] The well contacted g-C_3N_4 and MoS_2 were visible in the HR-TEM images along with the AFM images (Figure 19a,b). The photocatalytic activity of 2D/2D MoS_2/g-C_3N_4 catalysts was compared with 3% Pt/g-C_3N_4 benchmark catalyst and demonstrated that interfacial contact of g-C_3N_4 with MoS_2 affords more efficient charge separation. The TEM images of 3% Pt/g-C_3N_4 reveal homogeneously dispersed Pt nanoparticles on the surface of g-C_3N_4 (Figure 19a). Interestingly, when tested for the photocatalytic H_2 evolution, the 2D/2D MoS_2/g-C_3N_4 displayed an excellent H_2 evolution rate (1155 μmol g^{-1} h^{-1}) which was even higher than that of the 3% Pt/g-C_3N_4 benchmark photocatalysts (791 μmol g^{-1} h^{-1}). Additionally, experiments reveal that the presence of g-C_3N_4 in the form of 2D sheets was crucial, and a very poor H_2 evolution rate was obtained for MoS_2 and bulk g-C_3N_4. The gradually decreasing lifetime after adding MoS_2 shows better charge separation, while band structures calculated from the Mott−Schottky and Tauc plots reveal the formation of a type-I heterojunction (Figure 19c−e). In a recent report, 2H MoS_2 modified g-C_3N_4(MoS_2/g-C_3N_4) 2D/2D vdW heterojunction was synthesized using 12-phosphomolybdic acid ($H_3PMo_{12}O_{40}$, PMA) and thioacetamide (TAA) as Mo and sulfur sources.[509] The MoS_2/g-C_3N_4 catalyst displayed a significant H_2 production rate (1497 μmol g_{cat}^{-1} h^{-1}) with an associated apparent QY of 3.3% at 410 nm irradiation. The charge carrier density (N_d) of MoS_2/g-C_3N_4 samples was found in the range of 7.80×10^{17} to 5.13×10^{18} cm^{-3}, much larger than pristine g-C_3N_4 (7.10×10^{17} cm^{-3}), suggesting a better establishment of heterojunctions (Figure 19f). Even a ternary heterojunction constituted of g-C_3N_4-5%/MoS_2/graphene was also made, which exhibited an RhB degradation rate of 95% under 20 min.[510]

7.2. Carbon Nitride−WS_2. Another important layered TMDC of the group-VI family is tungsten disulfide (WS_2), which shows an indirect (1.4 eV) to direct (2.0 eV) band gap transition when bulk materials are transformed into monolayer sheets.[511,512] Like MoS_2, WS_2 also exists in a crystalline form called 2H-WS_2 and octahedral 1T WS_2. Additionally, 1T WS_2 has a metallic nature and can be synthesized by lithium exfoliation. Exceeding over MoS_2, the intrinsic electrical conductivity of WS_2 is higher than that of MoS_2, which makes it a suitable cocatalyst candidate. Indeed, numerous reports are available on the use of nanostructured WS_2 as a cocatalyst and sensitizer in photocatalysis.[513−515] Exfoliation of bulk WS_2 sheets via lithium intercalation led to phase

https://doi.org/10.1021/acs.chemmater.1c03166
Chem. Mater. 2021, 33, 9012−9092

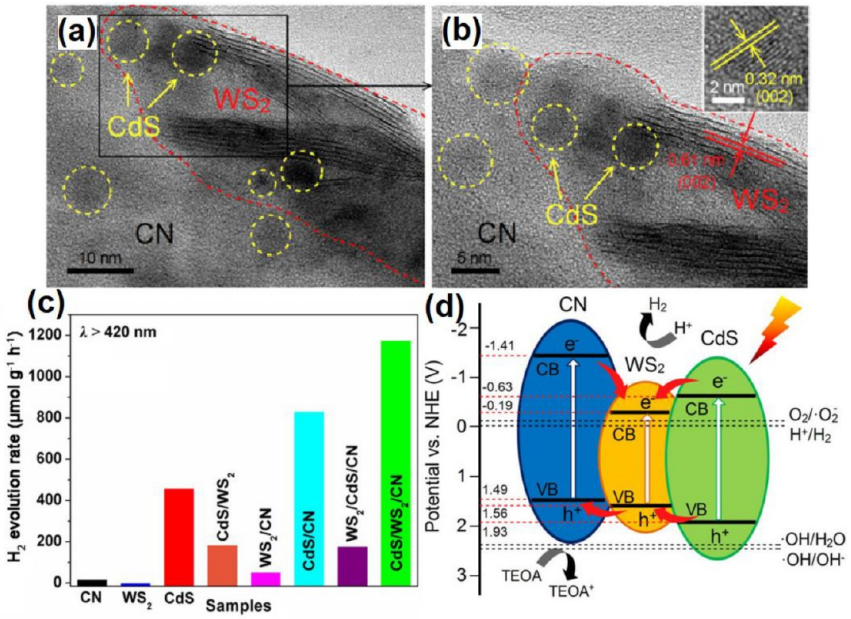

Figure 20. (a, b) TEM images of $CdS/WS_2/CN$. (c) Average photocatalytic H_2 production rates over different samples under visible-light irradiation ($\lambda > 420$ nm). (d) Photocatalytic mechanism in pathway III and the band positions of the samples, together with $O_2/^{\bullet}O_2^-$, $^{\bullet}OH/H_2O$, H^+/H_2, and $OH^-/^{\bullet}OH$ redox potentials. Reprinted with permission from ref 540. Copyright 2018 Wiley-VCH.

conversion (2H to the metallic 1T). The reversion of the 1T phase to 2H phase requires further annealing, which introduces plenty of defect states and a charge recombination center, which is undesirable for photocatalysis.

High-quality 2H WS_2 sheets without any 2H to 1T phase transition can be synthesized by micromechanical exfoliation; however, the yield of sheets remains too low for scalable production.[516] Xu et al. developed a scalable method to produce 2H WS_2 sheets in 18−22% yield, which involves preintercalation of a stoichiometric amount of lithium ions followed by exfoliation in sodium chlorate/water solution.[517] Interestingly, when coupled with CdS nanorods, the WS_2/CdS NRs hybrid displayed an impressive 26-fold increment of the H_2 evolution rate with an associated AQE of 67% at 420 nm. Additionally, stand-alone 2H WS_2 nanosheets decorated with Pd nanoparticles can promote Suzuki coupling under visible light with a turnover frequency as high as 1244 h^{-1}.[518] However, for water splitting, CO_2 reduction and degradation of pollutant high redox potential are needed and it became essential to integrate WS_2 with other semiconductors to meet the minimum energy (1.23 eV) requirement. Several heterojunctions using semiconductive WS_2, such as WS_2/TiO_2,[519] WS_2/Zn_2InS_4,[520] WS_2/BiOBr,[521] $WS_2/Bi_2O_2CO_3$,[522] and CdS/WS_2,[523,524] in various morphological forms have also been fabricated as they not only improve the visible absorption and the charge separation but also act as a cocatalyst.[525] To garner the superior properties of such as 2D structure, high surface area, excellent electronic mobility, and suitable low band gap 2D/2D vdW heterostructures such as WS_2/TiO_2,[526] MoS_2/WS_2,[527,528] WS_2/CdS,[529] Bi_2WO_6/WS_{2-x},[530] and WS_2/ZnO[531] have also been developed.

Although many WS_2/g-C_3N_4 hybrids have been developed, which showed increased photocatalytic performance, the formation of 2D/2D contact remains ambiguous in many of them and only a few demonstrated well-constructed heterojunctions between 2D WS_2 and g-C_3N_4 nanosheets.[532−537] Recently, Li et al. demonstrated the synthesis of a 2D/2D Pg-C_3N_4/WS_2 by the self-assembly of protonated g-C_3N_4 and WS_2 in sensing applications, reaching a fabulous detection limit of 3.8 pM for 5-formylcytosine.[538] In another study, to accelerate the charge transport between WS_2 and g-C_3N_4 nanosheets, a g-$C_3N_4/WS_2$2D/2D architecture bridged with Ag was prepared by sequential deposition of constituting components.[539] The WS_2/Ag/g-C_3N_4 displayed improved NO removal and H_2 production because the increased interlayer spacing reactant can access large numbers of active sites while Ag promotes a better charge separation. Similarly, CdS nanoparticle decorated WS_2/g-C_3N_4 2D/2D vdW heterostructures ($CdS/WS_2/CN$) were prepared by sequential deposition of Cd^{2+} and S^{2-} on WS_2/CN (Figure 20).[540] The HRTEM images show intimated contact between NMP assisted exfoliated CN and WS_2 nanosheets, and spherical CdS particles were sandwiched in a WS_2/CN hybrid (Figure 20a,b). The $CdS/WS_2/CN$ hybrid displayed an H_2 evolution rate of 1174.5 μmol g^{-1} h^{-1}, which was 67 times higher than that of CN (Figure 20c). The corresponding quantum efficiency was calculated to be 5.4% at 400 nm. The enhanced activity was assumed to be due to better electron transfer from CN and CdS to WS_2 while hole transfer occurred from CdS/WS_2 to CN (Figure 20d).

7.3. Carbon Nitride−$FeSe_2$. Iron-based binary chalcogenides such as iron pyrite (FeS_2; iron disulfide) and $FeSe_2$ can absorb a major fraction of electromagnetic radiation in the UV−visible to NIR region and thus found applications in many photocatalytic and electronic applications.[541−544] The representative member FeS_2 has an indirect band gap of ≈1.0 eV (2-fold high photon absorption coefficient, 10^5 cm^{-1} more than silicon), high carrier mobility, and a theoretical power conversion efficiency of 28% and can be easily synthesized using earth-abundant chemicals like iron (∼5% of the earth's crust) and sulfur (0.042% of the earth's crust) sources such as sulfur powder, Na_2S, thiourea, thioacetamide, etc.[545,546] FeS_2 has been widely investigated for solar cell application and heterojunction photocatalysis with numerous inorganic and organic semiconductors. Unfortunately, the performance of

https://doi.org/10.1021/acs.chemmater.1c03166
Chem. Mater. 2021, 33, 9012−9092

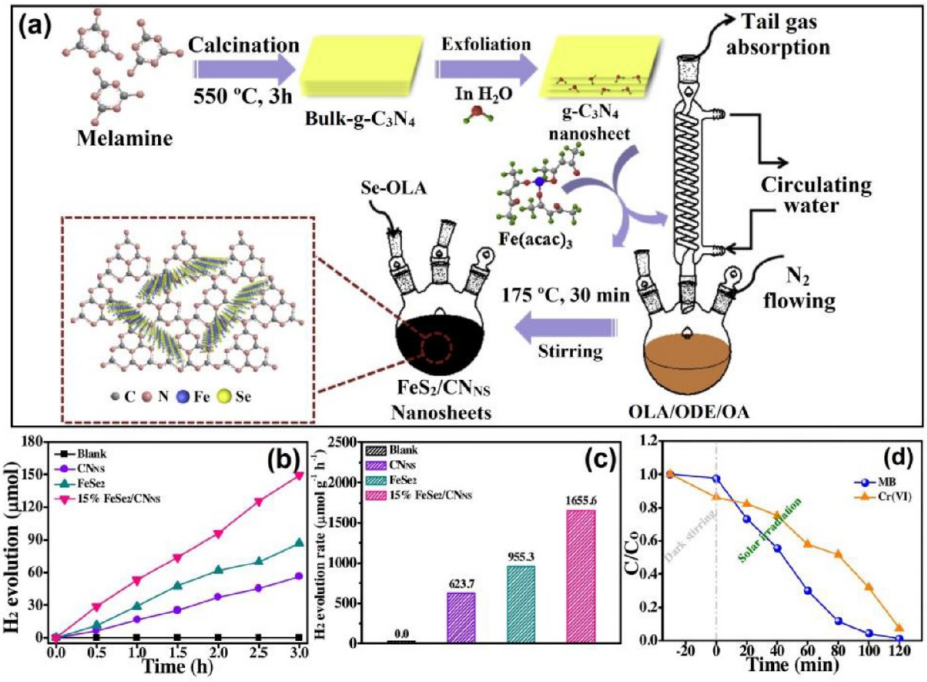

Figure 21. (a) Schematic image for the synthesis procedures of 2D/2D $FeSe_2/CN_{NS}$ interplane heterostructures. Photocatalytic H_2 evolution curves (b) and rates (c) for pure g-C_3N_4, $FeSe_2$, and various $FeSe_2/CN_{NS}$ heterostructures. The photocatalytic MB and Cr(VI) degradation performance of pure (d) 15% $FeSe_2/CN_{NS}$. Reprinted with permission from ref 557. Copyright 2020 Elsevier.

FeS_2 is plagued by prodigious charge recombination in grain boundaries and surface defects. Compared with metal sulfides, metal selenides are advantageous as they have a narrow band gap and improved carrier mobility. Although S and Se are the members of the same periodic group and have almost similar chemical properties, the bond strength of Se−H (276 kJ/mol) is significantly lower than that of S−H (363 kJ/mol), leading to better adsorption−desorption of the proton, which is essential to facilitate the product desorption from catalytic sites.[547]

$FeSe_2$ exists in two polymorphic forms (orthorhombic marcasite and cubic pyrite), possessing indirect band gaps of 0.86 and 0.67 eV.[548] $FeSe_2$ exhibits an excellent conductivity (resistivity $\approx 10^{-3}$ Ω·cm), populated surface iron atoms, low toxicity, and benign nature and is favorable for the water splitting due to the presence of abundant [Fe−Fe] hydrogenase type active centers accelerating proton adsorption and H_2O_2 decomposition.[549,550] Even with such excellent properties, photocatalytic applications of $FeSe_2$ are sparse, and most of the applications of $FeSe_2$ are limited to solar cells and the sodium-ion battery (SIB).[551−553,553] The 0D/1D hybrid $FeSe_2$ and ZnSe demonstrated increased photosplitting of water due to better charge separation in the type-I heterojunction.[554] Other heterojunctions such as 1D/2D $FeSe_2/MoSe_2$ and $FeSe_2$ nanodendrites decorated on GO and g-C_3N_4 have been reported[555,556]

Remarkable results were obtained by the marriage of 2D $FeSe_2$ and 2D sheets of g-C_3N_4 (CN_{NS}) (Figure 21).[557] The synthesis of 2D/2D $FeSe_2/CN_{NS}$ was achieved via the formation of g-C_3N_4 sheets followed by in situ growth of $FeSe_2$ using $Fe(acac)_3$ and Se precursors in the presence of 1-octadecene (ODE) and oleylamine (OLA) (Figure 21a). The close 2D/2D face-to-face contact between $FeSe_2$ and CN_{NS} was evident from the TEM and AFM images. The optimum photosplitting of water was observed for the 15% $FeSe_2/CN_{NS}$ reaching a value of 1655.6 μmol g^{-1} h^{-1}, almost 2.65 times that of pure g-C_3N_4 in the presence of Na_2S/Na_2SO_3 and solar simulated light (Figure 21b,c). Further, $FeSe_2/CN_{NS}$ also afforded enticing removal efficiencies of 92.6% for Cr(VI) and 99.8% for MB within 120 min while pristine g-C_3N_4 affords only 44.7% Cr(VI) and 66.1% MB removal efficiencies under identical conditions (Figure 21d). Interestingly, liquid chromatography−mass spectroscopy (LC-MS) demonstrated the ring-opening degradation followed by mineralization. The wide visible absorption extended up to 1200 nm, decreased the PL lifetime, decreased charge transfer resistance, and improved the transient photocurrent compared to pristine materials, validating better charge separation in the $FeSe_2/CN_{NS}$ composite structure. Photocatalytic experiments in the presence of scavengers and radical trapping agent DMPO demonstrated that $^{\bullet}OH$ radicals were responsible for the degradation activity. The validation of the origin of $^{\bullet}OH$ radicals from the derivatization of the superoxide anion radical ($O_2^{\bullet-}$) via H_2O_2 intermediate was done by the DPD-POD method, which showed increased $^{\bullet}OH$ radical concentration during reaction using UV−vis spectroscopy.

7.4. Carbon Nitride−PtS_2. Noble metal dichalcogenides (MX_2, M = Pt, Pd, Ir, Re, etc., X = S, Se, Te) are known to possess photocatalytic activity for a long time.[558−563] However, their use is limited due to the cost issue and small band gap. Recently, some excellent reports on 2D MX_2 have emerged and rejuvenated the field. Group 10 dichalcogenides such as PtS_2, $PtSe_2$, and $PtTe_2$ have shown great promise due to their superior properties.[564,565] For example, platinum disulfide (PtS_2), a layered material, has displayed high carrier mobility (3500 cm^2 V^{-1} S^{-1}) even larger than that of phosphorene (1000 cm^2 V^{-1} S^{-1}), which makes it suitable for various applications from photocatalysis to fast-moving electronic applications including gas sensors, field-effect transistors (FET), etc.[566] DFT calculation reveals that monolayer PtS_2

https://doi.org/10.1021/acs.chemmater.1c03166
Chem. Mater. 2021, 33, 9012−9092

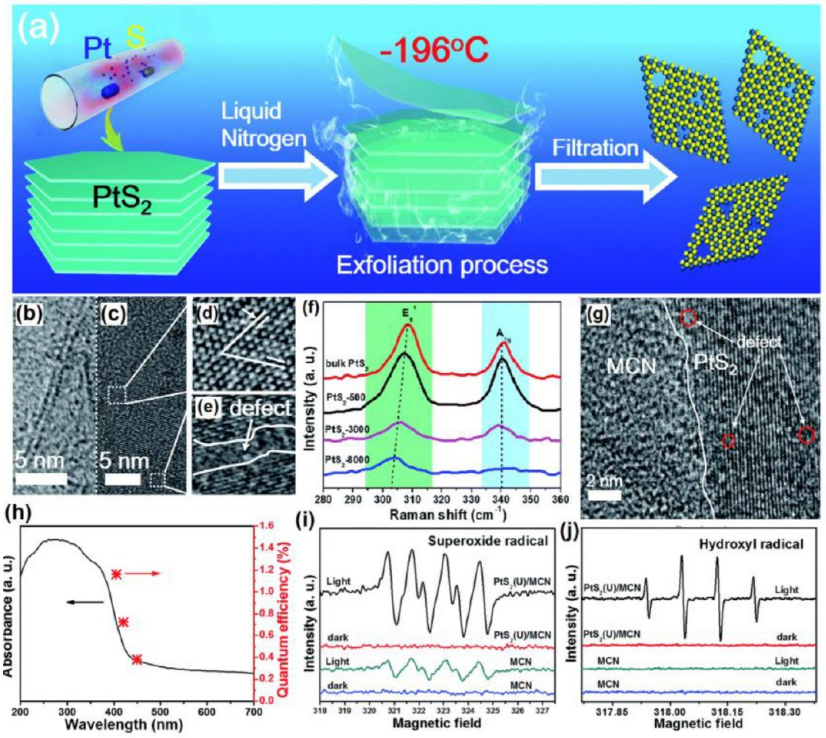

Figure 22. (a) Schematic illustrating the synthesis procedure of ultrathin PtS_2 nanosheets. (b) Enlarged TEM image of the PtS_2-8000. (c, d, e) High-resolution TEM image of PtS_2-8000; the insets correspond to the enlarged write frames. (f) Raman spectra. (g) HRTEM image of the 1 wt % PtS_2(U)/MCN composites. (h) Wavelength dependence of the external quantum efficiency for the PtS_2(U)/MCN composites. (i) ESR spectra of DMPO-$O_2^{\bullet-}$ and (j) DMPO-$^{\bullet}$OH adducts in the systems of pristine MCN and 1 wt % PtS_2(U)/MCN before and after visible-light irradiation. Reprinted with permission from ref 578. Copyright 2019 Royal Society of Chemistry.

is a semiconductor with an indirect energy gap between 1.60 and 1.80 eV, while bulk PtS_2 reveals band gaps of 0.95 and 0.87 eV. PtS_2 and $PtSe_2$ in the forms of nanoparticles and nanosheets can be synthesized via various routes such as high-pressure synthesis, chemical vapor transport, liquid-phase exfoliation, etc. Ajibade et al. demonstrated the synthesis of PtS_2 nanoparticles using a bis(morpholinyl-4-carbodithioato)-platinum(II) thermalization, which showed a visible light degradation of MB.[567] Due to its layered nature, PtS_2 is an ideal candidate for the fabrication of heterojunction with various semiconductors. For instance, DFT calculation suggests that PtS_2 and arsenene can make a 2D/2D Z-scheme heterojunction due to the epitaxial matching with the only mismatch of less than 2%. The calculated electrostatic potential unveils the potential difference can make a built-in electric field to make charge transfer feasible. To date, vdW PbI_2/PtS_2,[568] PtS_2/MoS_2,[569,570] $MoSe_2/PtS_2$,[571] graphene/PtS_2,[572] PtS_2/InSe,[573] $PtS_2/PtSe_2$,[574] etc. have demonstrated excellent electronic and optical properties for photodetectors, solar cells, FET, and other optoelectronics. A very recent theoretical report demonstrated that PtS_2 is an ideal substrate that can stabilize single atoms to make a single-atom catalyst (SACs). Among 15 kinds of possible SACs (Ti, V, Cr, Mn, Fe, Co, Ni, Zr, Nb, Mo, Rh, Ru, Pd, Ir, and Pt), Ru SAC-PtS_2 can optimally catalyze the N_2 reduction reaction (NRR).[575] PtS_2 exists in two forms, 1T PtX_2 and 3R PtX_2. Villaos et al. calculated the lattice constant band gap energy and concluded that octahedral 1T PtX_2 is the most stable form of bulk PtX_2 structure, which was consistent with experiment evidence.[558,576,577]

Bulk PtS_2 can be transformed into 2D sheets by taking advantage of weak vdW interaction between S−Pt−S bonded PtS_2 sheets, which can be overcome by mild sonication conditions. Liu et al. synthesized defect-rich PtS_2 by chemical vapor transport (CVT) followed by the cryo-mediated liquid-phase exfoliation (LPE) method (Figure 22).[578] The treatment with liquid N_2 and subsequent ultrasonication in isopropanol/H_2O afforded high-quality defect-rich sheets (Figure 22a). The PtS_2 sheets were coupled with liquid exfoliated mesoporous carbon nitride (MCN) sheets. The decrement of the (001) and (002) peaks for *c*-axis orientation along with TEM images and SAED suggests a successful exfoliation of sheets (Figure 22b−e). Blue and red Raman shifts of E^1_g and A_{1g} phonon modes integrated with decreasing peak intensity also demonstrate a transformation of bulk PtS_2 in nanosheets (Figure 22f). The average thickness of sheets was found to be 1.18 nm (equal to a two-unit-cell PtS_2 slab), while the interplanar spacing and dihedral angle were calculated to be 0.315 nm and 60°, respectively. The presence of a defect-rich state was evident from the TEM images and was further confirmed from the EPR signal at the g-value of 2.006 due to the presence of S vacancies. The intimate 2D/2D contact in 1 wt % PtS_2(U)/MCN hybrid was visible in HR-TEM images, showing amorphous MCN cemented with crystalline PtS_2 (Figure 22g). Optimization of the catalyst demonstrated that PtS_2 sheets prepared by centrifugation at 8000 (PtS_2-8000) and in a 1 wt % addition showed optimum photocatalytic performance for hydrogen evolution (1168 μmol g^{-1}) with an associated quantum efficiency (QE) of 1.16% at 405 nm (Figure 22h). Trapping the radicals with DMPO followed by ESR measurement demonstrated a strong signal of superoxide

https://doi.org/10.1021/acs.chemmater.1c03166
Chem. Mater. 2021, 33, 9012−9092

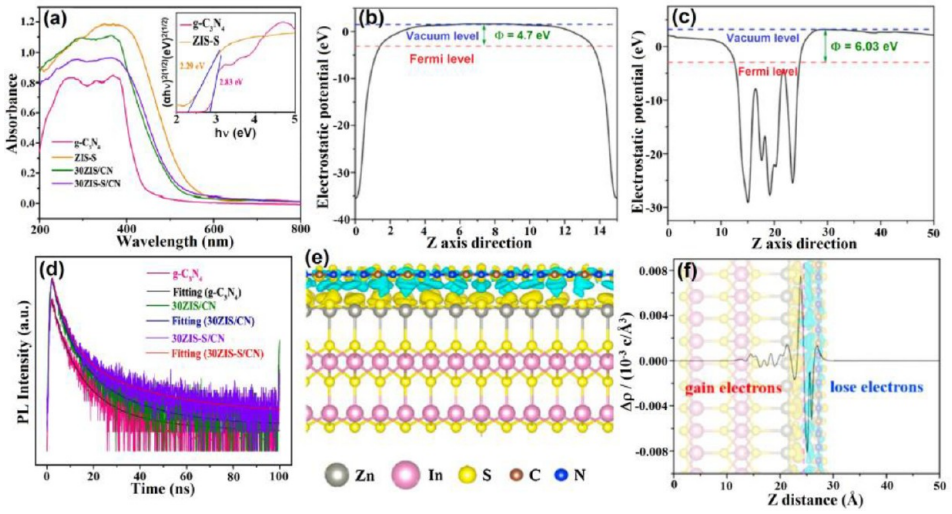

Figure 23. (a) UV−vis diffuse reflection spectra of g-C_3N_4, ZIS-S, 30ZIS/CN, and 30ZIS-S/CN and the band gap of g-C_3N_4 and ZIS-S (inset). Average potential profiles along *Z*-axis direction for (b) g-C_3N_4 and (c) ZIS-S. (d) Time-resolved fluorescence spectra of g-C_3N_4 and 30ZIS-S/CN. (e) Side-view differential charge density maps of g-C_3N_4 and ZIS-S. (The yellow and blue regions represent net electron accumulation and depletion, respectively. The gray, purple, yellow, brown, and blue spheres are Zn, In, S, C, and N atoms, respectively.) (f) Planar averaged charge density difference $\Delta\rho$ along the *Z*-direction for the ZIS-S/CN VDW heterojunction (the inset represents the 3D isosurface of the electron density difference for the ZIS-S/CN). Reprinted with permission from ref 602. Copyright 2020 Elsevier.

($O_2^{\bullet-}$) and hydroxyl ($^{\bullet}OH$) radicals (Figure 22i,j) which were very weak with MCN, clearly demonstrating the synergistic role of PtS_2 to facilitate better charge transportation and stabilization.

7.5. Carbon Nitride−$ZnIn_2S_4$. Compared to binary metal dichalcogenides, ternary metal dichalcogenides have gained significant interest due to their high photocorrosion resistance, tunable band gap, band positions, low toxicity, and easy synthesis. Among many ternary chalcogenides such as $CuGaS_2$, $Zn_3In_2S_6$, and $CuInS_2$, zinc indium sulfide ($ZnIn_2S_4$) is the most appealing because of the direct band gap (2.06−2.85 eV), layered structure, appropriate thermodynamic potential to meet photocatalytic demand, and facile synthesis from earth-abundant precursors.[579] Notably, the CB of $ZnIn_2S_4$ with d^{10} electronic configuration is constituted of the sp orbitals of In^{3+}, which is favorable for transferring the photogenerated electrons to the surface and thereby enhancing the photocatalytic performance.[580−582] $ZnIn_2S_4$ exists in three forms, cubic, hexagonal, and rhombohedral phase and all of them show photoactivity with optimum performance for the hexagonal phase. It has been widely used for numerous photocatalytic and optoelectronic applications such as CO_2 reduction, photo-organic transformation, water splitting, pollutant degradation, etc.[583,584] The main challenge using $ZnIn_2S_4$ is colossal bulk and surface charge recombination. The structural and electronic properties of $ZnIn_2S_4$ have been improved via various strategies such as surface area modification, morphological modification (i.e., microsphere, nanobelts, nanowires, and nanotubes), doping with metals/alkaline metal, etc.[585−589] Several types of nanoheterojunctions of $ZnIn_2S_4$ with other semiconductors have been reported to reduce charge recombination.[590−593] Transformation of $ZnIn_2S_4$ into mono- or few-layered sheets can shorten the electron travel pathway and, thus, can reduce the charge recombination rate.[594,595] Further, an enticing approach to extend the carrier lifetime of $ZnIn_2S_4$ is to construct a face-to-face interacting 2D/2D heterojunction with another semiconductor/conductor, which can either capture electrons or the hole and promote the charge separation. For example, the 2D/2D heterojunction of $CuInS_2/ZnIn_2S_4$ can achieve better charge separation that boosted the H_2 evolution rate than individual components ($CuInS_2$ and $ZnIn_2S_4$).[596]

Though numerous 2D/2D heterojunctions of $ZnIn_2S_4$ with other 2D semiconductors such as CoP[597] and ZnO[598] have been reported, the tedious fabrication, significant carrier loss at the mismatched lattice interfaces and grain boundaries, low quality of 2D films, and limited charge carrier mobility are still challenges. The fabrication of the 2D/2D vdW heterojunction of $ZnIn_2S_4$ with g-C_3N_4 can solve such issues due to the formation of the nonepitaxial heterojunction and the flexible surface.[599−604] The conjugated network of g-C_3N_4 can provide better charge mobility while the N-rich surface promotes the effective interaction between two surfaces, and well-tuned band edge positions promote both reduction and oxidation reactions. Zhou et al. were able to make a 2D/2D vdW heterojunction between ultrathin polymeric carbon nitride (PCN) and $ZnIn_2S_4$ subunits via an in situ self-assembling growth of $ZnIn_2S_4$ on thermally produced PCN sheets.[600] The intimate junctions between $ZnIn_2S_4$ and PCN were confirmed from HRTEM and elemental mapping. The PCN/$ZnIn_2S_4$ exhibited a high CO_2 uptake (17 $cm^3\ g^{-1}$) compared to pristine materials and was further used for CO_2 photoreduction. Using the PCN/$ZnIn_2S_4$ vdW heterostructure as a photocatalyst, triethanolamine (TEOA) as the electron donor, and $Co(bpy)_3^{2+}$ as the cocatalyst, the CO formation rate was found to be 44.6 μmol h^{-1}, which was almost 223 times that of the pristine PCN nanosheets. In another report, 2D g-C_3N_4 sheets were introduced in precursor solution which led to adsorption of Zn^{2+} and In^{3+} ions on the g-C_3N_4 sheets.[601] Finally, the growth of $ZnIn_2S_4$ takes place in the presence of thioacetamide as a sulfur source and trisodium citrate dihydrate as a surfactant under hydrothermal conditions. The developed 2D/2D g-C_3N_4@$ZnIn_2S_4$ system displayed a remarkable H_2 evolution rate (2.78 mmol $g^{-1}\ h^{-1}$), which was much higher than any carbon nitride-based catalyst with or without Pt decoration.

https://doi.org/10.1021/acs.chemmater.1c03166
Chem. Mater. 2021, 33, 9012−9092

To further improve the performance of the g-C_3N_4@ $ZnIn_2S_4$ vdW heterostructure, S vacancies were introduced in $ZnIn_2S_4$ sheets ,which can ameliorate the light absorption, lifetime of charge carriers, and also charge kinetics between two semiconductors (Figure 23, Table 6).[602] To attain this goal, the $ZnIn_2S_4$/g-C_3N_4 (ZIS-S/CN) vdW heterojunction was synthesized via a calcination−solvothermal method using CN sheets followed by high-temperature growth of ZIS-S. The intimate contact with ZIS-S and CN was evident from HRTEM, AFM, and elemental mapping. Due to improved UV−vis absorption and increased PL lifetime, the ZIS-S/CN displayed an increased photocurrent response compared to the pristine components such as CN and ZIS-S (Figure 23a,d). Electrostatic potential measurement using DFT calculations demonstrated that the work functions of g-C_3N_4 and ZIS-S were 4.70 and 6.03 eV, which implies that the Fermi level of g-C_3N_4 is higher than that of ZIS-S and electrons should flow from CN to ZIS-S (Figure 23b,c). The charge density difference of 30ZIS-S/CN vdW shows that the electronic charge centered on the surface of ZIS-S was primarily derived from g-C_3N_4 (Figure 23e). The charge redistribution in the 2D/2D heterojunction contact mainly focused on the 2D/2D interfaces and accumulated near the ZIS-S monolayer, which can efficiently annihilate holes that accumulate near the CN monolayer (Figure 23f). This results in the formation of a bias-less in-built electric field which facilitates better charge separation.

Apart from common layered chalcogenides such as WS_2 and MoS_2, various other chalcogenides including SnS_2,[605−608] Sn_2S_3,[609] TaS_2,[610] Bi_2Se_3,[611] NiS,[612] CdS,[613] $CuInS_2$,[614] $MnIn_2S_4$,[615] Cu_2WS_4,[616] $NiCo_2S_4$,[617] etc. have been reported for making 2D/2D photocatalysts.

8. CARBON NITRIDE−BISMUTH OXYHALIDE 2D/2D vdW STRUCTURES

8.1. Carbon Nitride−BiOX. Bismuth-based photocatalysts (fractional, binary/ternary oxides) have been proven as excellent photocatalytic materials due to their unique electronic and structural properties and visible light absorbance.[618−620] Most of the oxide-based bismuth catalysts such as $BiVO_4$, Bi_2MoO_6, $BiPO_4$, $Bi_2W_2O_6$, etc. have displayed poor visible light absorption limited to the blue region, compromising the photocatalytic performances.[621] Additionally, the fundamental problems of low quantum efficiency and lack of better charge transport properties are key limiting factors. Bismuth oxyhalides (BiOX; X = Cl, Br, and I) constituted of elements from the main group family (V−VI−VII) with a tetragonal matlockite configuration (PbFCl-type) are becoming a rising star in the photocatalysis field due to their astounding visible absorption with a band gap in the range of 1.7−3.2 eV, inert nature, easy processing, and corrosion resistance.[622] BiOX is constituted of $[Bi_2O_2]$ slabs interleaved with double halogen slabs giving rise to a layered structure. The interlayer atoms in the BiOX are connected through strong covalent bonding while layers remain bounded together through weak vdW interaction. Due to the specific crystalline structure and atomic polarization, an internal static electric field exists perpendicular to the $[Bi_2O_2]$ and [X] slices, resulting in effective charge separation. The band gap of BiOX is highly dependent on the types of halogen atoms, i.e., the band gaps for BiOCl, BiOBr, and BiOI were found to be ∼3.3, 2.7, and 1.8 eV, respectively. BiOF, due to its extremely high band gap (3.64 eV), is usually excluded from the general notion of the BiOX family.[623]

BiOX based compounds, either as a stand-alone catalyst (except BiOI) or in the form of a heterojunction, have been widely used for numerous photocatalytic applications such as water splitting, dye degradation, CO_2 reduction, N_2 reduction reactions, etc.[621,624,625] Like chalcogenides, the inherent trap assisted recombination reduces the performance of these catalysts. Various surface passivation approaches such as decorating with alkyl chains, carbon quantum dots, adding metal/metal oxides nanoparticles, and heterojunction formation with various semiconductors such as TiO_2, $BiVO_4$, Sn_3O_4, $Bi_2O_2CO_3$, etc. have been employed to improve the performance of these materials.[626−631] Due to the layered structure of BiOX with a residual surface positive charge and weak *p*-type nature, g-C_3N_4 is an ideal contender to make a p−n type vdW heterojunction.[632,633] The effective interaction between layered surfaces and the presence of a built-in electrical field after Fermi level equilibration can facilitate better charge separation.[634−636]

The inherent low band gap of BiOI associated with less negative CB restricts its usage as a stand-alone catalyst which again necessitates the formation of a heterojunction. Alam et al. have synthesized BiOI heterojunctions with few-layered g-C_3N_4 and F-doped and Cl-intercalated g-C_3N_4 (CNFCl) via an in situ approach displaying an enhanced photoelectrochemical water splitting performance reaching a photocurrent density of 0.70 mA cm^{-2} and 1.3 mA cm^{-2}, respectively, under AM 1.5G solar simulated light.[44,637] Kelvin probe force microscopy (KPFM) reveals better charge carrier generation and separation in the BiOI/carbon nitride heterojunctions. Further, after the formation of the heterojunction, the Fermi level of BiOI was uplifted, and then g-C_3N_4 facilitates the migration of electrons on conjugated carbon nitride sheets.

Most of the reported BiOI/g-C_3N_4 heterojunctions have displayed 3D platelets, microspheres, and flower-like morphologies due to the uncontrolled growth of BiOX lattices on g-C_3N_4.[638] The 3D structures limit catalytic performance due to hindered active sites, reduced active surface area, and minimum interfacial contact between two catalyst components. To surmount the drawback of unfavorable redox potential and stability of BiOI and BiOBr, the BiOCl with a wide indirect band gap and relatively more resilient nature seems to be a good replacement. Introducing the oxygen vacancies or Bi(0) doping in the BiOCl nanosheets was found to improve the photocatalytic performance significantly due to increased visible absorption and formation of subgap energy levels.[639,640] The performance can be further improved by making a 2D/2D vdW heterojunction.[641] Wang et al. synthesized an oxygen vacancy-rich ultrathin g-C_3N_4/BiOCl 2D/2D heterojunction using polyvinylpyrrolidone (PVP) which displayed excellent photocatalytic degradation performance for 4-chlorophenol (4-CP) and bisphenol A (BPA) degradation (Figure 24).[642] The morphological characterization using HR-TEM, EDS mapping, and AFM confirm intimate contact and formation of the 2D/2D structure (Figure 24a−c). The O1 XPS spectra displayed an increased intensity of the O_2 signature peak at 531.3 eV assigned to increased vacancies in the 2D/2D structure. ESR spectra of 50CN-50BC (prepared using PVP) compared to 50CN-50BC-P (without PVP) displayed increased ESR signals verifying the presence of oxygen vacancies. To deduce the mechanism of enhanced photoactivity, a scavenger test using $O_2^{\bullet-}$ (ascorbic acid, AA), holes (sodium oxalate, SO), and

https://doi.org/10.1021/acs.chemmater.1c03166
Chem. Mater. 2021, 33, 9012−9092

Table 6. 2D/2D Carbon Nitride–Chalcogenide Based Heterojunction Photocatalysts

photocatalyst	synthesis	application	light source	AQY/STH	remarks	ref
		Chalcogenides				
Metallic 1T-MoS_2/monolayer O-g-C_3N_4	Hydrothermal treatment of O-g-C_3N_4 and $MoCl_5$ at 200 °C for 24 h.	Photocatalytic H_2 evolution	300 W Xe lamp ($\lambda \geq 420$ nm)	~7.11% (420 nm)	H_2—1841.72 μmol g^{-1} h^{-1}, ~4 times of Pt/O-g-C_3N_4 (480.15 μmol g^{-1} h^{-1})	499
MoS_2/carbonyl linked g-C_3N_4 (MoS_2/CO-C_3N_4)	CO-C_3N_4 was mixed with the MoS_2 solution and pumped at ca. −100 kPa for 15 min under simulated sunlight and vacuum dried.	Photocatalytic H_2 evolution	200 W Xe lamp or LED lamps	-	H_2—823.4 μmol g^{-1} h^{-1} (10% MoS_2/CO-C_3N_4)	500
Carbon nitride/MoS_2	MoS_2 and SCN were sonicated in anhydrous ethanol for 2 h followed by stirring for 10 h and finally heating under N_2 at 300 °C for 1 h.	Photocatalytic H_2 evolution	300 W Xe lamp ($\lambda \geq 420$ nm)	5.7% (430 nm)	H_2—2120 μmol g^{-1} h^{-1} (MCN-3) PCN (with Pt)—11 μmol g^{-1} h^{-1}	502
MoS_2/g-C_3N_4 nanoflowers	Ammonium molybdate tetrahydrate and thiourea were added to a g-C_3N_4 dispersion followed by microwave treatment at 180 °C for 30 min.	Photocatalytic degradation of MB and fipronil	Visible light	-	MoS_2/g-C_3N_4—~94% MB and 77% fipronil degradation in 60 min	503
g-C_3N_4-Ni_2P-MoS_2	g-C_3N_4-1%Ni_2P and MoS_2 were dispersed together via ultrasonication and stirring.	Photocatalytic H_2 evolution	300 W Xe lamp ($\lambda \geq 400$ nm)	1.45% (405 nm)	H_2—g-C_3N_4-1%Ni_2P-1.5%MoS_2 2.47 and 5.15 times of g-C_3N_4-1.5%MoS_2 and g-C_3N_4-1%Ni_2P	504
g-C_3N_4-MoS_2-$M(OH)_x$	g-C_3N_4-MoS_2 $M(NO_3)_x{\cdot}6H_2O$ were dissolved in deionized water by ultrasonication, and aqueous ammonia was added dropwise. Finally, the resultant sample was obtained after evaporation and drying in an oven at 80 °C for 12 h.	Photocatalytic H_2 evolution	300 W Xe arc lamp	6.4% (420 ± 8 nm)	H_2—889.4 μmol g^{-1} h^{-1} (g-C_3N_4-MoS_2-Ni$(OH)_x$) g-C_3N_4—9.3 μmol g^{-1} h^{-1}	506
MoS_2/g-C_3N_4	Solvent-thermal method: g-C_3N_4 nanosheets and $[(NH_4)_2MoS_4]$ dissolved in DMF were hydrothermally treated at 210 °C for 24 h.	Photocatalytic H_2 evolution	300 W Xe lamp ($\lambda \geq 420$ nm)	6.8% (420 nm)	H_2—1155 μmol g^{-1} h^{-1} (MoS_2/g-C_3N_4) g-C_3N_4—25 μmol g^{-1} h^{-1}	508
MoS_2-modified graphitic carbon nitride (MoS_2/g-C_3N_4)	The exfoliated solution of g-C_3N_4 sheets and MoS_2 NSs were mixed and sonicated for another 2 h.	Photocatalytic H_2 evolution	300 W Xe lamp ($\lambda \geq 360$ nm)	3.3% (410 nm)	H_2—1497 μmol g^{-1} h^{-1} (MSCN-3)	509
Metallic 1T-WS_2/2D-C_3N_4	Grinding method: 1T-WS_2 was dispersed in hexane followed by the addition of 2D-C_3N_4 and 1T-WS_2 followed by grinding.	Photocatalytic H_2 evolution	300 W Xe lamp ($\lambda \geq 420$ nm)	1.12% (420 nm)	H_2—331.09 μmol g^{-1} h^{-1} (1T-WS_2/2D-C_3N_4 with 64.1% 1T phase) ~43.3 times bare 2D-C_3N_4	515
CdS/WS_2/CN	Simple mixing procedure: CN and WS_2 nanosheets were stirred together for 12 h. The obtained WS_2/CN was immersed in $Cd(CH_3COO)_2$ followed by immersion in Na_2S to deposit CdS.	Photocatalytic H_2 evolution	200 W Hg lamp ($\lambda \geq 420$ nm)	5.4% (400 nm)	H_2—1174.5 μmol g^{-1} h^{-1} (CdS/WS_2/CN) ~67 times CN (17.2 μmol g^{-1} h^{-1})	540
$FeSe_2$/g-C_3N_4	$Fe(acac)_3$, oleic acid (OA), 1-octadecene (ODE), and oleylamine (OLA) were mixed ultrasonically under a N_2 atmosphere followed by the addition of g-C_3N_4 nanosheets and heated to 175 °C. Finally, OLA solution containing Se powder was injected to form 2D/2D $FeSe_2/CN_{NS}$ heterostructures.	Photocatalytic H_2 evolution and removal of MB and Cr(VI)	300 W Xe lamp	-	H_2—1655.6 μmol g^{-1} h^{-1} ($FeSe_2/CN_{NS}$) ~2.65 times pure g-C_3N_4 (623.7 μmol g^{-1} h^{-1}) $FeSe_2/CN_{NS}$—92.6% Cr(VI) removal g-C_3N_4—44.7% Cr(VI) removal $FeSe_2/CN_{NS}$—99.8% MB degradation g-C_3N_4—66.1% MB degradation	557
PtS_2/MCN	MCN and PtS_2 nanosheets (PtS_2-8000) were stirred together for 6 h.	Photocatalytic H_2 evolution	300 W Xe lamp ($\lambda \geq 400$ nm)	1.16% (405 nm)	H_2—1168 μmol g^{-1} (PtS_2(U)/MCN)	578
$ZnIn_2S_4$/protonated g-C_3N_4	$ZnIn_2S_4$ and pCN were dispersed in DI water and mixed with ultrasonication.	Photocatalytic H_2 evolution and deg-	300 W Xe lamp (λ	0.92% (400 nm)	H_2—8601.16 μmol g^{-1} h^{-1} ($ZnIn_2S_4$/pCN) ~108 times of pCN	599

https://doi.org/10.1021/acs.chemmater.1c03166
Chem. Mater. 2021, 33, 9012−9092

Table 6. continued

photocatalyst	synthesis	application	light source	AQY/STH	remarks	ref
		Chalcogenides				
		radation of tetracycline (TC)	≥ 400 nm)			
Polymeric carbon nitride and $ZnIn_2S_4$ nanosheets, PCN/$ZnIn_2S_4$	Low-temperature hydrothermal method: PCN nanosheets, $ZnCl_2$, $InCl_3{\cdot}3H_2O$, and thioacetamide were stirred for 30 min and heated in an oil bath at 80 °C with stirring.	Photocatalytic CO_2 reduction	300 W Xe lamp (λ ≥ 420 nm)	2.4% (420 nm)	CO—44.6 μmol h^{-1} (PCN/$ZnIn_2S_4$) 223 higher than pristine PCN nanosheets (0.2 μmol h^{-1})	600
2D/2D g-C_3N_4 nanosheet@$ZnIn_2S_4$	Surfactant-assisted solvothermal method: $Zn(NO_3)_2{\cdot}6H_2O$, $In(NO_3)_3{\cdot}5H_2O$, trisodium citrate dihydrate, and g-C_3N_4 nanosheets were ultrasonically dispersed, and thioacetamide was added followed by hydrothermal treatment at 160 °C for 1 h.	Photocatalytic H_2 evolution	300 W Xe lamp (λ ≥ 420 nm)	7.05% (420 nm)	H_2—2.78 mmol g^{-1} h^{-1} (2D/2D GN@ZN) ~69.5 times of g-C_3N_4 nanosheet (0.04 mmol g^{-1} h^{-1}) pristine g-C_3N_4—negligible	601
$ZnIn_2S_4$/g-C_3N_4	$Zn(CH_3COO)_2{\cdot}2H_2O$, $InCl_3{\cdot}4H_2O$, g-C_3N_4, and TAA are added into the water−ethanol solution and hydrothermally treated at 180 °C for 24 h.	Photocatalytic H_2 evolution	200 W Hg lamp (λ ≥ 400 nm)	9.8% (420 nm)	H_2—6095.1 μmol g^{-1} h^{-1} (30ZIS-S/CN) pure g-C_3N_4—532.8 μmol g^{-1} h^{-1}	602
$Zn_xCd_{1-x}In_2S_4$ solid solution coupled with g-C_3N_4	Hydrothermal method: CN, $Zn(NO_3)_2{\cdot}6H_2O$, $Cd(CH_3COO)_2{\cdot}2H_2O$, $InCl_3{\cdot}4H_2O$, thioacetamide, and trisodium citrate were hydrothermally treated at 160 °C for 1.5 h.	Photocatalytic H_2 evolution	300 W Xe lamp (λ ≥ 420 nm)	8.5% (420 nm) STH-2.6%	H_2—37.8 μmol h^{-1} $Zn_{1/2}Cd_{1/2}In_2S_4$/g-C_3N_4	603
$Zn_3In_2S_6$/fluorinated polymeric carbon nitride nanosheets ($Zn_3In_2S_6$/FCN)	$In(NO_3)_3{\cdot}6H_2O$, $ZnCl_2$, and a double excess of thioacetamide were dissolved in DI water, followed by the addition of FCN and sonication for 30 min and 2 h of magnetic stirring. The obtained solution was hydrothermally treated in a Teflon-lined stainless-steel autoclave at 180 °C for 12 h.	Photocatalytic H_2 evolution and degradation of MO	300 W Xe lamp (λ ≥ 420 nm)	-	$Zn_3In_2S_6$/FCN (ZF3)—99% MO degradation efficiency Pure CN—32% MO degradation efficiency H_2—2553.9 μmol g^{-1} h^{-1}(ZF3) FCN—68.725 μmol g^{-1} h^{-1} ~3.66 times higher than ZIS	604
SnS_2/g-C_3N_4	CNNs and SnS_2 were stirred for 12 h and thermally treated at 300 °C for 2 h in a microwave muffle.	Photocatalytic H_2 evolution	300 W Xe lamp (λ ≥ 420 nm)	-	H_2—972.6 μmol g^{-1} h^{-1} (5-SCNNs) ~2.9 times higher than bulk g-C_3N_4 (335.8 μmol g^{-1} h^{-1})	605
SnS_2/g-C_3N_4	SnS_2 and 2D g-C_3N_4 were mixed in ethylene glycol using ultrasonication followed by hydrothermal treatment at 180 °C for 8 h.	Photocatalytic degradation of RhB	Visible light	-	2D SnS_2/g-C_3N_4—0.0302 min^{-1} RhB degradation rate 50.3 times that of bulk 2D g-C_3N_4	606
g-C_3N_4/SnS_2	DFT	Overall water splitting		-	N.A.	607
Porous graphitic C_3N_4/SnS_2 composite	Pg-C_3N_4, $SnCl_4{\cdot}5H_2O$, and TAA were hydrothermally treated at 453 K for 12 h.	Photocatalytic degradation MB	410 nm LED light	-	MB degradations of Pg-C_3N_4, SnS_2, 5% Pg-C_3N_4/SnS_2, 10% Pg-C_3N_4/SnS_2, and 20% Pg-C_3N_4/SnS_2 were calculated to be 18.9%, 39.1%, 90.3%, 98.7%, and 81.3%, respectively	608
TaS_2/2D-C_3N_4	Grinding: TaS_2 dispersed in hexane and 2D-C_3N_4 were grounded in an agate mortar.	Photocatalytic degradation of RhB	500 W Xe lamp (λ ≥ 420 nm)	-	TaS_2/2D-C_3N_4—92% RhB degradation efficiency 100 min ~25% higher than pure 2D-C_3N_4	610
C_3N_4/Sn_2S_3-DETA	Hydrothermal process: Pg-C_3N_4, $SnCl_4{\cdot}5H_2O$, and TAA were dispersed together by an ultrasonic cell grinder and hydrothermally treated at 453 K for 12 h.	Photocatalytic CO_2 reduction	Visible light (λ > 420 nm)	2.8% (>420 nm)	CH_4—4.93 μmol g^{-1} h^{-1} (5% Pg-C_3N_4/Sn_2S_3-DETA) CH_3OH—1.49 μmol g^{-1} h^{-1} (5% Pg-C_3N_4/Sn_2S_3-DETA)	609
Bi_2Se_3/g-C_3N_4	g-C_3N_4 was dispersed in 200 mL of ethanol/deionized water mixed with Bi_2Se_3 and sonicated for 12 h.	Photocatalytic CO_2 reduction to CO	300 W Xe lamp	-	CO—8.2 μmol g^{-1} h^{-1} (5BSCN) CO—1.3 μmol g^{-1} h^{-1} (g-C_3N_4)	611
g-C_3N_4-Ni-NiS	The ternary composite was prepared to make g-C_3N_4/Ni followed by deposition of NiS in the second step.	Photocatalytic H_2 evolution	300 W Xe lamp (λ ≥ 420 nm)	-	H_2—515 μmol g^{-1} h^{-1} (g-C_3N_4−0.5% Ni−1.0% NiS) pure g-C_3N_4 ~ negligible	612

https://doi.org/10.1021/acs.chemmater.1c03166
Chem. Mater. 2021, 33, 9012−9092

Table 6. continued

photocatalyst	synthesis	application	light source	AQY/STH	remarks	ref
Chalcogenides						
CdS/g-C_3N_4	In situ hydrothermal method: Exfoliated g-C_3N_4 powder and cadmium sulfate were dispersed in DI water followed by addition of thiourea and hydrothermal treatment at 180 °C for 12 h.	Photocatalytic degradation of RhB	500 W Xe lamp ($\lambda \geq 420$ nm)	-	CdS/g-C_3N_4—95.6% RhB degradation g-C_3N_4—33.4% RhB degradation	613
$CuInS_2$/g-C_3N_4	CuCl, $InCl_3$, sulfur powder, and g-C_3N_4 were mixed in triethylene glycol and hydrothermally treated at 200 °C for 48 h.	Photocatalytic degradation of TC	300 W Xe lamp ($\lambda \geq 420$ nm)	-	~83.7% TC degradation 60 min	614
$MnIn_2S_4$/g-C_3N_4	Hydrothermal route: CN nanosheets, manganese chloride tetrahydrate, indium chloride, and thiourea were treated in a polyphenylene-lined stainless steel autoclave at 240 °C for 24 h.	Photocatalytic degradation of Tetracycline hydrochloride (TCH)	300 W Xe lamp ($\lambda \geq 420$ nm)	-	MnISCN-20–100% TCH degradation after 120 min CN—60.5% TCH degradation after 120 min	615
Cu_2WS_4/g-C_3N_4	Hydrothermal method: a YC/g-C_3N_4 sample, PVP, and Cu_2WS_4 NS mixture was treated hydrothermally at 433.15 K for 6 h.	Photocatalytic decomposition of TC and reduction of Cr(VI)	300 W Xe lamp ($\lambda \geq 420$ nm)	-	Cu_2WS_4/g-C_3N_4- 80% TC degradation in 120 min g-C_3N_4—46.7% TC degradation in 120 min, complete Cr(VI) reduction	616
$NiCo_2S_4$ NSs/P-g-C_3N_4	Porous g-C_3N_4, $NiCl_2{\cdot}6H_2O$, and $CoCl_2{\cdot}6H_2O$ were dispersed together via ultrasonication followed by the addition of thiosemicarbazide. Finally, the mixture was hydrothermally treated at 180 °C for 12 h.	Supercapacitor applications	NA	-	$NiCo_2S_4$ NSs/P-g-C_3N_4—specific capacity (506 C g^{-1} at 1 A g^{-1}) Cycling stability—100% capacity retention after 1500 cycles at 3 A g^{-1})	617

•OH radical (isopropyl alcohol, IPA) scavengers followed by EPR using a DMPO trap agent demonstrated that $O_2^{\bullet-}$ and h^+ are the main reactive species facilitating degradation (Figure 24d–f). The more reductive CB of BiOCl than oxygen reduction potential ($O_2/^{\bullet}O_2^-$) (−0.33 eV vs NHE, pH 7) coupled with holes on BiOCl and g-C_3N_4 facilitated the efficient degradation of pollutants (Figure 24g).[643]

8.2. Carbon Nitride–$Bi_xO_yX_z$. Apart from defect/vacancy creation, increasing the Bi/O ratio of BiOX can improve the band alignment and visible absorption.[644−646] For BiOXs, the conduction band comprises Bi 6p orbitals while the valence band comprises O 2p and X*n* p-orbitals (n = 3, 4, and 5, for F, Br, Cl, and I). By decreasing the content of halogens in $Bi_xO_yX_z$ compounds, the valence and conduction bands can be tuned to afford maximum absorption without compromising the reduction and oxidation power.[622,647] In most such cases, the CB remains more negative, which makes them a favorable catalytic material for the CO_2, N_2, oxygen, and proton reduction. A number of Bi rich nonstoichiometric compounds such as $Bi_{12}O_{15}Cl_6$, $Bi_{24}O_{31}Br_{10}$, Bi_3O_4Cl, $Bi_{24}O_{31}Cl_{10}$, $Bi_4O_5Br_2$, $Bi_{12}O_{17}Cl_2$, etc. have been reported so far, which can be easily synthesized by varying different parameters, including the calcination, solvent adjustment, displacement reaction alkalization, etc.[648−650] It is interesting to note that the band gap of BiOCl can be adjusted from 3.64 eV to 2.84, 2.80, 2.36, and 2.08 eV in Bi_3O_4Cl, $Bi_{24}O_{31}Cl_{10}$, $Bi_{12}O_{15}Cl_6$, and $Bi_{12}O_{17}Cl_2$, respectively.[651,652] Further, the activities of these nonstoichiometric $Bi_xO_yX_z$ compounds can be improved by the decoration of nanoparticles, heterojunction formation, and coupling with metals complexes (i.e., cobalt phthalocyanine).[653,654]

Evident from the band gap, the series $Bi_{12}O_{17}Cl_2$ displays an optimum absorption in the visible region and is widely investigated as a standalone and hybrid heterojunction catalyst for various reactions.[655,656] For example, Di et al. prepared defect-rich $Bi_{12}O_{17}Cl_2$ superfine nanotubes with structural distortion for the improved photocatalytic CO_2 reduction to CO (48.6 μmol g^{-1} h^{-1} in water) without any cocatalyst or sacrificial donor.[657] In another work, Zhou et al. synthesized the AgI/$Bi_{12}O_{17}Cl_2$ heterojunction by a hydrothermal–precipitation protocol and demonstrated 7.8 and 35.2 times more activity than pristine $Bi_{12}O_{17}Cl_2$ and BiOCl toward photodegradation of sulfamethazine (SMZ; sulfonamide antibiotic).[658] Because BiOX has a *p*-type behavior and low conductivity, the formation of a heterojunction using their *n*-type low halogen counterpart $Bi_xO_yX_z$ can afford better charge separation in p–n type BiOX/$B_xO_yX_z$ heterojunctions.[659,660] Even couplings of two nonstochiometric $B_xO_yX_z$ such as $Bi_3O_4Cl/Bi_{12}O_{17}Cl_2$ have also been explored to fabricate the n–n type of heterojunction with Z-scheme configuration to improve the performance.[661] The heterojunction of $B_xO_yX_z$ can further achieve better performance due to the layered structure and appropriate band position. For instance, the g-$C_3N_4/Bi_4O_5I_2$ heterojunction can afford better oxidation and reduction reaction to convert CO_2 to CO due to the establishment of the Z-scheme heterojunction in the presence of an I_3^-/I^- redox mediator. 2D/2D contact and heteroatom doping of g-C_3N_4 will further boost the performance.[662−665] Zhou et al. demonstrated that the in situ fabrication of carbon-doped carbon nitride (CCN) with $Bi_{12}O_{17}Cl_2$ can boost photocatalytic degradation of tetracycline (TC) under visible light irradiation (Figure 25, Table 7).[666] An excellent interfacial contact displayed in the TEM image and increased

https://doi.org/10.1021/acs.chemmater.1c03166
Chem. Mater. 2021, 33, 9012−9092

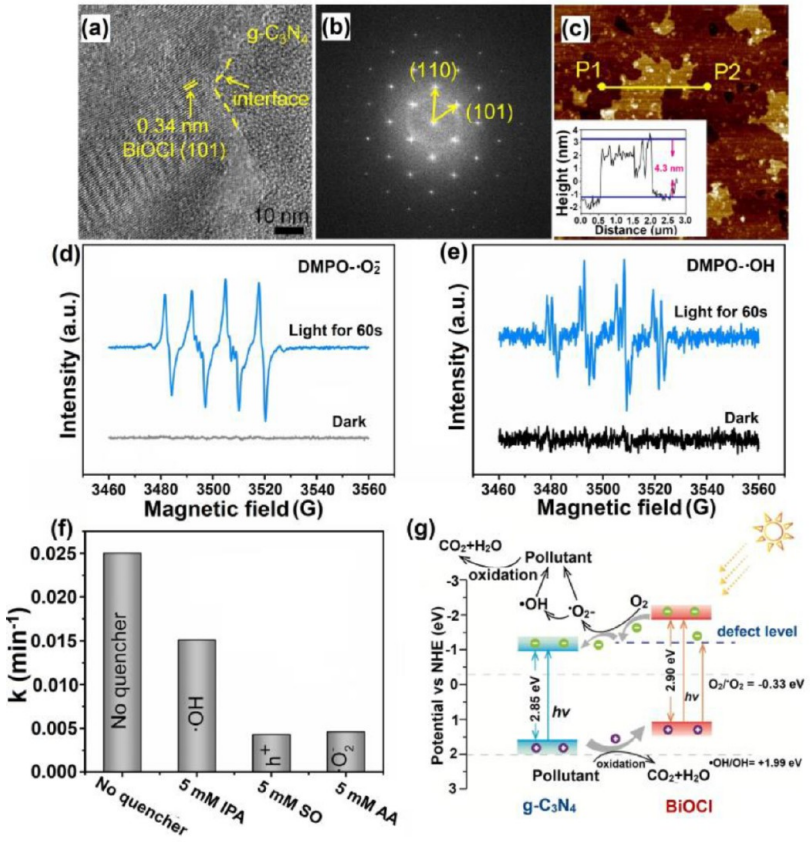

Figure 24. (a) HRTEM image of 50CN-50BC composite nanosheets and (b) the corresponding FFT image. (c) AFM image of 50CN-50BC composite nanosheets and the corresponding height profile shown in the inset of (c). ESR spectra of (d) DMPO-$^{\bullet}O_2^-$ (e) and DMPO-$^{\bullet}$OH in the presence of 50CN-50BC ultrathin nanosheets under dark and visible light irradiation, respectively. (f) Photocatalytic degradation of 4-CP over 50CN-50BC ultrathin nanosheets under visible light irradiation in the presence of different scavengers. (g) Schematic illustration of the visible light photocatalytic degradation pollutants over OVs-rich ultrathin 50CN-50BC nanosheets. Reprinted with permission from ref 642. Copyright 2018 Elsevier

visible absorption were responsible for such improvement (Figure 25a-b). 3D excitation−emission spectra (EEMs) displayed increased fluorescence intensity after 30 to 60 min of visible exposure due to the formation of humic acid. The fulvic acids peak (intermediates) was significantly decreased after 120 min, suggesting complete mineralization of TC during the photocatalytic process (also confirmed by HPLC-MS) (Figure 25c−h). The ESR spin trap experiment revealed the presence of $O_2^{\bullet-}$ and $^{\bullet}$OH radicals while band structures determined via a combination of Mott−Schottky and Tauc plots suggested a charge migration from CB of $Bi_{12}O_{17}Cl_2$ to CCN and vice versa, leading to increased degradation performance (Figure 25i,j).

9. CARBON NITRIDE−CARBON NITRIDE 2D/2D vdW STRUCTURES

9.1. Carbon Nitride-Doped/Undoped Carbon Nitride.

As carbon nitride has limited visible absorption, the doping of carbon nitride with various heteroatoms (P, B, F, I, S, N, C, etc.) and even metals has been widely investigated to improve the visible absorption.[70,667,668] Among heteroatom doping, P and O doping has demonstrated the most drastic change in the absorption profile.[669] For example, a mere 0.1% P doping in the carbon nitride framework using $BMiMPF_6$ ionic liquid can improve visible absorption throughout the visible range.[71] To further synergize doping effects, codoping using B and F, P and F, etc. has also been investigated. For example, recently, Kumar et al. synthesized highly porous P and F codoped carbon nitride with 260.93 m^2 g^{-1} surface area displaying excellent CO_2 reduction and catalytic activity for the conversion of cellulosic biomass to furanics.[670]

Incorporation of a small alkali metal such as potassium in the heptazine-based cavity has also been found to improve visible absorption and photocatalytic performance.[671−673] Again, codoping with K and P can ameliorate the performance.[674] Indeed, the aforementioned approaches improve the visible absorption profile of blue absorbing g-C_3N_4, but the problem of fast charge carrier recombination (inter and intrasheets) remains prevalent, resulting in a sluggish activity. The difference in band gap energy and band edge positions of pristine g-C_3N_4 and doped carbon nitride isotype heterojunction can afford better interlayer charge separation.[675,676] Such isotype heterojunction can be synthesized using two approaches: (1) in situ method creating doped sheets within materials, and (2) mixing doped and nondoped g-C_3N_4 after synthesis or growth of one on another by annealing. g-C_3N_4/doped g-C_3N_4 type 2D/2D vdW structures can afford better charge separation due to lattice match and differential band structure.[677−682] Since inorganic 2D semiconductors are hard to synthesize and in many cases get photobleached under solar excitation, it is desirable to develop a stable heterojunction between carbon nitride and the doped carbon nitride to resolve

https://doi.org/10.1021/acs.chemmater.1c03166
Chem. Mater. 2021, 33, 9012−9092

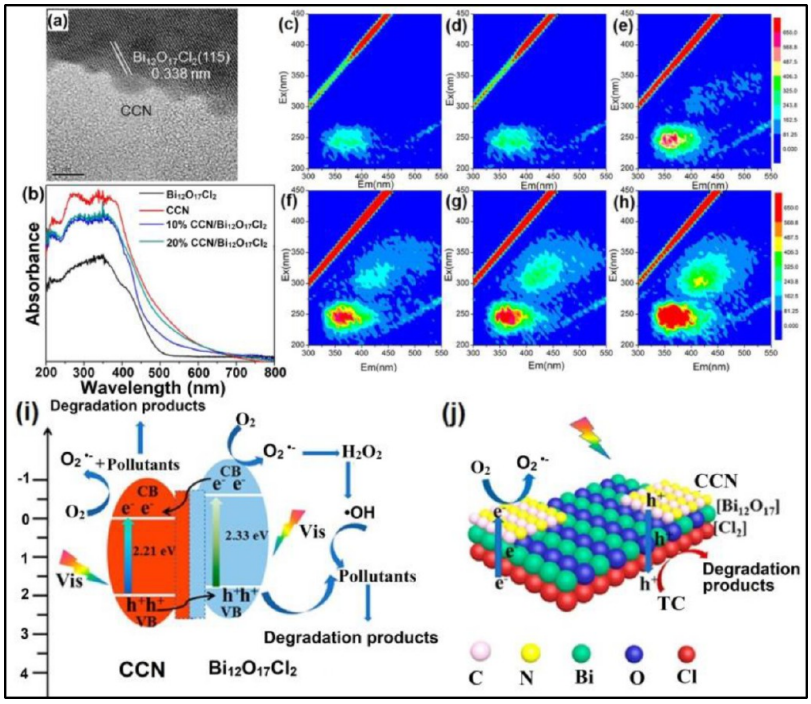

Figure 25. (a) HRTEM images of CCN/$Bi_{12}O_{17}Cl_2$. (b) UV−vis absorption spectra of samples. Three-dimensional EEMs of the aqueous solution: (c) Taken from the original solution, (d) collected after 60 min of adsorption in the dark, and (e−h) obtained after irradiation times of 30, 60, 80, and 120 min, respectively. (i, j) Proposed charge separation process in the CCN/$Bi_{12}O_{17}Cl_2$ heterostructures under visible-light irradiation. Reprinted with permission from ref 666. Copyright 2018 American Chemical Society.

the stability issue while minimizing synthesis cost.[683−685] Qin et al. reported the synthesis of S-doped g-C_3N_4 and porous g-C_3N_4 isotype heterojunction via an in situ approach using thiourea as a sulfur source for improved visible light H_2 evolution.[686] In another work, carbon nitride nanosheets (CNS) were prepared by thermal annealing of trithiocyanuric acid (TCA), and then CN was grown on these sheets by further annealing with dicyandiamide. The CB of bulk CN is much higher than that of CNS, which facilitates better charge separation. As a result, H_2 production rate can be increased almost 11-fold in comparison to bulk CN. Thiourea and urea can afford a differential band gap heptazine polymeric carbon nitride, which can facilitate better change separation. For example, Dong et al. synthesized a g-C_3N_4/g-C_3N_4 (CN-TU) 2D/2D heterojunction by sequential thermal annealing of urea and thiourea, respectively.[687] The inbuilt electric field in the n−n type of heterojunction enhances the charge separation. The CN-TU exhibited a NO removal ratio of 47.6%, which was significantly higher than that of thiourea and urea-based carbon nitride (27.3 and 31.7%). Later, carbon nitride (CN), B-modified graphitic carbon nitride (CNB) (CN-CNB), and g-C_3N_4/g-C_3N_4 (derived from urea and thiourea) isotype heterojunctions were also reported with the improved performance.[687,688] In a recent work, Zhao et al. reported the synthesis of boron-doped and nitrogen-deficient carbon nitride nanosheets (BDCNN) by rapid heating of carbon nitride nanosheets (CNN) in the presence of sodium borohydride (Figure 26a).[689] Due to simultaneous doping and N-deficiency and the introduction of mid gap energy states, the band gap was significantly reduced (2.37 eV), extending the band edge absorption up to NIR region (Figure 26b). Further, the CB and VB band positions of BDCNN were significantly shifted toward the positive side, idealizing it to integrate with the *n*-type carbon nitride nanosheets (CNN) (Figure 26c). When CNN and BDCNN were combined together in 2D/2D fashion by an electrostatic interaction, a Z-scheme heterointerface was realized, which facilitates better charge separation (Figure 26d,e). The Z-scheme CNN/BDCNN photocatalysts fabricated by taking a 1:1 ratio of CNN and BDCNN due to the presence of sufficient reduction and oxidation potential was able to split pure water. The resultant yields were 32.94 and 16.42 μmol h^{-1} H_2 and O_2, respectively, with AQY of 5.95% at 400 nm. The isotopic labeling experiment using ^{18}O labeled H_2O demonstrated that 97.10% O_2 was originated from water splitting and validated true photocatalytic behavior.

The condensation polymerization of carbon nitride precursors involves a variety of complex steps, so the band edge position and the band gap of the final carbon nitride materials depend upon the type of precursor.[690] Paradoxically, identical precursors annealed at the same temperature but with a different heating rate will afford a different band structure. Among various factors, the C/N content and degree of polymerization are of utmost importance. For example, thermal annealing of urea and DCDA proceeds via massive gaseous mass loss (95 and 40 wt %). And the peeling effect of oxygen functionalities resulting in a slightly higher atomic C/N ratio enhanced the surface area in CN synthesized by urea (UCN) compared to dicyandiamide synthesized CN (D-CN). This anomaly produces a variation in band position, which can be cultivated for the formation of isotype heterojunction. Wang et al. reported the synthesis of an isotype heterojunction by cothermal condensation of urea and DCDA (UD_x-CN).[691] The thin nanosheets of U-CN can be distinctly identified with wrinkled and relatively dense DCN. The hydrogen evolution rate using UD_1-CN prepared by using 1 wt % DCDA was optimal, reaching as high as 553 μmol h^{-1} g^{-1}, which is almost 17 and 5 times higher than those of the pristine D-CN and U-

https://doi.org/10.1021/acs.chemmater.1c03166
Chem. Mater. 2021, 33, 9012−9092

Table 7. 2D/2D Carbon Nitride-Bismuth Oxyhalides Based Heterojunction Photocatalysts

photocatalyst	synthesis	application	light source	AQY/ STH	remarks	ref
		Bismuth Oxyhalides				
g-C_3N_4/BiOBr	Solvothermal route: g-C_3N_4, $Bi(NO_3)_3{\cdot}5H_2O$, and CTAB solution in ethylene glycol were treated in a Teflon-lined autoclave, at 160 °C for 12 h.	Photocatalytic degradation of RhB	500 W Xe lamp (λ > 400 nm)	-	2.0% g-C_3N_4/BiOBr—97.9% of RhB degradation after 150 min	633
C_3N_4/BiOBr	$Bi(NO)_3{\cdot}5H_2O$, KBr, and Pg-C_3N_4 were dispersed in H_2O and EG and hydrothermally treated at 110 °C for 10 h.	Photocatalytic degradation of MB	50 W 410 nm LED light	-	20%Pg-C_3N_4/BiOBr—90% MB degradation in 40 min pure g-C_3N_4—40% MB degradation in 40 min	634
g-C_3N_4/BiOI	$Bi(NO_3)_3{\cdot}5H_2O$, Pg-C_3N_4, and KI were hydrothermally treated at 120 °C for 6 h.	Photocatalytic degradation of MB	50 W 410 nm LED light	-	degradation rate—0.01596 min^{-1} (Pg-C_3N_4/BiOI) ~5.7 times of g-C_3N_4 (0.0028 min^{-1})	635
BiOBr/graphitic C_3N_4 (BiOBr/CNNS)	Simple reflux process: $Bi(NO_3)_3{\cdot}5H_2O$ and KBr in EG and CNNS in DI water were mixed and refluxed at 80 °C under vigorous stirring for 2 h.	Photocatalytic degradation of RhB and BPA	300 W Xe lamp ($\lambda \geq$ 420 nm)	-	BiOBr/CNNS—88.5% TOC removal after 50 min	636
BiOCl/C_3N_4	C_3N_4 nanosheets and BiOCl nanoplates were mixed, and the obtained mixture was calcined at 250 °C for 3 h.	Photocatalytic degradation of MO	300 W Xe lamp ($\lambda \geq$ 420 nm)	-	BOC/CN-0.7−84.28% MO degradation after 180 min C_3N_4—22.49% MO degradation after 180 min	641
BiOCl-g-C_3N_4	g-C_3N_4 nanosheets, $Bi(NO_3)_3{\cdot}5H_2O$, PVP, and glycerol and NaCl were hydrothermally treated at 160 °C for 6 h.	Photocatalytic H_2 evolution	300 W Xe lamp ($\lambda \geq$ 420 nm)	-	50CN-50BC—95% 4-CP degradation efficiency in 120 min pure BC—22.7% 4-CP degradation efficiency in 120 min	642
g-C_3N_4/$Bi_{12}O_{17}Cl_2$ (PGCN/BOC)	$BiCl_3$ solution in ethanol was added to PGCN and was and calcined at 250 °C, 350 °C, 450 °C, and 550 °C for 2 h.	Photocatalytic CO_2 reduction	Visible light ($\lambda \geq$ 420 nm)	-	CH_4—24.4 μmmol g^{-1} h^{-1}(PGCN/BOC) PGCN ~ negligible	662
Bi_3O_4Cl/g-C_3N_4	Solid-phase calcination method: Bi_3O_4Cl and g-C_3N_4 were mixed in an agate mortar, and the obtained powder was calcined at 400 °C for 2 h.	Photocatalytic degradation of TC and RhB and reduction of Cr(VI)	250 W Xe lamp ($\lambda \geq$ 420 nm)	-	Bi_3O_4Cl/g-C_3N_4—98.3% RhB degradation Bi_3O_4Cl/g-C_3N_4 ~ 76% TC degradation Bi_3O_4Cl/g-C_3N_4—75.7% Cr(VI) removal efficiency ~2.86 times of g-C_3N_4—26.4% Cr(VI) removal efficiency	663
g-C_3N_4/$Bi_{12}O_{17}Cl_2$	g-C_3N_4 and $BiCl_3$ were dissolved in ethanol followed by the addition of NaOH and stirred.	Photocatalytic degradation of RhB and MO	300 W Xe lamp ($\lambda \geq$ 400 nm)	-	g-C_3N_4/$Bi_{12}O_{17}Cl_2$—85% RhB degradation in the 120 min g-C_3N_4—76% RhB degradation in the 120 min	664
g-C_3N_4/$Bi_4O_5Br_2$	$Bi(NO_3)_3{\cdot}5H_2O$, [C_{16}mim]Br, and 2D graphene-like g-C_3N_4 were dissolved in mannitol aqueous solution followed by the addition of NaOH and hydrothermally treated at 140 °C for 24 h.	Photocatalytic degradation of ciprofloxacin (CIP) and RhB	500 W Xe lamp	-	1 wt % g-C_3N_4/$Bi_4O_5Br_2$—50% CIP degradation in 30 min $Bi_4O_5Br_2$—30% CIP degradation	665
Carbon-doped carbon nitride/$Bi_{12}O_{17}Cl_2$ (CCN/$Bi_{12}O_{17}C_{l2}$)	In situ method: CCN and $Bi_{12}O_{17}Cl_2$ were mixed via sonication for another 1 h followed by stirring for 12 h. The obtained samples were further treated at 120 °C for 2 h.	Photocatalytic degradation of TC	300 W Xe lamp ($\lambda \geq$ 420 nm)	-	CCN/$Bi_{12}O_{17}Cl_2$—94% of TC was removed in 1 h CCN—82% of TC was removed in 1 h	666

https://doi.org/10.1021/acs.chemmater.1c03166
Chem. Mater. 2021, 33, 9012−9092

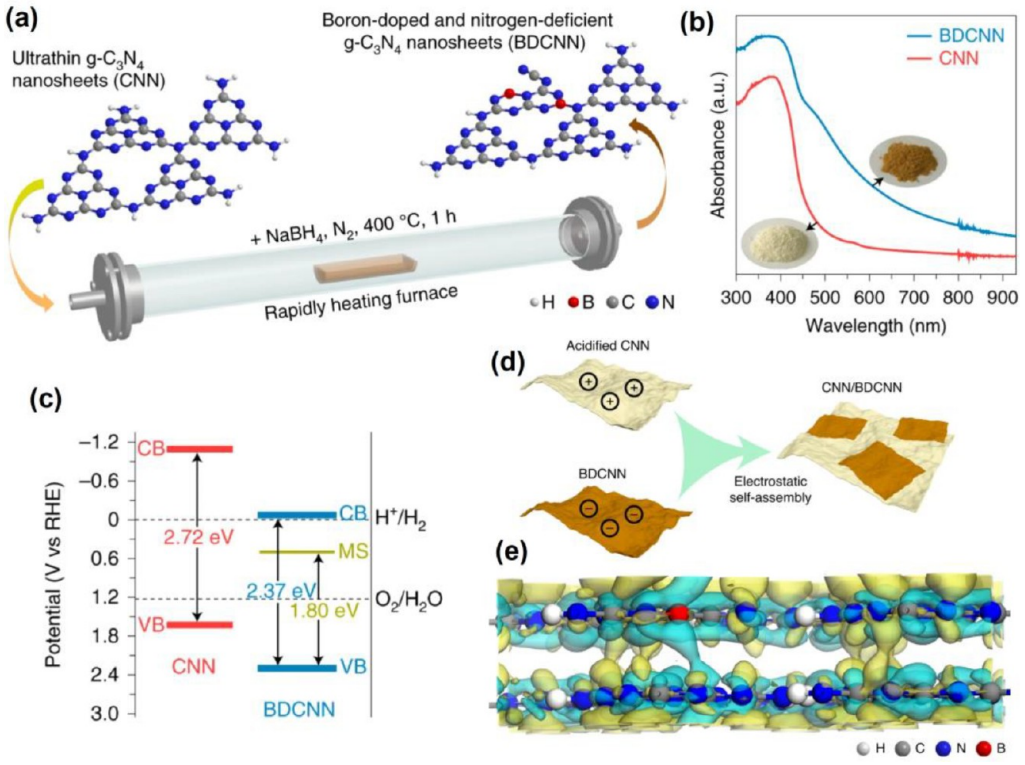

Figure 26. (a) Schematic of the synthesis of BDCNN derived from CNN. (b) UV−visible DRS of CNN and BDCNN, where the insets show photographs of the CNN and BDCNN. (c) Band structure alignments for CNN and BDCNN. (d) Schematic of the synthesis of the CNN/BDCNN heterostructure. (e) Side-view differential charge density map of CNN and BDCNN. The iso-surface value is 0.012 e Å^{-3}. The yellow and blue regions represent net electron accumulation and depletion, respectively. Reprinted with permission from ref 689 by Zhao et al. under exclusive license to Springer Nature. Copyright 2021 Springer Nature.

CN. Enhanced transient current responses and delayed charge recombination lifetime in TRPL measurement suggest the presence of cumulative charge separation in the UCN−DCN heterojunction.

Apart from doping, the band structure of carbon nitride can also be tuned by controlling the degree of polymerization due to its polymeric nature. Zhang et al. have demonstrated that the synthesis of carbon nitride in a sulfur medium (CNS) using trithiocyanuric acid (TCA) precursor can significantly influence the condensation/packing of the heptazine structure, resulting in a tuned electronic band structure.[692] Compared to regular pristine CN (E_{CB}: −1.42 V, E_{VB}: +1.28 V vs Ag/AgCl) the CB and VB positions of sulfur-mediated CN were shifted to −1.21 and +1.46 V, respectively, appropriate to fabricate the type-II isotype heterojunction with CN. Indeed, depending on the exposed surface of carbon nitride or doped carbon nitride in the CN/CNS isotype heterojunction, two possible configurations, i.e., CNS-CN (CN serving as the host) and CN-CNS (CNS serving as the host), are possible. The presence of an imperfectly condensed heptazine structure in CN and CNS structure provides plenty of $-NH_2$ terminated sites for the growth of a second carbon/doped nitride. The TEM image of CNS-CN displayed the presence of thick CN and paper-thin CNS sheets in close proximity. The deconvoluted HR-XPS spectra of CNS-CN exhibited two peak components (159.3 and 164.2 eV) that were identical to those of CNS, however, completely different those of from S doped carbon nitride (163.9 and 168.5 eV), validating the self-polymerization of the (TCA) precursor instead of doping in CN. The increased EPR signal in CNS-CN and prolonged PL lifetime of the excited state further confirm better charge migration in the CNS-CN heterojunction. Interestingly, the CNS-CN 2D/2D heterojunction demonstrated enhanced photocurrent generation without any applied bias. The optimized CNS-CN-2 and CN-CNS-2 (2 denotes the amount of DCDA and TCA precursors) catalysts can afford HER rates 11 and 2.3 times higher than that of pristine CN using triethanolamine as a sacrificial donor. Distinct from tris-*s*-triazine based carbon nitride isotype heterojunctions, the allotropic triazine-based carbon nitride (tri-C_3N_4) is also a promising candidate to form a vdW heterojunction due to structural similarity (C−N graphitic core) and identical physicochemical properties.[693] Zeng et al. prepared a crystalline heterojunction between triazine-based C_3N_4 and tris-*s*-triazine based C_3N_4 (tri/tri-*s*-tri-C_3N_4) via a sequential condensation in a LiCl + KCl mixture.[694] The close contact between tri-C_3N_4 and tris-tri-C_3N_4 was evident from the TEM image, and the surface area was increased up to 79.7 m^2/g. The HER and apparent quantum yield (AQY) of tri/tri-*s*-tri-C_3N_4 catalysts were found to be ∼150 μmol h^{-1} and 12.9% (TEOA was used as the electron donor)

9.2. Carbon Nitride−Metal Doped/Intercalated Carbon Nitride. Another more promising approach is the incorporation of atoms in between g-C_3N_4 sheets, pillaring, and incorporation of conjugated linkers. These approaches have been envisioned to improve the performance as such molecules provide interlayer galleries for better charge migration. When g-C_3N_4 was synthesized using an excess of NH_4Cl, the Cl atom gets intercalated between the CN sheets, which behave as a bridge between two CN sheets facilitating

https://doi.org/10.1021/acs.chemmater.1c03166
Chem. Mater. 2021, 33, 9012−9092

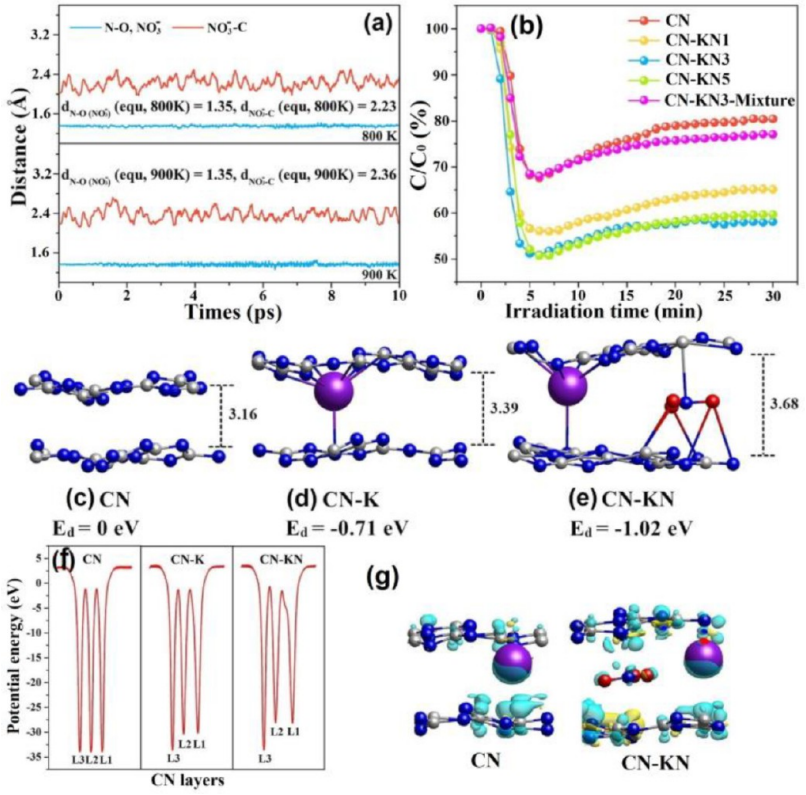

Figure 27. Crystal structures of CN-KN: (a) time evolution of the N−O length of NO_3^- and the fluctuation distance of doped NO_3^- in the CN interlayer at 800 and 900 K with an AIMD simulation in 10 ps and the optimized local structures of the individual. (b) Evaluation and analysis of the visible light photocatalytic performance of the as-prepared samples. (c) CN, (d) CN-K, and (e) KNO_3 doped CN. All the lengths and energies are given in Å. Gray, blue, purple, and red spheres represent C, N, K, and O atoms, respectively. E_d stands for the doping energy; negative values mean heat release. Analysis of electron mobility. (f) Electrostatic potential. (g) Charge difference distribution between metal atoms and CN layers: charge accumulation is in blue and depletion in yellow. The isosurfaces are set to 0.005 eV $Å^{-3}$. Reprinted with permission from ref 697. Copyright 2017 Elsevier.

better charge separation (H_2 evolution and NO removal). The presence of Cu metal and P−Cl codoping can further intensify the photoactivity due to better capturing of transported charges.[695,696] At first, such systems seem to be doped carbon nitrides; however, in a strict sense, they are 2D/2D homojunction composites having heteroatom charge mediators in between sheets.

In another interesting study, Cui et al. synthesized K and NO_3^- intercalated carbon nitride containing K and NO_3^- species between the neighboring layers (Figure 27).[697] The bioriented channels in CN-KN due to the presence of K and NO_3^- species in opposite sheets facilitate better steering of charge flow in opposite directions, overcoming the problem of charge accumulation on one sheet. DFT calculations reveal that the N−O bond in NO_3^- was highly stable up to 800 and 900 K, with average distances of 2.23 and 2.36 Å, respectively, which are shorter than the interlayer distance of CN (3.68 Å), verifying that NO_3^- can be intercalated between sheets (Figure 27a−e). The CN-KN showed excellent NO degradation compared to other components, including a physical mixture of CN and KNO_3, suggesting that the copyrolysis of thiourea and KNO_3 is essential for rational intercalation (Figure 27b). Trapping of free radicals using DMPO gave a strong signal of DMPO-$O_2^{\bullet-}$ and DMPO-$^{\bullet}$OH, suggesting generation of $O_2^{\bullet-}$ radical followed by their reduction to $^{\bullet}$OH radicals. The increased EPR signal of CN-KN after irradiation under light further demonstrated better charge separation. The calculated electrostatic potentials of CN, CN-K, and CN-KN between adjacent layers demonstrated a significant decrement of the energy barrier for CN-KN (−28.17 eV) compared to CN (−34.16 eV), corroborating the feasibility of better charge separation through interlayer electron delivery channels (Figure 27f,g).

Numerous multilayered vdW heterostructures have been investigated theoretically and experimentally. The biggest challenges associated with multilayered vdW heterostructures are poor separation of charge generated in each layer of heterojunction due to unoriented charges flowing in the multilayered structure bonded through weak vdW interactions.[698,699] Internal vdW heterostructures (IVDWHs) containing strong interaction between sheets and charge transport channels can overcome such issues to allow unidirectional interlayer charge flows for enhanced photocatalysis.[700,701] Li et al. demonstrated that sandwiching alkali atoms between carbon nitride sheets provides a channel for electron flow, and directionality of charge flow can be maintained by introducing O "adjuster" atoms (Figure 28).[702] To realize this goal, a cake model was simulated in which oxygen doped carbon nitride (OCN) and CN sheets were bridged together with K ions as a mediator, followed by a spaced O adjustor in the next layer. The OCN-K-CN IVDWHs were prepared via a copyrolysis of thiourea and K_2SO_4 by changing the amount of K_2SO_4. DFT calculation demonstrates that, after incorporation of O-adjustors, the band structure of OCN was favorably changed

https://doi.org/10.1021/acs.chemmater.1c03166
Chem. Mater. 2021, 33, 9012−9092

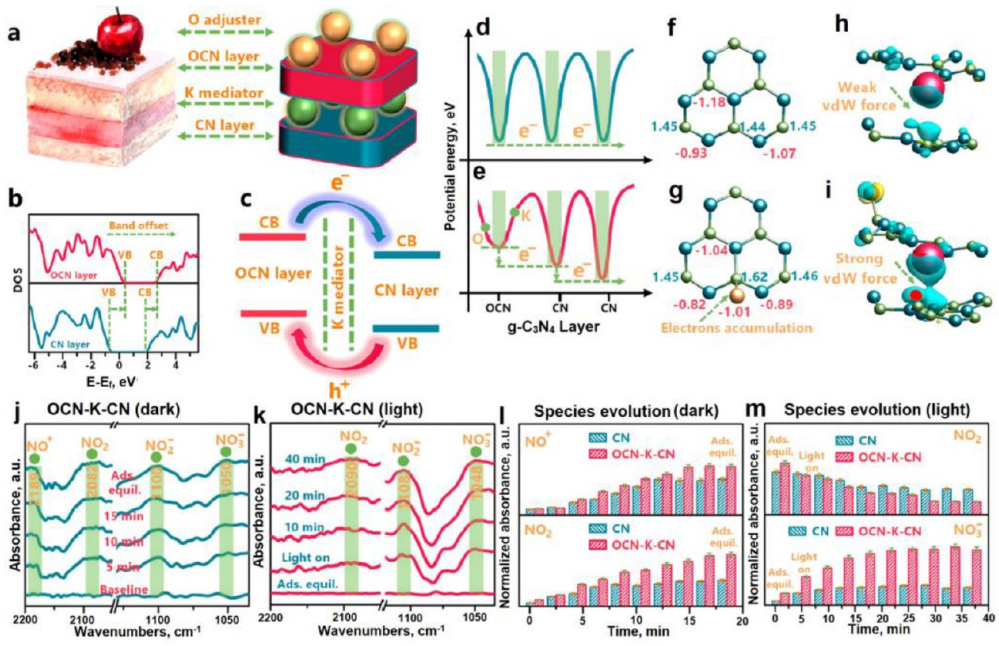

Figure 28. Schematic illustration of the internal van der Waals heterostructure (IVDWH): (a) "Cake Model" and structure of OCN-K-CN. (b) Calculated total density of states (TDOS) of CN and OCN layers. (c) Band sketch of the OCN-K-CN IVDWHF. Layered electrostatic potential energy for pristine (d) CN and (e) OCN-K-C. Calculated Bader effective charge for (f) pristine CN and (g) OCN-K-CN. Charge density difference of (h) K-CN and (i) OCN-K-CN. Blue, green, red, and gold spheres depict N, C, K, and O atoms. Charge accumulation is labeled in blue and depletion in yellow, and the isosurfaces were both set to 0.005 eV Å^{-3} for (i) and (j). Reaction process and intermediates: in situ DRIFTS spectra and species evolution of NO adsorption in (j and l) dark and (k and m) oxidation under visible light irradiation on CN and OCN-K-CN. Reprinted with permission from ref 702. Copyright 2018 American Chemical Society.

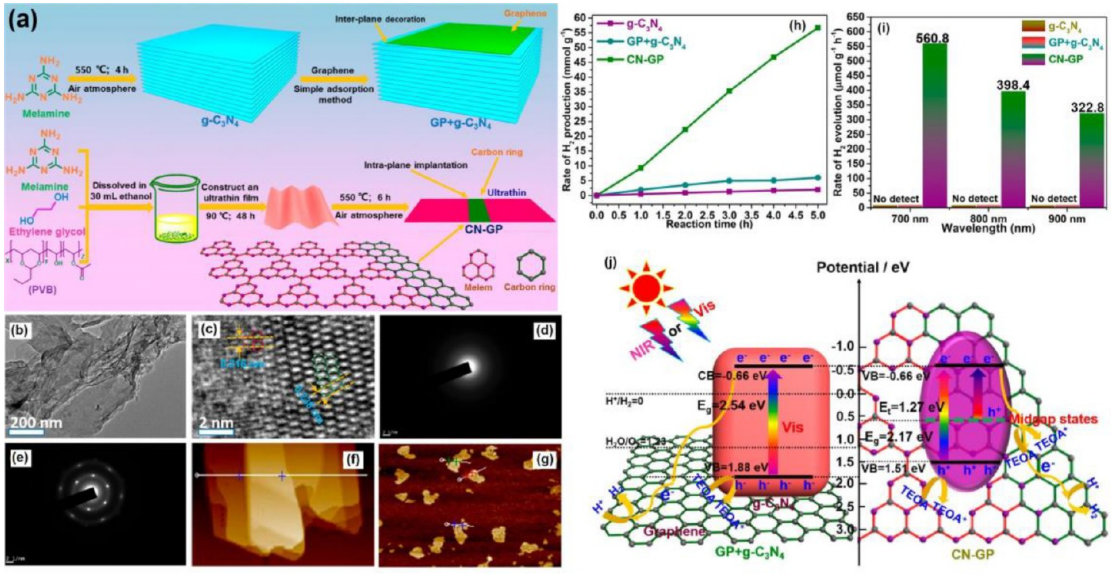

Figure 29. (a) Synthetic route for the ultrathin carbon nitride intraplane implanted with graphited carbon ring domain (CN-GP). (b, c) High-resolution TEM image of CN-GP. The selected area electron diffraction (SAED) patterns of (d) g-C_3N_4 and (e) CN-GP. AFM images of (f) g-C_3N_4 and (g) CN-GP. (h) Photocatalytic H_2 evolution rates of as-synthesized samples under vis−NIR irradiation. (i) Rates of H_2 evolution of the compounds determined, respectively, under irradiation with 700 nm wavelength, 800 nm wavelength, and 900 nm wavelength light. (j) Possible mechanism for the photocatalytic H_2 evolution of GP+g-C_3N_4 and CN-GP, respectively. Reprinted with permission from ref 714. Copyright 2019 American Chemical Society.

(CB and VB became more negative) to achieve better charge separation (Figure 28a−c). Comparison of the electrostatic potential energy using electronic structures shows that the potential energies of the OCN layer and CN sublayer in OCN-K-CN were drastically increased after the introduction of O and K. The O adjustor atoms improve the charge density between sheets and affords a strong van der Waals interaction, which was further reinforced by K atoms (Figure 28d−i). The OCN-K-CN afforded a fast NO degradation in the first 5 min with an excellent 100% activity retention after five recycles (purification efficiency of 45% compared to CN (24%). The EPR signals of the tapped radicals, DMPO-$O_2^{\bullet-}$, and

https://doi.org/10.1021/acs.chemmater.1c03166
Chem. Mater. 2021, 33, 9012−9092

DMPO-•OH generated from OCN-K-CN were found to be way higher than that of pristine CN, suggesting better charge separation in OCN-K-CN IVDWHs. Further, in situ diffuse reflectance infrared Fourier transform spectroscopy (DRIFTS) measurement of NO degradation under dark and visible light shows the NO_2 band at 2091 cm^{-1} was decreased after visible irradiation and more band for (NO_2^- and NO_3^-) were observed due to more prominent oxidation of NO over OCN-K-CN (Figure 28j−m).

Even though intersheet charge recombination can be suppressed via the above-mentioned strategies, intrasheet charge recombination within the 2D g-C_3N_4 sheet poses another challenge. To solve the problem of intrasheet charge recombination, incorporation of electron deficient units such as pyromellitic dianhydride (PMDA), mellitic acid trianhydride (MTA), and biphenyl tetracarboxylic dianhydride (BTCDA) to form polyimides has been suggested.[703−705] These electron-deficient units extract some charge from the sheets, preventing faster recombination. Additionally, band positions of the materials can be tuned based on the content of such units. For example, Shiraishi and co-workers demonstrated that the introduction of 51% PMDA units in the g-C_3N_4/PDI network can change the valence band to 1.86 V Ag/AgCl at pH 6.6 compared to g-C_3N_4 (1.40 V).[706] Because of the deep valence band, the catalyst was very efficient for the product of H_2O_2. The introduction of the graphene sheet in the g-C_3N_4/PDI scaffold in the 2D/2D assembly was found to again boost the H_2O_2 generation rate.[707] Additionally, some other approaches such as the introduction of donor−acceptor assemblies,[708] polyaromatic units,[709,710] increasing π conjugation, addition N and C rich units, etc. have also been used to reduce recombination on the sheets.[711,712]

Inspired by the success of the g-C_3N_4/graphene based 2D/2D van der Waals structure, researchers endeavor to introduce graphene-like conjugated fragments in the carbon nitride framework to facilitate better charge separation. For example, conjugated carbon rings were introduced in the g-C_3N_4 framework ((C_{ring})−C_3N_4) by thermal annealing of melem and glucose. The resulting (C_{ring})−C_3N_4 showed excellent charge separation due to the capture of photogenerated electrons on the sheets by conjugated carbon units and displayed almost 5% quantum efficiency in water splitting.[713] Indeed, these structures cannot be considered as van der Waals structures where two fragrants are interacting in a face-to-face manner. However, such structures can be categorized in the class of 2D/2D in-plane heterostructures where two 2D sheets interact laterally. In another work, the workgroup of Song et al. demonstrated the synthesis of an ultrathin carbon nitride intraplane implanted with a graphited carbon ring domain (CN-GP) via thermal polymerization of polyvinyl butyral and a melamine membrane (Figure 29a, Table 8).[714] To compare the performance, the CN-GP interplane decorated with graphene (GP + g-C_3N_4) was also prepared by decorating the graphene sheets on carbon nitride to make a vdW heterosystem. The presence of two-phase (1) g-C_3N_4 and (2) graphene was observable in HRTEM images, AFM images, and the SAED pattern (Figure 29b−g). Notably, in the photocatalytic H_2 evolution, rates of 560.8, 398.4, and 322.8 μmol g^{-1} h^{-1} were observed at 700, 800, and 900 nm irradiation, while under the same conditions GP + g-C_3N_4 achieved very poor yield (Figure 29h−i). Further, a benchmark apparent quantum efficiency (AQE) of 14.8% at 420 nm was observed, exceeding a previously reported yield on similar kinds of systems ((C_{ring})−C_3N_4 5%). The improved activity was observed due to prompt migration of the photogenerated charge from the carbon nitride domain to the graphene domain (Figure 29j).

10. CARBON NITRIDE−CARBON 2D/2D vdW STRUCTURES

The effective strategy to increase the performance of g-C_3N_4 based materials is to integrate with carbon-based materials which not only provide a better alternative to avoid metal-based semiconductors but also enhance the absorption and charge separation.[715,716] Carbon-based materials are earth-abundant and cheap, and, depending on the nature and hybridization of carbon in the materials, may be a semiconductor to the conductor. The improvement of the photocatalytic performance of g-C_3N_4 using carbon-based materials has been achieved mainly through the junction interaction, cocatalyst effect, surface reconstruction, modification of local electronic structure, electron sink, etc. With the advent of new carbon-based materials such as graphene, graphene oxide, carbon nanotubes, fullerene, carbon quantum dots (CQDs), graphdiyne, carbon nanofibers, etc., the catalytic and photocatalytic properties of various semiconductors have been dramatically improved.[717−719]

The syntheses of some specific nanostructured carbon materials is far from large-scale synthesis because they rely on costly and time-consuming methods. For example, high-quality graphene is synthesized by chemical vapor deposition (CVD) of methane at high temperature and pressure in the presence of metal catalysts.[720] Nanostructured carbon, which possesses a localized sp^2 carbon framework, seems to be a better alternative.[721] Carbon-based materials due to the localized conjugated sp^2 network facilitate better charge separation as they work as electron capturing agents/electron sinks in photocatalysis. Some carbon materials such as carbon quantum dots (CQDs) and graphene quantum dots (GQDs) due to the presence of a quasi-spherical state have sp^3 carbons at the edge, giving semiconductive properties and the opportunity to integrate with carbon nitride-based materials.[722] Additionally, the quantum confinement effect, up-conversion, and bright photoluminescence of quantum dots are appealing to harvest a major fraction of light. Indeed, extremely high numbers of reports are available on the use of carbon-based materials coupling with inorganic semiconductors to make 0D/2D, 0D/3D, 2D/2D, 2D/3D, and 3D/3D hybrids to improve photocatalytic properties.[723−726] Among them, 2D sheets of graphene and graphene oxide have proven to be the most promising due to their 2D nature and excellent optoelectronic properties.[727−729] Sticking to the scope of this review, we will revisit the scope of 2D carbon-based materials to integrate with g-C_3N_4 based semiconductors.

10.1. Carbon Nitride−Graphene. Graphene is the most celebrated member of the carbon family.[730,731] Since its discovery in 2004, it has revolutionized the field of 2D materials due to its astonishing thermal, chemical, and optoelectronic properties.[732] It is sufficient to see the potential of graphene by its calculated properties such as excellent charge carrier mobility (200 000 cm^2 V^{-1} s^{-1}), thermal conductivity (5000 W m^{-1} K^{-1}), electrical conductivity (2000 S m^{-1}), extremely high theoretical specific surface area (2630 m^2 g^{-1}), transparency (97.7%), mechanical strength (Young's modulus ∼ 1 TPa), excellent environmental compatibility, and adsorption capacity for organic and

https://doi.org/10.1021/acs.chemmater.1c03166
Chem. Mater. 2021, 33, 9012−9092

Table 8. 2D/2D Carbon Nitride-Doped Carbon Nitride-Based Isotype Heterojunction Photocatalysts

photocatalyst	synthesis	application	light source	AQY/STH	remarks	ref
		Isotype Heterojunctions				
P-doped g-C_3N_4 (PCN) and g-C_3N_4 (CN) isotype heterojunctions (PCN/CN)	PCN and melamine were mixed in an agate mortar and calcined at 550 °C.	Photocatalytic degradation of tetracycline (TC)	300 W Xe lamp ($\lambda \geq$ 400 nm)	-	CNP-1—89.7% TC degradation efficiency in 60 min pure CN—50.7% TC degradation in 60 min	676
oxygen-doped carbon nitride/graphitic carbon nitride (O-CN/CN-3)	Solvothermal method: Cyanuric chloride and CN were dispersed in acetonitrile, followed by autoclaving at 200 °C for 20 h.	Photocatalytic H_2 evolution	300 W Xe lamp ($\lambda \geq$ 420 nm)	21.4% (425 nm)	H_2—6.97 mmol g^{-1} h^{-1} (O-CN/CN-3) ~12.4 times that of CN (0.56 mmol g^{-1} h^{-1})	677
g-C_3N_4 isotype heterojunction	Urea and dicyandiamide were mixed with SBA-15 and calcined at 550 °C for 4 h under an N_2 atmosphere.	Photocatalytic degradation of methyl orange (MO) and tetracycline	300 W Xe lamp ($\lambda \geq$ 420 nm)	-	DUPG2—83% MO degradation UCN—54.16% MO degradation DUPG2—90.9% TC degradation UCN—51.7% TC degradation	678
P-doped carbon nitride/P and S co-doped carbon nitride isotype heterojunction (P-C_3N_4/PS-C_3N_4)	P-C_3N_4/PS-C_3N_4 was obtained via calcining melamine + HCCP and melamine + HCCP + thiourea, respectively, at 550 °C for 4.0 h.	Photocatalytic degradation of RhB	300 W Xe lamp ($\lambda \geq$ 420 nm)	-	P-C_3N_4/PS-C_3N_4—94.6% RhB degradation after 10 min C_3N_4—17.9% RhB degradation after 10 min	679
AA- and ABA-stacked carbon nitride (C_3N_4)	DFT calculations	Photocatalytic CO_2 reduction and H_2 evolution	Visible light	-	AA-stacked C_3N_4 is a more efficient photocatalyst for CO_2 photoreduction (CBM at −0.89 eV and VBM at 1.55 eV) CB of ABA-stacked C_3N_4 is more negative for better H_2 production	680
g-C_3N_4/g-C_3N_4 homojunction	Melamine, cyanuric acid, and thiourea were used to make supermolecule precursors. The supermolecule precursors were milled and heated at 550 °C for 2 h.	Photocatalytic degradation of RhB	300 W Xe lamp ($\lambda \geq$ 420 nm)	-	CN-MC—88% RhB degradation after 4 h CN-M—20% RhB degradation after 4 h	681
Liquid exfoliation and chemical blowing (le-CNNS and cb-CNNS) homojunction	Solid cb-CNNS was added into the colloidal suspension of le-CNNS and stirred for 12 h, followed by the addition of 1 M HCl, and the resulting precipitate was collected, washed, and dried.	Photocatalytic degradation of RhB	300 W Xe lamp ($\lambda \geq$ 420 nm)	-	le-CNNS and cb-CNNS—~76% RhB degradation after 1 h g-C_3N_4 ~ 23% RhB degradation in 2 h le-CNNS and cb-CNNS—k value 12.8 times that of g-C_3N_4	682
Co-condensed amorphous carbon/g-C_3N_4 (CNC)	Thermal co-condensation approach. Urea and glucose mixture was annealed at 500 °C for 2 h.	Photocatalytic H_2 evolution	350 W Xe lamp ($\lambda \geq$ 420 nm)	0.9% (420 nm)	H_2—212.8 μmol g^{-1} h^{-1} (CNC0.1) ~ 10 times of pure g-C_3N_4	683
Honeycomb-like CN isotype heterojunction	Urea and thiourea were mixed and heated to 674 and 724 K (1 h).	Photocatalytic nitric oxide (NO) removal	Visible light	-	UT_2-CN—68% NO degradation U-CN—49% NO degradation T-CN—24% NO degradation	684
Isotype heptazine-/triazine-based carbon nitride heterojunctions (HTCN)	Mel-T (prepared from melamine calcination) is ground with KCl and LiCl and annealed at 550 °C for 4 h.	Photocatalytic H_2 evolution	350 W Xe arc lamp	26.7% (420 nm)	H_2—890 μmol g^{-1} h^{-1} (HTCN-500) ~ 15 times of BCN	685
Isotype heterojunction g-C_3N_4/g-C_3N_4 nanosheets	One-pot heating: urea, thiourea, $Ce(NO_3)_3{\cdot}6H_2O$ or $Zn(CH_3COO)_2{\cdot}2H_2O$) were ground and heated at 500 °C for 2 h.	Photocatalytic degradation of MO and MB		-	CeO_2/CN-UT—57% MO degraded after 4 h 14 times higher than bulk CN-U CeO_2/CN-UT—complete degradation of MB CN-U—66.4% MB degradation	690
Nanostructured carbon nitrides into an isotype heterojunction (UD_x-CN)	Urea and DCDA were annealed at 550 °C for 4 h.	Photocatalytic H_2 evolution	300 W Xe lamp ($\lambda \geq$ 420 nm)	-	H_2—553 μmol g^{-1} h^{-1} (UD_x-CN) ~5 times of U-CN (104 μmol g^{-1} h^{-1})	691
Polytriazine/heptazine based carbon nitride heterojunctions	Ionothermal molten salt method: Urea with different amounts of the eutectic mixture KCl/LiCl·H_2O was finely ground in an agate mortar under IR and calcined at 450−550 °C for 5 h.	Photocatalytic H_2 evolution and degradation of MB	300 W Xe lamp ($\lambda \geq$ 420 nm)	-	H_2—4813.2 μmol g^{-1} h^{-1} (ms-CN-500-1) ~8 times higher than ms-CN-450-1	693
KNO_3 codoped CN (CN-KN)	Co-pyrolysis: thiourea and KNO_3 were calcined at 550 °C for 2 h.	Photocatalytic NO removal	Xe lamp (visible light)	-	CN-KNO_3—41.93% NO removal CN—19.60% NO removal	697

https://doi.org/10.1021/acs.chemmater.1c03166
Chem. Mater. 2021, 33, 9012−9092

Table 8. continued

photocatalyst	synthesis	application	light source	AQY/STH	remarks	ref
Isotype Heterojunctions						
OCN-K-CN	Co-pyrolysis of thiourea and K_2SO_4. Thiourea and K_2SO_4 were calcined at 550 °C for 2 h.	NO degradation	150 W tungsten halogen lamp	-	OCN-K-CN—45% NO degradation pristine CN (24%)	702

inorganic molecules.[55] Unfortunately, due to the absence of the band gap in graphene, standalone graphene cannot be used for photocatalytic application. The efforts to open up the band gap in graphene using various approaches such as heteroatom doping, incorporation of molecular units, modification of the edge to use the quantum-confinement effect, etc. have limited utility in photocatalysis due to the small band gap compared to the theoretical water splitting value and essentiality of band edge matching.[733−735] High electronic mobility of graphene has been harvested to intensify the charge separation in organic/inorganic semiconductors. The introduction of localized sp^3 carbon bonded oxygens via transformation of graphene into graphene oxide (GO) creates a significant band gap to use GO as a photocatalyst for water splitting and CO_2 reduction.[736−739] However, the electronic mobility is compromised, which puts GO in the series of other conventional photocatalysts with sluggish reaction rates.[740]

As the electronic structure of graphene is very sensitive to its surrounding environment, 2D/2D hybridization of graphene with g-C_3N_4 was investigated theoretically to open the band gap in graphene and elucidate the charge transfer mechanism between two interfaces. Due to the graphitic structure, g-C_3N_4 can establish a strong vdW interaction with graphene. The graphene/g-C_3N_4 interface showed strong interlayer electron coupling, resulting in band gap opening in graphene and increased visible absorption for g-C_3N_4.[741] Inspired from these initial findings, several 2D/2D vdW heterostructures of graphene/g-C_3N_4 have been reported for various photo-induced reactions.[742,743] Apart from conventional thermal annealing or mixing of graphene and g-C_3N_4, the g-C_3N_4/graphene architecture can also be synthesized by using molecular organic frameworks or supramolecular assemblies of g-C_3N_4 precursors. For example, Ma et al. reported the synthesis of the porous g-C_3N_4 and N-doped graphene (PCN/NG) hybrid by ball-milling and annealing of the melamine−urea conjugate and N-doped graphene.[744] During the establishment of a 2D/2D heterojunction between graphene and CN, It is not only the graphene whose charge distribution gets redistributed, but the carbon nitride is also influenced proportionally. Graphene and graphitic carbon nitrides share a common hexagonal lattice structure, so an efficient $\pi-\pi$ stacking can be realized with entirely new electronic properties. Inspired from the unique $\pi-\pi$ stacking interaction in tetrathiafulvalene (TTF) and tetracyanoquinodimethane (TCNQ) (TCNQ-TTF), which gave it a distinct metallic electrical conductance,[745] Zhang et al. visualize that the combination of graphene and carbon nitride heterojunction must produce intriguing properties.[746] To achieve this goal, they synthesized a 2D/2D vdW heterostructure of CN and rGO by thermal annealing of GO and DCDA. The condensation polymerization of DCDA provides a CN framework and also reduces the GO while protecting rGO oxidation at high temperatures. The signature G-band in the Raman spectra, diminished oxygen bonded peaks, dominant XRD peak at 27.4° for the 002 plane of carbon nitride, and absence of (001) GO peaks combined with TGA and TEM analysis clearly demonstrated the formation of an rGO-doped g-C_3N_4 structure. In contrast to carbon nitride, which indicated an ambipolar behavior in PEC measurement, the 2D/2D carbon nitride graphene (CNG) prepared in argon and air displayed anodic and cathodic photocurrents, respectively, assigned to n- and p-type nature. Furthermore, at an applied voltage of 0.4 V vs Ag/AgCl, the anodic photocurrent was

https://doi.org/10.1021/acs.chemmater.1c03166
Chem. Mater. 2021, 33, 9012−9092

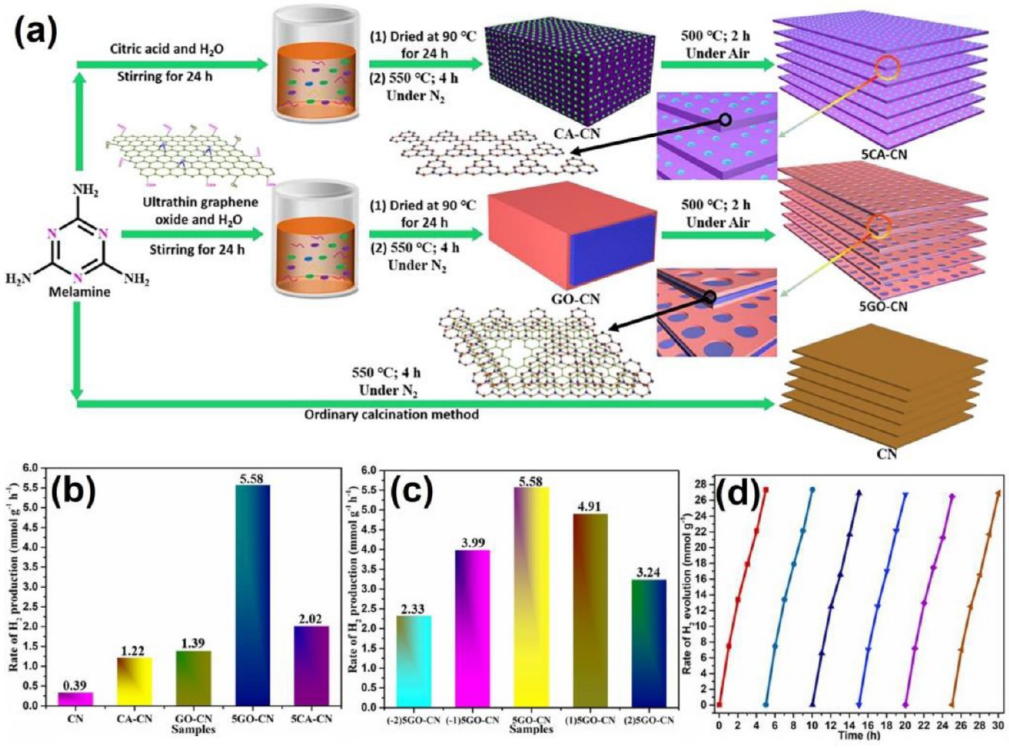

Figure 30. (a) Illustration of the preparation of the GO−CN samples. (b) Rate of hydrogen evolution on CN loaded with different quantities of GO. (c) Photocatalytic activities of CN, CA−CN, GO−CN, 5CA−CN, and 5GO−CN samples. (d) Cycling test of photocatalytic H_2 generation of the 5GO−CN hybrid. Reprinted with permission from ref 752. Copyright 2021 Elsevier.

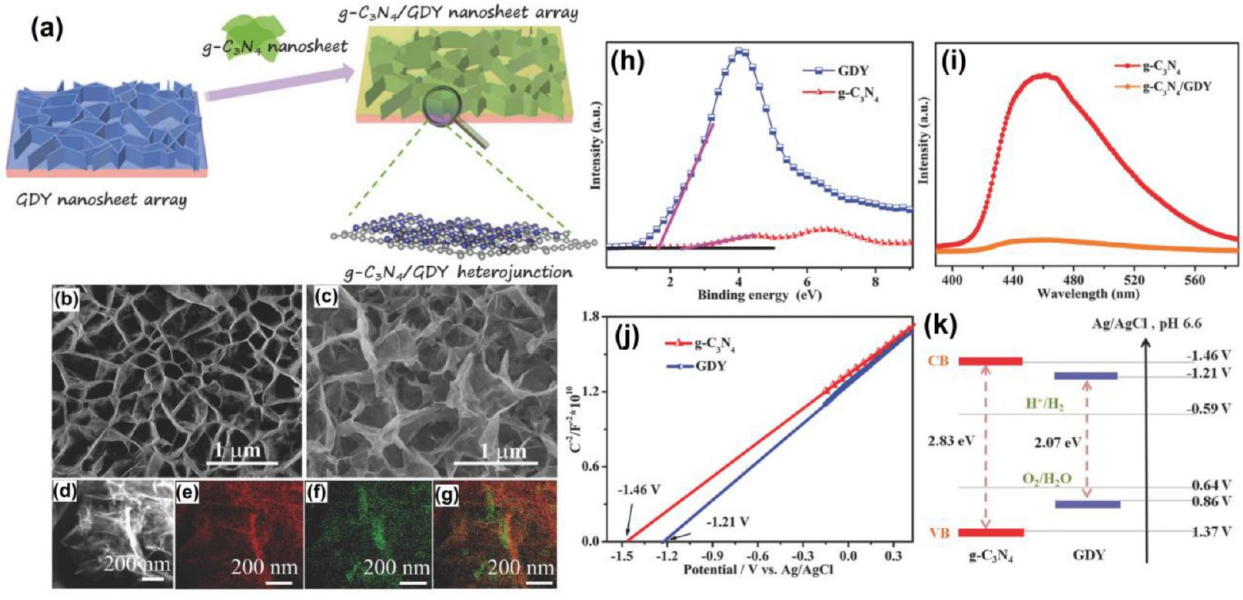

Figure 31. (a) Schematic illustration for the construction of 2D/2D graphitic carbon nitride/graphdiyne heterojunction on the 3D GDY nanosheet array. SEM images for (b) the 3D GDY nanosheet array and (c) g-C_3N_4/GDY. (d) HADDF image for g-C_3N_4/GDY. The corresponding elemental mapping images for (e) C, (f) N, (g) C, and N elements. (h) XPS valence spectra of GDY and g-C_3N_4. (i) Photoluminescence spectra of g-C_3N_4 and g-C_3N_4/GDY. (j) Mott−Schottky plots. (k) Band structures of g-C_3N_4 and GDY. Reprinted with permission from ref 762. Copyright 2018 Wiley-VCH.

300% higher after doping with rGO. Such behavior was explained based on the close packing in O defect free graphene compared with O-defect rich graphene and Fermi levels of CN and rGO equilibration, resulting in significant variation in the flat band potential under the PEC environment.

In comparison to graphene, the oxidized state graphene oxide with plenty of oxygen-carrying functionalities is more attractive to make a heterojunction with carbon nitrides due to better effective interaction and semiconductive nature.[707,742,747,748] A facile hydrothermal, mixing, or copyrolysis approach can afford the 2D/2D composite of GO and g-C_3N_4.

https://doi.org/10.1021/acs.chemmater.1c03166
Chem. Mater. 2021, 33, 9012−9092

For example, when GO and melamine were calcined together at 550 °C for 2 h, a 2D/2D composite was formed, which can degrade phenol more rapidly than other catalyst components.[749] Further, the hydrothermal treatment gives smaller graphenic fragments, which can improve the performance due to up-conversion. Utilizing the innate negative charge on the surface of GO, protonated carbon nitride prepared by the treatment of g-C_3N_4 with acids can form a 2D/2D heterostructure merely by simple mixing.[750] The protonated g-C_3N_4 and GO (pCN/GO) with 5% of GO demonstrated excellent visible light photodegradation of RhB (4 times of g-C_3N_4) due to better charge separation on the surface of GO. The GO/g-C_3N_4 nanocomposite synthesized via sonochemical synthesis displayed antibacterial activity (*E. coli*) under visible light irradiation.[751] Song et al. made a 2D CN@graphene@CN sandwich (5GO-CN) structure via in situ local thermal oxygen erosion strategy using melamine and GO precursor followed by two-step thermal annealing (Figure 30a).[752] The afforded structure demonstrated a porous sandwiched structure. Because of the addition of GO, the visible light absorption of the catalyst was significantly improved in the visible to NIR region. When used as a photocatalyst for water splitting, an impressive and repeatable H_2 evolution rate of 5.58 mmol g^{-1} h^{-1} was obtained, which was almost 14.3 times that of the pristine CN (0.39 mmol g^{-1} h^{-1}) (Figure 30b−d).

10.2. Carbon Nitride−Graphdiyne. Graphdiyine (GDY) is a member of a broad class of compounds called "graphynes" which are the 2D allotrope of carbon constituted of sp- and sp^2-hybridized carbon atoms.[753,754] Due to the unique 2D structures containing diacetylene linkages (−C≡C−C≡C−), the connected benzenic structure, GDY, shows some remarkable properties entirely different from sp^2 carbon-based structures such as graphene, CNTs, etc.[755,756] The theoretically calculated band gap for the GDY monolayer was found to be 0.44−1.47 eV.[757] Additionally, GDY has high hole mobility and has been used as hole-transporting materials in various applications.[758−760] The 2D nature, conjugated system, and high hole mobility make them a suitable candidate to integrate with 2D g-C_3N_4 in a 2D/2D fashion.[761]

Han and co-workers prepared a graphdiyne honeycomb structure on the copper substrate and then integrated it with carbon nitride sheets in a hydrothermal reaction to prepare g-C_3N_4/GDY 2D/2D heterostructure (Figure 31a).[762] The afforded C_3N_4/GDY 2D/2D heterojunction showed good structure interfacial interaction (Figure 31b−g). The valence band positions of g-C_3N_4 and GDY calculated from XPS valence spectra were found to be 2.4 and 1.7 eV, suggesting thermodynamically favorable hole transfer from g-C_3N_4 to GDY (Figure 31h). While the CB position of GDY was less negative than that of g-C_3N_4, the afforded structure was in a type I configuration. The efficient charge separation was evident from a decreased PL intensity in the g-C_3N_4/GDY heterojunction and increased photocurrent density in PEC water-splitting experiments (Figure 31i−k). In another work, a 2D/2D heterojunction of GDY and g-C_3N_4 was prepared by high temperature (400 °C) annealing, which established a C−N bond between GDY and g-C_3N_4 and served as a charge carrier channel to accelerate the migration of photogenerated electrons from g-C_3N_4 to GDY.[763] The prolonged charge carrier lifetime and decreased overpotential in g-C_3N_4/GDY enhanced the performance by a factor of 6.7 compared to g-C_3N_4. Furthermore, GDY interacted with a few-layered g-C_3N_4 exfoliated using liquid N_2 also increased the H_2 evolution performance by a multiplication factor of 3 over that of g-C_3N_4.[764]

10.3. Carbon Quantum Dot Implanted Carbon Nitride. Carbon quantum dots (CQDs) are quasi-spherical nanoparticles of graphitic or turbostratic carbon (sp^2 carbon) comprised of either amorphous or crystalline form.[765] Apart from amorphous carbon/graphitic carbon, a small fragment of graphene and graphene oxide also belongs to the CQD family.[766] Since the accidental discovery of CQDs during the purification of carbon nanotubes, CQDs have emerged as future quantum materials for various applications such as LEDs, bioimaging, sensing, photocatalysis, and energy applications due to their unique optoelectronic and physicochemical properties.[767−771] Recently, another new class of CQDs called carbon nitride quantum dots are replacing CQDs due to their high N content, bright luminescence, thermochemical stability, and resistance to photobleaching.[42,772−774] Due to their spherical to subspherical morphologies, CQDs are put in the 0D family, and their properties and applications including their 0D/2D and 0D/3D structures are discussed elsewhere.[722,775−777]

Focusing on the scope of this review, we will discuss the role of carbon quantum dots to achieve the 2D/2D heterojunction, which essentially is not limited to van der Waals interaction. Physical interaction of CQDs with g-C_3N_4 affords 0D/2D heterojunction, which shows leaching to the solution and self-degradation due to less effective interfacial contact and is not desirable for long-term usage. On the other hand, implantation of carbon quantum dots in the carbon nitride heptazine (C_6N_7) network using a thermal approach has been found to transform the 0D system into 2D graphene-like domains giving 2D/2D in-plane heterostructures.[778] This resulted because of graphitization of CQDs at elevated temperature and simultaneous accommodation in the polymerizing heptazine structure. Wang et al. demonstrated the implantation of CQDs in the g-C_3N_4 network by thermal annealing of freeze-dried urea and carbon quantum dot precursors.[779] The implanted CQDs were visible in HR-TEM images. Due to localized grafting of the conductive sp^2 carbon-rich domain in the g-C_3N_4 network, better intralayer charge separation was achieved, evident from the improved photocurrent response and H_2 evolution rate. In another study, Han et al. used a strategy to synthesize carbon dot implanted carbon nitride (CCNS) using dicyandiamide and selenium precursors.[780] Selenium not only prevents stacking of carbon nitride sheets during synthesis but also facilitates the release of nitrogen, ammonia and nitrile groups, which leads to the in situ formation of carbon quantum dots (CDs) without any added precursors. The presence of CDs in the carbon nitride scaffold was visible in HRTEM images, while the thickness of the sheets was 5.5 nm, which verifies the presence of CDs implanted in few-layered sheets. When used for the CO_2 reduction under visible light, the CCNS photocatalyst afforded an excellent CO_2 reduction, hydrogen evolution, and RhB degradation rate, which was attributed to better charge separation and electron transport on the few-layered sheets. The evidence of increased charge separation and transport came from PL and time-resolved PL (TRPL) measurement, which displayed a significant quenching and increased PL lifetime.

In addition to conventional CQDs incorporated in the g-C_3N_4 structure, a reversed configuration where carbon nitride quantum dots (CNQDs) were embedded in carbon nano-

https://doi.org/10.1021/acs.chemmater.1c03166
Chem. Mater. 2021, 33, 9012−9092

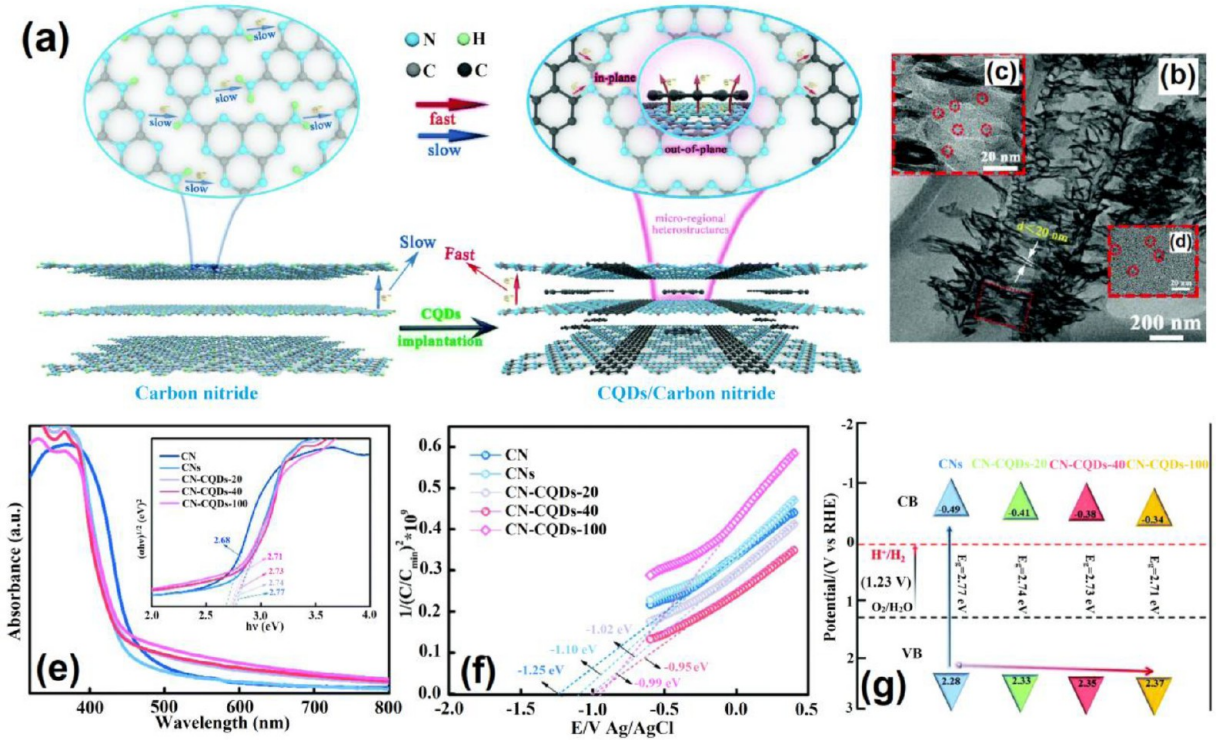

Figure 32. (a) Modulating the interfacial charge kinetic by simultaneously building two kinds of heterojunctions. The controllable CQD embedded CN nanoframes possess two kinds of heterogeneous interfaces within seamlessly stitched microarea two-dimensional in-plane and out-of-plane domains, which can effectively enhance its intrinsic driving force in different directions to accelerate the separation and transfer of charge. (b–d) CN-CQDs-40. (e) UV/vis absorption spectra and band gap energies (inset) of CN, CNs, CN-CQDs-20, CN-CQDs-40, and CN-CQDs-100. (f) Mott–Schottky plots for CN, CNs, CN-CQDs-20, CN-CQDs-40, and CN-CQDs-100 with 1000 Hz frequencies. (g) Band structure of alignments for CNs, CN-CQDs-20, CN-CQDs-40, and CN-CQDs-100. Reprinted with permission from ref 782. Copyright 2020 Royal Society of Chemistry.

sheets was synthesized using formamide as a single precursor and displayed remarkable apoptosis of cancer cells in the IR region.[781] In very recent work, Li et al. fabricated CQDs containing a double-deck frame-like carbon nitride (CN) nanostructure by using a melamine-cyanuric acid supermolecule (CM) and CQDs precursor (CM-CQDs) for enhancing the photocatalytic activity (Figure 32a, Table 9).[782] Due to the work function difference between CQDs and CN, two heterogeneous interfaces stitched in-plane and out-of-plane were obtained. CN-CQDs displayed towel gourd shape-like nanostructures where two channels were connected through a rod-like structure (Figure 32b–d). Such morphology arose because of the difference between the crystallization rate of the amino group-containing precursor, which crystallizes the edge faster, and gas that evolved from the central ladder-type eruption. Such morphology implanted with in-plane and out-of-plane CQDs affords better intra- and interplane charge separation increases TC and RhB degradation (Figure 32e,f). Due to the incorporation of CQDs in the CN framework, the CB and VB were downshifted while the band gap was reduced to 2.71 eV for CN-CQDs-100 (Figure 32g). In another work, an ultrathin tubular porous g-C_3N_4 implanted carbon dot (CN/C-Dots) lateral heterostructure was synthesized, which showed that electrostatic potential for the lateral structure was much less than the vertical heterostructure, which afforded a 113-fold increased H_2 evolution rate compared with that of pristine CN.[783]

11. CARBON NITRIDE–2D POLYMER 2D/2D vdW STRUCTURES

Polymeric semiconductors due to the possibility of facile band energy tuning by controlling the degree of polymerization, specific coordination, and chemical control over the nature of the constituting units are fast emerging as new candidates in photocatalysis. Poly(*p*-phenylene) was the first (1985) reported example of polymer photocatalysts demonstrating the hydrogen evolution under deep UV irradiation in the presence of sacrificial donors.[784] Polyaniline (PANI), a conducting polymer, was also among the first few organic polymeric materials explored for the photolytic applications due to certain advantages such as *p*-type hole conducting behavior, easy solution processability, solubility, reversible redox behavior, and photostability.[785,786] To better extract the holes and enhance the water oxidation kinetics, PANI has been integrated with several other organic/inorganic semiconductors including carbon nitride.[787,788] Later, a new combination including copolymers with electron donor–acceptor assembly such as phenyl and 2,1,3-benzothiadiazole units and metal chelated polymers (bipyridine ligand) has been reported for hydrogen evolution and other photocatalytic applications.[789] Such linear conducting polymers leave little room for further modification, and the 3D morphology of the bulk agglomerated state with unidirectional charge transport limits their application. However, 2D carbonized polydopamine was also prepared and integrated into carbon nitride for accelerated RhB degradation.[790,791] Later, several new organic semiconductor materials such as poly(azomethine) networks, conjugated microporous polymers (CMPs), covalent triazine-

https://doi.org/10.1021/acs.chemmater.1c03166
Chem. Mater. 2021, 33, 9012–9092

Table 9. 2D/2D Carbon Nitride−Carbon/Conductive Carbon Based Heterojunction Photocatalysts

photocatalyst	synthesis	application	light source	AQY/STH	remarks	ref
		Carbon/Conductive Carbon				
Carbonized poly (furfural alcohol)/g-C_3N_4 (CPFA/g-C_3N_4)	To melamine and a furfuryl alcohol suspension, H_2SO_4 was added, and precursor was obtained by completely volatilizing the solution at room temperature. The obtained solid was calcined at 60 °C for 2 h.	Photocatalytic H_2 evolution	300 W Xe lamp ($\lambda \geq$ 400 nm)	-	H_2—584.7 μmol g^{-1} h^{-1}(CPFA/g-C_3N_4) ~4 times higher than pure g-C_3N_4 (156.2 μmol g^{-1} h^{-1})	726
Cyanamide functionalized carbon nitride/GO/NiP ($^{NCN}CN_x$/GO/NiP)	Solution mediated electrostatic interaction	Photocatalytic H_2 evolution	300 W Xe lamp ($\lambda \geq$ 400 nm)	-	H_2—1159 ± 29 μmol H_2 (g $^{NCN}CN_x)^{-1}$ h^{-1} using 4-MBA $^{NCN}CN_x$—676 ± 27 μmol H_2 (g $^{NCN}CN_x)^{-1}$ h^{-1}	727
NrGO on carbon and S modified g-C_3N_4 isotype heteojunction (NrGO/g-gPSCN)	Two step thermal annealing	Degradation of 4-nitrophenol	250 W Hg lamp ($\lambda \geq$ 400 nm)	-	NrGO/g-gPSCN—64.83% degradation of 4-NP in 60 min g-g PSCN—5.62% degradation of 4-NP in 60 min	729
Graphitic carbon nitride/graphdiyne heterojunction (g-C_3N_4/GDY)	3D graphdiyne nanosheet array and g-C_3N_4 nanosheets were dispersed together and heated in a Teflon-lined autoclave at 50 °C for 10 h.	Photoelectrochemical water splitting	300 W Xe lamp	-	Current density——98 μA cm^{-2} at a potential of 0 V versus NHE (g-C_3N_4/GDY) Current density——32 μA cm^{-2} at a potential of 0 V versus NHE (g-C_3N_4/GDY)	762
Graphdiyne/g-C_3N_4 hybrid	Calcination method: GD suspension in methanol was added in g-C_3N_4 and calcined at 400 °C for 2 h.	Photocatalytic H_2 evolution	350 W Xe lamp ($\lambda \geq$ 420 nm)	-	H_2—39.6 μmol h^{-1} (graphdiyne/g-C_3N_4) 6.7-fold of g-C_3N_4 (5.9 μmol h^{-1})	763
Graphdiyne CN sheets (CN/GDY)	GDY and CN were interacted via electrostatic interaction.	Photocatalytic H_2 evolution	300 W Xe lamp	2.65% (420 nm)	CO—5.8 μmol/g (CN/GDY) ~19.2 times of CNs (4.98 μmol/g)	761
Carbon quantum dot implanted carbon nitride double-deck nanoframes (CN-CQD)	Melamine, cyanuric acid, and a certain amount of carbon quantum dots (CQDs) were mixed at 125 °C for 4 h, followed by thermal annealing.	Photocatalytic degradation of tetracycline (TC) and RhB	40 W LED lamp	-	CN-CQDs—40−100% TC degradation after 2 h CN—33% TC degradation after 4 h	782

https://doi.org/10.1021/acs.chemmater.1c03166
Chem. Mater. 2021, 33, 9012−9092

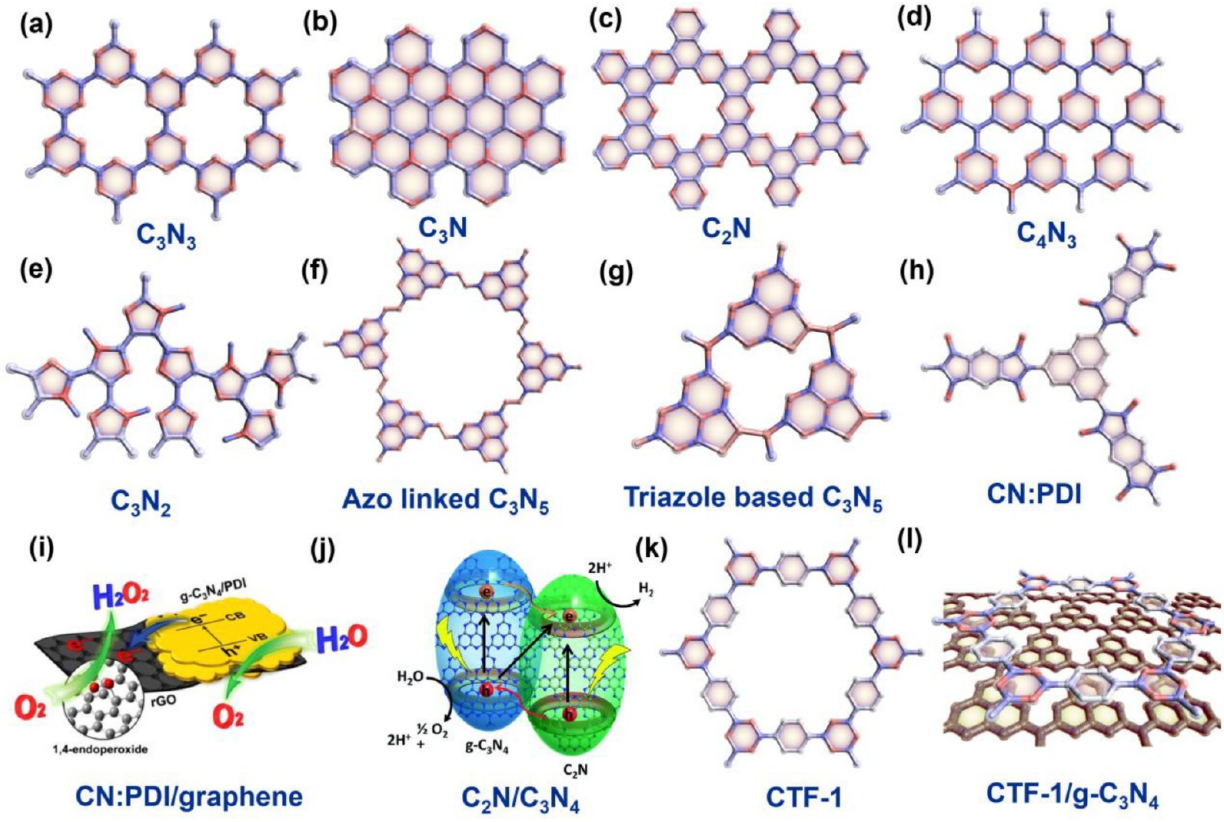

Figure 33. Chemical structures of potential polymeric materials to form the vdW heterojunction with g-C_3N_4: (a) C_3N_3, (b) C_3N, (c) C_2N, (d) C_4N_3, (e) C_3N_2, (f) azo-linked C_3N_5, (g) triazole containing C_3N_5, (h) melem/PMDA carbon nitride polydiimide CN/PDI, and (i) 2D/2D heterostructure of CN:PDI/graphene. (a) Adapted with permission from ref 810. Copyright 2020 Wiley-VCH. (b) Adapted with permission from ref 811. Copyright 2016 National Academy of Sciences. (c) Adapted with permission from ref 812 by Mahmood et al. under the terms of the Creative Commons Attribution 4.0 International License (CC BY) (https://creativecommons.org/licenses/by/4.0/). Copyright 2015 Mahmood et al. (d) Adapted with permission from ref 813 by Zhou et al. under the terms of the Creative Commons Attribution 4.0 International License (CC BY) (https://creativecommons.org/licenses/by/4.0/). Copyright 2018 Zhou et al. (e) Adapted with permission from ref 814. Copyright 2021 Elsevier. (f) Adapted with permission from ref 73. Copyright 2019 American Chemical Society. (g) Adapted with permission from ref 815. Copyright 2018 Wiley-VCH. (h) Adapted with permission from ref 706 Copyright 2014 Wiley-VCH. (i) Reprinted with permission from ref 707. Copyright 2016 American Chemical Society. (j) DFT calculated 2D/2D heterojunction between C_2N and g-C_3N_4. Reprinted and modified with permission from refs 77 and 817. Copyright 2018 Royal Society of Chemistry and Copyright 2016 Wiley-VCH, respectively. (k) Chemical structure of CTF-1. Adapted with permission from ref 819. Copyright 2021 American Chemical Society. (l) 2D/2D heterojunction of CTF-1/g-C_3N_4. Adapted with permission from ref 804. Copyright 2020 Elsevier.

based frameworks (CTFs), covalent organic frameworks (COFs), and planarized-fluorene-based conjugated polymers have been investigated, some of which display photoactivity higher than molecular and carbon nitride photocatalysts.[792,793] The pioneering work by the Cooper group on pyrene based conjugated microporous polymers (CMPs) synthesis using Suzuki Miyaura polycondensation demonstrates that the band gap of CMPs can be tuned in the whole spectrum just by varying the precursor stoichiometric ratio and polymerization degree.[794] Contemporary development by the Wang group demonstrates the insertion of electron output tentacle dibenzothiophene-*S*,*S*-dioxide units in pyrene based donor−acceptor CPs reaching AQYs as high as 8.5% at 420 nm.[795] Considering the 2D planarity and surface properties such as high surface area and tunable optical band gap, covalent organic frameworks (COFs) and covalent triazine frameworks (CTFs) are more successful candidates for photocatalysis.[796−798] Various synthetic approaches, chemical attributes, and photophysics of polymer photocatalysts are magnificently summarized in previous reports.[799,800] Thomas et al. demonstrated TAPD-$(Me)_2$ and TAPD-$(OMe)_2$ COFs prepared by condensation of *N*,*N*,*N*′,*N*′-tetrakis(4-aminophenyl)-1,4-phenylenediamine with 2,5-dimethylbenzene-1,4-dicarboxaldehyde/2,5-dimethoxybenzene-1,4-dicarboxaldehyde ($(OMe)_2$, which produces H_2O_2 from water at a rate of 22.6 μmol/16 h.[801] Luo et al. demonstrated that when imine based COFs are grown on carbon nitride sheets (CNS) via an in situ approach, the CNS-COF heterostructure can reach HER as high as 9.1 mmol h^{-1} g^{-1} with an associated AQY 31.8% (425 nm).[802] Such improved performance was attributed to surface passivation of CNS by utilization of the residual $-NH_2$ group on CN in imination. As evident from the enhanced EPR signal, the CNS-COF assembly can achieve a better charge separation. CTFs with high nitrogen content and compositional similarity (CN_xH_y) with carbon nitride are more appealing for photocatalytic applications. CTFs are generally prepared by molten salt or low temperature coupling routes. Tang et al. demonstrated CTF-0 with relatively high N content synthesized by a microwave-assisted heating route in a stacked AB-fashion compared to the ionothermal approach (AA stacking) that positively influenced band edge alignments to benefit HER and OER.[803] Similarly, the 2D/2D heterojunction

https://doi.org/10.1021/acs.chemmater.1c03166
Chem. Mater. 2021, 33, 9012−9092

Table 10. 2D/2D Carbon Nitride−2D Polymers-Based Heterojunction Photocatalysts

photocatalyst	synthesis	application	light source	AQY/ STH	remarks	ref
		2D Polymers				
2D/2D graphitic carbon nitride nanosheet/carbonized polydopamine (CNNS/CPDA)	Thermal annealing of CN and PANI precursors	RhB degradation	visible light ($\lambda \geq 420$ nm)	-	CNNS/CPDA-2—98.2% RhB degradation within 60 min.	790
Polydopamine/graphitic carbon nitride PDA/g-C_3N_4	Dopamine hydrochloride was added to the aqueous dispersion of g-C_3N_4 sheets followed by the addition of tris-HCl solution and adjustment of pH to 8.5 by using 1 M NaOH solution and vigorous stirring at 60 °C for 24 h.	Photocatalytic degradation of MB	500 Xe lamp with a cutoff filter	-	PDA/g-C_3N_4—98.84% MB degradation ~4 times higher than pure g-C_3N_4	791
Imine linked COF/g-C_3N_4 nanosheets (CNS-COF)	In situ reaction of 4,4′,4″-(1,3,5-triazine-2,4,6-triyl) trianiline (TTA) and 1,3,5-triformylphloroglucinol (TP) in the presence of CNS	Photocatalytic H_2 evolution	300 W Xe ($\lambda >$ 420 nm)	31.8% (425 nm)	H_2—9.1 mmol h^{-1} g^{-1} (CNS-COF) CN—1.2 mmol h^{-1} g^{-1}	802
Carboxyl rich CTF nanosheets and graphitic carbon nitride nanosheets (CTFNS/CNNS)	H_2SO_4 assisted exfoliation followed by electrostatic assembly	Photocatalytic sulfamethazine (SMT) degradation	500 W Xe lamp	-	5% CTFNS/CNNS—of 94.9% SMT degradation in 180 min	804
Benzo[ghi]perylenetriimide/graphitic carbon nitride (BPTI/g-C_3N_4)	Solution phase self-assembly of BPDI and g-C_3N_4 in quinoline for 8 h at 150 °C.	RhB degradation	Visible light ($\lambda >$ 420 nm).	-	1:3 BPTI/g-C_3N_4 ~ 89% RhB degradation ~36% is higher than that of g-C_3N_4	809
PI/g-C_3N_4	Sonication thermal approach	Degradation of 2,4-dichlorophenol	300 W Xe lamp	-	30% PI/g-C_3N_4—~99% DCP degradation in 4 h ~3.8 times of pristine g-C_3N_4	820

https://doi.org/10.1021/acs.chemmater.1c03166
Chem. Mater. 2021, 33, 9012−9092

Table 11. Miscellaneous 2D/2D Carbon Nitride Based Heterojunction Photocatalysts

photocatalyst	synthesis	application	light source	AQY/STH	remarks	ref
		Miscellaneous				
$Ni(OH)_2$/2D-CN	Oil bath method: to a 2D-CN dispersion in DI water, TSC, HMT, and $Ni(NO_3)_2 \cdot 6H_2O$ were added, and the obtained solution was heated at 90 °C for 10 h.	Photocatalytic H_2 evolution	300 W Xe lamp ($\lambda \geq$ 400 nm)	5.21% (400 nm)	H_2—921.4 μmol in 5 h ($Ni(OH)_2$/2D-CN) ~135.5 times of 2D-CN (0.34 μmol in 5 h)	821
Molybdenum nitride/ultrathin graphitic carbon nitride (Mo_2N/CN)	Mo_2N dispersed in water and CN dispersed in anhydrous ethanol were mixed and stirred for 8 h at 60 °C.	Photocatalytic H_2 evolution	300 W Xe lamp ($\lambda \geq$ 420 nm)	1.75% (400 ± 15 nm)	H_2—0.89 μmol g^{-1} h^{-1} (Mo_2N/CN-1) ~143 times than pure CN	822
MoN/2D g-C_3N_4	Self-assembly and high-temperature annealing method: a MoN and 2D g-C_3N_4 dispersion in hexane was freeze-dried and annealed at 400 °C in NH_3 atmosphere for 1 h.	Photocatalytic H_2 evolution and degradation of RhB	300 W Xe lamp ($\lambda \geq$ 400 nm)	-	H_2—1802.7 μmol g^{-1} h^{-1} (10% MoN/2D g-C_3N_4) bare 2D g-C_3N_4—0.34 μmol for 5 h	823
Montmorillonite (Mt) coupled graphitic carbon nitride (m-CN) (Mt/m-CN)	Ultrasonication method: Mt was exfoliated in methanol under stirring and sonication followed by the addition of 2D m-CN nanosheets and drying.	Photocatalytic CO_2 reduction	35 W Xe lamp	CO—0.83; CH_4—2.17 (420 nm)	CO—505 μmol g-cat^{-1} (Mt/m-CN) ~3.14 times of m-CN CH_4—330 μmol g-cat^{-1} (Mt/m-CN) ~5.02 times of mCN	824
CoP/g-C_3N_4	To a solution of $Co(OAc)_2$ dissolved in DI water and CMC solution g-C_3N_4 was added and ultrasonicated. Finally, diluted ammonia solution was added dropwise, and the obtained solution was hydrothermally treated at 80 °C for 12 h.	Photocatalytic H_2 evolution	300 W Xe lamp ($\lambda \geq$ 400 nm)	4.3% (420 nm)	H_2—~4.2 mmol g^{-1} (2% CoP/g-C_3N_4) g-C_3N_4 negligible	825
UNiMOF/g-C_3N_4	g-C_3N_4 and UNiMOF were mixed in methanol.	Photocatalytic H_2 evolution	300 W Xe lamp ($\lambda \geq$ 420 nm)	0.979 (420 nm)	H_2—20.03 μmol h^{-1} (UNG-25.0) g-C_3N_4—0.4 μmol h^{-1}	826
g-C_3N_4/MgFe MMO nanosheet heterojunctions	MgFe-MMO and urea were thermally annealed.	Photocatalytic H_2 evolution	300 W Xe lamp ($\lambda \geq$ 420 nm)	6.9% (420 nm)	H_2—1.26 mmol g^{-1} h^{-1} ~6.64 times of pure g-C_3N_4	827
g-C_3N_4/In_2Se_3	In situ solution process synthesis using Se, $InCl_3 \cdot 4H_2O$, $N_2H_4 \cdot H_2O$, and g-C_3N_4	Photocatalytic H_2 evolution	36 W visible LED lamp	-	H_2—4.81 mmol g^{-1} h^{-1} (CNIS-6) g-C_3N_4—0.94 mmol g^{-1} h^{-1}	828
Mo_2C/g-C_3N_4 (MCN NS)	Electrostatic assembly of Mo_2C nanosheets and CN sheets	Photodegradation of TC	300 W Xe lamp ($\lambda \geq$ 420 nm)	-	MCN NS—97% TC degradation in 1 h pure CNS—64% in 1 h	829
Carbon nitride/C-doped BN (CN/BCN) van der Waals (VdW) heterojunctions	C-doped BN (BCN) sample and CN were ground and heated at 500 °C for 4 h.	Photocatalytic H_2 evolution	300 W Xe lamp ($\lambda \geq$ 420 nm)	16.3% (420 nm)	H_2—3357.1 μmol g^{-1} h^{-1} (CN/BCN) ~ 2.6 times of CN (1298.8 μmol g^{-1} h^{-1})	830
2D BN/g-C_3N_4	Hydrothermal process: BN, g-C_3N_4, and NH_4Cl mixture was hydrothermally treated at 180 °C for 12 h and finally calcined at 350 °C for 2 h.	Photocatalytic degradation of RhB	300 W Xe lamp ($\lambda \geq$ 400 nm)	-	2D BN/g-C_3N_4—98.2% RhB degradation within 120 min pure bulk g-C_3N_4—49.3% RhB degradation within 120 min	831

https://doi.org/10.1021/acs.chemmater.1c03166
Chem. Mater. 2021, 33, 9012−9092

between polymer semiconductors and carbon nitrides can be realized for mutually benefitted interaction including band edge modulation, enhance visible absorption, and charge separation (Figure 33). Cao et al. demonstrated the synthesis of an all organic 2D/2D heterojunction between amine-functionalized graphitic carbon nitride (GCN) nanosheets (CNNS) and carboxyl rich CTF nanosheets (CTFNS) via electrostatic interaction.[804] Acid-assisted exfoliation of CTFs not only provides CTFNS but also overcomes the size requirement for efficient interaction, resulting in improved photocurrent generation and 95.8% removal efficiency for sulfamethazine. Isolated heptazine or triazine-based carbon nitride struggle with the issue of charge separation due to the absence of charge collection sites. Coupling triazine and heptazine units together in the same carbon nitride framework was found to solve this issue by the formation of a donor−acceptor network. Zhang et al. displayed that changing the LiCl/KCl with NaCl/KCl in the ionothermal molten salt method led to a diversion of the polymerization process due to the high melting point of the NaCl/KCl mixture and afforded triazine−heptazine based carbon nitride.[805] The HER for CN-NaK was found to be 278 mmol h^{-1} with an AQE of 32% (at 420 nm). Molten salt assisted synthesis in the presence of LiCl/KCl usually produces crystalline polytriazine imides (PTI) in which two triazine units are connected with the −NH− group; however, 5-aminotetrazole precursor under identical conditions leads to formation of polyheptazine imides (PHI).[806] CN is not considered as a good water oxidation catalyst due to less positive VB, limiting its application in high oxidation potential demanding reactions such as H_2O_2 formation. Polydiimides (PDI) synthesized by coupling of anhydrides and melem/melamine units have more positive valence bands than have been widely explored for H_2O_2 generation. Apart from the previously mentioned melem-PMDA based PDI, several other substituents such as naphthalene dianhydride, biphenyl tetracarboxylic dianhydride (BTCDA), perylene dianhydride, mellitic trianhydride with three coordination sites, melamine, etc. have been used for PDI synthesis.[703,705,807] Taking advantage of the layered structure of the CN/PDI polymer, a 2D/2D hybrid with graphene was prepared which can photocatalyze water oxidation to H_2O_2 at a high rate, reaching a solar to hydrogen (STH) efficiency of 0.20%.[707] When a high CB position containing carbon nitride with less positive VB is integrated with CN/PDI, usually a solid-state Z-scheme is the preferred mechanism of charge separation, leading to enhanced kinetics of overall water splitting. For example, Miao et al. demonstrated a perylenetetracarboxylic diimide (PDI) and carbon nitride Z-scheme heterojunction that can reach an H_2 evolution rate of g-C_3N_4/PDI (1649.93 μmol g^{-1} h^{-1}), which is 2.03 times higher than that of the g-C_3N_4 nanosheet (814.03 μmol g^{-1} h^{-1}).[808] In another work, benzo[ghi]-perylenetriimide/graphitic carbon nitride (BPTI/g-C_3N_4) synthesized by N-amidation reaction displayed enhanced RhB degradation in a direct scheme mechanism.[809] With the advent of new 2D polymeric semiconductor materials such as C_2N, C_3N, C_3N_2, C_3N_3, C_4N_3, C_3N_5, C_3N_6, etc., the choices of fabrication of 2D/2D vdW heterojunctions are expanding (Figure 33, Table 10).[73,810−816] For example, distinct from traditional six-member ring carbon nitride, a novel five-member ring (imidazole) containing carbon nitride with C_3N_2 stoichiometric composition and C−C bridging coordination can demonstrate a band gap as low as 0.81 eV and is employed for PEC biosensing applications.[814] Apart from photo/photoelectrochemical applications, the new band gap tuned carbon nitride containing 2D/2D heterojunctions will find applications in other fields including optoelectronic device, FET, LEDs/OLEDs, organic solar cells, etc. As CTF, PTI, and PHI iso-element conjugates (C_xN_y), there exists no distinct boundary. While generally referring to carbon nitrides, depending upon their coordination (bridging N in CN, fused benezenic ring), C/N content, and structural similarity, they can be categorized as graphene type (low band gap) and carbon nitride type structures (moderate band gap). For example, C_2N, also called nitrogenated holey graphene, has a direct band gap of 1.96 eV.[812] Theoretical studies using DFT suggests C_2N stacking on carbon nitride sheets forms a direct scheme type-II heterojunction with suitable band edge positions for water splitting.[817] Sadly, most of such semiconductor heterojunctions with g-C_3N_4 are just reported based on the theoretical calculation, and more work is needed in this direction. 2D conjugated metal complex polymers such as a Schiff base polymer synthesized by reaction of *tert*-amino functionalized porphyrin and 2,5-dihydroxyterephthalaldehyde, which demonstrated almost 10 mA cm^{-2} current density, might also be explored for such applications.[818]

12. MISCELLANEOUS 2D/2D vdW STRUCTURES

Apart from the above-mentioned materials, several other layered materials such as $Ni(OH)_2$, Mo_2N, montmorillonite, cobalt phosphide (CoP), UNiMOF, MgFe MMO, and In_2Se_3 MO_2C have been reported, forming a 2D/2D vdW heterojunction with carbon nitrides to improve the photocatalytic performance (Table 11).[821−829] Among them, the large band gap hexagonal boron nitride (*h*-BN) is worth mentioning.[830−832] The *h*-BN possesses a 2D graphene-like structure, an excellent chemical stability, a high thermal conductivity, and a melting point which makes it suitable for various applications including lubricants to the high surface area supporting materials. However, due to a significantly high band gap (5.5 eV), it is among the less explored 2D materials in photocatalytic application. Though from the point of visible light collection, *h*-BN does not fit in visible light mediated photocatalysis but essentially provides the large oxidation potential necessary for the oxidation of various recalcitrant pollutants and water oxidation.[833,834] Further, like graphene, the charge distribution on the *h*-BN surface can be manipulated by the formation of a 2D/2D interface. Indeed, various 2D/2D interfacial catalysts amalgamated with *h*-BN and inorganic semiconductors have been reported. BN can form excellent lattice matched stacking with CN due to analogous structure followed by favorable charge redistribution in the close-packed CN-BN heterostructure. Besides band gap modulation, the high electronegativity of BN compared to CN facilitates efficient hole collection from the CN to accelerate rate-limiting oxidation kinetics.[835] In the CN-BN 2D/2D host−guest structure, due to the electron-rich and deficient pattern, a donor−acceptor relationship can be established while close 2D/2D interfacial contact will minimize the recombination losses. In a study, Tu et al. reported the synthesis of *h*-BN and g-C_3N_4 heterojunction by a thermal recrystallization process using diluted aqueous HNO_3 at 180 °C in an autoclave.[836] Unexpectedly, the visible absorption of *h*-BN/g-C_3N_4 was found to be higher than that of the carbon nitride, suggesting an electronic charge redistribution. The band gap with 40% BN containing material was shifted to 2.44

https://doi.org/10.1021/acs.chemmater.1c03166
Chem. Mater. 2021, 33, 9012−9092

eV compared to 2.70 eV for the pristine CN material that resulted in 99% degradation of acid red in 90 min under UV−vis irradiation. Further, the doping of BN with carbon, which provides extra electrons in the π-conjugated system, resulted in narrowing the band gap value.[837,838] The band gap value can be tuned by controlling the amount of carbon doping in the BN lattice, and frequently it is referred to as boron carbon nitride. In recent work, metal-free 2D/2D carbon nitride/C-doped BN (CN/BCN) van der Waals (VdW) heterojunctions were prepared where the BN due to significant C doping has a smaller band gap than CN with less electronegative behavior.[830] In such cases, a Z-scheme mechanism was preferred where electrons from the CB of CN were recombining with holes of BCN. The combination of CN/BCN was able to afford an astonishing HER (3357.1 μmol h^{-1} g^{-1}) with an associated AQE of 16.3% that was much higher than single CN (1298.8 μmol h^{-1} g^{-1}) under the visible light.

13. CONCLUSIONS AND FUTURE PERSPECTIVES

The development of a photocatalyst with sufficient visible absorption, better electron−hole separation, and a long lifetime to actuate a reaction before the annihilation of charges are a few key factors that will decide the future of the photocatalysis field. Almost 48 years have passed since the first photoelectrode promoting water splitting using energy from light was observed. Significant progress has been made to demonstrate the potential of photocatalysis to solve energy and environmental issues. Hitherto, no photocatalyst materials exist which can sustain the oxidation and reduction reaction at both ends of their band edges. Indeed, increasing visible absorption and galvanizing both reactions are paradoxical as one can be attained at the cost of sacrificing the other. Another ultimate challenge is to chain the electrons and protons derived from the oxidation reaction at the valence band with the reduction reaction at the conduction band. Heterojunction formation between two semiconductors envisaged solving these problems by harvesting more light without sacrificing the redox power of the catalysts. Particularly, the Z-scheme and S-scheme heterojunction constituted of two different reducing and oxidizing catalytic components has shown great promise. However, a significantly large number of traveling charge carriers trying to reach another semiconductor gets to recombine in the bulk and at the epitaxially mismatched interface.

2D materials, due to their large specific surface area available for maximum effective interaction, numbers of the active site, and excellent electronic mobility, found a specific place in the photocatalysis field. Fabrication of the 2D/2D heterojunction using two different semiconductors not only provides benefits of conventional heterojunction such as synergistic absorption and large band potential difference but also overcomes the issue of charge separation due to effective interaction between two interfaces and angstrom to nano regime travel distance between 2D sheets. With the advancement of materials genomics, numerous new 2D semiconductor/conductor materials have been developed that can be easily exfoliated in the monolayer to few-layered sheets. The past few years have witnessed the evolution of many resilient and effective 2D/2D heterointerface photocatalysts showing a 20- to 200-fold increment in the performance for many photocatalytic applications. Still, the efficiency is far from a realistic use due to the presence of the defect state, the requirement of specific plane matching from various permutations for effective charge transport, limited electronic mobility, etc.

The carbon nitride-based 2D/2D heterojunction is giving hope as g-C_3N_4 possesses a suitable band structure and electronic mobility, and 2D electron-rich sheets can interact with almost any semiconductor to form a vdW heterostructure. New 2D materials such as phosphorene, antimonene, tellurene, transition metal oxides, dichalcogenides, LDHs, etc., due to their unique properties, are expanding the choice of the materials to fabricate an optimized vdW heterostructure. Unfortunately, nonchanneled bidirectional charge transport between two 2D sheets results in colossal carrier recombination on the second semiconductors. Tangible advancements to channel the charge transport between 2D sheets was achieved by intercalation of alkali metals (K^+) and noble metals (Ag), which provide an interlayer gallery and, in some cases, better light absorption too.[697] The directionality of charge flow can be controlled by coupling "adjuster" atoms in the system.[702] We observed that, in most of the cases, only a modest fraction of 2D sheets were present in the 2D/2D state, divergent from ideally represented schematics which might be another reason for lower performance than expected. Ideally, 2D/2D heterojunctions should be the more efficient catalyst; unexpectedly, lateral heterojunction triumphed on some occasions due to better charge separation in conductive domains present in high precision.[713,714] Unfortunately, pristine carbon nitride synthesized at high temperature has some inherent drawbacks such as limited blue photon excitation, insolubility in most of the solvents, undisciplined polymerization, lack of long-range crystallinity, low electronic mobility, and uncondensed hydrogen-bonded fragments working as trap centers. Most of the reported 2D/2D vdW heterojunction catalysts utilized conventional carbon nitride and concomitantly inherit the bottlenecks of regular carbon nitride, and the reported yield is still in the micromole regime. Considering the future development of the 2D/2D vdW heterostructure, switching to new carbon nitride-based materials is essential to fully cultivate the benefits of 2D/2D configuration. Molecular engineering by doping (nonmetal, alkali metal, and single atoms), alteration of the coordination pattern (bridging N, C atoms, or azo linkages), insertion of N-rich units such as triazole units, and replacing the basic triazine/heptazine units with new construction units are some fundamental strategies to advancing the intrinsic physicochemical properties of carbon nitrides.[839,840] Several new variants of the C_xN_y family with an entirely different stoichiometric C:N ratio such as C_2N, C_3N, C_3N_2, C_3N_3, C_4N_3, C_3N_5, and C_3N_6 and novel photophysical behavior have been synthesized in recent years to conquer the drawbacks of conventional C_3N_4.[810,813,814,841] Another grueling issue with carbon nitride-based 2D/2D heterojunctions is the indigent surface adsorption of the reactant and poor adsorption−desorption kinetics. Surface engineering of carbon nitride by introducing certain functional groups/units with a high affinity for reactants can solve this problem. C_3N_5 with two six-membered ring triazines and one five-membered ring triazole due to the presence of basic N on the triazole unit can virtually adsorb CO_2, while the presence of a suitable band gap promotes on-site photoreduction.[842] Two closely packed flat 2D sheets with a differential band gap is an ideal arrangement for efficient 2D/2D heterojunction to ensure flawless charge flow from one semiconductor to another. The faulty condensation due to cross-linking and intersheet hydrogen bonding in CN disrupts

https://doi.org/10.1021/acs.chemmater.1c03166
Chem. Mater. 2021, 33, 9012−9092

the periodicity/crystallinity, resulting in a poorly interacted heterojunction. Thus, maintaining crystallinity in carbon nitride will ensure uninterrupted charge migration on the CN surface. Molten salt (LiCl/NaCl/KCl) assisted ionothermal synthesis has proven to be a promising approach for the synthesis of crystalline CN and PTI polymers but needs further improvement due to the associated disadvantage of pressurized reaction conditions, surface contamination, >NH bridging coordination, and undesirable doping.[92,843] Based on current knowledge, we can predict the ideal 2D/2D photocatalyst design constituted of two semiconductors with sufficient oxidative and reductive band edges coupled with intercalated atoms and adjustors for directional charge flow. Additionally, the fabrication of the 2D/2D heterojunction between two lateral heterojunction sheets containing a conductive (graphenic or carbonaceous) zone in a manner that the conductive zone of one sheet is facing the semiconductive part of the other sheets will ensure the efficient charge capture and separation. We believe that the present report will encourage the photocatalytic community to gain a current understanding of the field and excel in the knowledge to develop resilient and sustainable photocatalysts for future applications.

AUTHOR INFORMATION

Corresponding Authors

Pawan Kumar − *Department of Chemical and Petroleum Engineering, University of Calgary, Calgary, Alberta T2N 1N4, Canada;* orcid.org/0000-0003-2804-9298; Email: pawan.kumar@ucalgary.ca

Ajayan Vinu − *School of Engineering, College of Engineering, Science and Environment, The University of Newcastle, Callaghan, New Sourth Wales 2308, Australia;* orcid.org/0000-0002-7508-251X; Email: ajayan.vinu@newcastle.edu.au

Jinguang Hu − *Department of Chemical and Petroleum Engineering, University of Calgary, Calgary, Alberta T2N 1N4, Canada;* orcid.org/0000-0001-8033-7102; Email: jinguang.hu@ucalgary.ca

Md. Golam Kibria − *Department of Chemical and Petroleum Engineering, University of Calgary, Calgary, Alberta T2N 1N4, Canada;* orcid.org/0000-0003-3105-5576; Email: md.kibria@ucalgary.ca

Authors

Devika Laishram − *Department of Chemistry, Indian Institute of Technology Jodhpur, Jodhpur, Rajasthan, India 34201;* Present Address: (D.L.) School of Chemical and Bioprocess Engineering, University College Dublin, Belfield, Dublin 4, Ireland; orcid.org/0000-0001-6953-8309

Rakesh K. Sharma − *Department of Chemistry, Indian Institute of Technology Jodhpur, Jodhpur, Rajasthan, India 34201;* orcid.org/0000-0002-0984-8281

Complete contact information is available at: https://pubs.acs.org/10.1021/acs.chemmater.1c03166

Notes

The authors declare no competing financial interest.

ACKNOWLEDGMENTS

The authors would like to thank the Department of Chemical and Petroleum Engineering in the Schulich School of Engineering and the University of Calgary CFREF fund for financial assistance.

REFERENCES

(1) Rao, N. D.; Pachauri, S. Energy Access and Living Standards: Some Observations on Recent Trends. *Environ. Res. Lett.* **2017**, *12* (2), 025011.

(2) Iyer, G. A Decent Life. *Nat. Energy* **2019**, *4* (12), 1010−1011.

(3) International Energy Agency, IEA. *Key World Energy Statistics 2020*; IEA: Paris, 2020; https://www.iea.org/reports/key-world-energy-statistics-2020 (accessed 2021-10-05).

(4) UC San Diego/Scripps Institution of Oceanograohy, Mauna Loa Observatory, Hawaii. *Scripps CO_2 Program Data*; UC San Diego Library Digital Collections; https://keelingcurve.ucsd.edu/ (accessed 2021-10-05).

(5) Obama, B. The Irreversible Momentum of Clean Energy. *Science* **2017**, *355* (6321), 126−129.

(6) Topf, A. These Countries Have The Highest Energy Usage Per Person, *Insider*, Oct. 1, 2014. https://www.businessinsider.com/countries-with-highest-energy-users-per-person-2014-10 (accessed 2021-10-05).

(7) *Center for Climate and Energy soulutions*. https://www.https://www.c2es.org/content/u-s-emissions/#:~:text=In%202017%2C%20the%20United%20States (accessed 2021-10-05).

(8) Koncagül, E.; Tran, M.; Connor, R. Wastewater the Untapped Resource. *Facts Figures. The United Nations World Water Development Report*; UNESCO: Paris, 2017; p *12*.

(9) *Nature-based Solutions for Water*; 2018 UN World Water Development Report; UNESCO: 2018; ISBN 978-92-3-100264-9.

(10) Gita, S.; Hussan, A.; Choudhury, T. Impact of Textile Dyes Waste on Aquatic Environments and Its Treatment. *Environ. Ecol.* **2017**, *35* (3C), 2349−2353.

(11) Tkaczyk, A.; Mitrowska, K.; Posyniak, A. Synthetic Organic Dyes as Contaminants of the Aquatic Environment and Their Implications for Ecosystems: A Review. *Sci. Total Environ.* **2020**, *717*, 137222.

(12) Perera, A.; Nik, V. M.; Chen, D.; Scartezzini, J.-L.; Hong, T. Quantifying the Impacts of Climate Change and Extreme Climate Events on Energy Systems. *Nat. Energy* **2020**, *5* (2), 150−159.

(13) Reser, J. P.; Bradley, G. L. The Nature, Significance, and Influence of Perceived Personal Experience of Climate Change. *Wiley Interdiscip. Rev. Clim. Change* **2020**, *11* (5), No. e668.

(14) Forster, P. M.; Maycock, A. C.; McKenna, C. M.; Smith, C. Latest Climate Models Confirm Need for Urgent Mitigation. *Nat. Clim. Change* **2020**, *10* (1), 7−10.

(15) Warren, R.; Price, J.; Graham, E.; Forstenhaeusler, N.; Van Der Wal. The Projected Effect on Insects, Vertebrates, and Plants of Limiting Global Warming to 1.5 °C rather than 2 °C. *Science* **2018**, *360* (6390), 791−795.

(16) Armstrong, R. C.; Wolfram, C.; De Jong, K. P.; Gross, R.; Lewis, N. S.; Boardman, B.; Ragauskas, A. J.; Ehrhardt-Martinez, K.; Crabtree, G.; Ramana, M. The Frontiers of Energy. *Nat. Energy* **2016**, *1* (1), 15020 2021−10−29.

(17) Taylor, M. *Energy subsidies: Evolution in the Global Energy Transformation to 2050*; International Renewable Energy Agency: Abu Dhabi, 2020; ISBN 978-92-9260-125-6.

(18) Hayat, M. B.; Ali, D.; Monyake, K. C.; Alagha, L.; Ahmed, N. Solar Energy-A Look into Power Generation, Challenges, and A Solar-Powered Future. *Int. J. Energy Res.* **2019**, *43* (3), 1049−1067.

(19) Creutzig, F.; Agoston, P.; Goldschmidt, J. C.; Luderer, G.; Nemet, G.; Pietzcker, R. C. The Underestimated Potential of Solar energy to Mitigate Climate Change. *Nat. Energy* **2017**, *2* (9), 17140.

(20) Lackner, D.; Höhn, O.; Müller, R.; Beutel, P.; Schygulla, P.; Hauser, H.; Predan, F.; Siefer, G.; Schachtner, M.; Schön, J.; et al. Two-Terminal Direct Wafer-Bonded GaInP/AlGaAs//Si Triple-Junction Solar Cell with AM1. 5g Efficiency of 34.1%. *Solar RRL* **2020**, *4* (9), 2000210.

(21) Wali, Q.; Elumalai, N. K.; Iqbal, Y.; Uddin, A.; Jose, R. Tandem Perovskite Solar Cells. *Renewable Sustainable Energy Rev.* **2018**, *84*, 89−110.
(22) Qi, Y.; Zhang, F. Artificial Photosynthesis near the Biological Limit. *Joule* **2020**, *4* (7), 1364−1366.
(23) Green, M. A. Commercial Progress and Challenges for Photovoltaics. *Nat. Energy* **2016**, *1* (1), 15015.
(24) Kornienko, N.; Zhang, J. Z.; Sakimoto, K. K.; Yang, P.; Reisner, E. Interfacing Nature's Catalytic Machinery with Synthetic Materials for Semi-artificial Photosynthesis. *Nat. Nanotechnol.* **2018**, *13* (10), 890−899.
(25) Kannan, N.; Vakeesan, D. Solar Energy for Future World: A Review. *Renewable Sustainable Energy Rev.* **2016**, *62*, 1092−1105.
(26) Roy, S.; Cherevotan, A.; Peter, S. C. Thermochemical CO_2 Hydrogenation to Single Carbon Products: Scientific and Technological Challenges. *ACS Energy Lett.* **2018**, *3* (8), 1938−1966.
(27) Li, J.; He, Y.; Tan, L.; Zhang, P.; Peng, X.; Oruganti, A.; Yang, G.; Abe, H.; Wang, Y.; Tsubaki, N. Integrated Tuneable Synthesis of Liquid Fuels via Fischer−Tropsch Technology. *Nat. Catal.* **2018**, *1* (10), 787−793.
(28) Ulmer, U.; Dingle, T.; Duchesne, P. N.; Morris, R. H.; Tavasoli, A.; Wood, T.; Ozin, G. A. Fundamentals and Applications of Photocatalytic CO_2 Methanation. *Nat. Commun.* **2019**, *10* (1), 3169.
(29) Cheng, Z.; Baser, D. S.; Shah, V.; Fan, J. A.; Fan, L.-S. Mechanistic Insight into Hydrogen-Assisted Carbon Dioxide Reduction with Ilmenite. *Energy Fuels* **2020**, *34* (12), 15370−15378.
(30) Mazloomi, K.; Gomes, C. Hydrogen as An Energy Carrier: Prospects and Challenges. *Renewable Sustainable Energy Rev.* **2012**, *16* (5), 3024−3033.
(31) Züttel, A.; Remhof, A.; Borgschulte, A.; Friedrichs, O. Hydrogen: The Future Energy Carrier. *Philos. Trans. R. Soc., A* **2010**, *368* (1923), 3329−3342.
(32) Luo, J.; Zhang, S.; Sun, M.; Yang, L.; Luo, S.; Crittenden, J. C. A Critical Review on Energy Conversion and Environmental Remediation of Photocatalysts with Remodeling Crystal Lattice, Surface, and Interface. *ACS Nano* **2019**, *13* (9), 9811−9840.
(33) Xu, C.; Ravi Anusuyadevi, P.; Aymonier, C.; Luque, R.; Marre, S. Nanostructured Materials for Photocatalysis. *Chem. Soc. Rev.* **2019**, *48* (14), 3868−3902.
(34) Kumar, A.; Kumar, A.; Krishnan, V. Perovskite Oxide Based Materials for Energy and Environment-Oriented Photocatalysis. *ACS Catal.* **2020**, *10* (17), 10253−10315.
(35) Hisatomi, T.; Domen, K. Reaction Systems for Solar Hydrogen Production via Water Splitting with Particulate Semiconductor Photocatalysts. *Nat. Catal.* **2019**, *2* (5), 387−399.
(36) Stroyuk, O.; Raevskaya, A.; Gaponik, N. Solar Light Harvesting with Multinary Metal Chalcogenide Nanocrystals. *Chem. Soc. Rev.* **2018**, *47* (14), 5354−5422.
(37) Ganguly, P.; Harb, M.; Cao, Z.; Cavallo, L.; Breen, A.; Dervin, S.; Dionysiou, D. D.; Pillai, S. C. 2D Nanomaterials for Photocatalytic Hydrogen Production. *ACS Energy Lett.* **2019**, *4* (7), 1687−1709.
(38) Ganguly, P.; Byrne, C.; Breen, A.; Pillai, S. C. Antimicrobial Activity of Photocatalysts: Fundamentals, Mechanisms, Kinetics and Recent Advances. *Appl. Catal., B* **2018**, *225*, 51−75.
(39) Ran, J.; Zhang, J.; Yu, J.; Jaroniec, M.; Qiao, S. Z. Earth-Abundant Cocatalysts for Semiconductor-based Photocatalytic Water Splitting. *Chem. Soc. Rev.* **2014**, *43* (22), 7787−7812.
(40) Wang, H.; Zhang, L.; Chen, Z.; Hu, J.; Li, S.; Wang, Z.; Liu, J.; Wang, X. Semiconductor Heterojunction Photocatalysts: Design, Construction, and Photocatalytic Performances. *Chem. Soc. Rev.* **2014**, *43* (15), 5234−5244.
(41) Zeng, S.; Vahidzadeh, E.; VanEssen, C. G.; Kar, P.; Kisslinger, R.; Goswami, A.; Zhang, Y.; Mahdi, N.; Riddell, S.; Kobryn, A. E.; et al. Optical Control of Selectivity of High rate CO_2 Photoreduction via Interband-or Hot Electron Z-Scheme Reaction Pathways in Au-TiO_2 Plasmonic Photonic Crystal Photocatalyst. *Appl. Catal., B* **2020**, *267*, 118644.
(42) Kumar, P.; Kar, P.; Manuel, A. P.; Zeng, S.; Thakur, U. K.; Alam, K. M.; Zhang, Y.; Kisslinger, R.; Cui, K.; Bernard, G. M.; Michaelis, V. K.; Shankar, K. Noble Metal Free, Visible Light Driven Photocatalysis Using TiO_2 Nanotube Arrays Sensitized by P-Doped C_3N_4 Quantum Dots. *Adv. Opt. Mater.* **2020**, *8* (4), 1901275.
(43) Low, J.; Yu, J.; Jaroniec, M.; Wageh, S.; Al-Ghamdi, A. A. Heterojunction Photocatalysts. *Adv. Mater.* **2017**, *29* (20), 1601694.
(44) Alam, K. M.; Kumar, P.; Kar, P.; Thakur, U. K.; Zeng, S.; Cui, K.; Shankar, K. Enhanced Charge Separation in g-C_3N_4-BiOI Heterostructures for Visible Light Driven Photoelectrochemical Water Splitting. *Nanoscale Adv.* **2019**, *1* (4), 1460−1471.
(45) Xu, Q.; Zhang, L.; Cheng, B.; Fan, J.; Yu, J. S-Scheme Heterojunction Photocatalyst. *Chem.* **2020**, *6*, 1543−1559.
(46) Kumar, P.; Joshi, C.; Barras, A.; Sieber, B.; Addad, A.; Boussekey, L.; Szunerits, S.; Boukherroub, R.; Jain, S. L. Core-Shell Structured Reduced Graphene Oxide Wrapped Magnetically Separable rGO@CuZnO@Fe_3O_4 Microspheres as Superior Photocatalyst for CO_2 Reduction under Visible Light. *Appl. Catal., B* **2017**, *205*, 654−665.
(47) Cai, H.; Wang, B.; Xiong, L.; Bi, J.; Yuan, L.; Yang, G.; Yang, S. Orienting the Charge Transfer path of Type-II Heterojunction for Photocatalytic hydrogen evolution. *Appl. Catal., B* **2019**, *256*, 117853.
(48) Wang, Y.; Suzuki, H.; Xie, J.; Tomita, O.; Martin, D. J.; Higashi, M.; Kong, D.; Abe, R.; Tang, J. Mimicking Natural Photosynthesis: Solar to Renewable H_2 Fuel Synthesis by Z-Scheme Water Splitting Systems. *Chem. Rev.* **2018**, *118* (10), 5201−5241.
(49) Low, J.; Jiang, C.; Cheng, B.; Wageh, S.; Al-Ghamdi, A. A.; Yu, J. A Review of Direct Z-Scheme Photocatalysts. *Small Methods* **2017**, *1* (5), 1700080.
(50) Moniz, S. J.; Shevlin, S. A.; Martin, D. J.; Guo, Z.-X.; Tang, J. Visible-Light Driven Heterojunction Photocatalysts for Water Splitting-A Critical Review. *Energy Environ. Sci.* **2015**, *8* (3), 731−759.
(51) Guerrero-Araque, D.; Ramírez-Ortega, D.; Acevedo-Peña, P.; Tzompantzi, F.; Calderón, H. A.; Gómez, R. Interfacial Charge-Transfer Process Across ZrO_2-TiO_2 Heterojunction and Its Impact on Photocatalytic Activity. *J. Photochem. Photobiol., A* **2017**, *335*, 276−286.
(52) Jariwala, D.; Sangwan, V. K.; Lauhon, L. J.; Marks, T. J.; Hersam, M. C. Carbon Nanomaterials for Electronics, Optoelectronics, Photovoltaics, and Sensing. *Chem. Soc. Rev.* **2013**, *42* (7), 2824−2860.
(53) Liu, C.; Huang, K.; Park, W.-T.; Li, M.; Yang, T.; Liu, X.; Liang, L.; Minari, T.; Noh, Y.-Y. A Unified Understanding of Charge Transport in Organic Semiconductors: The Importance of Attenuated Delocalization for the Carriers. *Mater. Horiz.* **2017**, *4* (4), 608−618.
(54) Sangwan, V. K.; Hersam, M. C. Electronic Transport in Two-Dimensional Materials. *Annu. Rev. Phys. Chem.* **2018**, *69*, 299−325.
(55) Li, X.; Yu, J.; Wageh, S.; Al-Ghamdi, A. A.; Xie, J. Graphene in Photocatalysis: A Review. *Small* **2016**, *12* (48), 6640−6696.
(56) Lherbier, A.; Blase, X.; Niquet, Y.-M.; Triozon, F.; Roche, S. Charge Transport in Chemically Doped 2D Graphene. *Phys. Rev. Lett.* **2008**, *101* (3), 036808.
(57) Wang, X.; Li, X.; Zhang, L.; Yoon, Y.; Weber, P. K.; Wang, H.; Guo, J.; Dai, H. N-Doping of Graphene Through Electrothermal Reactions with Ammonia. *Science* **2009**, *324* (5928), 768−771.
(58) Wang, H.; Maiyalagan, T.; Wang, X. Review on Recent Progress in Nitrogen-Doped Graphene: Synthesis, Characterization, and Its Potential Applications. *ACS Catal.* **2012**, *2* (5), 781−794.
(59) Caldwell, J. D.; Aharonovich, I.; Cassabois, G.; Edgar, J. H.; Gil, B.; Basov, D. Photonics with Hexagonal Boron Nitride. *Nat. Rev. Mater.* **2019**, *4* (8), 552−567.
(60) Manzeli, S.; Ovchinnikov, D.; Pasquier, D.; Yazyev, O. V.; Kis, A. 2D Transition Metal Dichalcogenides. *Nat. Rev. Mater.* **2017**, *2* (8), 17033.
(61) Choi, W.; Choudhary, N.; Han, G. H.; Park, J.; Akinwande, D.; Lee, Y. H. Recent Development of Two-Dimensional Transition Metal Dichalcogenides and Their Applications. *Mater. Today* **2017**, *20* (3), 116−130.
(62) Mak, K. F.; Shan, J. Photonics and Optoelectronics of 2D Semiconductor Transition Metal Dichalcogenides. *Nat. Photonics* **2016**, *10* (4), 216−226.

https://doi.org/10.1021/acs.chemmater.1c03166
Chem. Mater. 2021, 33, 9012−9092

(63) Wu, C.; Zhang, J.; Tong, X.; Yu, P.; Xu, J. Y.; Wu, J.; Wang, Z. M.; Lou, J.; Chueh, Y. L. A Critical Review on Enhancement of Photocatalytic Hydrogen Production by Molybdenum Disulfide: From Growth to Interfacial Activities. *Small* **2019**, *15* (35), 1900578.
(64) Wang, Q. H.; Kalantar-Zadeh, K.; Kis, A.; Coleman, J. N.; Strano, M. S. Electronics and Optoelectronics of Two-Dimensional Transition Metal Dichalcogenides. *Nat. Nanotechnol.* **2012**, *7* (11), 699−712.
(65) Ye, M. Y.; Li, S.; Zhao, X.; Tarakina, N. V.; Teutloff, C.; Chow, W. Y.; Bittl, R.; Thomas, A. Cobalt-Exchanged Poly (Heptazine Imides) as Transition Metal-N_x Electrocatalysts for the Oxygen Evolution Reaction. *Adv. Mater.* **2020**, *32* (9), 1903942.
(66) Kessler, F. K.; Zheng, Y.; Schwarz, D.; Merschjann, C.; Schnick, W.; Wang, X.; Bojdys, M. J. Functional Carbon Nitride Materials-Design Strategies for Electrochemical Devices. *Nat. Rev. Mater.* **2017**, *2* (6), 17030.
(67) Ong, W.-J.; Tan, L.-L.; Ng, Y. H.; Yong, S.-T.; Chai, S.-P. Graphitic Carbon Nitride ($g\text{-}C_3N_4$)-based Photocatalysts for Artificial Photosynthesis and Environmental Remediation: Are We a Step Closer to Achieving Sustainability? *Chem. Rev.* **2016**, *116* (12), 7159−7329.
(68) Wang, Y.; Vogel, A.; Sachs, M.; Sprick, R. S.; Wilbraham, L.; Moniz, S. J.; Godin, R.; Zwijnenburg, M. A.; Durrant, J. R.; Cooper, A. I.; et al. Current Understanding and Challenges of Solar-Driven Hydrogen Generation using Polymeric Photocatalysts. *Nat. Energy* **2019**, *4*, 746−760.
(69) Qin, J.; Barrio, J.; Peng, G.; Tzadikov, J.; Abisdris, L.; Volokh, M.; Shalom, M. Direct Growth of Uniform Carbon Nitride Layers with Extended Optical Absorption Towards Efficient Water-Splitting Photoanodes. *Nat. Commun.* **2020**, *11* (1), 4701.
(70) Jiang, L.; Yuan, X.; Pan, Y.; Liang, J.; Zeng, G.; Wu, Z.; Wang, H. Doping of Graphitic Carbon Nitride for Photocatalysis: A Reveiw. *Appl. Catal., B* **2017**, *217*, 388−406.
(71) Zhang, Y.; Mori, T.; Ye, J.; Antonietti, M. Phosphorus-Doped Carbon Nitride Solid: Enhanced Electrical Conductivity and Photocurrent Generation. *J. Am. Chem. Soc.* **2010**, *132* (18), 6294−6295.
(72) Talapaneni, S. N.; Singh, G.; Kim, I. Y.; AlBahily, K.; Al-Muhtaseb, A. a. H.; Karakoti, A. S.; Tavakkoli, E.; Vinu, A. Nanostructured Carbon Nitrides for CO_2 Capture and Conversion. *Adv. Mater.* **2020**, *32* (18), 1904635.
(73) Kumar, P.; Vahidzadeh, E.; Thakur, U. K.; Kar, P.; Alam, K. M.; Goswami, A.; Mahdi, N.; Cui, K.; Bernard, G. M.; Michaelis, V.; Karthik, K.; et al. C_3N_5: A Low Bandgap Semiconductor Containing An Azo-Linked Carbon Nitride Framework for Photocatalytic, Photovoltaic and Adsorbent Applications. *J. Am. Chem. Soc.* **2019**, *141* (13), 5415−5436.
(74) Kumar, A.; Kumar, P.; Joshi, C.; Ponnada, S.; Pathak, A. K.; Ali, A.; Sreedhar, B.; Jain, S. L. A $[Fe(bpy)_3]^{2+}$ Grafted Graphitic Carbon Nitride Hybrid for Visible Light Assisted Oxidative Coupling of Benzylamines Under Mild Reaction Conditions. *Green Chem.* **2016**, *18* (8), 2514−2521.
(75) Kumar, A.; Kumar, P.; Borkar, R.; Bansiwal, A.; Labhsetwar, N.; Jain, S. L. Metal-Organic Hybrid: Photoreduction of CO_2 using Graphitic Carbon Nitride Supported Heteroleptic Iridium Complex under Visible Light Irradiation. *Carbon* **2017**, *123*, 371−379.
(76) Ott, C.; Reiter, F.; Baumgartner, M.; Pielmeier, M.; Vogel, A.; Walke, P.; Burger, S.; Ehrenreich, M.; Kieslich, G.; Daisenberger, D.; Armstrong, J.; Thakur, U. K.; Kumar, P.; Chen, S.; Donadio, D.; Walter, L. S.; Weitz, R. T.; Shankar, K.; Nilges, T. Flexible and Ultrasoft Inorganic 1D Semiconductor and Heterostructure Systems Based on SnIP. *Adv. Funct. Mater.* **2019**, *29* (18), 1900233.
(77) Kumar, P.; Boukherroub, R.; Shankar, K. Sunlight-Driven Water-Splitting using Two-Dimensional Carbon based Semiconductors. *J. Mater. Chem. A* **2018**, *6* (27), 12876−12931.
(78) Lin, L.; Yu, Z.; Wang, X. Crystalline Carbon Nitride Semiconductors for Photocatalytic Water Splitting. *Angew. Chem.* **2019**, *131* (19), 6225−6236.
(79) Kang, Y.; Yang, Y.; Yin, L. C.; Kang, X.; Wang, L.; Liu, G.; Cheng, H. M. Selective Breaking of Hydrogen Bonds of Layered Carbon Nitride for Visible Light Photocatalysis. *Adv. Mater.* **2016**, *28* (30), 6471−6477.
(80) Zhang, J.; Chen, Y.; Wang, X. Two-Dimensional Covalent Carbon Nitride Nanosheets: Synthesis, Functionalization, and Applications. *Energy Environ. Sci.* **2015**, *8* (11), 3092−3108.
(81) Niu, P.; Zhang, L.; Liu, G.; Cheng, H. M. Graphene-Like Carbon Nitride Nanosheets for Improved Photocatalytic Activities. *Adv. Funct. Mater.* **2012**, *22* (22), 4763−4770.
(82) Ma, L.; Fan, H.; Wang, J.; Zhao, Y.; Tian, H.; Dong, G. Water-Assisted Ions In-Situ Intercalation for Porous Polymeric Graphitic Carbon Nitride Nanosheets with Superior Photocatalytic Hydrogen Evolution Performance. *Appl. Catal., B* **2016**, *190*, 93−102.
(83) Zhang, J.; Zhang, M.; Lin, L.; Wang, X. Sol Processing of Conjugated Carbon Nitride Powders for Thin-film Fabrication. *Angew. Chem.* **2015**, *127* (21), 6395−6399.
(84) Gao, X.; Feng, J.; Su, D.; Ma, Y.; Wang, G.; Ma, H.; Zhang, J. In-Situ Exfoliation of Porous Carbon Nitride Nanosheets for Enhanced Hydrogen Evolution. *Nano Energy* **2019**, *59*, 598−609.
(85) Zhang, X.; Xie, X.; Wang, H.; Zhang, J.; Pan, B.; Xie, Y. Enhanced Photoresponsive Ultrathin Graphitic-Phase C_3N_4 Nanosheets for Bioimaging. *J. Am. Chem. Soc.* **2013**, *135* (1), 18−21.
(86) Xu, J.; Zhang, L.; Shi, R.; Zhu, Y. Chemical Exfoliation of Graphitic Carbon Nitride for Efficient Heterogeneous Photocatalysis. *J. Mater. Chem. A* **2013**, *1* (46), 14766−14772.
(87) Li, G.; Li, L.; Yuan, H.; Wang, H.; Zeng, H.; Shi, J. Alkali-Assisted Mild Aqueous Exfoliation for Single-Layered and Structure-Preserved Graphitic Carbon Nitride Nanosheets. *J. Colloid Interface Sci.* **2017**, *495*, 19−26.
(88) Teng, Z.; Lv, H.; Wang, C.; Xue, H.; Pang, H.; Wang, G. Bandgap Engineering of Ultrathin Graphene-like Carbon Nitride Nanosheets with Controllable Oxygenous Functionalization. *Carbon* **2017**, *113*, 63−75.
(89) Lu, X.; Xu, K.; Chen, P.; Jia, K.; Liu, S.; Wu, C. Facile One Step Method Realizing Scalable Production of $g\text{-}C_3N_4$ Nanosheets and Study of Their Photocatalytic H_2 Evolution Activity. *J. Mater. Chem. A* **2014**, *2* (44), 18924−18928.
(90) She, X.; Xu, H.; Xu, Y.; Yan, J.; Xia, J.; Xu, L.; Song, Y.; Jiang, Y.; Zhang, Q.; Li, H. Exfoliated Graphene-like Carbon Nitride in Organic Solvents: Enhanced Photocatalytic Activity and Highly Selective and Sensitive Sensor for the Detection of Trace Amounts of Cu^{2+}. *J. Mater. Chem. A* **2014**, *2* (8), 2563−2570.
(91) Li, Y.; Ouyang, S.; Xu, H.; Hou, W.; Zhao, M.; Chen, H.; Ye, J. Targeted Exfoliation and Reassembly of Polymeric Carbon Nitride for Efficient Photocatalysis. *Adv. Funct. Mater.* **2019**, *29* (27), 1901024.
(92) Ou, H.; Lin, L.; Zheng, Y.; Yang, P.; Fang, Y.; Wang, X. Tri-s-triazine-based Crystalline Carbon Nitride Nanosheets for An Improved Hydrogen Evolution. *Adv. Mater.* **2017**, *29* (22), 1700008.
(93) Ren, W.; Cheng, J.; Ou, H.; Huang, C.; Titirici, M. M.; Wang, X. Enhancing Visible-Light Hydrogen Evolution Performance of Crystalline Carbon Nitride by Defect Engineering. *ChemSusChem* **2019**, *12* (14), 3257−3262.
(94) Wang, Y.; Hou, X.; Zhang, J.; Xu, T.; Liu, S.; Liu, B. Highly Crystalline Carbon Nitride Nanosheets for Ultrahigh Photocatalytic Hydrogen Evolution. *ChemPhotoChem.* **2018**, *2* (6), 490−497.
(95) Zhou, Z.; Zhang, Y.; Shen, Y.; Liu, S.; Zhang, Y. Molecular Engineering of Polymeric Carbon Nitride: Advancing Applications from Photocatalysis to Biosensing and More. *Chem. Soc. Rev.* **2018**, *47* (7), 2298−2321.
(96) Wang, H.; Zhao, R.; Hu, H.; Fan, X.; Zhang, D.; Wang, D. 0D/2D Heterojunctions of Ti_3C_2 MXene QDs/SiC as An Efficient and Robust Photocatalyst for Boosting the Visible Photocatalytic NO Pollutant Removal Ability. *ACS Appl. Mater. Interfaces* **2020**, *12* (36), 40176−40185.
(97) He, Z.; Zhang, J.; Li, X.; Guan, S.; Dai, M.; Wang, S. 1D/2D Heterostructured Photocatalysts: from Design and Unique Properties to Their Environmental Applications. *Small* **2020**, *16* (46), 2005051.
(98) Bie, C.; Cheng, B.; Fan, J.; Ho, W.; Yu, J. Enhanced Solar-to-Chemical Energy Conversion of Graphitic Carbon Nitride by Two-Dimensional Cocatalysts. *EnergyChem.* **2021**, *3* (2), 100051.

(99) Xia, P.; Cao, S.; Zhu, B.; Liu, M.; Shi, M.; Yu, J.; Zhang, Y. Designing a 0D/2D S-Scheme Heterojunction over Polymeric Carbon Nitride for Visible-Light Photocatalytic Inactivation of Bacteria. *Angew. Chem., Int. Ed.* **2020**, *59* (13), 5218−5225.
(100) Hou, H.; Zhang, X. Rational Design of 1D/2D Heterostructured Photocatalyst for Energy and Environmental Applications. *Chem. Eng. J.* **2020**, *395*, 125030.
(101) Wang, J.; Wang, G.; Wang, X.; Wu, Y.; Su, Y.; Tang, H. 3D/2D Direct Z-Scheme Heterojunctions of Hierarchical TiO_2 Microflowers/g-C_3N_4 Nanosheets with Enhanced Charge Carrier Separation for Photocatalytic H_2 Evolution. *Carbon* **2019**, *149*, 618−626.
(102) Novoselov, K. S.; Mishchenko, A.; Carvalho, A.; Castro Neto, A. H. 2D Materials and van der Waals Heterostructures. *Science* **2016**, *353* (6298), No. aac9439.
(103) Jariwala, D.; Marks, T. J.; Hersam, M. C. Mixed-dimensional van der Waals Heterostructures. *Nat. Mater.* **2017**, *16* (2), 170−181.
(104) Wang, X.; Xia, F. Van der Waals Heterostructures: Stacked 2D Materials Shed Light. *Nat. Mater.* **2015**, *14* (3), 264−265.
(105) Liu, Y.; Weiss, N. O.; Duan, X.; Cheng, H. C.; Huang, Y.; Duan, X. Van der Waals Heterostructures and Devices. *Nat. Rev. Mater.* **2016**, *1* (9), 16042.
(106) Chen, J.; He, X.; Sa, B.; Zhou, J.; Xu, C.; Wen, C.; Sun, Z. III-VI van der Waals Heterostructures for Sustainable Energy Related Applications. *Nanoscale* **2019**, *11* (13), 6431−6444.
(107) Rawat, A.; Ahammed, R.; Dimple; Jena, N.; Mohanta, M. K.; De Sarkar, A. Solar Energy Harvesting in Type II van der Waals Heterostructures of Semiconducting Group III Monochalcogenide Monolayers. *J. Phys. Chem. C* **2019**, *123* (20), 12666−12675.
(108) Choudhary, N.; Park, J.; Hwang, J. Y.; Chung, H.-S.; Dumas, K. H.; Khondaker, S. I.; Choi, W.; Jung, Y. Centimeter Scale Patterned Growth of Vertically Stacked Few Layer only 2D MoS_2/WS_2 van der Waals Heterostructure. *Sci. Rep.* **2016**, *6*, 25456.
(109) Cao, S.; Shen, B.; Tong, T.; Fu, J.; Yu, J. 2D/2D Heterojunction of Ultrathin MXene/Bi_2WO_6 Nanosheets for Improved Photocatalytic CO_2 Reduction. *Adv. Funct. Mater.* **2018**, *28* (21), 1800136.
(110) Su, Q.; Li, Y.; Hu, R.; Song, F.; Liu, S.; Guo, C.; Zhu, S.; Liu, W.; Pan, J. Heterojunction Photocatalysts Based on 2D Materials: The Role of Configuration. *Adv. Sust. Systems* **2020**, *4* (9), 2000130.
(111) Ren, K.; Wang, K.; Cheng, Y.; Tang, W.; Zhang, G. Two-Dimensional Heterostructures for Photocatalytic Water Splitting: A Review of Recent Progress. *Nano Futures* **2020**, *4* (3), 032006.
(112) Liu, X.; Zhang, Q.; Ma, D. Advances in 2D/2D Z-Scheme Heterojunctions for Photocatalytic Applications. *Solar RRL* **2021**, *5* (2), 2000397.
(113) Wang, B.-J.; Li, X.-H.; Zhao, R.; Cai, X.-L.; Yu, W.-Y.; Li, W.-B.; Liu, Z.-S.; Zhang, L.-W.; Ke, S.-H. Electronic Structures and Enhanced Photocatalytic Properties of Blue Phosphorene/BSe van der Waals Heterostructures. *J. Mater. Chem. A* **2018**, *6* (19), 8923−8929.
(114) Hou, H.; Zeng, X.; Zhang, X. 2D/2D Heterostructured Photocatalyst: Rational Design for Energy and Environmental Applications. *Sci. China Mater.* **2020**, *63*, 2119−2152.
(115) Yan, Y.; Zhai, D.; Liu, Y.; Gong, J.; Chen, J.; Zan, P.; Zeng, Z.; Li, S.; Huang, W.; Chen, P. van der Waals Heterojunction between A Bottom-up Grown Doped Graphene Quantum Dot and Graphene for Photoelectrochemical Water Splitting. *ACS Nano* **2020**, *14* (1), 1185−1195.
(116) Zhou, X.; Hu, X.; Yu, J.; Liu, S.; Shu, Z.; Zhang, Q.; Li, H.; Ma, Y.; Xu, H.; Zhai, T. 2D Layered Material-based van der Waals Heterostructures for Optoelectronics. *Adv. Funct. Mater.* **2018**, *28* (14), 1706587.
(117) Liang, S. J.; Cheng, B.; Cui, X.; Miao, F. Van der Waals Heterostructures for High-Performance Device Applications: Challenges and Opportunities. *Adv. Mater.* **2019**, *32* (27), 1903800.
(118) He, J.; Wang, C.; Zhou, B.; Zhao, Y.; Tao, L.; Zhang, H. 2D van der Waals Heterostructures: Processing, Optical Properties and Applications in Ultrafast Photonics. *Mater. Horiz.* **2020**, *7* (11), 2903−2921.
(119) Bian, R.; Li, C.; Liu, Q.; Cao, G.; Fu, Q.; Meng, P.; Zhou, J.; Liu, F.; Liu, Z. Recent Progress in the Synthesis of Novel Two-Dimensional van der Waals Materials. *National Sci. Rev.* **2021**, No. nwab164.
(120) Yan, Y.; Zeng, Z.; Huang, M.; Chen, P. Van der Waals Heterojunctions for Catalysis. *Mater. Today Adv.* **2020**, *6*, 100059.
(121) Liu, Y.; Zhou, H.; Cheng, R.; Yu, W.; Huang, Y.; Duan, X. Highly Flexible Electronics from Scalable Vertical Thin Film Transistors. *Nano Lett.* **2014**, *14* (3), 1413−1418.
(122) Chaves, A.; Azadani, J.; Alsalman, H.; da Costa, D. R.; Frisenda, R.; Chaves, A.; Song, S. H.; Kim, Y.; He, D.; Zhou, J.; et al. Bandgap Engineering of Two-Dimensional Semiconductor Materials. *NPJ. 2D Mater. Appl.* **2020**, *4* (1), 29.
(123) Ong, W.-J. 2D/2D Graphitic Carbon Nitride (g-C_3N_4) Heterojunction Nanocomposites for Photocatalysis: Why does Face-to-Face Interface Matter? *Front. Mater.* **2017**, *4*, 11.
(124) Li, C.-I.; Lin, J.-C.; Liu, H.-J.; Chu, M.-W.; Chen, H.-W.; Ma, C.-H.; Tsai, C.-Y.; Huang, H.-W.; Lin, H.-J.; Liu, H.-L.; et al. Van der Waal Epitaxy of Flexible and Transparent VO_2 Film on Muscovite. *Chem. Mater.* **2016**, *28* (11), 3914−3919.
(125) Ellis, J. E.; Sorescu, D. C.; Hwang, S. I.; Burkert, S. C.; White, D. L.; Kim, H.; Star, A. Modification of Carbon Nitride/Reduced Graphene Oxide van der Waals Heterostructure with Copper Nanoparticles To Improve CO_2 Sensitivity. *ACS Appl. Mater. Interfaces* **2019**, *11* (44), 41588−41594.
(126) Zong, X.; Hu, H.; Ouyang, G.; Wang, J.; Shi, R.; Zhang, L.; Zeng, Q.; Zhu, C.; Chen, S.; Cheng, C.; et al. Black Phosphorus-based van der Waals Heterostructures for Mid-Infrared Light-Emission Applications. *Light: Sci. Appl.* **2020**, *9* (1), 114.
(127) Zhu, Y.; Peng, W.; Li, Y.; Zhang, G.; Zhang, F.; Fan, X. Multiple Roles of a Heterointerface in Two-Dimensional van der Waals Heterostructures: Insights into Energy-Related Applications. *J. Mater. Chem. A* **2019**, *7* (41), 23577−23603.
(128) Su, J.; Li, G. D.; Li, X. H.; Chen, J. S. 2D/2D Heterojunctions For Catalysis. *Adv. Sci.* **2019**, *6* (7), 1801702.
(129) Song, B.; Zeng, Z.; Zeng, G.; Gong, J.; Xiao, R.; Ye, S.; Chen, M.; Lai, C.; Xu, P.; Tang, X. Powerful Combination of g-C_3N_4 and LDHs for Enhanced Photocatalytic Performance: A Review of Strategy, Synthesis, and Applications. *Adv. Colloid Interface Sci.* **2019**, *272*, 101999.
(130) Bian, J.; Zhang, Z.; Feng, J.; Thangamuthu, M.; Yang, F.; Sun, L.; Li, Z.; Qu, Y.; Tang, D.; Lin, Z.; et al. Energy Platform for Directed Charge Transfer in the Cascade Z-Scheme Heterojunction: CO_2 Photoreduction without a Cocatalyst. *Angew. Chem., Int. Ed.* **2021**, *60* (38), 20906−20914.
(131) Zhang, M.; Lai, C.; Li, B.; Huang, D.; Zeng, G.; Xu, P.; Qin, L.; Liu, S.; Liu, X.; Yi, H.; et al. Rational Design 2D/2D BiOBr/CDs/g-C_3N_4 Z-Scheme Heterojunction Photocatalyst with Carbon Dots as Solid-state Electron Mediators for Enhanced Visible and NIR Photocatalytic Activity: Kinetics, Intermediates, and Mechanism Insight. *J. Catal.* **2019**, *369*, 469−481.
(132) Ranjan, P.; Lee, J. M.; Kumar, P.; Vinu, A. Borophene: New Sensation in Flatland. *Adv. Mater.* **2020**, *32* (34), 2000531.
(133) Wu, W.; Qiu, G.; Wang, Y.; Wang, R.; Ye, P. Tellurene: Its Physical Properties, Scalable Nanomanufacturing, and Device Applications. *Chem. Soc. Rev.* **2018**, *47* (19), 7203−7212.
(134) Hartman, T.; Sofer, Z. Beyond Graphene: Chemistry of Group 14 Graphene Analogues: Silicene, Germanene, and Stanene. *ACS Nano* **2019**, *13* (8), 8566−8576.
(135) Zheng, Y.; Chen, Y.; Gao, B.; Lin, B.; Wang, X. Phosphorene-based Heterostructured Photocatalysts. *Engineering* **2021**, *7* (7), 991−1001.
(136) Yi, Z.-J.; Wu, M.; Pang, Y.; Jia, R.; Xu, R.-R. Non-Local Dielectric Screening Effects in Phosphorene/g-C_3N_4 Heterojunctions. *Appl. Surf. Sci.* **2021**, *567*, 150842.
(137) Qiu, B.; Wang, C.; Wang, J.; Lin, Z.; Zhang, N.; Cai, L.; Tao, X.; Chai, Y. Metal-free Tellurene Cocatalyst with Tunable Bandgap for Enhanced Photocatalytic Hydrogen Production. *Mater. Today Energy* **2021**, *21*, 100720.

https://doi.org/10.1021/acs.chemmater.1c03166
Chem. Mater. 2021, 33, 9012−9092

(138) Fang, Y.; Fu, X.; Wang, X. Diverse Polymeric Carbon Nitride-based Semiconductors for Photocatalysis and Variations. *ACS Mater. Lett.* **2020**, *2* (8), 975−980.
(139) Wang, G.; Zhang, T.; Yu, W.; Si, R.; Liu, Y.; Zhao, Z. Modulating Location of Single Copper Atoms in Polymeric Carbon Nitride for Enhanced Photoredox Catalysis. *ACS Catal.* **2020**, *10*, 5715−5722.
(140) Gu, Z.; Cui, Z.; Wang, Z.; Qin, K. S.; Asakura, Y.; Hasegawa, T.; Tsukuda, S.; Hongo, K.; Maezono, R.; Yin, S. Carbon Vacancies and Hydroxyls in Graphitic Carbon Nitride: Promoted Photocatalytic NO Removal Activity and Mechanism. *Appl. Catal., B* **2020**, *279*, 119376.
(141) Mo, Z.; Di, J.; Yan, P.; Lv, C.; Zhu, X.; Liu, D.; Song, Y.; Liu, C.; Yu, Q.; Li, H.; et al. An All-Organic D-A System for Visible-Light-Driven Overall Water Splitting. *Small* **2020**, *16* (48), 2003914.
(142) Barrio, J.; Volokh, M.; Shalom, M. Polymeric Carbon Nitrides and Related Metal-free Materials for Energy and Environmental Applications. *J. Mater. Chem. A* **2020**, *8* (22), 11075−11116.
(143) Zhang, L.; Long, R.; Zhang, Y.; Duan, D.; Xiong, Y.; Zhang, Y.; Bi, Y. Direct Observation of Dynamic Bond Evolution in Single-Atom Pt/C_3N_4 Catalysts. *Angew. Chem., Int. Ed.* **2020**, *59* (15), 6224−6229.
(144) Carvalho, A.; Wang, M.; Zhu, X.; Rodin, A. S.; Su, H.; Castro Neto, A. H. Phosphorene: From Theory to Applications. *Nat. Rev. Mater.* **2016**, *1* (11), 16061.
(145) Lange, S.; Schmidt, P.; Nilges, T. Au_3SnP_7@Black Phosphorus: An Easy Access to Black Phosphorus. *Inorg. Chem.* **2007**, *46* (10), 4028−4035.
(146) Nilges, T.; Kersting, M.; Pfeifer, T. A Fast Low-Pressure Transport Route to Large Black Phosphorus Single Crystals. *J. Solid State Chem.* **2008**, *181* (8), 1707−1711.
(147) Yuan, H.; Liu, X.; Afshinmanesh, F.; Li, W.; Xu, G.; Sun, J.; Lian, B.; Curto, A. G.; Ye, G.; Hikita, Y.; et al. Polarization-sensitive Broadband Photodetector using A Black Phosphorus Vertical p-n Junction. *Nat. Nanotechnol.* **2015**, *10* (8), 707−713.
(148) Del Rio Castillo, A. E.; Pellegrini, V.; Sun, H.; Buha, J.; Dinh, D. A.; Lago, E.; Ansaldo, A.; Capasso, A.; Manna, L.; Bonaccorso, F. Exfoliation of Few-layer Black Phosphorus in Low-Boiling-point Solvents and Its Application in Li-ion Batteries. *Chem. Mater.* **2018**, *30* (2), 506−516.
(149) Lin, S.; Chui, Y.; Li, Y.; Lau, S. P. Liquid-phase Exfoliation of Black Phosphorus and Its Applications. *FlatChem.* **2017**, *2*, 15−37.
(150) Zhang, Y.; Wang, H.; Luo, Z.; Tan, H. T.; Li, B.; Sun, S.; Li, Z.; Zong, Y.; Xu, Z. J.; Yang, Y.; et al. An Air-stable Densely Packed Phosphorene-Graphene Composite Toward Advanced Lithium Storage Properties. *Adv. Energy Mater.* **2016**, *6* (12), 1600453.
(151) Vishnoi, P.; Gupta, U.; Pandey, R.; Rao, C. N. Stable Functionalized Phosphorenes with Photocatalytic HER Activity. *J. Mater. Chem. A* **2019**, *7* (12), 6631−6637.
(152) Yasaei, P.; Kumar, B.; Foroozan, T.; Wang, C.; Asadi, M.; Tuschel, D.; Indacochea, J. E.; Klie, R. F.; Salehi-Khojin, A. High-quality Black Phosphorus Atomic Layers by Liquid-phase Exfoliation. *Adv. Mater.* **2015**, *27* (11), 1887−1892.
(153) Kang, J.; Wood, J. D.; Wells, S. A.; Lee, J.-H.; Liu, X.; Chen, K.-S.; Hersam, M. C. Solvent Exfoliation of Electronic-Grade, Two-Dimensional Black Phosphorus. *ACS Nano* **2015**, *9* (4), 3596−3604.
(154) Hanlon, D.; Backes, C.; Doherty, E.; Cucinotta, C. S.; Berner, N. C.; Boland, C.; Lee, K.; Harvey, A.; Lynch, P.; Gholamvand, Z.; et al. Liquid Exfoliation of Solvent-Stabilized Few-Layer Black Phosphorus for Applications Beyond Electronics. *Nat. Commun.* **2015**, *6* (1), 8563.
(155) Batmunkh, M.; Bat-Erdene, M.; Shapter, J. G. Phosphorene and Phosphorene-Based Materials-Prospects for Future Applications. *Adv. Mater.* **2016**, *28* (39), 8586−8617.
(156) Tran, V.; Soklaski, R.; Liang, Y.; Yang, L. Layer-Controlled Band gap and Anisotropic Excitons in Few-layer Black Phosphorus. *Phys. Rev. B: Condens. Matter Mater. Phys.* **2014**, *89* (23), 235319.
(157) Liu, H.; Neal, A. T.; Zhu, Z.; Luo, Z.; Xu, X.; Tománek, D.; Ye, P. D. Phosphorene: An Unexplored 2D Semiconductor with A High Hole Mobility. *ACS Nano* **2014**, *8* (4), 4033−4041.
(158) Shen, Z.; Sun, S.; Wang, W.; Liu, J.; Liu, Z.; Yu, J. C. A Black-Red Phosphorus Heterostructure for Efficient Visible-Light-Driven Photocatalysis. *J. Mater. Chem. A* **2015**, *3* (7), 3285−3288.
(159) Lei, W.; Zhang, T.; Liu, P.; Rodriguez, J. A.; Liu, G.; Liu, M. Bandgap-and Local Field-Dependent Photoactivity of Ag/Black Phosphorus Nanohybrids. *ACS Catal.* **2016**, *6* (12), 8009−8020.
(160) Li, B.; Lai, C.; Zeng, G.; Huang, D.; Qin, L.; Zhang, M.; Cheng, M.; Liu, X.; Yi, H.; Zhou, C.; et al. Black Phosphorus, a Rising Star 2D Nanomaterial in the Post-Graphene Era: Synthesis, Properties, Modifications, and Photocatalysis Applications. *Small* **2019**, *15* (8), 1804565.
(161) Wang, H.; Zhang, X.; Xie, Y. Photocatalysis in Two-dimensional Black Phosphorus: The Roles of Many-body Effects. *ACS Nano* **2018**, *12* (10), 9648−9653.
(162) Shen, Z.-K.; Yuan, Y.-J.; Pei, L.; Yu, Z.-T.; Zou, Z. Black Phosphorus Photocatalysts for Photocatalytic H_2 Generation: A Review. *Chem. Eng. J.* **2020**, *386*, 123997.
(163) Bian, S.; Wen, M.; Wang, J.; Yang, N.; Chu, P. K.; Yu, X.-F. Edge-Rich Black Phosphorus for Photocatalytic Nitrogen Fixation. *J. Phys. Chem. Lett.* **2020**, *11* (3), 1052−1058.
(164) Rahman, M. Z.; Kwong, C. W.; Davey, K.; Qiao, S. Z. 2D Phosphorene as A Water Splitting Photocatalyst: Fundamentals to Applications. *Energy Environ. Sci.* **2016**, *9* (3), 709−728.
(165) Sa, B.; Li, Y.-L.; Qi, J.; Ahuja, R.; Sun, Z. Strain Engineering for Phosphorene: The Potential Application as A Photocatalyst. *J. Phys. Chem. C* **2014**, *118* (46), 26560−26568.
(166) Hu, W.; Lin, L.; Zhang, R.; Yang, C.; Yang, J. Highly Efficient Photocatalytic Water Splitting over Edge-modified Phosphorene Nanoribbons. *J. Am. Chem. Soc.* **2017**, *139* (43), 15429−15436.
(167) Feng, R.; Lei, W.; Liu, G.; Liu, M. Visible-and NIR-Light Responsive Black-Phosphorus-Based Nanostructures in Solar Fuel Production and Environmental Remediation. *Adv. Mater.* **2018**, *30* (49), 1804770.
(168) Üzer, E.; Kumar, P.; Kisslinger, R.; Kar, P.; Thakur, U. K.; Zeng, S.; Shankar, K.; Nilges, T. Vapor Deposition of Semiconducting Phosphorus Allotropes into TiO_2 Nanotube Arrays for Photoelectrocatalytic Water Splitting. *ACS Appl. Nano Mater.* **2019**, *2* (6), 3358−3367.
(169) Boppella, R.; Yang, W.; Tan, J.; Kwon, H.-C.; Park, J.; Moon, J. Black Phosphorus Supported Ni_2P Co-catalyst on Graphitic Carbon Nitride Enabling Simultaneous Boosting Charge Separation and Surface Reaction. *Appl. Catal., B* **2019**, *242*, 422−430.
(170) Lei, W.; Mi, Y.; Feng, R.; Liu, P.; Hu, S.; Yu, J.; Liu, X.; Rodriguez, J. A.; Wang, J.-o.; Zheng, L.; et al. Hybrid 0D-2D Black Phosphorus Quantum Dots-Graphitic Carbon Nitride Nanosheets for Efficient Hydrogen Evolution. *Nano Energy* **2018**, *50*, 552−561.
(171) Kong, Z.; Chen, X.; Ong, W.-J.; Zhao, X.; Li, N. Atomic-level Insight into the Mechanism of 0D/2D Black Phosphorus Quantum Dot/Graphitic Carbon Nitride (BPQD/GCN) Metal-free Heterojunction for Photocatalysis. *Appl. Surf. Sci.* **2019**, *463*, 1148−1153.
(172) Wang, W.; Niu, Q.; Zeng, G.; Zhang, C.; Huang, D.; Shao, B.; Zhou, C.; Yang, Y.; Liu, Y.; Guo, H.; et al. 1D Porous Tubular g-C_3N_4 Capture Black Phosphorus Quantum Dots as 1D/0D Metal-free Photocatalysts for Oxytetracycline Hydrochloride Degradation and Hexavalent Chromium Reduction. *Appl. Catal., B* **2020**, *273*, 119051.
(173) Kong, L.; Ji, Y.; Dang, Z.; Yan, J.; Li, P.; Li, Y.; Liu, S. g-C_3N_4 Loading Black Phosphorus Quantum Dot for Efficient and Stable Photocatalytic H_2 Generation under Visible Light. *Adv. Funct. Mater.* **2018**, *28* (22), 1800668.
(174) Zhang, Q.; Yang, F.; Zhou, S.; Bao, N.; Xu, Z.; Chaker, M.; Ma, D. Broadband Photocatalysts Enabled by 0D/2D Heterojunctions of Near-Infrared Quantum Dots/Graphitic Carbon Nitride Nanosheets. *Appl. Catal., B* **2020**, *270*, 118879.
(175) Zhang, X.; Xie, H.; Liu, Z.; Tan, C.; Luo, Z.; Li, H.; Lin, J.; Sun, L.; Chen, W.; Xu, Z.; et al. Black Phosphorus Quantum Dots. *Angew. Chem., Int. Ed.* **2015**, *54* (12), 3653−3657.

(176) Gui, R.; Jin, H.; Wang, Z.; Li, J. Black Phosphorus Quantum Dots: Synthesis, Properties, Functionalized Modification and Applications. *Chem. Soc. Rev.* **2018**, *47* (17), 6795−6823.
(177) Zheng, Y.; Yu, Z.; Ou, H.; Asiri, A. M.; Chen, Y.; Wang, X. Black Phosphorus and Polymeric Carbon Nitride Heterostructure for Photoinduced Molecular Oxygen Activation. *Adv. Funct. Mater.* **2018**, *28* (10), 1705407.
(178) Zhu, M.; Kim, S.; Mao, L.; Fujitsuka, M.; Zhang, J.; Wang, X.; Majima, T. Metal-free Photocatalyst for H_2 Evolution in Visible to Near-Infrared Region: Black Phosphorus/Graphitic Carbon Nitride. *J. Am. Chem. Soc.* **2017**, *139* (37), 13234−13242.
(179) Wen, M.; Wang, J.; Tong, R.; Liu, D.; Huang, H.; Yu, Y.; Zhou, Z. K.; Chu, P. K.; Yu, X. F. A Low-cost Metal-free Photocatalyst based on Black Phosphorus. *Adv. Sci.* **2019**, *6* (1), 1801321.
(180) Ran, J.; Guo, W.; Wang, H.; Zhu, B.; Yu, J.; Qiao, S. Z. Metal-free 2D/2D Phosphorene/g-C_3N_4 Van der Waals Heterojunction for Highly Enhanced Visible-light Photocatalytic H_2 Production. *Adv. Mater.* **2018**, *30* (25), 1800128.
(181) He, D.; Zhang, Z.; Xing, Y.; Zhou, Y.; Yang, H.; Liu, H.; Qu, J.; Yuan, X.; Guan, J.; Zhang, Y.-n. Black Phosphorus/Graphitic Carbon Nitride: A Metal-free Photocatalyst for "Green" Photocatalytic Bacterial Inactivation under Visible Light. *Chem. Eng. J.* **2020**, *384*, 123258.
(182) Zhang, Q.; Huang, S.; Deng, J.; Gangadharan, D. T.; Yang, F.; Xu, Z.; Giorgi, G.; Palummo, M.; Chaker, M.; Ma, D. Ice-Assisted Synthesis of Black Phosphorus Nanosheets as a Metal-Free Photocatalyst: 2D/2D Heterostructure for Broadband H_2 Evolution. *Adv. Funct. Mater.* **2019**, *29* (28), 1902486.
(183) Zhu, Y.; Ren, J.; Zhang, X.; Yang, D. Elemental Red Phosphorus-Based Materials for Photocatalytic Water Purification and Hydrogen Production. *Nanoscale* **2020**, *12*, 13297−13310.
(184) Hu, Z.; Shen, Z.; Yu, J. C. Phosphorus Containing Materials for Photocatalytic Hydrogen Evolution. *Green Chem.* **2017**, *19* (3), 588−613.
(185) Liu, Y.; Li, J.; Hu, Z.; Yu, J. C. Photocatalytic Property of Phosphorus. In *Fundamentals and Applications of Phosphorus Nanomaterials*; American Chemical Society: 2019; pp 155−177.
(186) Wang, F.; Ng, W. K. H.; Yu, J. C.; Zhu, H.; Li, C.; Zhang, L.; Liu, Z.; Li, Q. Red Phosphorus: An Elemental Photocatalyst for Hydrogen Formation from Water. *Appl. Catal., B* **2012**, *111*, 409−414.
(187) Ren, X.; Philo, D.; Li, Y.; Shi, L.; Chang, K.; Ye, J. Recent Advances of Low-dimensional Phosphorus-based Nanomaterials for Solar-driven Photocatalytic Reactions. *Coord. Chem. Rev.* **2020**, *424*, 213516.
(188) Hu, Z.; Yuan, L.; Liu, Z.; Shen, Z.; Yu, J. C. An Elemental Phosphorus Photocatalyst with A Record High Hydrogen Evolution Efficiency. *Angew. Chem.* **2016**, *128* (33), 9732−9737.
(189) Zhang, Z.; Xing, D.-H.; Li, J.; Yan, Q. Hittorf's Phosphorus: The Missing Link during Transformation of Red Phosphorus to Black Phosphorus. *CrystEngComm* **2017**, *19* (6), 905−909.
(190) Bachhuber, F.; von Appen, J.; Dronskowski, R.; Schmidt, P.; Nilges, T.; Pfitzner, A.; Weihrich, R. The Extended Stability Range of Phosphorus Allotropes. *Angew. Chem., Int. Ed.* **2014**, *53* (43), 11629−11633.
(191) Ruck, M.; Hoppe, D.; Wahl, B.; Simon, P.; Wang, Y.; Seifert, G. Fibrous Red Phosphorus. *Angew. Chem., Int. Ed.* **2005**, *44* (46), 7616−7619.
(192) Sansone, G.; Maschio, L.; Usvyat, D.; Schütz, M.; Karttunen, A. Toward An Accurate Estimate of the Exfoliation Energy of Black Phosphorus: A Periodic Quantum Chemical Approach. *J. Phys. Chem. Lett.* **2016**, *7* (1), 131−136.
(193) Schusteritsch, G.; Uhrin, M.; Pickard, C. J. Single-Layered Hittorf's Phosphorus: A Wide-Bandgap High Mobility 2D Material. *Nano Lett.* **2016**, *16* (5), 2975−2980.
(194) Qiao, J.; Kong, X.; Hu, Z.-X.; Yang, F.; Ji, W. High-Mobility Transport Anisotropy and Linear Dichroism in Few-Layer Black Phosphorus. *Nat. Commun.* **2014**, *5* (1), 4475.
(195) Chan, D. K.L.; Yu, J. C.; Li, Y.; Hu, Z. A Metal-free Composite Photocatalyst of Graphene Quantum Dots Deposited on Red Phosphorus. *J. Environ. Sci.* **2017**, *60*, 91−97.
(196) Lei, X.; Wang, J.; Shi, Y.; Yao, W.; Wu, Q.; Wu, Q.; Zou, R. Constructing Novel Red Phosphorus Decorated Iron-based Metal Organic Framework Composite with Efficient Photocatalytic Performance. *Appl. Surf. Sci.* **2020**, *528*, 146963.
(197) Chen, J.; Huang, S.; Long, Y.; Wu, J.; Li, H.; Li, Z.; Zeng, Y.-J.; Ruan, S. Fabrication of ZnO/Red Phosphorus Heterostructure for Effective Photocatalytic H_2 Evolution from Water Splitting. *Nanomaterials* **2018**, *8* (10), 835.
(198) Ansari, S. A.; Khan, Z.; Ansari, M. O.; Cho, M. H. Earth-Abundant Stable Elemental Semiconductor Red Phosphorus-based Hybrids for Environmental Remediation and Energy Storage Applications. *RSC Adv.* **2016**, *6* (50), 44616−44629.
(199) Ansari, S. A.; Cho, M. H. Highly Visible Light Responsive, Narrow Band Gap TiO_2 Nanoparticles Modified by Elemental Red Phosphorus for Photocatalysis and Photoelectrochemical Applications. *Sci. Rep.* **2016**, *6* (1), 25405.
(200) Üzer, E.; Kumar, P.; Kisslinger, R.; Kar, P.; Thakur, U. K.; Shankar, K.; Nilges, T. Vapor Growth of Binary and Ternary Phosphorus-based Semiconductors into TiO_2 Nanotube Arrays and Application in Visible Light Driven Water Splitting. *Nanoscale Adv.* **2019**, *1* (8), 2881−2890.
(201) Zhang, Q.; Liu, X.; Tan, L.; Cui, Z.; Li, Z.; Liang, Y.; Zhu, S.; Yeung, K.; Zheng, Y.; Wu, S. An UV to NIR-driven Platform based on Red Phosphorus/Graphene Oxide Film for Rapid Microbial Inactivation. *Chem. Eng. J.* **2020**, *383*, 123088.
(202) Xu, M.; Jiang, L.; Wang, J.; Feng, S.; Tremblay, P.-L.; Zhang, T. Efficient Photocatalytic Hydrogen Evolution with High-Crystallinity and Noble Metal-Free Red Phosphorus-CdS Nanorods. *Int. J. Hydrogen Energy* **2020**, *45*, 17354−17366.
(203) Li, J.; Liu, X.; Tan, L.; Liang, Y.; Cui, Z.; Yang, X.; Zhu, S.; Li, Z.; Zheng, Y.; Yeung, K. W. K.; et al. Light-Activated Rapid Disinfection by Accelerated Charge Transfer in Red Phosphorus/ZnO Heterointerface. *Small Methods* **2019**, *3* (3), 1900048.
(204) Zhu, Y.; Li, J.; Dong, C.-L.; Ren, J.; Huang, Y.-C.; Zhao, D.; Cai, R.; Wei, D.; Yang, X.; Lv, C.; et al. Red Phosphorus Decorated and Doped TiO_2 Nanofibers for Efficient Photocatalytic Hydrogen Evolution from Pure Water. *Appl. Catal., B* **2019**, *255*, 117764.
(205) Shi, R.; Liu, F.; Wang, Z.; Weng, Y.; Chen, Y. Black/Red Phosphorus Quantum Dots for Photocatalytic Water Splitting: From a Type I Heterostructure to a Z-Scheme System. *Chem. Commun.* **2019**, *55* (83), 12531−12534.
(206) Liu, F.; Shi, R.; Wang, Z.; Weng, Y.; Che, C. M.; Chen, Y. Direct Z-Scheme Hetero-phase Junction of Black/Red Phosphorus for Photocatalytic Water Splitting. *Angew. Chem.* **2019**, *131* (34), 11917−11921.
(207) Muhmood, T.; Xia, M.; Lei, W.; Wang, F. Under Vacuum Synthesis of Type-I Heterojunction between Red Phosphorus and Graphene like Carbon Nitride with Enhanced Catalytic, Electrochemical and Charge Separation Ability for Photodegradation of An Acute Toxicity Category-III Compound. *Appl. Catal., B* **2018**, *238*, 568−575.
(208) Eken Korkut, S.; Küçükkeçeci, H. s.; Metin, O. n. Mesoporous Graphitic Carbon Nitride/Black Phosphorus/AgPd Alloy Nanoparticles Ternary Nanocomposite: A Highly Efficient Catalyst for the Methanolysis of Ammonia Borane. *ACS Appl. Mater. Interfaces* **2020**, *12* (7), 8130−8139.
(209) Zhao, H.; Sun, S.; Wu, Y.; Jiang, P.; Dong, Y.; Xu, Z. J. Ternary Graphitic Carbon Nitride/Red Phosphorus/Molybdenum Disulfide Heterostructure: An Efficient and Low Cost Photocatalyst for Visible-Light-Driven H_2 Evolution from Water. *Carbon* **2017**, *119*, 56−61.
(210) Jing, L.; Zhu, R.; Phillips, D. L.; Yu, J. C. Effective Prevention of Charge Trapping in Graphitic Carbon Nitride with Nanosized Red Phosphorus Modification for Superior Photo (Electro) Catalysis. *Adv. Funct. Mater.* **2017**, *27* (46), 1703484.

(211) Zhu, Y.; Lv, C.; Yin, Z.; Ren, J.; Yang, X.; Dong, C. L.; Liu, H.; Cai, R.; Huang, Y. C.; Theis, W.; et al. A [001]-Oriented Hittorf's Phosphorus Nanorods/Polymeric Carbon Nitride Heterostructure for Boosting Wide-Spectrum-Responsive Photocatalytic Hydrogen Evolution from Pure Water. *Angew. Chem.* **2020**, *132* (2), 878−883.
(212) Wang, M.; Qin, Z.; Diao, Z.; Li, R.; Zhong, J.; Ma, D.; Chen, Y. Red Phosphorus/Carbon Nitride van der Waals Heterostructure for Photocatalytic Pure Water Splitting under Wide-Spectrum Light Irradiation. *ACS Sustainable Chem. Eng.* **2020**, *8* (35), 13459−13466.
(213) Ares, P.; Palacios, J. J.; Abellán, G.; Gómez-Herrero, J.; Zamora, F. Recent Progress on Antimonene: A New Bidimensional Material. *Adv. Mater.* **2018**, *30* (2), 1703771.
(214) Wang, X.; Song, J.; Qu, J. Antimonene: From Experimental Preparation to Practical Application. *Angew. Chem., Int. Ed.* **2019**, *58* (6), 1574−1584.
(215) Zhang, S.; Yan, Z.; Li, Y.; Chen, Z.; Zeng, H. Atomically Thin Arsenene and Antimonene: Semimetal-Semiconductor and Indirect-Direct Band-Gap Transitions. *Angew. Chem.* **2015**, *127* (10), 3155−3158.
(216) Gibaja, C.; Rodriguez-San-Miguel, D.; Ares, P.; Gómez-Herrero, J.; Varela, M.; Gillen, R.; Maultzsch, J.; Hauke, F.; Hirsch, A.; Abellán, G.; et al. Few-layer Antimonene by Liquid-phase Exfoliation. *Angew. Chem.* **2016**, *128* (46), 14557−14561.
(217) Ares, P.; Aguilar-Galindo, F.; Rodríguez-San-Miguel, D.; Aldave, D. A.; Díaz-Tendero, S.; Alcamí, M.; Martín, F.; Gómez-Herrero, J.; Zamora, F. Mechanical Isolation of Highly Stable Antimonene under Ambient Conditions. *Adv. Mater.* **2016**, *28* (30), 6332−6336.
(218) Gu, J.; Du, Z.; Zhang, C.; Ma, J.; Li, B.; Yang, S. Liquid-Phase Exfoliated Metallic Antimony Nanosheets toward High Volumetric Sodium Storage. *Adv. Energy Mater.* **2017**, *7* (17), 1700447.
(219) Ji, J.; Song, X.; Liu, J.; Yan, Z.; Huo, C.; Zhang, S.; Su, M.; Liao, L.; Wang, W.; Ni, Z.; et al. Two-Dimensional Antimonene Single Crystals Grown by van der Waals Epitaxy. *Nat. Commun.* **2016**, *7* (1), 13352.
(220) Tao, W.; Ji, X.; Xu, X.; Islam, M. A.; Li, Z.; Chen, S.; Saw, P. E.; Zhang, H.; Bharwani, Z.; Guo, Z.; et al. Antimonene Quantum Dots: Synthesis and Application as Near-Infrared Photothermal Agents for Effective Cancer Therapy. *Angew. Chem.* **2017**, *129* (39), 12058−12062.
(221) Lu, L.; Tang, X.; Cao, R.; Wu, L.; Li, Z.; Jing, G.; Dong, B.; Lu, S.; Li, Y.; Xiang, Y.; et al. Broadband Nonlinear Optical Response in Few-layer Antimonene and Antimonene Quantum Dots: A Promising Optical kerr Media with Enhanced Stability. *Adv. Opt. Mater.* **2017**, *5* (17), 1700301.
(222) Lei, T.; Liu, C.; Zhao, J.-L.; Li, J.-M.; Li, Y.-P.; Wang, J.-O.; Wu, R.; Qian, H.-J.; Wang, H.-Q.; Ibrahim, K. Electronic Structure of Antimonene Grown on Sb_2Te_3 (111) and Bi_2Te_3 Substrates. *J. Appl. Phys.* **2016**, *119* (1), 015302.
(223) Zhang, S.; Zhou, W.; Ma, Y.; Ji, J.; Cai, B.; Yang, S. A.; Zhu, Z.; Chen, Z.; Zeng, H. Antimonene Oxides: Emerging Tunable Direct Bandgap Semiconductor and Novel Topological Insulator. *Nano Lett.* **2017**, *17* (6), 3434−3440.
(224) Xie, M.; Zhang, S.; Cai, B.; Gu, Y.; Liu, X.; Kan, E.; Zeng, H. Van der Waals Bilayer Antimonene: A Promising Thermophotovoltaic Cell Material with 31% Energy Conversion Efficiency. *Nano Energy* **2017**, *38*, 561−568.
(225) Wang, X.; He, J.; Zhou, B.; Zhang, Y.; Wu, J.; Hu, R.; Liu, L.; Song, J.; Qu, J. Bandgap-Tunable Preparation of Smooth and Large Two-Dimensional Antimonene. *Angew. Chem.* **2018**, *130* (28), 8804−8809.
(226) Li, F.; Xue, M.; Li, J.; Ma, X.; Chen, L.; Zhang, X.; MacFarlane, D. R.; Zhang, J. Unlocking the Electrocatalytic Activity of Antimony for CO_2 Reduction by Two-dimensional Engineering of the Bulk Material. *Angew. Chem.* **2017**, *129* (46), 14910−14914.
(227) Ren, X.; Li, Z.; Qiao, H.; Liang, W.; Liu, H.; Zhang, F.; Qi, X.; Liu, Y.; Huang, Z.; Zhang, D.; et al. Few-layer Antimonene Nanosheet: A Metal-free Bifunctional Electrocatalyst for Effective Water Splitting. *ACS Appl. Energy Mater.* **2019**, *2* (7), 4774−4781.
(228) Ji, X.; Kang, Y.; Fan, T.; Xiong, Q.; Zhang, S.; Tao, W.; Zhang, H. An Antimonene/Cp* Rh (phen) Cl/Black Phosphorus Hybrid Nanosheet-based Z-Scheme Artificial Photosynthesis for Enhanced Photo/bio-catalytic CO_2 Reduction. *J. Mater. Chem. A* **2020**, *8*, 323−333.
(229) Barrio, J.; Gibaja, C.; Tzadikov, J.; Shalom, M.; Zamora, F. 2D/2D Graphitic Carbon Nitride/Antimonene Heterostructure: Structural Characterization and Application in Photocatalysis. *Adv. Sust. Sys.* **2019**, *3* (2), 1800138.
(230) Naguib, M.; Kurtoglu, M.; Presser, V.; Lu, J.; Niu, J.; Heon, M.; Hultman, L.; Gogotsi, Y.; Barsoum, M. W. Two-dimensional Nanocrystals Produced by Exfoliation of Ti_3AlC_2. *Adv. Mater.* **2011**, *23* (37), 4248−4253.
(231) Chen, C.; Xie, X.; Anasori, B.; Sarycheva, A.; Makaryan, T.; Zhao, M.; Urbankowski, P.; Miao, L.; Jiang, J.; Gogotsi, Y. MoS_2-on-MXene Heterostructures as Highly Reversible Anode Materials for Lithium-ion Batteries. *Angew. Chem., Int. Ed.* **2018**, *57* (7), 1846−1850.
(232) Xia, Y.; Mathis, T. S.; Zhao, M.-Q.; Anasori, B.; Dang, A.; Zhou, Z.; Cho, H.; Gogotsi, Y.; Yang, S. Thickness-Independent Capacitance of Vertically Aligned Liquid-crystalline MXenes. *Nature* **2018**, *557* (7705), 409−412.
(233) Yuan, W.; Cheng, L.; An, Y.; Wu, H.; Yao, N.; Fan, X.; Guo, X. MXene Nanofibers as Highly Active Catalysts for Hydrogen Evolution Reaction. *ACS Sustainable Chem. Eng.* **2018**, *6* (7), 8976−8982.
(234) Huang, K.; Li, Z.; Lin, J.; Han, G.; Huang, P. Two-Dimensional Transition Metal Carbides and Nitrides (MXenes) for Biomedical Applications. *Chem. Soc. Rev.* **2018**, *47* (14), 5109−5124.
(235) Su, T.; Hood, Z. D.; Naguib, M.; Bai, L.; Luo, S.; Rouleau, C. M.; Ivanov, I. N.; Ji, H.; Qin, Z.; Wu, Z. 2D/2D Heterojunction of Ti_3C_2/g-C_3N_4 Nanosheets for Enhanced Photocatalytic Hydrogen Evolution. *Nanoscale* **2019**, *11* (17), 8138−8149.
(236) Zhao, T.; Zhang, S.; Guo, Y.; Wang, Q. TiC_2: A New Two-dimensional Sheet Beyond MXenes. *Nanoscale* **2016**, *8* (1), 233−242.
(237) Mashtalir, O.; Cook, K. M.; Mochalin, V. N.; Crowe, M.; Barsoum, M. W.; Gogotsi, Y. Dye Adsorption and Decomposition on Two-dimensional Titanium Carbide in Aqueous Media. *J. Mater. Chem. A* **2014**, *2* (35), 14334−14338.
(238) Hong, L.-f.; Guo, R.-t.; Yuan, Y.; Ji, X.-y.; Li, Z.-s.; Lin, Z.-d.; Pan, W.-g. Recent Progress of Two-Dimensional MXenes in Photocatalytic Applications: A Review. *Mater. Today Energy* **2020**, *18*, 100521.
(239) Xie, X.; Zhang, N. Positioning MXenes in the Photocatalysis Landscape: Competitiveness, Challenges, and Future Perspectives. *Adv. Funct. Mater.* **2020**, *30* (36), 2002528.
(240) Sun, Y.; Meng, X.; Dall'Agnese, Y.; Dall'Agnese, C.; Duan, S.; Gao, Y.; Chen, G.; Wang, X.-F. 2D MXenes as Co-catalysts in Photocatalysis: Synthetic Methods. *Nano-Micro Lett.* **2019**, *11* (1), 79.
(241) Zhao, Y.; Que, M.; Chen, J.; Yang, C. MXenes as Co-catalysts for the Solar-driven Photocatalytic Reduction of CO_2. *J. Mater. Chem. C* **2020**, *8*, 16258−16281.
(242) Prasad, C.; Yang, X.; Liu, Q.; Tang, H.; Rammohan, A.; Zulfiqar, S.; Zyryanov, G. V.; Shah, S. Recent Advances in MXenes Supported Semiconductors based Photocatalysts: Properties, Synthesis and Photocatalytic Applications. *J. Ind. Eng. Chem.* **2020**, *85*, 1−33.
(243) Cheng, L.; Li, X.; Zhang, H.; Xiang, Q. Two-dimensional Transition Metal MXene-based Photocatalysts for Solar Fuel Generation. *J. Phys. Chem. Lett.* **2019**, *10* (12), 3488−3494.
(244) Li, J.-Y.; Li, Y.-H.; Zhang, F.; Tang, Z.-R.; Xu, Y.-J. Visible-Light-Driven Integrated Organic Synthesis and Hydrogen Evolution over 1D/2D CdS-$Ti_3C_2T_x$ MXene Composites. *Appl. Catal., B* **2020**, *269*, 118783.
(245) Halim, J.; Kota, S.; Lukatskaya, M. R.; Naguib, M.; Zhao, M. Q.; Moon, E. J.; Pitock, J.; Nanda, J.; May, S. J.; Gogotsi, Y.; et al. Synthesis and Characterization of 2D Molybdenum Carbide (MXene). *Adv. Funct. Mater.* **2016**, *26* (18), 3118−3127.

https://doi.org/10.1021/acs.chemmater.1c03166
Chem. Mater. 2021, 33, 9012−9092

(246) Zhou, J.; Zha, X.; Chen, F. Y.; Ye, Q.; Eklund, P.; Du, S.; Huang, Q. A Two-dimensional Zirconium Carbide by Selective Etching of Al_3C_3 from Nanolaminated $Zr_3Al_3C_5$. *Angew. Chem., Int. Ed.* **2016**, *55* (16), 5008−5013.
(247) Zhou, J.; Zha, X.; Zhou, X.; Chen, F.; Gao, G.; Wang, S.; Shen, C.; Chen, T.; Zhi, C.; Eklund, P.; et al. Synthesis and Electrochemical Properties of Two-dimensional Hafnium Carbide. *ACS Nano* **2017**, *11* (4), 3841−3850.
(248) Wong, Z. M.; Tan, T. L.; Yang, S.-W.; Xu, G. Q. Enhancing the Photocatalytic Performance of MXenes via Stoichiometry Engineering of Their Electronic and Optical Properties. *ACS Appl. Mater. Interfaces* **2018**, *10* (46), 39879−39889.
(249) Hart, J. L.; Hantanasirisakul, K.; Lang, A. C.; Anasori, B.; Pinto, D.; Pivak, Y.; van Omme, J. T.; May, S. J.; Gogotsi, Y.; Taheri, M. L. Control of MXenes' Electronic Properties Through Termination and Intercalation. *Nat. Commun.* **2019**, *10* (1), 522.
(250) Sun, W.; Xie, Y.; Kent, P. R. Double Transition Metal MXenes with Wide Band Gaps and Novel Magnetic Properties. *Nanoscale* **2018**, *10* (25), 11962−11968.
(251) Huang, B.; Li, N.; Ong, W.-J.; Zhou, N. Single Atom-supported MXene: How Single-Atomic-Site Catalysts Tune the High Activity and Selectivity of Electrochemical Nitrogen Fixation. *J. Mater. Chem. A* **2019**, *7* (48), 27620−27631.
(252) Zhao, D.; Chen, Z.; Yang, W.; Liu, S.; Zhang, X.; Yu, Y.; Cheong, W.-C.; Zheng, L.; Ren, F.; Ying, G.; et al. MXene (Ti_3C_2) Vacancy-confined Single-atom Catalyst for Efficient Functionalization of CO_2. *J. Am. Chem. Soc.* **2019**, *141* (9), 4086−4093.
(253) Yang, X.; Lu, Z.; Cheng, C.; Wang, Y.; Zhang, X.; Yang, Z.; Lu, W. Identification of Efficient Single-Atom Catalysts Based on V_2CO_2 MXene by Ab Initio Simulations. *J. Phys. Chem. C* **2020**, *124* (7), 4090−4100.
(254) Ramalingam, V.; Varadhan, P.; Fu, H. C.; Kim, H.; Zhang, D.; Chen, S.; Song, L.; Ma, D.; Wang, Y.; Alshareef, H. N.; et al. Heteroatom-Mediated Interactions between Ruthenium Single Atoms and an MXene Support for Efficient Hydrogen Evolution. *Adv. Mater.* **2019**, *31* (48), 1903841.
(255) Huang, K.; Li, C.; Li, H.; Ren, G.; Wang, L.; Wang, W.; Meng, X. Photocatalytic Applications of Two-Dimensional Ti_3C_2 MXenes: A Review. *ACS Appl. Nano Mater.* **2020**, *3* (10), 9581−9603.
(256) Liu, N.; Lu, N.; Yu, H.; Chen, S.; Quan, X. Efficient Day-Night Photocatalysis Performance of 2D/2D Ti_3C_2/Porous g-C_3N_4 Nanolayers Composite and Its Application in the Degradation of Organic Pollutants. *Chemosphere* **2020**, *246*, 125760.
(257) Saravanan, A.; Kumar, P. S.; Vo, D.-V. N.; Yaashikaa, P. R.; Karishma, S.; Jeevanantham, S.; Gayathri, B.; Bharathi, V. D. Photocatalysis for Removal of Environmental Pollutants and Fuel Production: A Review. *Environ. Chem. Lett.* **2021**, *19*, 441−463.
(258) Shao, M.; Shao, Y.; Chai, J.; Qu, Y.; Yang, M.; Wang, Z.; Yang, M.; Ip, W. F.; Kwok, C. T.; Shi, X.; et al. Synergistic Effect of 2D Ti_2C and g-C_3N_4 for Efficient Photocatalytic Hydrogen Production. *J. Mater. Chem. A* **2017**, *5* (32), 16748−16756.
(259) Lin, P.; Shen, J.; Yu, X.; Liu, Q.; Li, D.; Tang, H. Construction of Ti_3C_2 MXene/O-doped g-C_3N_4 2D-2D Schottky-Junction for Enhanced Photocatalytic Hydrogen Evolution. *Ceram. Int.* **2019**, *45* (18), 24656−24663.
(260) Yang, C.; Tan, Q.; Li, Q.; Zhou, J.; Fan, J.; Li, B.; Sun, J.; Lv, K. 2D/2D Ti_3C_2 MXene/g-C_3N_4 Nanosheets Heterojunction for High Efficient CO_2 Reduction Photocatalyst: Dual Effects of Urea. *Appl. Catal., B* **2020**, *268*, 118738.
(261) Xu, H.; Xiao, R.; Huang, J.; Jiang, Y.; Zhao, C.; Yang, X. J. C. J. o. C. In Situ Construction of Protonated g-C_3N_4/Ti_3C_2 MXene Schottky Heterojunctions for Efficient Photocatalytic Hydrogen Production. *Chin. J. Catal.* **2021**, *42* (1), 107−114.
(262) Vigneshwaran, S.; Karthikeyan, P.; Park, C. M.; Meenakshi, S. Boosted Insights of Novel Accordion-like (2D/2D) Hybrid Photocatalyst for the Removal of Cationic Dyes: Mechanistic and Degradation Pathways. *J. Environ. Manage.* **2020**, *273*, 111125.
(263) Sun, Z.; Xie, H.; Tang, S.; Yu, X. F.; Guo, Z.; Shao, J.; Zhang, H.; Huang, H.; Wang, H.; Chu, P. K. Ultrasmall Black Phosphorus Quantum Dots: Synthesis and Use as Photothermal Agents. *Angew. Chem., Int. Ed.* **2015**, *54* (39), 11526−11530.
(264) Xiang, Q.; Yu, J.; Jaroniec, M. Graphene-based Semiconductor Photocatalysts. *Chem. Soc. Rev.* **2012**, *41* (2), 782−796.
(265) Song, T.; Hou, L.; Long, B.; Ali, A.; Deng, G.-J. Ultrathin MXene "Bridge" to Accelerate Charge Transfer in Ultrathin Metal-free 0D/2D Black Phosphorus/g-C_3N_4 Heterojunction Toward Photocatalytic Hydrogen Production. *J. Colloid Interface Sci.* **2021**, *584*, 474−483.
(266) Kang, J.; Byun, S.; Kim, S.; Lee, J.; Jung, M.; Hwang, H.; Kim, T. W.; Song, S. H.; Lee, D. Design of Three-Dimensional Hollow-Sphere Architecture of Ti_3C_2Tx MXene with Graphitic Carbon Nitride Nanoshells for Efficient Photocatalytic Hydrogen Evolution. *ACS Appl. Energy Mater.* **2020**, *3* (9), 9226−9233.
(267) Tahir, M.; Tahir, B. Constructing a Stable 2D/2D Heterojunction of Oxygen-Cluster-Modified Ti_3AlC_2 MAX Cocatalyst with Proton-Rich C_3N_4 for Highly Efficient Photocatalytic CO_2 Methanation. *Ind. Eng. Chem. Res.* **2020**, *59* (21), 9841−9857.
(268) Zhang, M.; Qin, J.; Rajendran, S.; Zhang, X.; Liu, R. Heterostructured d-Ti_3C_2/TiO_2/g-C_3N_4 Nanocomposites with Enhanced Visible-Light Photocatalytic Hydrogen Production Activity. *ChemSusChem* **2018**, *11* (24), 4226−4236.
(269) He, F.; Zhu, B.; Cheng, B.; Yu, J.; Ho, W.; Macyk, W. 2D/2D/0D TiO_2/C_3N_4/Ti_3C_2 MXene Composite S-Scheme Photocatalyst with Enhanced CO_2 Reduction Activity. *Appl. Catal., B* **2020**, *272*, 119006.
(270) Hernández-Alonso, M. D.; Fresno, F.; Suárez, S.; Coronado, J. M. Development of Alternative Photocatalysts to TiO_2: Challenges and Opportunities. *Energy Environ. Sci.* **2009**, *2* (12), 1231−1257.
(271) Wenderich, K.; Mul, G. Methods, Mechanism, and Applications of Photodeposition in Photocatalysis: A Review. *Chem. Rev.* **2016**, *116* (23), 14587−14619.
(272) Batzill, M. Fundamental Aspects of Surface Engineering of Transition Metal Oxide Photocatalysts. *Energy Environ. Sci.* **2011**, *4* (9), 3275−3286.
(273) Hisatomi, T.; Kubota, J.; Domen, K. Recent Advances in Semiconductors for Photocatalytic and Photoelectrochemical Water Splitting. *Chem. Soc. Rev.* **2014**, *43* (22), 7520−7535.
(274) Hoffmann, M. R.; Martin, S. T.; Choi, W.; Bahnemann, D. W. Environmental Applications of Semiconductor Photocatalysis. *Chem. Rev.* **1995**, *95* (1), 69−96.
(275) Chen, S.; Takata, T.; Domen, K. Particulate Photocatalysts for Overall Water Splitting. *Nat. Rev. Mater.* **2017**, *2* (10), 17050.
(276) Djurisic, A. B.; Leung, Y. H.; Ching Ng, A. M. Strategies for Improving the Efficiency of Semiconductor Metal Oxide Photocatalysis. *Mater. Horiz.* **2014**, *1* (4), 400−410.
(277) Sakai, N.; Ebina, Y.; Takada, K.; Sasaki, T. Photocurrent Generation from Semiconducting Manganese Oxide Nanosheets in Response to Visible Light. *J. Phys. Chem. B* **2005**, *109* (19), 9651−9655.
(278) Masih, D.; Ma, Y.; Rohani, S. Graphitic C_3N_4 based Noble-Metal-Free Photocatalyst Systems: A Review. *Appl. Catal., B* **2017**, *206*, 556−588.
(279) Zhou, P.; Yu, J.; Jaroniec, M. All-Solid-state Z-Scheme Photocatalytic Systems. *Adv. Mater.* **2014**, *26* (29), 4920−4935.
(280) Yu, W.; Chen, J.; Shang, T.; Chen, L.; Gu, L.; Peng, T. Direct Z-scheme g-C_3N_4/WO_3 Photocatalyst with Atomically Defined Junction for H_2 Production. *Appl. Catal., B* **2017**, *219*, 693−704.
(281) Kumar, S.; Reddy, N. L.; Kumar, A.; Shankar, M. V.; Krishnan, V. Two Dimensional N-Doped ZnO-Graphitic Carbon Nitride Nanosheets Heterojunctions with Enhanced Photocatalytic Hydrogen Evolution. *Int. J. Hydrogen Energy* **2018**, *43* (8), 3988−4002.
(282) Ji, H.; Fei, T.; Zhang, L.; Yan, J.; Fan, Y.; Huang, J.; Song, Y.; Man, Y.; Tang, H.; Xu, H.; et al. Synergistic Effects of MoO_2 Nanosheets and Graphene-like C_3N_4 for Highly Improved Visible Light Photocatalytic Activities. *Appl. Surf. Sci.* **2018**, *457*, 1142−1150.
(283) Zhu, X.; Ji, H.; Yi, J.; Yang, J.; She, X.; Ding, P.; Li, L.; Deng, J.; Qian, J.; Xu, H.; et al. A Specifically Exposed Cobalt Oxide/Carbon

https://doi.org/10.1021/acs.chemmater.1c03166
Chem. Mater. 2021, 33, 9012−9092

Nitride 2D Heterostructure for Carbon Dioxide Photoreduction. *Ind. Eng. Chem. Res.* **2018**, *57* (51), 17394−17400.
(284) Murillo-Sierra, J.; Hernández-Ramírez, A.; Hinojosa-Reyes, L.; Guzmán-Mar, J. A Review on the Development of Visible Light-Responsive WO_3-based Photocatalysts for Environmental Applications. *Chem. Eng. J. Adv.* **2021**, *5*, 100070.
(285) Dong, P.; Hou, G.; Xi, X.; Shao, R.; Dong, F. WO_3-based Photocatalysts: Morphology Control, Activity Enhancement and Multifunctional Applications. *Environ. Sci.: Nano* **2017**, *4* (3), 539−557.
(286) Amano, F.; Ishinaga, E.; Yamakata, A. Effect of Particle Size on the Photocatalytic Activity of WO_3 Particles for Water Oxidation. *J. Phys. Chem. C* **2013**, *117* (44), 22584−22590.
(287) Aslam, M.; Ismail, I. M.; Chandrasekaran, S.; Hameed, A. Morphology Controlled Bulk Synthesis of Disc-shaped WO_3 Powder and Evaluation of Its Photocatalytic Activity for the Degradation of Phenols. *J. Hazard. Mater.* **2014**, *276*, 120−128.
(288) Wicaksana, Y.; Liu, S.; Scott, J.; Amal, R. Tungsten Trioxide as a Visible Light Photocatalyst for Volatile Organic Carbon Removal. *Molecules* **2014**, *19* (11), 17747−17762.
(289) Jin, J.; Yu, J.; Guo, D.; Cui, C.; Ho, W. A Hierarchical Z-Scheme CdS-WO_3 Photocatalyst with Enhanced CO_2 Reduction Activity. *Small* **2015**, *11* (39), 5262−5271.
(290) Cheng, C.; Shi, J.; Hu, Y.; Guo, L. WO_3/g-C_3N_4 Composites: One-pot Preparation and Enhanced Photocatalytic H_2 Production under Visible-light Irradiation. *Nanotechnology* **2017**, *28* (16), 164002.
(291) Cui, L.; Ding, X.; Wang, Y.; Shi, H.; Huang, L.; Zuo, Y.; Kang, S. Facile Preparation of Z-scheme WO_3/g-C_3N_4 Composite Photocatalyst with Enhanced Photocatalytic Performance under Visible Light. *Appl. Surf. Sci.* **2017**, *391*, 202−210.
(292) Yang, Y.; Qiu, M.; Li, L.; Pi, Y.; Yan, G.; Yang, L. A Direct Z-Scheme Van Der Waals Heterojunction (WO_3·H_2O/g-C_3N_4) for High Efficient Overall Water Splitting under Visible-Light. *Solar RRL* **2018**, *2* (9), 1800148.
(293) Liu, D.; Zhang, S.; Wang, J.; Peng, T.; Li, R. Direct Z-Scheme 2D/2D Photocatalyst based on Ultrathin g-C_3N_4 and WO_3 Nanosheets for Efficient Visible-Light-Driven H_2 Generation. *ACS Appl. Mater. Interfaces* **2019**, *11* (31), 27913−27923.
(294) Fu, J.; Xu, Q. S. S.; Low, J.; Jiang, C.; Yu, J. Ultrathin 2D/2D WO_3/g-C_3N_4 Step-Scheme H_2-Production Photocatalyst. *Appl. Catal., B* **2019**, *243*, 556−565.
(295) Xing, Z.; Zhang, J.; Cui, J.; Yin, J.; Zhao, T.; Kuang, J.; Xiu, Z.; Wan, N.; Zhou, W. Recent Advances in Floating TiO_2-based Photocatalysts for Environmental Application. *Appl. Catal., B* **2018**, *225*, 452−467.
(296) Naldoni, A.; Altomare, M.; Zoppellaro, G.; Liu, N.; Kment, S.; Zbořil, R.; Schmuki, P. Photocatalysis with Reduced TiO_2: From Black TiO_2 to Cocatalyst-Free Hydrogen Production. *ACS Catal.* **2019**, *9* (1), 345−364.
(297) Ma, Y.; Wang, X.; Jia, Y.; Chen, X.; Han, H.; Li, C. Titanium Dioxide-based Nanomaterials for Photocatalytic Fuel Generations. *Chem. Rev.* **2014**, *114* (19), 9987−10043.
(298) Li, L.; Yan, J.; Wang, T.; Zhao, Z.-J.; Zhang, J.; Gong, J.; Guan, N. Sub-10 nm Rutile Titanium Dioxide Nanoparticles for Efficient Visible-Light-Driven Photocatalytic Hydrogen Production. *Nat. Commun.* **2015**, *6* (1), 5881.
(299) Mitoraj, D.; Kisch, H. The Nature of Nitrogen-Modified Titanium Dioxide Photocatalysts Active in Visible Light. *Angew. Chem., Int. Ed.* **2008**, *47* (51), 9975−9978.
(300) Hirakawa, H.; Hashimoto, M.; Shiraishi, Y.; Hirai, T. Photocatalytic Conversion of Nitrogen to Ammonia with Water on Surface Oxygen Vacancies of Titanium Dioxide. *J. Am. Chem. Soc.* **2017**, *139* (31), 10929−10936.
(301) Zhang, T.; Low, J.; Huang, X.; Al-Sharab, J. F.; Yu, J.; Asefa, T. Copper-Decorated Microsized Nanoporous Titanium Dioxide Photocatalysts for Carbon Dioxide Reduction by Water. *ChemCatChem* **2017**, *9* (15), 3054−3062.
(302) Selcuk, S.; Zhao, X.; Selloni, A. Structural Evolution of Titanium Dioxide during Reduction in High-Pressure Hydrogen. *Nat. Mater.* **2018**, *17* (10), 923−928.
(303) Aguirre, M. E.; Zhou, R.; Eugene, A. J.; Guzman, M. I.; Grela, M. A. Cu_2O/TiO_2 Heterostructures for CO_2 Reduction Through A Direct Z-Scheme: Protecting Cu_2O from Photocorrosion. *Appl. Catal., B* **2017**, *217*, 485−493.
(304) Zhong, R.; Zhang, Z.; Yi, H.; Zeng, L.; Tang, C.; Huang, L.; Gu, M. Covalently bonded 2D/2D Og-C_3N_4/TiO_2 Heterojunction for Enhanced Visible-light Photocatalytic Hydrogen Evolution. *Appl. Catal., B* **2018**, *237*, 1130−1138.
(305) Gu, W.; Lu, F.; Wang, C.; Kuga, S.; Wu, L.; Huang, Y.; Wu, M. Face-to-Face Interfacial Assembly of Ultrathin g-C_3N_4 and Anatase TiO_2 Nanosheets for Enhanced Solar Photocatalytic Activity. *ACS Appl. Mater. Interfaces* **2017**, *9* (34), 28674−28684.
(306) Li, K.; Huang, Z.; Zeng, X.; Huang, B.; Gao, S.; Lu, J. Synergetic Effect of Ti^{3+} and Oxygen Doping on Enhancing Photoelectrochemical and Photocatalytic Properties of TiO_2/g-C_3N_4 Heterojunctions. *ACS Appl. Mater. Interfaces* **2017**, *9* (13), 11577−11586.
(307) Li, K.; Gao, S.; Wang, Q.; Xu, H.; Wang, Z.; Huang, B.; Dai, Y.; Lu, J. In-Situ-Reduced Synthesis of Ti^{3+} Self-doped TiO_2/g-C_3N_4 Heterojunctions with High Photocatalytic Performance under LED Light irradiation. *ACS Appl. Mater. Interfaces* **2015**, *7* (17), 9023−9030.
(308) Khan, A. A.; Tahir, M. Well-Designed 2D/2D Ti_3C_2TA/R MXene coupled g-C_3N_4 Heterojunction with In-situ Growth of Anatase/Rutile TiO_2 Nucleates for Boosting Photocatalytic Dry-reforming of Methane (DRM) for Syngas Production under Visible Light. *Appl. Catal., B* **2021**, *285*, 119777.
(309) Shafi, P. M.; Dhanabal, R.; Chithambararaj, A.; Velmathi, S.; Bose, A. C. α-MnO_2/h-MoO_3 Hybrid Material for High Performance Supercapacitor Electrode and Photocatalyst. *ACS Sustainable Chem. Eng.* **2017**, *5* (6), 4757−4770.
(310) Das, S.; Samanta, A.; Jana, S. Light-Assisted Synthesis of Hierarchical Flower-Like MnO_2 Nanocomposites with Solar Light Induced Enhanced Photocatalytic Activity. *ACS Sustainable Chem. Eng.* **2017**, *5* (10), 9086−9094.
(311) Dare-Edwards, M.; Goodenough, J.; Hamnett, A.; Nicholson, N. Photoelectrochemistry of Nickel (II) Oxide. *J. Chem. Soc., Faraday Trans. 2* **1981**, *77* (4), 643−661.
(312) Roche, I.; Chaînet, E.; Chatenet, M.; Vondrák, J. Carbon-supported Manganese Oxide Nanoparticles as Electrocatalysts for the Oxygen Reduction Reaction (ORR) in Alkaline Medium: Physical Characterizations and ORR Mechanism. *J. Phys. Chem. C* **2007**, *111* (3), 1434−1443.
(313) Wu, B.; Li, Y.; Su, K.; Tan, L.; Liu, X.; Cui, Z.; Yang, X.; Liang, Y.; Li, Z.; Zhu, S.; et al. The Enhanced Photocatalytic Properties of MnO_2/g-C_3N_4 Heterostructure for Rapid Sterilization under Visible Light. *J. Hazard. Mater.* **2019**, *377*, 227−236.
(314) Xia, P.; Zhu, B.; Cheng, B.; Yu, J.; Xu, J. 2D/2D g-C_3N_4/MnO_2 Nanocomposite as A Direct Z-Scheme Photocatalyst for Enhanced Photocatalytic Activity. *ACS Sustainable Chem. Eng.* **2018**, *6* (1), 965−973.
(315) Wang, M.; Shen, M.; Zhang, L.; Tian, J.; Jin, X.; Zhou, Y.; Shi, J. 2D-2D MnO_2/g-C_3N_4 Heterojunction Photocatalyst: In-situ Synthesis and Enhanced CO_2 Reduction Activity. *Carbon* **2017**, *120*, 23−31.
(316) Wang, N.; Li, J.; Wu, L.; Li, X.; Shu, J. MnO_2 and Carbon Nanotube Co-modified C_3N_4 Composite Catalyst for Enhanced Water Splitting Activity under Visible Light Irradiation. *Int. J. Hydrogen Energy* **2016**, *41* (48), 22743−22750.
(317) Liu, H.; Tian, K.; Ning, J.; Zhong, Y.; Zhang, Z.; Hu, Y. One-Step Solvothermal Formation of Pt Nanoparticles Decorated Pt^{2+}-doped α-Fe_2O_3 Nanoplates with Enhanced Photocatalytic O_2 Evolution. *ACS Catal.* **2019**, *9* (2), 1211−1219.
(318) Pan, Z.; Zhang, G.; Wang, X. Polymeric Carbon Nitride/Reduced Graphene Oxide/Fe_2O_3: All-Solid-State Z-Scheme System

for Photocatalytic Overall Water Splitting. *Angew. Chem.* **2019**, *131* (21), 7176−7180.
(319) Zhou, H.; Wong, S. S. A Facile and Mild Synthesis of 1-D ZnO, CuO, and α-Fe_2O_3 Nanostructures and Nanostructured Arrays. *ACS Nano* **2008**, *2* (5), 944−958.
(320) Kim, H. S.; Piao, Y.; Kang, S. H.; Hyeon, T.; Sung, Y.-E. Uniform Hematite Nanocapsules based on An Anode Material for Lithium Ion Batteries. *Electrochem. Commun.* **2010**, *12* (3), 382−385.
(321) Kennedy, J. H.; Frese Jr, K. W. Photooxidation of Water at α-Fe_2O_3 Electrodes. *J. Electrochem. Soc.* **1978**, *125* (5), 709.
(322) Joly, A. G.; Williams, J. R.; Chambers, S. A.; Xiong, G.; Hess, W. P.; Laman, D. M. Carrier Dynamics in α-Fe_2O_3 (0001) Thin Films and Single Crystals Probed by Femtosecond Transient Absorption and Reflectivity. *J. Appl. Phys.* **2006**, *99* (5), 053521.
(323) Zhou, X.; Lan, J.; Liu, G.; Deng, K.; Yang, Y.; Nie, G.; Yu, J.; Zhi, L. Facet-mediated Photodegradation of Organic Dye over Hematite Architectures by Visible Light. *Angew. Chem., Int. Ed.* **2012**, *51* (1), 178−182.
(324) Han, H.; Riboni, F.; Karlicky, F.; Kment, S.; Goswami, A.; Sudhagar, P.; Yoo, J.; Wang, L.; Tomanec, O.; Petr, M.; et al. α-Fe_2O_3/TiO_2 3D Hierarchical Nanostructures for Enhanced Photoelectrochemical Water Splitting. *Nanoscale* **2017**, *9* (1), 134−142.
(325) Shi, Y.; Li, H.; Wang, L.; Shen, W.; Chen, H. Novel α-Fe_2O_3/CdS Cornlike Nanorods with Enhanced Photocatalytic Performance. *ACS Appl. Mater. Interfaces* **2012**, *4* (9), 4800−4806.
(326) Liu, X.; Chen, K.; Shim, J.-J.; Huang, J. Facile Synthesis of Porous Fe_2O_3 Nanorods and Their Photocatalytic Properties. *J. Saudi Chem. Soc.* **2015**, *19* (5), 479−484.
(327) Mendiola-Alvarez, S.; Hernández-Ramírez, A.; Guzmán-Mar, J.; Maya-Treviño, M.; Caballero-Quintero, A.; Hinojosa-Reyes, L. A Novel P-doped Fe_2O_3-TiO_2 Mixed Oxide: Synthesis, Characterization and Photocatalytic Activity under Visible Radiation. *Catal. Today* **2019**, *328*, 91−98.
(328) Franceschi, G.; Kraushofer, F.; Meier, M.; Parkinson, G. S.; Schmid, M.; Diebold, U.; Riva, M. A Model System for Photocatalysis: Ti-Doped α-Fe_2O_3 (1102) Single-Crystalline Films. *Chem. Mater.* **2020**, *32* (9), 3753−3764.
(329) Cesar, I.; Kay, A.; Gonzalez Martinez, J. A.; Grätzel, M. Translucent Thin Film Fe_2O_3 Photoanodes for Efficient Water Splitting by Sunlight: Nanostructure-directing Effect of Si-Doping. *J. Am. Chem. Soc.* **2006**, *128* (14), 4582−4583.
(330) She, X.; Wu, J.; Xu, H.; Zhong, J.; Wang, Y.; Song, Y.; Nie, K.; Liu, Y.; Yang, Y.; Rodrigues, M. T. F.; et al. High Efficiency Photocatalytic Water Splitting using 2D α-Fe_2O_3/g-C_3N_4 Z-Scheme Catalysts. *Adv. Energy Mater.* **2017**, *7* (17), 1700025.
(331) Xu, Q.; Zhu, B.; Jiang, C.; Cheng, B.; Yu, J. Constructing 2D/2D Fe_2O_3/g-C_3N_4 Direct Z-Scheme Photocatalysts with Enhanced H_2 Generation Performance. *Solar RRL* **2018**, *2* (3), 1800006.
(332) Zhang, H.; Zhu, C.; Cao, J.; Tang, Q.; Li, M.; Kang, P.; Shi, C.; Ma, M. Ultrasonic-Assisted Synthesis of 2D α-Fe_2O_3@g-C_3N_4 Composite with Excellent Visible Light Photocatalytic Activity. *Catalysts* **2018**, *8* (10), 457.
(333) Tian, C.; Zhang, Q.; Wu, A.; Jiang, M.; Liang, Z.; Jiang, B.; Fu, H. Cost-Effective Large-Scale Synthesis of ZnO Photocatalyst with Excellent Performance for Dye Photodegradation. *Chem. Commun.* **2012**, *48* (23), 2858−2860.
(334) Ye, Y.; Wang, K.; Huang, X.; Lei, R.; Zhao, Y.; Liu, P. Integration of Piezoelectric Effect into a Au/ZnO Photocatalyst for Efficient Charge Separation. *Catal. Sci. Technol.* **2019**, *9* (14), 3771−3778.
(335) Fu, X.; Tang, W.; Ji, L.; Chen, S. V_2O_5/Al_2O_3 Composite Photocatalyst: Preparation, Characterization, and the Role of Al_2O_3. *Chem. Eng. J.* **2012**, *180*, 170−177.
(336) Shanmugam, M.; Alsalme, A.; Alghamdi, A.; Jayavel, R. Enhanced Photocatalytic Performance of the Graphene-V_2O_5 Nanocomposite in the Degradation of Methylene Blue Dye under Direct Sunlight. *ACS Appl. Mater. Interfaces* **2015**, *7* (27), 14905−14911.
(337) Saravanan, R.; Gupta, V.; Mosquera, E.; Gracia, F. Preparation and Characterization of V_2O_5/ZnO Nanocomposite System for Photocatalytic Application. *J. Mol. Liq.* **2014**, *198*, 409−412.
(338) Yin, H.; Yu, K.; Song, C.; Huang, R.; Zhu, Z. Synthesis of Au-Decorated V_2O_5@ ZnO Heteronanostructures and Enhanced Plasmonic Photocatalytic Activity. *ACS Appl. Mater. Interfaces* **2014**, *6* (17), 14851−14860.
(339) Sreedhar, A.; Reddy, I. N.; Hoai Ta, Q. T.; Phuong Doan, T. H.; Shim, J.; Noh, J.-S.; et al. Unveiling the Impact of Interfacially Engineered Selective V_2O_5 Nanobelt Bundles with Flake-like ZnO and Co-ZnO Thin Films for Multifunctional Visible-light Water Splitting and Toxic Gas Sensing. *J. Power Sources* **2020**, *478*, 229081.
(340) Wang, Y.; Tan, G.; Liu, T.; Su, Y.; Ren, H.; Zhang, X.; Xia, A.; Lv, L.; Liu, Y. Photocatalytic Properties of the g-C_3N_4/{010} facets $BiVO_4$ Interface Z-Scheme Photocatalysts Induced by $BiVO_4$ Surface Heterojunction. *Appl. Catal., B* **2018**, *234*, 37−49.
(341) Lu, M.; Li, Q.; Zhang, C.; Fan, X.; Li, L.; Dong, Y.; Chen, G.; Shi, H. Remarkable Photocatalytic Activity Enhancement of CO_2 Conversion over 2D/2D g-C_3N_4/$BiVO_4$ Z-Scheme Heterojunction Promoted by Efficient Interfacial Charge Transfer. *Carbon* **2020**, *160*, 342−352.
(342) Mei, F.; Dai, K.; Zhang, J.; Li, W.; Liang, C. Construction of Ag SPR-promoted Step-Scheme Porous g-C_3N_4/Ag_3VO_4 Heterojunction for Improving Photocatalytic Activity. *Appl. Surf. Sci.* **2019**, *488*, 151−160.
(343) Butt, F. K.; Cao, C.; Wan, Q.; Li, P.; Idrees, F.; Tahir, M.; Khan, W. S.; Ali, Z.; Zapata, M. J.; Safdar, M.; et al. Synthesis, Evolution and Hydrogen Storage Properties of ZnV_2O_4 Glomerulus Nano/microspheres: A Prospective Material for Energy Storage. *Int. J. Hydrogen Energy* **2014**, *39* (15), 7842−7851.
(344) Sameie, H.; Sabbagh Alvani, A. A.; Naseri, N.; Du, S.; Rosei, F. First-Principles Study on ZnV_2O_6 and $Zn_2V_2O_7$: Two New Photoanode Candidates for Photoelectrochemical Water Oxidation. *Ceram. Int.* **2018**, *44* (6), 6607−6613.
(345) Tang, R.; Li, Y.; Li, N.; Han, D.; Li, H.; Zhao, Y.; Gao, C.; Zhu, P.; Wang, X. Reversible Structural Phase Transition in ZnV_2O_6 at High Pressures. *J. Phys. Chem. C* **2014**, *118* (20), 10560−10566.
(346) Butt, F. K.; Idrees, F.; Tahir, M.; Cao, C.; Hussain, R.; Ahmed, R.; Ul Haq, B. Fabrication of ZnV_2O_6 Nanostructures: Their Energy Storage and PL Properties. *Mater. Lett.* **2015**, *155*, 15−17.
(347) Sun, Y.; Li, C.; Wang, L.; Wang, Y.; Ma, X.; Ma, P.; Song, M. Ultralong Monoclinic ZnV_2O_6 Nanowires: Their Shape-controlled Synthesis, New Growth Mechanism, and Highly Reversible Lithium Storage in Lithium-ion Batteries. *RSC Adv.* **2012**, *2* (21), 8110−8115.
(348) De Juan-Corpuz, L. M. Z.; Nguyen, M. T.; Corpuz, R. D.; Yonezawa, T.; Rosero-Navarro, N. C.; Tadanaga, K.; Tokunaga, T.; Kheawhom, S. Porous ZnV_2O_4 Nanowire for Stable and High-Rate Lithium-Ion Battery Anodes. *ACS Appl. Nano Mater.* **2019**, *2* (7), 4247−4256.
(349) Bafaqeer, A.; Tahir, M.; Amin, N. A. S. Synthesis of Hierarchical ZnV_2O_6 Nanosheets with Enhanced Activity and Stability for Visible Light Driven CO_2 Reduction to Solar Fuels. *Appl. Surf. Sci.* **2018**, *435*, 953−962.
(350) Sameie, H.; Alvani, A. S.; Naseri, N.; Rosei, F.; Mul, G.; Mei, B. Photocatalytic Activity of ZnV_2O_6/Reduced Graphene Oxide Nanocomposite: From Theory to Experiment. *J. Electrochem. Soc.* **2018**, *165* (7), H353.
(351) Bafaqeer, A.; Tahir, M.; Amin, N. A. S. Synergistic Effects of 2D/2D ZnV_2O_6/RGO Nanosheets Heterojunction for Stable and High Performance Photo-induced CO_2 Reduction to Solar Fuels. *Chem. Eng. J.* **2018**, *334*, 2142−2153.
(352) Xiao, B.; Huang, H.; Yu, X.; Song, J.; Qu, J. Facile Synthesis of Layered V_2O_5/ZnV_2O_6 Heterostructures with Enhanced Sensing Performance. *Appl. Surf. Sci.* **2018**, *447*, 569−575.
(353) Bafaqeer, A.; Tahir, M.; Amin, N. A. S. Well-Designed ZnV_2O_6/g-C_3N_4 2D/2D Nanosheets Heterojunction with Faster Charges Separation via pCN as Mediator Towards Enhanced Photocatalytic Reduction of CO_2 to Fuels. *Appl. Catal., B* **2019**, *242*, 312−326.

https://doi.org/10.1021/acs.chemmater.1c03166
Chem. Mater. 2021, 33, 9012−9092

(354) Bafaqeer, A.; Tahir, M.; Ali Khan, A.; Saidina Amin, N. A. Indirect Z-scheme Assembly of 2D ZnV_2O_6/RGO/g-C_3N_4 Nanosheets with RGO/pCN as Solid-State Electron Mediators Toward Visible-Light-Enhanced CO_2 Reduction. *Ind. Eng. Chem. Res.* **2019**, *58* (20), 8612−8624.
(355) Ma, S.; Huang, L.; Ma, L.; Shim, Y.; Islam, S. M.; Wang, P.; Zhao, L.-D.; Wang, S.; Sun, G.; Yang, X.; et al. Efficient Uranium Capture by Polysulfide/Layered Double Hydroxide Composites. *J. Am. Chem. Soc.* **2015**, *137* (10), 3670−3677.
(356) Zou, Y.; Wang, P.; Yao, W.; Wang, X.; Liu, Y.; Yang, D.; Wang, L.; Hou, J.; Alsaedi, A.; Hayat, T.; et al. Synergistic Immobilization of UO_2^{2+} by Novel Graphitic Carbon Nitride@ Layered Double Hydroxide Nanocomposites from Wastewater. *Chem. Eng. J.* **2017**, *330*, 573−584.
(357) Mohapatra, L.; Parida, K. A Review on the Recent Progress, Challenges and Perspective of Layered Double Hydroxides as Promising Photocatalysts. *J. Mater. Chem. A* **2016**, *4* (28), 10744−10766.
(358) Xu, S.-M.; Pan, T.; Dou, Y.-B.; Yan, H.; Zhang, S.-T.; Ning, F.-Y.; Shi, W.-Y.; Wei, M. Theoretical and Experimental Study on $M^{II}M^{III}$-Layered Double Hydroxides as Efficient Photocatalysts Toward Oxygen Evolution from Water. *J. Phys. Chem. C* **2015**, *119* (33), 18823−18834.
(359) Shirotori, M.; Nishimura, S.; Ebitani, K. Fine-crystallized LDHs prepared with SiO_2 Spheres as Highly Active Solid Base Catalysts. *J. Mater. Chem. A* **2017**, *5* (15), 6947−6957.
(360) Chauhan, D. K.; Kumar, P.; Painuly, R.; Kumar, S.; Jain, S. L.; Ganguly, S. K. Kinetics and Feasibility Studies of Thiol Oxidation using Magnetically Separable Mg-Al Layered Double Hydroxide Supported Cobalt Phthalocyanine Catalyst. *Fuel Process. Technol.* **2017**, *162*, 135−146.
(361) Gao, Z.; Xie, R.; Fan, G.; Yang, L.; Li, F. Highly Efficient and Stable Bimetallic AuPd Over La-Doped Ca-Mg-Al Layered Double Hydroxide for Base-Free Aerobic Oxidation of 5-Hydroxymethylfurfural in Water. *ACS Sustainable Chem. Eng.* **2017**, *5* (7), 5852−5861.
(362) Kumar, P.; Gill, K.; Kumar, S.; Ganguly, S. K.; Jain, S. L. Magnetic Fe_3O_4@ MgAl-LDH Composite Grafted with Cobalt Phthalocyanine as An Efficient Heterogeneous Catalyst for the Oxidation of Mercaptans. *J. Mol. Catal. A: Chem.* **2015**, *401*, 48−54.
(363) Teramura, K.; Iguchi, S.; Mizuno, Y.; Shishido, T.; Tanaka, T. Photocatalytic Conversion of CO_2 in Water over Layered Double Hydroxides. *Angew. Chem., Int. Ed.* **2012**, *51* (32), 8008−8011.
(364) Meng, Y.; Dai, T.; Zhou, X.; Pan, G.; Xia, S. Photodegradation of Volatile Organic Compounds Catalyzed by MCr-LDHs and Hybrid MO@MCr-LDHs (M= Co, Ni, Cu, Zn): The Comparison of Activity, Kinetics and Photocatalytic Mechanism. *Catal. Sci. Technol.* **2020**, *10* (2), 424−439.
(365) Izumi, Y. Recent Advances in the Photocatalytic Conversion of Carbon Dioxide to Fuels with Water and/or Hydrogen using Solar Energy and Beyond. *Coord. Chem. Rev.* **2013**, *257* (1), 171−186.
(366) Mikami, G.; Grosu, F.; Kawamura, S.; Yoshida, Y.; Carja, G.; Izumi, Y. Harnessing Self-Supported Au Nanoparticles on Layered Double Hydroxides Comprising Zn and Al for Enhanced Phenol Decomposition under Solar Light. *Appl. Catal., B* **2016**, *199*, 260−271.
(367) Kawamura, S.; Zhang, H.; Tamba, M.; Kojima, T.; Miyano, M.; Yoshida, Y.; Yoshiba, M.; Izumi, Y. Efficient Volcano-type Dependence of Photocatalytic CO_2 Conversion into Methane using Hydrogen at Reaction Pressures up to 0.80 MPa. *J. Catal.* **2017**, *345*, 39−52.
(368) Wein, L. A.; Zhang, H.; Urushidate, K.; Miyano, M.; Izumi, Y. Optimized Photoreduction of CO_2 Exclusively into Methanol Utilizing Liberated Reaction Space in Layered Double Hydroxides Comprising Zinc, Copper, and Gallium. *Appl. Surf. Sci.* **2018**, *447*, 687−696.
(369) Chen, C.; Tao, L.; Du, S.; Chen, W.; Wang, Y.; Zou, Y.; Wang, S. Advanced Exfoliation Strategies for Layered Double Hydroxides and Applications in Energy Conversion and Storage. *Adv. Funct. Mater.* **2020**, *30* (14), 1909832.
(370) Chen, G.; Wan, H.; Ma, W.; Zhang, N.; Cao, Y.; Liu, X.; Wang, J.; Ma, R. Layered Metal Hydroxides and Their Derivatives: Controllable Synthesis, Chemical Exfoliation, and Electrocatalytic Applications. *Adv. Energy Mater.* **2020**, *10* (11), 1902535.
(371) Peng, Y.; Sun, Y.; Tsang, D. C.; Hanif, A.; Shang, J.; Shen, Z.; Hou, D.; Zhou, Y.; Chen, Q.; Ok, Y. S. Design and Fabrication of Exfoliated Mg/Al Layered Double Hydroxides on Biochar Support. *J. Cleaner Prod.* **2021**, *289*, 125142.
(372) Sun, H.; Miao, Y.; Wu, T.; Wang, Q. Exfoliation of Bimetallic (Ni, Co) Carbonate Hydroxide Nanowires by Ar Plasma for Enhanced Oxygen Evolution. *Chem. Commun.* **2020**, *56* (6), 872−875.
(373) Liu, X.; Liang, J.; Song, X.; Yang, H.; Li, X.; Dai, H.; Song, Y.; Liu, Y.; Hu, J.; Pan, X.; et al. Enhanced Water Dissociation Performance of graphitic-C_3N_4 Assembled with ZnCr-layered Double Hydroxide. *Chem. Eng. J.* **2018**, *337*, 560−566.
(374) Liu, J.; Li, J.; Bing, X.; Ng, D. H.; Cui, X.; Ji, F.; Kionga, D. D. ZnCr-LDH/N-doped Graphitic Carbon-Incorporated g-C_3N_4 2D/2D Nanosheet Heterojunction with Enhanced Charge Transfer for Photocatalysis. *Mater. Res. Bull.* **2018**, *102*, 379−390.
(375) Luo, B.; Song, R.; Jing, D. ZnCr-LDH Nanosheets Modified Graphitic Carbon Nitride for Enhanced Photocatalytic Hydrogen Production. *Int. J. Hydrogen Energy* **2017**, *42* (37), 23427−23436.
(376) Hasija, V.; Raizada, P.; Hosseini-Bandegharaei, A.; Singh, P.; Nguyen, V.-H. Synthesis and Photocatalytic Activity of Ni-Fe Layered Double Hydroxide Modified Sulphur Doped Graphitic Carbon Nitride (SGCN/Ni-Fe LDH) Photocatalyst for 2, 4-Dinitrophenol Degradation. *Top. Catal.* **2020**, *63* (11), 1030−1045.
(377) Chen, Y.; Xu, L.; Dong, J.; Yan, P.; Chen, F.; Qian, J.; Li, H. An Enhanced Photoelectrochemical Ofloxacin Aptasensor using NiFe Layered Double Hydroxide/Graphitic Carbon Nitride Heterojunction. *Electrochim. Acta* **2021**, *368*, 137595.
(378) Si, H.; Deng, Q.; Yin, C.; Tavakoli, M. M.; Zhang, J.; Kong, J. Graphdiyne Coupled with g-C_3N_4/NiFe-Layered Double Hydroxide, a Layered Nanohybrid for Highly Efficient Photoelectrochemical Water Oxidation. *Adv. Mater. Interfaces* **2020**, *7* (8), 1902083.
(379) Zhang, J.; Zhu, Q.; Wang, L.; Nasir, M.; Cho, S.-H.; Zhang, J. g-C_3N_4/CoAl-LDH 2D/2D Hybrid Heterojunction for Boosting Photocatalytic Hydrogen Evolution. *Int. J. Hydrogen Energy* **2020**, *45* (41), 21331−21340.
(380) Tripathi, A.; Narayanan, S. Stimulation of n-π^* Transition of g-C_3N_4 Through ZnAl-Layered Double Hydroxide for Solar Light Assisted Phenol Degradation. *Mater. Sci. Semicond. Process.* **2020**, *108*, 104892.
(381) Guru, S.; Kumar, S.; Bellamkonda, S.; Gangavarapu, R. R. Synthesis of CuTi-LDH Supported on g-C_3N_4 for Electrochemical and Photoelectrochemical Oxygen Evolution Reactions. *Int. J. Hydrogen Energy* **2021**, *46* (30), 16414−16430.
(382) Huang, Z.; Song, H.; Li, A.; An, Z.; Zhang, K.; Xiang, X.; Shu, X.; He, J. Z-Scheme ZnM-LDHs/g-C3N4 (M= Al, Cr) Photocatalysts: Their Desulfurization Performance and Mechanism for Model Oil with Air. *Energy Fuels* **2020**, *34* (11), 14676−14687.
(383) Ou, B.; Wang, J.; Wu, Y.; Zhao, S.; Wang, Z. Efficient Removal of Cr(VI) by Magnetic and Recyclable Calcined CoFe-LDH/g-C_3N_4 via the Synergy of Adsorption and Photocatalysis under Visible Light. *Chem. Eng. J.* **2020**, *380*, 122600.
(384) Li, X.; Yu, Z.; Shao, L.; Zeng, H.; Liu, Y.; Feng, X. A Novel Strategy to Construct a Visible-Light-Driven Z-Scheme (ZnAl-LDH with Active Phase/g-C_3N_4) Heterojunction Catalyst via Polydopamine Bridge (A Similar "Bridge" Structure). *J. Hazard. Mater.* **2020**, *386*, 121650.
(385) Wu, H.; Yang, X.; Zhang, H.; Shi, D.; Xia, Y.; Zhang, W.; Pan, Z.; Wang, D. Removal of Tetracycline, 2, 4-Dichlorophenol, and Glyphosate from Aqueous Solution by Novel Humic Acid-Modified g-C_3N_4-Supported Hydrotalcite-like Compounds: Kinetics, Isotherm, Thermodynamics, and Reusability Exploration. *J. Chem. Eng. Data* **2020**, *65* (10), 4914−4923.
(386) Zeng, H.; Zhang, H.; Deng, L.; Shi, Z. Peroxymonosulfate-Assisted Photocatalytic Degradation of Sulfadiazine using Self-

assembled Multi-layered CoAl-LDH/g-C_3N_4 Heterostructures: Performance, Mechanism and Eco-toxicity Evaluation. *J. Water Process Eng.* **2020**, *33*, 101084.
(387) Guru, S.; G, R. R. Bismuth Oxycarbonate Grafted NiFe-LDH Supported on g-C_3N_4 as Bifunctional Catalyst for Photoelectrochemical Water Splitting. *Int. J. Hydrogen Energy* **2021**, *46* (22), 12145−12157.
(388) Ni, J.; Xue, J.; Xie, L.; Shen, J.; He, G.; Chen, H. Construction of Magnetically Separable NiAl-LDH/Fe_3O_4-RGO Nanocomposites with Enhanced Photocatalytic Performance Under Visible Light. *Phys. Chem. Chem. Phys.* **2018**, *20* (1), 414−421.
(389) Li, S.; Wang, L.; Li, Y.; Zhang, L.; Wang, A.; Xiao, N.; Gao, Y.; Li, N.; Song, W.; Ge, L.; et al. Novel Photocatalyst Incorporating Ni-Co Layered Double Hydroxides with P-doped CdS for Enhancing Photocatalytic Activity Towards Hydrogen Evolution. *Appl. Catal., B* **2019**, *254*, 145−155.
(390) Nayak, S.; Parida, K. Dynamics of Charge-Transfer Behavior in A Plasmon-induced Quasi-Type-II p-n/n-n Dual Heterojunction in Ag@Ag_3PO_4/g-C_3N_4/NiFe LDH Nanocomposites for Photocatalytic Cr(VI) Reduction and Phenol Oxidation. *ACS Omega* **2018**, *3* (7), 7324−7343.
(391) Xu, S.-M.; Yan, H.; Wei, M. Band Structure Engineering of Transition-metal-based Layered Double Hydroxides Toward Photocatalytic Oxygen Evolution from Water: A Theoretical-Experimental Combination Study. *J. Phys. Chem. C* **2017**, *121* (5), 2683−2695.
(392) Das, S.; Patnaik, S.; Parida, K. Dynamic Charge Transfer Through Fermi Level Equilibration in the p-$CuFe_2O_4$/n-NiAl-LDH Interface Towards Photocatalytic Application. *Catal. Sci. Technol.* **2020**, *10* (18), 6285−6298.
(393) Miao, Y.-f.; Guo, R.-t.; Gu, J.-w.; Liu, Y.-z.; Wu, G.-l.; Duan, C.-p.; Zhang, X.-d.; Pan, W.-g. Fabrication of β-In_2S_3/NiAl-LDH Heterojunction Photocatalyst with Enhanced Separation of Charge Carriers for Efficient CO_2 Photocatalytic Reduction. *Appl. Surf. Sci.* **2020**, *527*, 146792.
(394) Tonda, S.; Jo, W.-K. Plasmonic Ag Nanoparticles Decorated NiAl-Layered Double Hydroxide/Graphitic Carbon Nitride Nanocomposites for Efficient Visible-Light-Driven Photocatalytic Removal of Aqueous Organic Pollutants. *Catal. Today* **2018**, *315*, 213−222.
(395) Salehi, G.; Abazari, R.; Mahjoub, A. R. Visible-Light-Induced Graphitic-C_3N_4@Nickel-Aluminum Layered Double Hydroxide Nanocomposites with Enhanced Photocatalytic Activity for Removal of Dyes in Water. *Inorg. Chem.* **2018**, *57* (14), 8681−8691.
(396) Tonda, S.; Kumar, S.; Bhardwaj, M.; Yadav, P.; Ogale, S. g-C_3N_4/NiAl-LDH 2D/2D Hybrid Heterojunction for High-Performance Photocatalytic Reduction of CO_2 into Renewable Fuels. *ACS Appl. Mater. Interfaces* **2018**, *10* (3), 2667−2678.
(397) Bhuvaneswari, K.; Palanisamy, G.; Pazhanivel, T.; Maiyalagan, T.; Bharathi, G. Photodegradation Activity of Nitrogen-rich Graphitic Carbon Nitride Intercalated ZnO\Mg-Al Layered Double Hydroxide Ternary Nanocomposites on Methylene Blue Dye. *ChemistrySelect* **2019**, *4* (11), 2982−2990.
(398) Feizi, H.; Bagheri, R.; Song, Z.; Shen, J.-R.; Allakhverdiev, S. I.; Najafpour, M. M. Cobalt/Cobalt Oxide Surface for Water Oxidation. *ACS Sustainable Chem. Eng.* **2019**, *7* (6), 6093−6105.
(399) Zhang, G.; Zang, S.; Lin, L.; Lan, Z.-A.; Li, G.; Wang, X. Ultrafine Cobalt Catalysts on Covalent Carbon Nitride Frameworks for Oxygenic Photosynthesis. *ACS Appl. Mater. Interfaces* **2016**, *8* (3), 2287−2296.
(400) Wu, Y.; Wang, H.; Sun, Y.; Xiao, T.; Tu, W.; Yuan, X.; Zeng, G.; Li, S.; Chew, J. W. Photogenerated Charge Transfer via Interfacial Internal Electric Field for Significantly Improved Photocatalysis in Direct Z-Scheme Oxygen-doped Carbon Nitrogen/CoAl-Layered Double Hydroxide Heterojunction. *Appl. Catal., B* **2018**, *227*, 530−540.
(401) Jo, W.-K.; Tonda, S. Novel CoAl-LDH/g-C_3N4/RGO Ternary Heterojunction with Notable 2D/2D/2D Configuration for Highly Efficient Visible-Light-Induced Photocatalytic Elimination of Dye and Antibiotic Pollutants. *J. Hazard. Mater.* **2019**, *368*, 778−787.
(402) Zhang, G.; Zang, S.; Wang, X. Layered $Co(OH)_2$ Deposited Polymeric Carbon Nitrides for Photocatalytic Water Oxidation. *ACS Catal.* **2015**, *5* (2), 941−947.
(403) Zhang, Y.; Cui, B.; Zhao, C.; Lin, H.; Li, J. Co-Ni Layered Double Hydroxides for Water Oxidation in Neutral Electrolyte. *Phys. Chem. Chem. Phys.* **2013**, *15* (19), 7363−7369.
(404) Wang, C.; Jiahui, Z.; Caiyan, S.; Dandan, C. Facile Synthesis of Ni-Co LDH Nanocages with Improved Electrocatalytic Activity for Water Oxidation Reaction. *Int. J. Electrochem. Sci.* **2017**, *12*, 10003−10014.
(405) Zhang, M.; Luo, Z.; Zhou, M.; Zhang, G.; Alamry, K. A.; Taib, L. A.; Asiri, A. M.; Wang, X. Ni-Co Layered Double Hydroxides Cocatalyst for Sustainable Oxygen Photosynthesis. *Appl. Catal., B* **2017**, *210*, 454−461.
(406) Xiang, W.; Tress, W. Review on Recent Progress of All-Inorganic Metal Halide Perovskites and Solar Cells. *Adv. Mater.* **2019**, *31* (44), 1902851.
(407) Khan, R.; Mehran, M. T.; Naqvi, S. R.; Khoja, A. H.; Mahmood, K.; Shahzad, F.; Hussain, S. Role of Perovskites as a Bifunctional Catalyst for Electrochemical Water Splitting: A Review. *Int. J. Energy Res.* **2020**, *44* (12), 9714−9747.
(408) Wang, K.; Subhani, W. S.; Wang, Y.; Zuo, X.; Wang, H.; Duan, L.; Liu, S. Metal Cations in Efficient Perovskite Solar Cells: Progress and Perspective. *Adv. Mater.* **2019**, *31* (50), 1902037.
(409) Grancini, G.; Nazeeruddin, M. K. Dimensional Tailoring of Hybrid Perovskites for Photovoltaics. *Nat. Rev. Mater.* **2019**, *4* (1), 4−22.
(410) Parida, B.; Yoon, S.; Jeong, S. M.; Cho, J. S.; Kim, J.-K.; Kang, D.-W. Recent Progress on Cesium Lead/Tin Halide-based Inorganic Perovskites for Stable and Efficient Solar Cells: A Review. *Sol. Energy Mater. Sol. Cells* **2020**, *204*, 110212.
(411) Singh, M.; Sinha, I. Halide Perovskite-based Photocatalysis Systems for Solar-Driven Fuel Generation. *Sol. Energy* **2020**, *208*, 296−311.
(412) Zhang, Z.; Liang, Y.; Huang, H.; Liu, X.; Li, Q.; Chen, L.; Xu, D. Stable and Highly Efficient Photocatalysis with Lead-Free Double-Perovskite of $Cs_2AgBiBr_6$. *Angew. Chem., Int. Ed.* **2019**, *58* (22), 7263−7267.
(413) Zhu, X.; Lin, Y.; San Martin, J.; Sun, Y.; Zhu, D.; Yan, Y. Lead Halide Perovskites for Photocatalytic Organic Synthesis. *Nat. Commun.* **2019**, *10* (1), 2843.
(414) deQuilettes, D. W.; Frohna, K.; Emin, D.; Kirchartz, T.; Bulovic, V.; Ginger, D. S.; Stranks, S. D. Charge-Carrier Recombination in Halide Perovskites: Focus Review. *Chem. Rev.* **2019**, *119* (20), 11007−11019.
(415) Fan, Y.; Meng, H.; Wang, L.; Pang, S. Review of Stability Enhancement for Formamidinium-Based Perovskites. *Solar RRL* **2019**, *3* (9), 1900215.
(416) Li, Z.; Kong, L.; Huang, S.; Li, L. Highly Luminescent and Ultrastable $CsPbBr_3$ Perovskite Quantum Dots Incorporated into A Silica/Alumina Monolith. *Angew. Chem.* **2017**, *129* (28), 8246−8250.
(417) Xu, Y.-F.; Yang, M.-Z.; Chen, B.-X.; Wang, X.-D.; Chen, H.-Y.; Kuang, D.-B.; Su, C.-Y. A $CsPbBr_3$ Perovskite Quantum Dot/Graphene Oxide Composite for Photocatalytic CO_2 Reduction. *J. Am. Chem. Soc.* **2017**, *139* (16), 5660−5663.
(418) Liao, J.-F.; Xu, Y.-F.; Wang, X.-D.; Chen, H.-Y.; Kuang, D.-B. $CsPbBr_3$ Nanocrystal/MO_2 (M= Si, Ti, Sn) Composites: Insight into Charge-Carrier Dynamics and Photoelectrochemical Applications. *ACS Appl. Mater. Interfaces* **2018**, *10* (49), 42301−42309.
(419) Wang, W.; Xu, M.; Xu, X.; Zhou, W.; Shao, Z. Perovskite Oxide Based Electrodes for High-Performance Photoelectrochemical Water Splitting. *Angew. Chem., Int. Ed.* **2020**, *59* (1), 136−152.
(420) Schanze, K. S.; Kamat, P. V.; Yang, P.; Bisquert, J. Progress in Perovskite Photocatalysis. *In ACS Publications: ACS Energy Lett.* **2020**, *5*, 2602−2604.
(421) Li, Q.; Lu, M.; Wang, W.; Zhao, W.; Chen, G.; Shi, H. Fabrication of 2D/2D g-C_3N_4/Au/Bi_2WO_6 Z-Scheme Photocatalyst with Enhanced Visible-Light-Driven Photocatalytic Activity. *Appl. Surf. Sci.* **2020**, *508*, 144182.

(422) Guo, W.; Fan, K.; Zhang, J.; Xu, C. 2D/2D Z-Scheme Bi_2WO_6/Porous-g-C_3N_4 with Synergy of Adsorption and Visible-Light-Driven Photodegradation. *Appl. Surf. Sci.* **2018**, *447*, 125−134.
(423) Wang, J.; Tang, L.; Zeng, G.; Deng, Y.; Liu, Y.; Wang, L.; Zhou, Y.; Guo, Z.; Wang, J.; Zhang, C. Atomic Scale g-C_3N_4/Bi_2WO_6 2D/2D Heterojunction with Enhanced Photocatalytic Degradation of Ibuprofen under Visible Light Irradiation. *Appl. Catal., B* **2017**, *209*, 285−294.
(424) Xu, J.; Sun, C.; Wang, Z.; Hou, Y.; Ding, Z.; Wang, S. Perovskite Oxide $LaNiO_3$ Nanoparticles for Boosting H_2 Evolution over Commercial CdS with Visible Light. *Chem. - Eur. J.* **2018**, *24* (69), 18512−18517.
(425) Grabowska, E. Selected Perovskite Oxides: Characterization, Preparation and Photocatalytic Properties-A Review. *Appl. Catal., B* **2016**, *186*, 97−126.
(426) Shi, R.; Waterhouse, G. I.; Zhang, T. Recent Progress in Photocatalytic CO_2 Reduction over Perovskite Oxides. *Solar RRL* **2017**, *1* (11), 1700126.
(427) Zeng, S.; Kar, P.; Thakur, U. K.; Shankar, K. A Review on Photocatalytic CO_2 Reduction using Perovskite Oxide Nanomaterials. *Nanotechnology* **2018**, *29* (5), 052001.
(428) Nguyen, V.-H.; Do, H. H.; Van Nguyen, T.; Singh, P.; Raizada, P.; Sharma, A.; Sana, S. S.; Grace, A. N.; Shokouhimehr, M.; Ahn, S. H.; et al. Perovskite Oxide-based Photocatalysts for Solar-Driven Hydrogen Production: Progress and Perspectives. *Sol. Energy* **2020**, *211*, 584−599.
(429) Jiang, Z.; Wang, B.; Li, Y.; Chan, H. S.; Sun, H.; Wang, T.; Li, H.; Yuan, S.; Leung, M. K.; Lu, A.; et al. Solar-Light-Driven Rapid Water Disinfection by Ultrathin Magnesium Titanate/Carbon Nitride Hybrid Photocatalyst: Band Structure Analysis and Role of Reactive Oxygen Species. *Appl. Catal., B* **2019**, *257*, 117898.
(430) Guo, R.; Zhang, X.; Li, B.; Zhang, H.; Gou, J.; Cheng, X. 2D-Bi_2MoO_6/2D-g-C_3N_4 Nanosheet Heterojunction Composite: Synthesis and Enhanced Visible Light Photocatalytic Mechanism. *J. Phys. D: Appl. Phys.* **2019**, *52* (8), 085302.
(431) Li, B.; Lai, C.; Qin, L.; Chu, C.; Zhang, M.; Liu, S.; Liu, X.; Yi, H.; He, J.; Li, L.; et al. Anchoring Single-unit-cell Defect-rich Bismuth Molybdate Layers on Ultrathin Carbon Nitride Nanosheet with Boosted Charge Transfer for Efficient Photocatalytic Ciprofloxacin Degradation. *J. Colloid Interface Sci.* **2020**, *560*, 701−713.
(432) Jiang, D.; Ma, W.; Xiao, P.; Shao, L.; Li, D.; Chen, M. Enhanced Photocatalytic Activity of Graphitic Carbon Nitride/Carbon Nanotube/Bi_2WO_6 Ternary Z-scheme Heterojunction with Carbon Nanotube as Efficient Electron Mediator. *J. Colloid Interface Sci.* **2018**, *512*, 693−700.
(433) Vasala, S.; Karppinen, M. $A_2B'B''O_6$ Perovskites: A Review. *Prog. Solid State Chem.* **2015**, *43* (1−2), 1−36.
(434) Kubicek, M.; Bork, A. H.; Rupp, J. L. Perovskite Oxides-A review on A Versatile Material Class for Solar-to-Fuel Conversion Processes. *J. Mater. Chem. A* **2017**, *5* (24), 11983−12000.
(435) Chen, X.; Xu, J.; Xu, Y.; Luo, F.; Du, Y. Rare Earth Double Perovskites: A fertile Soil in the Field of Perovskite Oxides. *Inorg. Chem. Front.* **2019**, *6* (9), 2226−2238.
(436) Idris, A. M.; Liu, T.; Hussain Shah, J.; Malik, A. S.; Zhao, D.; Han, H.; Li, C. Sr_2NiWO_6 Double Perovskite Oxide as a Novel Visible Light Responsive Water Oxidation Photocatalyst. *ACS Appl. Mater. Interfaces* **2020**, *12*, 25938−25948.
(437) Han, B.; Stoerzinger, K. A.; Tileli, V.; Gamalski, A. D.; Stach, E. A.; Shao-Horn, Y. Nanoscale Structural Oscillations in Perovskite Oxides Induced by Oxygen Evolution. *Nat. Mater.* **2017**, *16* (1), 121−126.
(438) Xiao, H.; Liu, P.; Wang, W.; Ran, R.; Zhou, W.; Shao, Z. Fuels, Ruddlesden-Popper Perovskite Oxides for Photocatalysis-Based Water Splitting and Wastewater Treatment. *Energy Fuels* **2020**, *34* (8), 9208−9221.
(439) Hu, Y.; Mao, L.; Guan, X.; Tucker, K. A.; Xie, H.; Wu, X.; Shi, J. Layered Perovskite Oxides and Their Derivative Nanosheets Adopting Different Modification Strategies Towards Better Photocatalytic Performance of Water Splitting. *Renewable Sustainable Energy Rev.* **2020**, *119*, 109527.
(440) Rodionov, I. A.; Zvereva, I. A. Photocatalytic Activity of Layered Perovskite-like Oxides in Practically Valuable Chemical Reactions. *Russ. Chem. Rev.* **2016**, *85* (3), 248.
(441) Verduzco, L.; Garcia-Diaz, R.; Oliva, J.; Martinez, A.; Gomez-Solis, C.; Garcia, C.; Fuentes, A.; Padmasree, K. Enhanced Photocatalytic Activity of Layered Perovskite Oxides $Sr_{2.7-x}Ca_xLn_{0.3}Fe_2O_{7-\delta}$ for MB Degradation. *Ceram. Int.* **2018**, *44* (14), 17079−17086.
(442) Wang, K.; Li, J.; Zhang, G. Ag-bridged Z-Scheme 2D/2D $Bi_5FeTi_3O_{15}$/g-C_3N_4 Heterojunction For Enhanced Photocatalysis: Mediator-induced Interfacial Charge Transfer and Mechanism Insights. *ACS Appl. Mater. Interfaces* **2019**, *11* (31), 27686−27696.
(443) Wang, K.; Li, Y.; Li, J.; Zhang, G. Boosting Interfacial Charge Separation of $Ba_5Nb_4O_{15}$/g-C_3N_4 Photocatalysts by 2D/2D Nanojunction Towards Efficient Visible-light Driven H_2 Generation. *Appl. Catal., B* **2020**, *263*, 117730.
(444) Liang, X.; Zhang, Y.; Li, D.; Wen, B.; Jiang, D.; Chen, M. 2D/2D BiOCl/$K^+Ca_2Nb_3O_{10}$- Heterostructure with Z-Scheme Charge Carrier Transfer Pathways for Tetracycline Degradation under Simulated Solar Light. *Appl. Surf. Sci.* **2019**, *466*, 863−873.
(445) Ma, X.; Jiang, D.; Xiao, P.; Jin, Y.; Meng, S.; Chen, M. 2D/2D Heterojunctions of WO_3 Nanosheet/$K^+Ca_2Nb_3O_{10}$- Ultrathin Nanosheet with Improved Charge Separation Efficiency for Significantly Boosting Photocatalysis. *Catal. Sci. Technol.* **2017**, *7* (16), 3481−3491.
(446) Gu, W.; Li, X.; Zhang, W.; Wang, J.; Yin, X.; Zhu, L.; Chen, Z.; Zou, W.; Fu, Z.; Lu, Y. Self-limited Ion-exchange Grown $Bi_6Fe_2Ti_3O_{18}$-BiOBr Ferroelectric Heterostructure and the Enhanced Photocatalytic Oxygen Evolution. *Appl. Surf. Sci.* **2019**, *479*, 137−147.
(447) Luo, D.; Huang, Y.; Zhao, Y.; Fang, Y.; Li, Z.; Guo, Q.; Wei, Y.; Fan, L.; Wu, J. Visible-Light-Driven $HSr_2Nb_3O_{10}$/CdS Heterojunctions for High Hydrogen Evolution Activity. *Int. J. Hydrogen Energy* **2020**, *45* (4), 2896−2908.
(448) Ding, Y.; Luo, D.; Huang, Y.; Rong, B.; Chen, X.; Wei, Y.; Fan, L.; Wu, J. Microwave-Mechanochemistry-Assisted Synthesis of Z-Scheme $HSr_2Nb_3O_{10}$/WO_3 Heterojunctions for Improved Simulated Sunlight Driven Photocatalytic Activity. *J. Environ. Chem. Eng.* **2021**, *9*, 104624.
(449) Gao, X.; Feng, Y.; Dong, P.; Zhang, B.; Chen, T.; Chen, X.; Liu, C.; Xi, X.; Zou, Z. Rational Design 2D/2D BiOCl/$H^+Ti_2NbO_7$- Heterojunctions for Enhanced Photocatalytic Degradation Activity. *Appl. Surf. Sci.* **2020**, *521*, 146334.
(450) Xu, Y.; You, Y.; Huang, H.; Guo, Y.; Zhang, Y. Bi_4NbO_8Cl {001} Nanosheets Coupled with g-C_3N_4 as 2D/2D Heterojunction for Photocatalytic Degradation and CO_2 Reduction. *J. Hazard. Mater.* **2020**, *381*, 121159.
(451) Kumar, P.; Mulmi, S.; Laishram, D.; Alam, K. M.; Thakur, U. K.; Thangadurai, V.; Shankar, K. Water-Splitting Photoelectrodes Consisting of Heterojunctions of Carbon Nitride with A P-Type Low Bandgap Double Perovskite Oxide. *Nanotechnology* **2021**, *32*, 485407.
(452) Jiang, D.; Wang, T.; Xu, Q.; Li, D.; Meng, S.; Chen, M. Perovskite Oxide Ultrathin Nanosheets/g-C_3N_4 2D-2D Heterojunction Photocatalysts with Significantly Enhanced Photocatalytic Activity Towards the Photodegradation of Tetracycline. *Appl. Catal., B* **2017**, *201*, 617−628.
(453) Shi, J.; Mao, L.; Cai, C.; Li, G.; Cheng, C.; Zheng, B.; Hu, Y.; Huang, Z.; Hu, X.; Żyła, G. One-pot Fabrication of 2D/2D $HCa_2Nb_3O_{10}$/g-C_3N_4 Type II Heterojunctions Towards Enhanced Photocatalytic H_2 Evolution under Visible-Light Irradiation. *Catal. Sci. Technol.* **2020**, *10* (17), 5896−5902.
(454) Sun, Y.; Cheng, H.; Gao, S.; Sun, Z.; Liu, Q.; Liu, Q.; Lei, F.; Yao, T.; He, J.; Wei, S.; et al. Freestanding tin Disulfide Single-layers Realizing Efficient Visible-light Water Splitting. *Angew. Chem., Int. Ed.* **2012**, *51* (35), 8727−8731.
(455) Rahmanian, E.; Malekfar, R.; Pumera, M. Nanohybrids of Two-Dimensional Transition-Metal Dichalcogenides and Titanium

Dioxide for Photocatalytic Applications. *Chem. - Eur. J.* **2018**, *24* (1), 18−31.
(456) Yuan, Y.-J.; Chen, D.; Yu, Z.-T.; Zou, Z.-G. Cadmium Sulfide-based Nanomaterials for Photocatalytic Hydrogen Production. *J. Mater. Chem. A* **2018**, *6* (25), 11606−11630.
(457) DiMeglio, J. L.; Bartlett, B. M. Interplay of Corrosion and Photocatalysis during Nonaqueous Benzylamine Oxidation on Cadmium Sulfide. *Chem. Mater.* **2017**, *29* (17), 7579−7586.
(458) Li, J.-Y.; Li, Y.-H.; Qi, M.-Y.; Lin, Q.; Tang, Z.-R.; Xu, Y.-J. Selective Organic Transformations over Cadmium Sulfide-Based Photocatalysts. *ACS Catal.* **2020**, *10* (11), 6262−6280.
(459) Liu, M.; Jing, D.; Zhou, Z.; Guo, L. Twin-Induced One-Dimensional Homojunctions Yield High Quantum Efficiency for Solar Hydrogen Generation. *Nat. Commun.* **2013**, *4* (1), 2278.
(460) Su, D.; Ran, J.; Zhuang, Z.; Chen, C.; Qiao, S.; Li, Y.; Wang, G. Atomically Dispersed Ni in Cadmium-Zinc Sulfide Quantum Dots for High-Performance Visible-light Photocatalytic Hydrogen Production. *Sci. Adv.* **2020**, *6* (33), No. eaaz8447.
(461) Chen, M.-M.; Xue, H.-G.; Guo, S.-P. Multinary Metal Chalcogenides with Tetrahedral Structures for Second-order Nonlinear Optical, Photocatalytic, and Photovoltaic Applications. *Coord. Chem. Rev.* **2018**, *368*, 115−133.
(462) Liu, Y. L.; Yang, C. L.; Wang, M. S.; Ma, X. G.; Yi, Y. G. Ternary Chalcogenides $XGaS_2$ (X= Ag or Cu) for Photocatalytic Hydrogen Generation from Water Splitting under Irradiation of Visible Light. *Int. J. Quantum Chem.* **2020**, *120* (10), No. e26166.
(463) Guo, S.-P.; Guo, G.-C. Crystal Structure and Magnetic and Photocatalytic Properties of a New Ternary Rare-earth Mixed Chalcogenide, $Dy_4S_4Te_3$. *J. Mater. Chem. A* **2014**, *2* (48), 20621−20628.
(464) Nie, L.; Zhang, Q. Recent Progress in Crystalline Metal Chalcogenides as Efficient Photocatalysts for Organic Pollutant Degradation. *Inorg. Chem. Front.* **2017**, *4* (12), 1953−1962.
(465) Xu, W.; Wang, R.; Zheng, B.; Wu, X.; Xu, H. Two-Dimensional Li-Based Ternary Chalcogenides for Photocatalysis. *J. Phys. Chem. Lett.* **2019**, *10* (20), 6061−6066.
(466) Lim, J. Y.; Kim, M.; Jeong, Y.; Ko, K. R.; Yu, S.; Shin, H. G.; Moon, J. Y.; Choi, Y. J.; Yi, Y.; Kim, T.; et al. Van der Waals Junction Field Effect Transistors with Both n-and p-Channel Transition Metal Dichalcogenides. *2D Mater. Appl.* **2018**, *2* (1), 37.
(467) Ashraf, W.; Bansal, S.; Singh, V.; Barman, S.; Khanuja, M. BiOCl/WS_2 Hybrid Nanosheet (2D/2D) Heterojunctions for Visible-Light-Driven Photocatalytic Degradation of Organic/inorganic Water Pollutants. *RSC Adv.* **2020**, *10* (42), 25073−25088.
(468) Huang, Y. L.; Zheng, Y. J.; Song, Z.; Chi, D.; Wee, A. T.; Quek, S. Y. The Organic-2D Transition Metal Dichalcogenide Heterointerface. *Chem. Soc. Rev.* **2018**, *47* (9), 3241−3264.
(469) Guo, Y.; Robertson, J. Band Engineering in Transition Metal Dichalcogenides: Stacked versus Lateral Heterostructures. *Appl. Phys. Lett.* **2016**, *108* (23), 233104.
(470) Swain, G.; Sultana, S.; Parida, K. Constructing a Novel Surfactant-free MoS_2 Nanosheet Modified $MgIn_2S_4$ Marigold Microflower: An Efficient Visible-Light Driven 2D-2D pn Heterojunction Photocatalyst toward HER and pH Regulated NRR. *ACS Sustainable Chem. Eng.* **2020**, *8* (12), 4848−4862.
(471) Li, M.; Chen, J.-S.; Cotlet, M. Light-Induced Interfacial Phenomena in Atomically Thin 2D van der Waals Material Hybrids and Heterojunctions. *ACS Energy Lett.* **2019**, *4* (9), 2323−2335.
(472) Bettis Homan, S.; Sangwan, V. K.; Balla, I.; Bergeron, H.; Weiss, E. A.; Hersam, M. C. Ultrafast Exciton Dissociation and Long-lived Charge Separation in a Photovoltaic Pentacene-MoS_2 van der Waals Heterojunction. *Nano Lett.* **2017**, *17* (1), 164−169.
(473) Padgaonkar, S.; Amsterdam, S. H.; Bergeron, H.; Su, K.; Marks, T. J.; Hersam, M. C.; Weiss, E. A. Molecular-Orientation-Dependent Interfacial Charge Transfer in Phthalocyanine/MoS_2 Mixed-dimensional Heterojunctions. *J. Phys. Chem. C* **2019**, *123* (21), 13337−13343.
(474) Yang, S.; Li, W.; Ye, C.; Wang, G.; Tian, H.; Zhu, C.; He, P.; Ding, G.; Xie, X.; Liu, Y.; et al. C_3N-A 2D Crystalline, Hole-free, Tunable-Narrow-Bandgap Semiconductor with Ferromagnetic Properties. *Adv. Mater.* **2017**, *29* (16), 1605625.
(475) Bafekry, A.; Stampfl, C.; Akgenc, B.; Ghergherehchi, M. Control of C_3N_4 and C_4N_3 Carbon Nitride Nanosheets' Electronic and Magnetic Properties through Embedded Atoms. *Phys. Chem. Chem. Phys.* **2020**, *22* (4), 2249−2261.
(476) Bafekry, A.; Yagmurcukardes, M.; Akgenc, B.; Ghergherehchi, M.; Nguyen, C. V. Van der Waals Heterostructures of MoS_2 and Janus MoSSe Monolayers on Graphitic Boron-carbon-nitride (BC_3, C_3N, C_3N_4 and C_4N_3) Nanosheets: A First-Principles Study. *J. Phys. D: Appl. Phys.* **2020**, *53* (35), 355106.
(477) Xu, J.; Mahmood, J.; Dou, Y.; Dou, S.; Li, F.; Dai, L.; Baek, J. B. 2D Frameworks of C_2N and C_3N as New Anode Materials for Lithium-ion Batteries. *Adv. Mater.* **2017**, *29* (34), 1702007.
(478) Zhu, L.; Xue, Q.; Li, X.; Wu, T.; Jin, Y.; Xing, W. C_2N: An Excellent Two-dimensional Monolayer Membrane for He Separation. *J. Mater. Chem. A* **2015**, *3* (42), 21351−21356.
(479) Kumar, R.; Das, D.; Singh, A. K. C_2N/WS_2 van der Waals Type-II Heterostructure as a Promising Water Splitting Photocatalyst. *J. Catal.* **2018**, *359*, 143−150.
(480) Guan, Z.; Lian, C.-S.; Hu, S.; Ni, S.; Li, J.; Duan, W. Tunable Structural, Electronic, and Optical Properties of Layered Two-dimensional C_2N and MoS_2 van der Waals Heterostructure as Photovoltaic Material. *J. Phys. Chem. C* **2017**, *121* (6), 3654−3660.
(481) Wang, B.; Yuan, H.; Chang, J.; Chen, X.; Chen, H. Two Dimensional InSe/C_2N van der Waals Heterojunction as Enhanced Visible-Light-Responsible Photocatalyst for Water Splitting. *Appl. Surf. Sci.* **2019**, *485*, 375−380.
(482) Zhang, X.; Chen, A.; Zhang, Z.; Jiao, M.; Zhou, Z. Rational design of C_2N-based Type-II Heterojunctions for Overall Photocatalytic Water Splitting. *Nanoscale Adv.* **2019**, *1* (1), 154−161.
(483) Ashwin Kishore, M.; Larsson, K.; Ravindran, P. Two-Dimensional CdX/C2N (X= S, Se) Heterostructures as Potential Photocatalysts for Water Splitting: A DFT Study. *ACS Omega* **2020**, *5* (37), 23762−23768.
(484) Xu, X.; Luo, F.; Zhou, G.; Hu, J.; Zeng, H.; Zhou, Y. Self-Assembly Optimization of Cadmium/Molybdenum Sulfide Hybrids by Cation Coordination Competition Toward Extraordinarily Efficient Photocatalytic Hydrogen Evolution. *J. Mater. Chem. A* **2018**, *6* (38), 18396−18402.
(485) Li, Z.; Meng, X.; Zhang, Z. Recent Development on MoS_2-based Photocatalysis: A Review. *J. Photochem. Photobiol., C* **2018**, *35*, 39−55.
(486) Yu, M.; Zhao, S.; Feng, H.; Hu, L.; Zhang, X.; Zeng, Y.; Tong, Y.; Lu, X. Engineering thin MoS_2 Nanosheets on TiN Nanorods: Advanced Electrochemical Capacitor Electrode and Hydrogen Evolution Electrocatalyst. *ACS Energy Lett.* **2017**, *2* (8), 1862−1868.
(487) Wang, H.; Kong, D.; Johanes, P.; Cha, J. J.; Zheng, G.; Yan, K.; Liu, N.; Cui, Y. $MoSe_2$ and WSe_2 Nanofilms with Vertically Aligned Molecular Layers on Curved and Rough Surfaces. *Nano Lett.* **2013**, *13* (7), 3426−3433.
(488) Ding, Q.; Song, B.; Xu, P.; Jin, S. Efficient Electrocatalytic and Photoelectrochemical Hydrogen Generation using MoS_2 and Related Compounds. *Chem.* **2016**, *1* (5), 699−726.
(489) Nguyen, T. N.; Kampouri, S.; Valizadeh, B.; Luo, W.; Ongari, D.; Planes, O. l. M.; Züttel, A.; Smit, B.; Stylianou, K. C. Photocatalytic Hydrogen Generation from a Visible-Light-Responsive Metal-Organic Framework System: Stability versus Activity of Molybdenum Sulfide Cocatalysts. *ACS Appl. Mater. Interfaces* **2018**, *10* (36), 30035−30039.
(490) Venkata Subbaiah, Y.; Saji, K.; Tiwari, A. Atomically thin MoS_2: A Versatile Nongraphene 2D Material. *Adv. Funct. Mater.* **2016**, *26* (13), 2046−2069.
(491) Han, B.; Hu, Y. H. MoS_2 as A Co-catalyst for Photocatalytic Hydrogen Production from Water. *Energy Sci. Eng.* **2016**, *4* (5), 285−304.
(492) Liang, Z.; Shen, R.; Ng, Y. H.; Zhang, P.; Xiang, Q.; Li, X. A Review on 2D MoS_2 Cocatalysts in Photocatalytic H_2 Production. *J. Mater. Sci. Technol.* **2020**, *56*, 89−121.

https://doi.org/10.1021/acs.chemmater.1c03166
Chem. Mater. 2021, 33, 9012−9092

(493) Jiao, Y.; Hafez, A. M.; Cao, D.; Mukhopadhyay, A.; Ma, Y.; Zhu, H. Metallic MoS_2 for High Performance Energy Storage and Energy Conversion. *Small* **2018**, *14* (36), 1800640.
(494) Gupta, D.; Chauhan, V.; Kumar, R. A Comprehensive Review on Synthesis and Applications of Molybdenum Disulfide (MoS_2) Material: Past and Recent Developments. *Inorg. Chem. Commun.* **2020**, *121*, 108200.
(495) Goloveshkin, A. S.; Bushmarinov, I. S.; Korlyukov, A. A.; Buzin, M. I.; Zaikovskii, V. I.; Lenenko, N. D.; Golub, A. S. Stabilization of 1T-MoS_2 Sheets by Iimidazolium Molecules in Self-Assembling Hetero-layered Nanocrystals. *Langmuir* **2015**, *31* (32), 8953−8960.
(496) Somoano, R.; Hadek, V.; Rembaum, A. Alkali Metal Intercalates of Molybdenum Disulfide. *J. Chem. Phys.* **1973**, *58* (2), 697−701.
(497) Wang, X.; Shen, X.; Wang, Z.; Yu, R.; Chen, L. Atomic-Scale Clarification of Structural Transition of MoS_2 upon Sodium Intercalation. *ACS Nano* **2014**, *8* (11), 11394−11400.
(498) Liang, Z.; Guo, Y.; Xue, Y.; Cui, H.; Tian, J. 1T-phase MoS_2 Quantum Dots as a Superior Co-catalyst to Pt Decorated on Carbon Nitride Nanorods for Photocatalytic Hydrogen Evolution from Water. *Mater. Chem. Front.* **2019**, *3* (10), 2032−2040.
(499) Xu, H.; Yi, J.; She, X.; Liu, Q.; Song, L.; Chen, S.; Yang, Y.; Song, Y.; Vajtai, R.; Lou, J.; et al. 2D Heterostructure Comprised of Metallic 1T-MoS_2/Monolayer Og-C_3N_4 Towards Efficient Photocatalytic Hydrogen Evolution. *Appl. Catal., B* **2018**, *220*, 379−385.
(500) Kong, L.; Yan, J.; Liu, S. F. Carbonyl Linked Carbon Nitride Loading Few Layered MoS_2 for Boosting Photocatalytic Hydrogen Generation. *ACS Sustainable Chem. Eng.* **2019**, *7* (1), 1389−1398.
(501) Qian, X.; Ding, J.; Zhang, J.; Zhang, Y.; Wang, Y.; Kan, E.; Wang, X.; Zhu, J. Ultrathin Molybdenum Disulfide/Carbon Nitride Nanosheets with Abundant Active Sites for Enhanced Hydrogen Evolution. *Nanoscale* **2018**, *10* (4), 1766−1773.
(502) Dong, G.; Qiu, P.; Meng, F.; Wang, Y.; He, B.; Yu, Y.; Liu, X.; Li, Z. Facile Synthesis of Sulfur-doped Polymeric Carbon Nitride/MoS_2 Face-to-Face Heterojunction for Highly Efficient Photocatalytic Interfacial Charge Separation. *Chem. Eng. J.* **2020**, *384*, 123330.
(503) Monga, D.; Ilager, D.; Shetti, N. P.; Basu, S.; Aminabhavi, T. M. 2D/2D Heterojunction of MoS_2/g-C_3N_4 Nanoflowers for Enhanced Visible-Light-Driven Photocatalytic and Electrochemical Degradation of Organic Pollutants. *J. Environ. Manage.* **2020**, *274*, 111208.
(504) Lu, X.; Xie, J.; Chen, X.; Li, X. Engineering MPx (M= Fe, Co or Ni) Interface Electron Transfer Channels for Boosting Photocatalytic H_2 Evolution over g-C_3N_4/MoS_2 Layered Heterojunctions. *Appl. Catal., B* **2019**, *252*, 250−259.
(505) Li, Y.; Wang, H.; Xie, L.; Liang, Y.; Hong, G.; Dai, H. MoS_2 Nanoparticles Grown on Graphene: An Advanced Catalyst for the Hydrogen Evolution Reaction. *J. Am. Chem. Soc.* **2011**, *133* (19), 7296−7299.
(506) Qin, L.-Z.; Lin, Y.-Z.; Dou, Y.-C.; Yang, Y.-J.; Li, K.; Li, T.; Liu, F. Toward Enhanced Photocatalytic Activity of Graphite Carbon Nitride Through Rational Design of Noble Metal-free Dual Cocatalyst. *Nanoscale* **2020**, *12*, 13829−13837.
(507) Hou, Y.; Laursen, A. B.; Zhang, J.; Zhang, G.; Zhu, Y.; Wang, X.; Dahl, S.; Chorkendorff, I. Layered Nanojunctions for Hydrogen-Evolution Catalysis. *Angew. Chem.* **2013**, *125* (13), 3709−3713.
(508) Yuan, Y.-J.; Shen, Z.; Wu, S.; Su, Y.; Pei, L.; Ji, Z.; Ding, M.; Bai, W.; Chen, Y.; Yu, Z.-T.; et al. Liquid Exfoliation of g-C_3N_4 Nanosheets to Construct 2D-2D MoS_2/g-C_3N_4 Photocatalyst for Enhanced Photocatalytic H_2 Production Activity. *Appl. Catal., B* **2019**, *246*, 120−128.
(509) Koutsouroubi, E. D.; Vamvasakis, I.; Papadas, I. T.; Drivas, C.; Choulis, S. A.; Kennou, S.; Armatas, G. S. Interface Engineering of MoS_2-Modified Graphitic Carbon Nitride Nano-photocatalysts for an Efficient Hydrogen Evolution Reaction. *ChemPlusChem* **2020**, *85* (7), 1379−1388.
(510) Tian, H.; Liu, M.; Zheng, W. Constructing 2D Graphitic Carbon Nitride Nanosheets/Layered MoS_2/Graphene Ternary Nanojunction with Enhanced Photocatalytic Activity. *Appl. Catal., B* **2018**, *225*, 468−476.
(511) Eftekhari, A. Tungsten Dichalcogenides (WS_2, WSe_2, and WTe_2): Materials Chemistry and Applications. *J. Mater. Chem. A* **2017**, *5* (35), 18299−18325.
(512) Mahler, B.; Hoepfner, V.; Liao, K.; Ozin, G. A. Colloidal Synthesis of 1T-WS_2 and 2H-WS_2 Nanosheets: Applications for Photocatalytic Hydrogen Evolution. *J. Am. Chem. Soc.* **2014**, *136* (40), 14121−14127.
(513) Zong, X.; Han, J.; Ma, G.; Yan, H.; Wu, G.; Li, C. Photocatalytic H_2 Evolution on CdS loaded with WS_2 as Cocatalyst under Visible Light Irradiation. *J. Phys. Chem. C* **2011**, *115* (24), 12202−12208.
(514) Zhang, Q.; Tai, M.; Zhou, Y.; Zhou, Y.; Wei, Y.; Tan, C.; Wu, Z.; Li, J.; Lin, H. Enhanced Photocatalytic Property of γ-$CsPbI_3$ Perovskite Nanocrystals with WS_2. *ACS Sustainable Chem. Eng.* **2020**, *8* (2), 1219−1229.
(515) Yi, J.; She, X.; Song, Y.; Mao, M.; Xia, K.; Xu, Y.; Mo, Z.; Wu, J.; Xu, H.; Li, H. Solvothermal Synthesis of Metallic 1T-WS_2: A Supporting Co-catalyst on Carbon Nitride Nanosheets Toward Photocatalytic Hydrogen Evolution. *Chem. Eng. J.* **2018**, *335*, 282−289.
(516) Li, H.; Wu, J.; Yin, Z.; Zhang, H. Preparation and Applications of Mechanically Exfoliated Single-layer and Multilayer MoS_2 and WSe_2 Nanosheets. *Acc. Chem. Res.* **2014**, *47* (4), 1067−1075.
(517) Xu, D.; Xu, P.; Zhu, Y.; Peng, W.; Li, Y.; Zhang, G.; Zhang, F.; Mallouk, T. E.; Fan, X. High Yield Exfoliation of WS_2 Crystals into 1−2 Layer Semiconducting Nanosheets and Efficient Photocatalytic Hydrogen Evolution from WS_2/CdS Nanorod Composites. *ACS Appl. Mater. Interfaces* **2018**, *10* (3), 2810−2818.
(518) Raza, F.; Yim, D.; Park, J. H.; Kim, H.-I.; Jeon, S.-J.; Kim, J.-H. Structuring Pd Nanoparticles on 2H-WS_2 Nanosheets Induces Excellent Photocatalytic Activity for Cross-Coupling Reactions under Visible Light. *J. Am. Chem. Soc.* **2017**, *139* (41), 14767−14774.
(519) Luo, S.; Dong, S.; Lu, C.; Yu, C.; Ou, Y.; Luo, L.; Sun, J.; Sun, J. Rational and Green Synthesis of Novel Two-Dimensional WS_2/MoS_2 Heterojunction via Direct Exfoliation in Ethanol-Water Targeting Advanced Visible-Light-Responsive Photocatalytic Performance. *J. Colloid Interface Sci.* **2018**, *513*, 389−399.
(520) Xiong, M.; Chai, B.; Yan, J.; Fan, G.; Song, G. Few-layer WS_2 Decorating $ZnIn_2S_4$ with Markedly Promoted Charge Separation and Photocatalytic H_2 Evolution Activity. *Appl. Surf. Sci.* **2020**, *514*, 145965.
(521) Fu, S.; Liu, X.; Yan, Y.; Li, L.; Liu, H.; Zhao, F.; Zhou, J. Few-layer WS_2 Modified BiOBr Nanosheets with Enhanced Broad-Spectrum Photocatalytic Activity Towards Various Pollutants Removal. *Sci. Total Environ.* **2019**, *694*, 133756.
(522) Li, L.; Cai, J.; Yan, Y.; Zhao, F.; Zhou, J. Flower-like direct Z-scheme WS_2/$Bi_2O_2CO_3$ Photocatalyst with Enhanced Photocatalytic Activity. *J. Alloys Compd.* **2019**, *810*, 151872.
(523) He, J.; Chen, L.; Yi, Z.-Q.; Au, C.-T.; Yin, S.-F. CdS Nanorods Coupled with WS_2 Nanosheets for Enhanced Photocatalytic Hydrogen Evolution Activity. *Ind. Eng. Chem. Res.* **2016**, *55* (30), 8327−8333.
(524) Archana, B.; Kottam, N.; Nayak, S.; Chandrasekhar, K. B.; Sreedhara, M. B. Superior Photocatalytic Hydrogen Evolution Performances of WS_2 over MoS_2 Integrated with CdS Nanorods. *J. Phys. Chem. C* **2020**, *124* (27), 14485−14495.
(525) Hill, H. M.; Rigosi, A. F.; Rim, K. T.; Flynn, G. W.; Heinz, T. F. Band Alignment in MoS_2/WS_2 Transition Metal Dichalcogenide Heterostructures Probed by Scanning Tunneling Microscopy and Spectroscopy. *Nano Lett.* **2016**, *16* (8), 4831−4837.
(526) Wu, Y.; Liu, Z.; Li, Y.; Chen, J.; Zhu, X.; Na, P. Construction of 2D-2D TiO_2 Nanosheet/Layered WS_2 Heterojunctions with Enhanced Visible-Light-Responsive Photocatalytic Activity. *Chin. J. Catal.* **2019**, *40* (1), 60−69.
(527) Shi, J.; Tong, R.; Zhou, X.; Gong, Y.; Zhang, Z.; Ji, Q.; Zhang, Y.; Fang, Q.; Gu, L.; Wang, X.; et al. Temperature-Mediated Selective Growth of MoS_2/WS_2 and WS_2/MoS_2 Vertical Stacks on Au Foils for

Direct Photocatalytic Applications. *Adv. Mater.* **2016**, *28* (48), 10664−10672.
(528) Reddy, D. A.; Park, H.; Ma, R.; Kumar, D. P.; Lim, M.; Kim, T. K. Heterostructured WS_2-MoS_2 Ultrathin Nanosheets Integrated on CdS Nanorods to Promote Charge Separation and Migration and Improve Solar-Driven Photocatalytic Hydrogen Evolution. *ChemSusChem* **2017**, *10* (7), 1563−1570.
(529) Zhang, K.; Fujitsuka, M.; Du, Y.; Majima, T. 2D/2D Heterostructured CdS/WS_2 with Efficient Charge Separation Improving H_2 Evolution under Visible Light Irradiation. *ACS Appl. Mater. Interfaces* **2018**, *10* (24), 20458−20466.
(530) Hou, X.; Shi, T.; Wei, C.; Zeng, H.; Hu, X.; Yan, B. A 2D-2D Heterojunction Bi_2WO_6/WS_{2-x} as A Broad-spectrum Bactericide: Sulfur Vacancies Mediate the Interface Interactions between Biology and Nanomaterials. *Biomaterials* **2020**, *243*, 119937.
(531) Bhatt, V. K.; Patel, M.; Pataniya, P. M.; Iyer, B. D.; Sumesh, C.; Late, D. J. Enhanced Antifungal Activity of WS_2/ZnO Nanohybrid Against Candida albicans. *ACS Biomater. Sci. Eng.* **2020**, *6* (11), 6069−6075.
(532) Akple, M. S.; Low, J.; Wageh, S.; Al-Ghamdi, A. A.; Yu, J.; Zhang, J. Enhanced Visible Light Photocatalytic H_2-Production of g-C_3N_4/WS_2 Composite Heterostructures. *Appl. Surf. Sci.* **2015**, *358*, 196−203.
(533) Shao, M.; Chen, W.; Ding, S.; Lo, K. H.; Zhong, X.; Yao, L.; Ip, W. F.; Xu, B.; Wang, X.; Pan, H. WX_y/g-C_3N_4 (WX_y= W_2C, WS_2, or W_2N) Composites for Highly Efficient Photocatalytic Water Splitting. *ChemSusChem* **2019**, *12* (14), 3355−3362.
(534) Hou, Y.; Zhu, Y.; Xu, Y.; Wang, X. Photocatalytic Hydrogen Production over Carbon Nitride Loaded with WS_2 as Cocatalyst under Visible Light. *Appl. Catal., B* **2014**, *156*, 122−127.
(535) Li, F.; Zhou, Y.; Wang, S.; Yin, H.; Chen, Y.; Luo, H.; Ai, S. One Step Preparation of CN-WS_2 Nanocomposite with Enhanced Photoactivity and Its Application for Photoelectrochemical Detection of 5-formylcytosine in the Genomic DNA of Maize Seedling. *Biosens. Bioelectron.* **2020**, *151*, 111973.
(536) Zhou, Y.; Ye, X.; Lin, D. One-Pot Synthesis of Non-Noble Metal WS_2/g-C_3N_4 Photocatalysts with Enhanced Photocatalytic Hydrogen Production. *Int. J. Hydrogen Energy* **2019**, *44* (29), 14927−14937.
(537) Tran, H. H.; Truong, D. H.; Truong, T. T.; Xuan Dieu Nguyen, T.; Jin, Y. S.; Kim, S. J.; Vo, V. A Facile Synthesis of WS_2/g-C_3N_4 Composites with Improved Photocatalytic Activity. *Bull. Korean Chem. Soc.* **2018**, *39* (8), 965−971.
(538) Li, F.; Yin, H.; Chen, Y.; Wang, S.; Li, J.; Zhang, Y.; Li, C.; Ai, S. Preparation of Pg-C_3N_4-WS_2 Nanocomposite and Its Application in Photoelectrochemical Detection of 5-formylcytosine. *J. Colloid Interface Sci.* **2020**, *561*, 348−357.
(539) Ma, Y.; Li, J.; Liu, E.; Wan, J.; Hu, X.; Fan, J. High Efficiency for H_2 Evolution and NO Removal over the Ag Nanoparticles Bridged g-C_3N_4 and WS_2 Heterojunction Photocatalysts. *Appl. Catal., B* **2017**, *219*, 467−478.
(540) Zou, Y.; Shi, J. W.; Ma, D.; Fan, Z.; Cheng, L.; Sun, D.; Wang, Z.; Niu, C. WS_2/Graphitic Carbon Nitride Heterojunction Nanosheets Decorated with CdS Quantum Dots for Photocatalytic Hydrogen Production. *ChemSusChem* **2018**, *11* (7), 1187−1197.
(541) Chen, Y.; Liang, W.; Li, Y.; Wu, Y.; Chen, Y.; Xiao, W.; Zhao, L.; Zhang, J.; Li, H. Modification, Application and Reaction Mechanisms of Nano-sized Iron Sulfide Particles for Pollutant Removal from Soil and Water: A Review. *Chem. Eng. J.* **2019**, *362*, 144−159.
(542) Gautam, J.; Tran, D. T.; Singh, T. I.; Kim, N. H.; Lee, J. H. Mesoporous Iron Sulfide Nanoparticles Anchored Graphene Sheet as An Efficient and Durable Catalyst for Oxygen Reduction Reaction. *J. Power Sources* **2019**, *427*, 91−100.
(543) Bhar, S. K.; Jana, S.; Mondal, A.; Mukherjee, N. Photocatalytic Degradation of Organic Dye on Porous Iron Sulfide Film Surface. *J. Colloid Interface Sci.* **2013**, *393*, 286−290.
(544) Jin, Z.; Zhang, M.; Wang, M.; Feng, C.; Wang, Z.-S. Metal Selenides as Efficient Counter Electrodes for Dye-sensitized Solar Cells. *Acc. Chem. Res.* **2017**, *50* (4), 895−904.
(545) Steinhagen, C.; Harvey, T. B.; Stolle, C. J.; Harris, J.; Korgel, B. A. Pyrite Nanocrystal Solar Cells: Promising, or Fool's Gold? *J. Phys. Chem. Lett.* **2012**, *3* (17), 2352−2356.
(546) Ou, J.; Liang, J.; Xiang, J.; Sun, L.; Liu, J. Highly Transparent Nickel and Iron Sulfide on Nitrogen-doped Carbon Films as Counter Electrodes for Bifacial Quantum Dot Sensitized Solar Cells. *Sol. Energy* **2019**, *193*, 766−773.
(547) Zhu, T.; Chong, M. N.; Chan, E. S. Nanostructured Tungsten Trioxide Thin Films Synthesized for Photoelectrocatalytic Water Oxidation: A Review. *ChemSusChem* **2014**, *7* (11), 2974−2997.
(548) Ganga, B.; Ganeshraj, C.; Krishna, A. G.; Santhosh, P. Electronic and Optical Properties of $FeSe_2$ Polymorphs: Solar Cell Absorber. *arXiv*; submission date 2013-03-06; Section: Condensed Matter (Materials Science); 1303.1381; 2013; article link https://arxiv.org/abs/1303.1381 (accessed 2021-10-29).
(549) Jia, J.; Zhang, Q.; Li, Z.; Hu, X.; Liu, E.; Fan, J. Lateral Heterojunctions within Ultrathin FeS-$FeSe_2$ Nanosheet Semiconductors for Photocatalytic Hydrogen Evolution. *J. Mater. Chem. A* **2019**, *7* (8), 3828−3841.
(550) DeRosha, D. E.; Chilkuri, V. G.; Van Stappen, C.; Bill, E.; Mercado, B. Q.; DeBeer, S.; Neese, F.; Holland, P. L. Planar Three-coordinate Iron Sulfide in A Synthetic [4Fe-3S] Cluster with Biomimetic Reactivity. *Nat. Chem.* **2019**, *11*, 1019−1025.
(551) Wang, W.; Pan, X.; Liu, W.; Zhang, B.; Chen, H.; Fang, X.; Yao, J.; Dai, S. $FeSe_2$ Films with Controllable Morphologies as Efficient Counter Electrodes for Dye-sensitized Solar Cells. *Chem. Commun.* **2014**, *50* (20), 2618−2620.
(552) Cho, J. S.; Lee, J.-K.; Kang, Y. C. Graphitic Carbon-Coated $FeSe_2$ Hollow Nanosphere-Decorated Reduced Graphene Oxide Hybrid Nanofibers as an Efficient Anode Material for Sodium Ion Batteries. *Sci. Rep.* **2016**, *6* (1), 23699.
(553) Ge, P.; Hou, H.; Li, S.; Yang, L.; Ji, X. Tailoring Rod-Like $FeSe_2$ Coated with Nitrogen-Doped Carbon for High-Performance Sodium Storage. *Adv. Funct. Mater.* **2018**, *28* (30), 1801765.
(554) Zhang, J.; Tian, P.; Tang, T.; Huang, G.; Zeng, J.; Cui, B.; Shen, Z.; Wang, H.; Kong, Z.; Xi, J.; et al. Excellent Photoelectrochemical Hydrogen Evolution Performance of $FeSe_2$ Nanorod/ZnSe 0D/1D Heterostructure as Efficiency Carriers Migrate Channel. *Int. J. Hydrogen Energy* **2020**, *45*, 8526−8539.
(555) Kong, Z.; Zhang, J.; Wang, H.; Cui, B.; Zeng, J.; Chen, X.; Tian, P.; Huang, G.; Xi, J.; Ji, Z. Constructing 1D/2D Heterojunction Photocatalyst from $FeSe_2$ Nanorods and $MoSe_2$ Nanoplates with High Photocatalytic and Photoelectrochemical Performance. *Int. J. Energy Res.* **2020**, *44* (2), 1205−1217.
(556) Shwetharani, R.; Kapse, S.; Thapa, R.; Nagaraju, D.; Balakrishna, R. G. Dendritic Ferroselite ($FeSe_2$) with 2D Carbon-Based Nanosheets of rGO and g-C_3N_4 as Efficient Catalysts for Electrochemical Hydrogen Evolution. *ACS Appl. Energy Mater.* **2020**, *3*, 12682−12691.
(557) Jia, J.; Sun, W.; Zhang, Q.; Zhang, X.; Hu, X.; Liu, E.; Fan, J. Inter-plane Heterojunctions within 2D/2D $FeSe_2$/g-C_3N_4 Nanosheet Semiconductors for Photocatalytic Hydrogen Generation. *Appl. Catal., B* **2020**, *261*, 118249.
(558) Chen, E.; Xu, W.; Chen, J.; Warner, J. 2D Layered Noble Metal Dichalcogenides (Pt, Pd, Se, S) for Electronics and Energy Applications. *Mater. Today Adv.* **2020**, *7*, 100076.
(559) Rufus, I. B.; Viswanathan, B.; Ramakrishnan, V.; Kuriacose, J. Cadmium Sulfide with Iridium Sulfide and Platinum Sulfide Deposits as A Photocatalyst for the Decomposition of Aqueous Sulfide. *J. Photochem. Photobiol., A* **1995**, *91* (1), 63−66.
(560) Han, S.; Li, Y.; Wang, Z. PtSe2/SiH van der Waals Type-II Heterostructure: A High Efficiency Photocatalyst for Water Splitting. *Phys. Chem. Chem. Phys.* **2020**, *22* (30), 17145−17151.
(561) Du, J.; Song, P.; Fang, L.; Wang, T.; Wei, Z.; Li, J.; Xia, C. Elastic, Electronic and Optical Properties of the Two-dimensional

PtX_2 (X= S, Se, and Te) Monolayer. *Appl. Surf. Sci.* **2018**, *435*, 476−482.
(562) Khan, A.; Din, H.; Idrees, M.; Khan, F.; Alrebdi, T. A.; Nguyen, C. V.; Shafiq, M.; Amin, B. First-Principles Study of Metal-Semiconductor Contact between MX_2 (M= Nb, Pt; X= S, Se) Monolayers. *Phys. Lett. A* **2019**, *383* (30), 125867.
(563) Saraf, D.; Chakraborty, S.; Kshirsagar, A.; Ahuja, R. In Pursuit of Bifunctional Catalytic Activity in PdS_2 Pseudo-monolayer Through Reaction Coordinate Mapping. *Nano Energy* **2018**, *49*, 283−289.
(564) McManus, J. B.; Horvath, D.; Browne, M.; Cullen, C. P.; Cunningham, G.; Hallam, T.; Zhussupbekov, K.; Mullarkey, D.; Coileáin, C. Ó.; Shvets, I. V.; et al. Low-Temperature Synthesis and Electrocatalytic Application of Large-Area $PtTe_2$ Thin Films. *Nanotechnology* **2020**, *31*, 375601.
(565) Gong, Y.; Lin, Z.; Chen, Y.-X.; Khan, Q.; Wang, C.; Zhang, B.; Nie, G.; Xie, N.; Li, D. Two-Dimensional Platinum Diselenide: Synthesis, Emerging Applications, and Future Challenges. *Nano-Micro Lett.* **2020**, *12* (1), 174.
(566) Huang, Z.; Zhang, W.; Zhang, W. Computational Search for Two-Dimensional MX_2 Semiconductors with Possible High Electron Mobility at Room Temperature. *Materials* **2016**, *9* (9), 716.
(567) Ajibade, P. A.; Oluwalana, A. E.; Andrew, F. P. Morphological Studies, Photocatalytic Activity, and Electrochemistry of Platinum Disulfide Nanoparticles from Bis (morpholinyl-4-carbodithioato)-platinum (II). *ACS Omega* **2020**, *5* (42), 27142−27153.
(568) Le, P.; Thuan, D. V.; Phuc, H. V.; Hieu, N. N.; Bui, H.; Amin, B.; Nguyen, C. V. Computational Understanding of the Band Alignment Engineering in PbI_2/PtS_2 Heterostructure: Effects of Electric Field and Vertical Strain. *Phys. E* **2020**, *115*, 113706.
(569) Muhsen Almayyali, A. O.; Kadhim, B. B.; Jappor, H. R. Retracted: Tunable Electronic and Optical Properties of 2D PtS_2/MoS_2 van der Waals Heterostructure. *Phys. E* **2020**, *118*, 113866.
(570) Deng, S.; Zhang, Y.; Li, L. Study on Electronic and Optical Properties of the Twisted and Strained MoS_2/PtS_2 Heterogeneous Interface. *Appl. Surf. Sci.* **2019**, *476*, 308−316.
(571) Almayyali, A. O. M.; Kadhim, B. B.; Jappor, H. R. Stacking Impact on the Optical and Electronic Properties of Two-dimensional $MoSe_2/PtS_2$ Heterostructures formed by PtS_2 and $MoSe_2$ Monolayers. *Chem. Phys.* **2020**, *532*, 110679.
(572) Nguyen, C. V.; Phung, H. T.; Pham, K. D. Computational Understanding of Electronic Properties of Graphene/PtS_2 Heterostructure under Electric Field. *Appl. Phys. A: Mater. Sci. Process.* **2019**, *125* (8), 536.
(573) Nguyen, C. V.; Bui, H.; Nguyen, T. D.; Pham, K. D. Controlling Electronic Properties of PtS_2/InSe van der Waals Heterostructure via External Electric Field and Vertical Strain. *Chem. Phys. Lett.* **2019**, *724*, 1−7.
(574) Yuan, J.; Sun, T.; Hu, Z.; Yu, W.; Ma, W.; Zhang, K.; Sun, B.; Lau, S. P.; Bao, Q.; Lin, S.; et al. Wafer-Scale Fabrication of Two-dimensional $PtS_2/PtSe_2$ Heterojunctions for Efficient and Broad Band Photodetection. *ACS Appl. Mater. Interfaces* **2018**, *10* (47), 40614−40622.
(575) Cai, L.; Zhang, N.; Qiu, B.; Chai, Y. Computational Design of Transition Metal Single-Atom Electrocatalysts on PtS_2 for Efficient Nitrogen Reduction. *ACS Appl. Mater. Interfaces* **2020**, *12* (18), 20448−20455.
(576) Villaos, R. A. B.; Crisostomo, C. P.; Huang, Z.-Q.; Huang, S.-M.; Padama, A. A. B.; Albao, M. A.; Lin, H.; Chuang, F.-C. Thickness Dependent Electronic Properties of Pt Dichalcogenides. *NPJ. 2D Mater. Appl.* **2019**, *3* (1), 2.
(577) Furuseth, S.; Selte, K.; Kjekshus, A.; Gronowitz, S.; Hoffman, R. A.; Westerdahl, A. Redetermined Crystal Structures of $NiTe_2$ $PdTe_2$ PtS_2 $PtSe_2$ and $PtTe_2$. *Acta Chem. Scand.* **1965**, *19*, 257.
(578) Liu, J.; Xu, H.; Yan, J.; Huang, J.; Song, Y.; Deng, J.; Wu, J.; Ding, C.; Wu, X.; Yuan, S.; et al. Efficient Photocatalytic Hydrogen Evolution Mediated by Defect-Rich 1T-PtS_2 Atomic Layer Nanosheet Modified Mesoporous Graphitic Carbon Nitride. *J. Mater. Chem. A* **2019**, *7* (32), 18906−18914.
(579) Pan, Y.; Yuan, X.; Jiang, L.; Yu, H.; Zhang, J.; Wang, H.; Guan, R.; Zeng, G. Recent Advances in Synthesis, Modification and Photocatalytic Applications of Micro/Nano-Structured Zinc Indium Sulfide. *Chem. Eng. J.* **2018**, *354*, 407−431.
(580) Ding, K.; Li, Y.; Chen, B.; Zhang, Y. Original Investigation of a Novel Photocatalyst Driven by Visible Light: $ZnIn_2S_4$. *J. Phys. Soc. Jpn.* **2014**, *83* (7), 074301.
(581) Du, C.; Zhang, Q.; Lin, Z.; Yan, B.; Xia, C.; Yang, G. Half-unit-cell $ZnIn_2S_4$ Monolayer with Sulfur Vacancies for Photocatalytic Hydrogen Evolution. *Appl. Catal., B* **2019**, *248*, 193−201.
(582) Du, C.; Yan, B.; Lin, Z.; Yang, G. Cross-linked Bond Accelerated Interfacial Charge Transfer in Monolayer Zinc Indium Sulfide ($ZnIn_2S_4$)/Reduced Graphene Oxide (RGO) Heterostructure for Photocatalytic Hydrogen Production with Mechanistic Insight. *Catal. Sci. Technol.* **2019**, *9* (15), 4066−4076.
(583) Zhang, H.; Xie, S.; Hu, J.; Wu, X.; Zhang, Q.; Cheng, J.; Wang, Y. C-H Activations of Methanol and Ethanol and C-C Couplings into Diols by Zinc-Indium-Sulfide under Visible Light. *Chem. Commun.* **2020**, *56* (12), 1776−1779.
(584) Feng, C.; Yang, X.; Sun, Z.; Xue, J.; Sun, L.; Wang, J.; He, Z.; Yu, J. Dual Interfacial Synergism in Au-Pd/$ZnIn_2S_4$ for Promoting Photocatalytic Selective Oxidation of Aromatic Alcohol. *Appl. Surf. Sci.* **2020**, *501*, 144018.
(585) Chai, B.; Peng, T.; Zeng, P.; Zhang, X.; Liu, X. Template-Free Hydrothermal Synthesis of $ZnIn_2S_4$ Floriated Microsphere as An Efficient Photocatalyst for H_2 Production under Visible-Light Irradiation. *J. Phys. Chem. C* **2011**, *115* (13), 6149−6155.
(586) Zeng, D.; Xiao, L.; Ong, W. J.; Wu, P.; Zheng, H.; Chen, Y.; Peng, D. L. Hierarchical $ZnIn_2S_4/MoSe_2$ Nanoarchitectures for Efficient Noble-Metal-Free Photocatalytic Hydrogen Evolution under Visible Light. *ChemSusChem* **2017**, *10* (22), 4624−4631.
(587) Li, F.; Luo, J.; Chen, G.; Fan, Y.; Huang, Q.; Luo, Y.; Li, D.; Meng, Q. Hydrothermal Synthesis of Zinc Indium Sulfide Microspheres with Ag^+ Doping for Enhanced H_2 Production by Photocatalytic Water Splitting under Visible Light. *Catal. Sci. Technol.* **2014**, *4* (4), 1144−1150.
(588) Shen, S.; Zhao, L.; Zhou, Z.; Guo, L. Enhanced Photocatalytic Hydrogen Evolution over Cu-doped $ZnIn_2S_4$ under Visible Light Irradiation. *J. Phys. Chem. C* **2008**, *112* (41), 16148−16155.
(589) Wang, S.; Guan, B. Y.; Wang, X.; Lou, X. W. D. Formation of Hierarchical Co_9S_8@$ZnIn_2S_4$ Heterostructured Cages as An Efficient Photocatalyst for Hydrogen Evolution. *J. Am. Chem. Soc.* **2018**, *140* (45), 15145−15148.
(590) Chen, W.; Chang, L.; Ren, S.-B.; He, Z.-C.; Huang, G.-B.; Liu, X.-H. Direct Z-scheme 1D/2D $WO_{2.72}/ZnIn_2S_4$ Hybrid Photocatalysts with Highly-efficient Visible-Light-Driven Photodegradation Towards Tetracycline hydrochloride Removal. *J. Hazard. Mater.* **2020**, *384*, 121308.
(591) Zhu, Q.; Sun, Y.; Xu, S.; Li, Y.; Lin, X.; Qin, Y. Rational design of 3D/2D In_2O_3 Nanocube/$ZnIn_2S_4$ Nanosheet Heterojunction Photocatalyst with Large-Area "High-Speed Channels" for Photocatalytic Oxidation of 2, 4-Dichlorophenol under Visible Light. *J. Hazard. Mater.* **2020**, *382*, 121098.
(592) Wang, H.; Sun, Y.; Wu, Y.; Tu, W.; Wu, S.; Yuan, X.; Zeng, G.; Xu, Z. J.; Li, S.; Chew, J. W. Electrical Promotion of Spatially Photoinduced Charge Separation via Interfacial-Built-In Quasi-Alloying Effect in Hierarchical $Zn_2In_2S_5/Ti_3C_2$ (O, OH)x Hybrids Toward Efficient Photocatalytic Hydrogen Evolution and Environmental Remediation. *Appl. Catal., B* **2019**, *245*, 290−301.
(593) Mu, F.; Cai, Q.; Hu, H.; Wang, J.; Wang, Y.; Zhou, S.; Kong, Y. Construction of 3D Hierarchical Microarchitectures of Z-scheme UiO-66-$(COOH)_2/ZnIn_2S_4$ Hybrid Decorated with Non-noble MoS_2 Cocatalyst: A Highly Efficient Photocatalyst for Hydrogen Evolution and Cr(VI) Reduction. *Chem. Eng. J.* **2020**, *384*, 123352.
(594) Liu, Y.; Li, C.-F.; Li, X.-Y.; Yu, W.-B.; Dong, W.-D.; Zhao, H.; Hu, Z.-Y.; Deng, Z.; Wang, C.; Wu, S.-J.; et al. Molybdenum Disulfide Quantum Dots Directing Zinc Indium Sulfide Heterostructures for Enhanced Visible Light Hydrogen Production. *J. Colloid Interface Sci.* **2019**, *551*, 111−118.

(595) Zhang, M.; Yao, J.; Arif, M.; Qiu, B.; Yin, H.; Liu, X.; Chen, S.-m. 0D/2D $CeO_2/ZnIn_2S_4$ Z-Scheme Heterojunction for Visible-light-driven Photocatalytic H_2 Evolution. *Appl. Surf. Sci.* **2020**, *526*, 145749.
(596) Guan, Z.; Pan, J.; Li, Q.; Li, G.; Yang, J. Boosting Visible-Light Photocatalytic Hydrogen Evolution with An Efficient $CuInS_2/ZnIn_2S_4$ 2D/2D Heterojunction. *ACS Sustainable Chem. Eng.* **2019**, *7* (8), 7736−7742.
(597) Xiang, Z.; Guan, H.; Zhang, B.; Zhao, Y. Electrostatic Self-assembly of 2D-2D $CoP/ZnIn_2S_4$ Nanosheets for Efficient Photocatalytic Hydrogen Evolution. *J. Am. Ceram. Soc.* **2021**, *104*, 504−513.
(598) Swain, G.; Sultana, S.; Parida, K. One-Pot-Architectured Au-Nanodot-Promoted $MoS_2/ZnIn_2S_4$: A Novel p-n Heterojunction Photocatalyst for Enhanced Hydrogen Production and Phenol Degradation. *Inorg. Chem.* **2019**, *58* (15), 9941−9955.
(599) Yang, H.; Cao, R.; Sun, P.; Yin, J.; Zhang, S.; Xu, X. Constructing Electrostatic Self-Assembled 2D/2D Ultra-thin $ZnIn_2S_4$/protonated g-C_3N_4 Heterojunctions for Excellent Photocatalytic Performance under Visible Light. *Appl. Catal., B* **2019**, *256*, 117862.
(600) Zhou, M.; Wang, S.; Yang, P.; Luo, Z.; Yuan, R.; Asiri, A. M.; Wakeel, M.; Wang, X. Layered Heterostructures of Ultrathin Polymeric Carbon Nitride and $ZnIn_2S_4$ Nanosheets for Photocatalytic CO_2 Reduction. *Chem. - Eur. J.* **2018**, *24* (69), 18529−18534.
(601) Lin, B.; Li, H.; An, H.; Hao, W.; Wei, J.; Dai, Y.; Ma, C.; Yang, G. Preparation of 2D/2D g-C_3N_4 Nanosheet@$ZnIn_2S_4$ Nanoleaf Heterojunctions with Well-Designed High-Speed Charge Transfer Nanochannels Towards High-Efficiency Photocatalytic Hydrogen Evolution. *Appl. Catal., B* **2018**, *220*, 542−552.
(602) Qin, Y.; Li, H.; Lu, J.; Feng, Y.; Meng, F.; Ma, C.; Yan, Y.; Meng, M. Synergy between van der Waals Heterojunction and Vacancy in $ZnIn_2S_4$/g-C_3N_4 2D/2D Photocatalysts for Enhanced Photocatalytic Hydrogen Evolution. *Appl. Catal., B* **2020**, *277*, 119254.
(603) Zou, Y.; Shi, J.-W.; Sun, L.; Ma, D.; Mao, S.; Lv, Y.; Cheng, Y. Energy-Band-Controlled $Zn_xCd_{1-x}In_2S_4$ Solid Solution Coupled with g-C_3N_4 Nanosheets as 2D/2D Heterostructure Toward Efficient Photocatalytic H_2 Evolution. *Chem. Eng. J.* **2019**, *378*, 122192.
(604) Wu, Y.; Wang, H.; Tu, W.; Liu, Y.; Wu, S.; Tan, Y. Z.; Chew, J. W. Construction of Hierarchical 2D-2D $Zn_3In_2S_6$/Fluorinated Polymeric Carbon Nitride Nanosheets Photocatalyst for Boosting Photocatalytic Degradation and Hydrogen Production Performance. *Appl. Catal., B* **2018**, *233*, 58−69.
(605) Liu, E.; Chen, J.; Ma, Y.; Feng, J.; Jia, J.; Fan, J.; Hu, X. Fabrication of 2D SnS_2/g-C_3N_4 Heterojunction with Enhanced H_2 Evolution during Photocatalytic Water Splitting. *J. Colloid Interface Sci.* **2018**, *524*, 313−324.
(606) Song, Y.; Gu, J.; Xia, K.; Yi, J.; Chen, H.; She, X.; Chen, Z.; Ding, C.; Li, H.; Xu, H. Construction of 2D SnS_2/g-C_3N_4 Z-Scheme Composite with Superior Visible-Light Photocatalytic Performance. *Appl. Surf. Sci.* **2019**, *467*, 56−64.
(607) Liu, J.; Hua, E. High Photocatalytic Activity of Heptazine-based g-C_3N_4/SnS_2 Heterojunction and Its Origin: Insights from Hybrid DFT. *J. Phys. Chem. C* **2017**, *121* (46), 25827−25835.
(608) Huo, Y.; Yang, Y.; Dai, K.; Zhang, J. Construction of 2D/2D Porous Graphitic C_3N_4/SnS_2 Composite as A Direct Z-Scheme System for Efficient Visible Photocatalytic Activity. *Appl. Surf. Sci.* **2019**, *481*, 1260−1269.
(609) Huo, Y.; Zhang, J.; Dai, K.; Li, Q.; Lv, J.; Zhu, G.; Liang, C. All-Solid-State Artificial Z-Scheme Porous g-C_3N_4/Sn_2S_3-DETA Heterostructure Photocatalyst with Enhanced Performance in Photocatalytic CO_2 Reduction. *Appl. Catal., B* **2019**, *241*, 528−538.
(610) Chen, H.; Zhang, X.; Ji, H.; Xia, K.; Yi, J.; Ke, F.; Xu, H.; Chen, M.; Li, H. Integration of Metallic TaS_2 Co-catalyst on Carbon Nitride Photoharvester for Enhanced Photocatalytic Performance. *Can. J. Chem. Eng.* **2019**, *97* (6), 1821−1827.
(611) Huang, Y.; Wang, K.; Guo, T.; Li, J.; Wu, X.; Zhang, G. Construction of 2D/2D Bi_2Se_3/g-C_3N_4 Nanocomposite with High Interfacial Charge Separation and Photo-heat Conversion Efficiency for Selective Photocatalytic CO_2 Reduction. *Appl. Catal., B* **2020**, *277*, 119232.
(612) Wen, J.; Xie, J.; Zhang, H.; Zhang, A.; Liu, Y.; Chen, X.; Li, X. Constructing Multifunctional Metallic Ni Interface Layers in the g-C_3N_4 Nanosheets/Amorphous NiS Heterojunctions for Efficient Photocatalytic H_2 Generation. *ACS Appl. Mater. Interfaces* **2017**, *9* (16), 14031−14042.
(613) Liu, X.; Liu, Y.; Zhang, W.; Zhong, Q.; Ma, X. In Situ Self-Assembly of 3D Hierarchical 2D/2D CdS/g-C_3N_4 Hereojunction with Excellent Photocatalytic Performance. *Mater. Sci. Semicond. Process.* **2020**, *105*, 104734.
(614) Guo, F.; Shi, W.; Li, M.; Shi, Y.; Wen, H. 2D/2D Z-Scheme Heterojunction of $CuInS_2$/g-C_3N_4 for Enhanced Visible-Light-Driven Photocatalytic Activity Towards the Degradation of Tetracycline. *Sep. Purif. Technol.* **2019**, *210*, 608−615.
(615) Chen, W.; He, Z.-C.; Huang, G.-B.; Wu, C.-L.; Chen, W.-F.; Liu, X.-H. Direct Z-scheme 2D/2D $MnIn_2S_4$/g-C_3N_4 Architectures with Highly Efficient Photocatalytic Activities Towards Treatment of Pharmaceutical Wastewater and Hydrogen Evolution. *Chem. Eng. J.* **2019**, *359*, 244−253.
(616) Che, H.; Che, G.; Zhou, P.; Liu, C.; Dong, H. Yeast-derived Carbon Sphere as A Bridge of Charge Carriers Towards to Enhanced Photocatalytic Activity of 2D/2D Cu_2WS_4/g-C_3N_4 Heterojunction. *J. Colloid Interface Sci.* **2019**, *546*, 262−275.
(617) Li, Z.; Wu, L.; Wang, L.; Gu, A.; Zhou, Q. Nickel Cobalt Sulfide Nanosheets Uniformly Anchored on Porous Graphitic Carbon Nitride for Supercapacitors with High Cycling Performance. *Electrochim. Acta* **2017**, *231*, 617−625.
(618) Meng, X.; Zhang, Z. Bismuth-based Photocatalytic Semiconductors: Introduction, Challenges and Possible Approaches. *J. Mol. Catal. A: Chem.* **2016**, *423*, 533−549.
(619) Ye, L.; Deng, Y.; Wang, L.; Xie, H.; Su, F. Bismuth-Based Photocatalysts for Solar Photocatalytic Carbon Dioxide Conversion. *ChemSusChem* **2019**, *12* (16), 3671−3701.
(620) Hao, Q.; Liu, C.; Jia, G.; Wang, Y.; Arandiyan, H.; Wei, W.; Ni, B.-J. Catalytic Reduction of Nitrogen to Produce Ammonia by Bismuth-based Catalysts: State of the Art and Future Prospects. *Mater. Horiz.* **2020**, *7* (4), 1014−1029.
(621) Huang, Y.; Zhang, N.; Wu, Z.; Xie, X. Artificial Nitrogen Fixation over Bismuth-based Photocatalysts: Fundamentals and Future Perspectives. *J. Mater. Chem. A* **2020**, *8* (10), 4978−4995.
(622) Sharma, K.; Dutta, V.; Sharma, S.; Raizada, P.; Hosseini-Bandegharaei, A.; Thakur, P.; Singh, P. Recent Advances in Enhanced Photocatalytic Activity of Bismuth Oxyhalides for Efficient Photocatalysis of Organic Pollutants in Water: A Review. *J. Ind. Eng. Chem.* **2019**, *78*, 1−20.
(623) Chen, C.-C.; Fu, J.-Y.; Chang, J.-L.; Huang, S.-T.; Yeh, T.-W.; Hung, J.-T.; Huang, P.-H.; Liu, F.-Y.; Chen, L.-W. Bismuth Oxyfluoride/Bismuth Oxyiodide Nanocomposites Enhance Visible-Light-Driven Photocatalytic Activity. *J. Colloid Interface Sci.* **2018**, *532*, 375−386.
(624) Li, J.; Yu, Y.; Zhang, L. Bismuth Oxyhalide Nanomaterials: Layered Structures Meet Photocatalysis. *Nanoscale* **2014**, *6* (15), 8473−8488.
(625) Lee, G.-J.; Zheng, Y.-C.; Wu, J. J. Fabrication of Hierarchical Bismuth Oxyhalides (BiOX, X= Cl, Br, I) Materials and Application of Photocatalytic Hydrogen Production from Water Splitting. *Catal. Today* **2018**, *307*, 197−204.
(626) Bhachu, D. S.; Moniz, S. J.; Sathasivam, S.; Scanlon, D. O.; Walsh, A.; Bawaked, S. M.; Mokhtar, M.; Obaid, A. Y.; Parkin, I. P.; Tang, J.; et al. Bismuth Oxyhalides: Synthesis, Structure and Photoelectrochemical Activity. *Chem. Sci.* **2016**, *7* (8), 4832−4841.
(627) Yang, J.; Liang, Y.; Li, K.; Yang, G.; Yin, S. One-Step Low-Temperature Synthesis of 0D CeO_2 Quantum Dots/2D BiOX (X= Cl, Br) Nanoplates Heterojunctions for Highly Boosting Photooxidation and Reduction Ability. *Appl. Catal., B* **2019**, *250*, 17−30.
(628) Razavi-Khosroshahi, H.; Mohammadzadeh, S.; Hojamberdiev, M.; Kitano, S.; Yamauchi, M.; Fuji, M. $BiVO_4$/BiOX (X= F, Cl, Br, I)

https://doi.org/10.1021/acs.chemmater.1c03166
Chem. Mater. 2021, 33, 9012−9092

Heterojunctions for Degrading Organic Dye under Visible Light. *Adv. Powder Technol.* **2019**, *30* (7), 1290−1296.
(629) Hu, J.; Li, X.; Wang, X.; Li, Q.; Wang, F. Novel Hierarchical Sn_3O_4/BiOX (X= Cl, Br, I) p-n Heterostructures with Enhanced Photocatalytic Activity under Simulated Solar Light Irradiation. *Dalton Trans.* **2019**, *48* (24), 8937−8947.
(630) Yu, L.; Zhang, X.; Li, G.; Cao, Y.; Shao, Y.; Li, D. Highly Efficient $Bi_2O_2CO_3$/BiOCl Photocatalyst based on Heterojunction with Enhanced Dye-sensitization under Visible Light. *Appl. Catal., B* **2016**, *187*, 301−309.
(631) Ye, L.; Liu, J.; Gong, C.; Tian, L.; Peng, T.; Zan, L. Two Different Roles of Metallic Ag on Ag/AgX/BiOX (X= Cl, Br) Visible Light Photocatalysts: Surface Plasmon Resonance and Z-Scheme Bridge. *ACS Catal.* **2012**, *2* (8), 1677−1683.
(632) Mafa, P. J.; Kuvarega, A. T.; Mamba, B. B.; Ntsendwana, B. Photoelectrocatalytic Degradation of Sulfamethoxazole on g-C_3N_4/BiOI/EG p-n Heterojunction Photoanode under Visible Light Irradiation. *Appl. Surf. Sci.* **2019**, *483*, 506−520.
(633) Zhou, M.; Huang, W.; Zhao, Y.; Jin, Z.; Hua, X.; Li, K.; Tang, L.; Cai, Z. 2D g-C_3N_4/BiOBr Heterojunctions with Enhanced Visible Light Photocatalytic Activity. *J. Nanopart. Res.* **2020**, *22* (1), 13.
(634) Lv, J.; Dai, K.; Zhang, J.; Liu, Q.; Liang, C.; Zhu, G. Facile Constructing Novel 2D Porous g-C_3N_4/BiOBr Hybrid with Enhanced Visible-Light-Driven Photocatalytic Activity. *Sep. Purif. Technol.* **2017**, *178*, 6−17.
(635) Zhang, J.; Fu, J.; Wang, Z.; Cheng, B.; Dai, K.; Ho, W. Direct Z-Scheme Porous g-C_3N_4/BiOI Heterojunction for Enhanced Visible-Light Photocatalytic Activity. *J. Alloys Compd.* **2018**, *766*, 841−850.
(636) Liu, C.; Wu, Q.; Ji, M.; Zhu, H.; Hou, H.; Yang, Q.; Jiang, C.; Wang, J.; Tian, L.; Chen, J.; et al. Constructing Z-Scheme Charge Separation in 2D Layered Porous BiOBr/Graphitic C_3N_4 Nanosheets Nanojunction with Enhanced Photocatalytic Activity. *J. Alloys Compd.* **2017**, *723*, 1121−1131.
(637) Alam, K. M.; Kumar, P.; Kar, P.; Goswami, A.; Thakur, U. K.; Zeng, S.; Vahidzadeh, E.; Cui, K.; Shankar, K. Heterojunctions of Halogen-doped Carbon Nitride Nanosheets and BiOI for Sunlight-Friven Water-Splitting. *Nanotechnology* **2020**, *31* (8), 084001.
(638) Cheng, H.; Huang, B.; Dai, Y. Engineering BiOX (X= Cl, Br, I) Nanostructures for Highly Efficient Photocatalytic Applications. *Nanoscale* **2014**, *6* (4), 2009−2026.
(639) Guan, M.; Xiao, C.; Zhang, J.; Fan, S.; An, R.; Cheng, Q.; Xie, J.; Zhou, M.; Ye, B.; Xie, Y. Vacancy Associates Promoting Solar-driven Photocatalytic Activity of Ultrathin Bismuth Oxychloride Nanosheets. *J. Am. Chem. Soc.* **2013**, *135* (28), 10411−10417.
(640) Dandapat, A.; Horovitz, I.; Gnayem, H.; Sasson, Y.; Avisar, D.; Luxbacher, T.; Mamane, H. Solar Photocatalytic Degradation of Trace Organic Pollutants in Water by Bi(0)-Doped Bismuth Oxyhalide Thin Films. *ACS Omega* **2018**, *3* (9), 10858−10865.
(641) Liu, W.; Qiao, L.; Zhu, A.; Liu, Y.; Pan, J. Constructing 2D BiOCl/C_3N_4 Layered Composite with Large Contact Surface for Visible-Light-Driven Photocatalytic Degradation. *Appl. Surf. Sci.* **2017**, *426*, 897−905.
(642) Wang, Q.; Wang, W.; Zhong, L.; Liu, D.; Cao, X.; Cui, F. Oxygen Vacancy-rich 2D/2D BiOCl-g-C_3N_4 Ultrathin Heterostructure Nanosheets for Enhanced Visible-Light-Driven Photocatalytic Activity in Environmental Remediation. *Appl. Catal., B* **2018**, *220*, 290−302.
(643) Hu, X.; Tian, J.; Xue, Y.; Li, Y.; Cui, H. Bi_2WO_6 Nanosheets Decorated with Au Nanorods for Enhanced Near-Infrared Photocatalytic Properties Based on Surface Plasmon Resonance Effects and Wide-Range Near-Infrared Light Harvesting. *ChemCatChem* **2017**, *9* (8), 1511−1516.
(644) Jin, X.; Ye, L.; Xie, H.; Chen, G. Bismuth-Rich Bismuth Oxyhalides for Environmental and Energy Photocatalysis. *Coord. Chem. Rev.* **2017**, *349*, 84−101.
(645) Xiong, J.; Song, P.; Di, J.; Li, H. Bismuth-Rich Bismuth Oxyhalides: A New Opportunity to Trigger High-Efficiency Photocatalysis. *J. Mater. Chem. A* **2020**, *8* (41), 21434−21454.
(646) Wang, Z.; Chen, M.; Huang, D.; Zeng, G.; Xu, P.; Zhou, C.; Lai, C.; Wang, H.; Cheng, M.; Wang, W. Multiply Structural Optimized Strategies for Bismuth Oxyhalide Photocatalysis and Their Environmental Application. *Chem. Eng. J.* **2019**, *374*, 1025−1045.
(647) Wang, X.; Zhou, C.; Yin, L.; Zhang, R.; Liu, G. Iodine-Deficient BiOI Nanosheets with Lowered Valence Band Maximum to Enable Visible Light Photocatalytic Activity. *ACS Sustainable Chem. Eng.* **2019**, *7* (8), 7900−7907.
(648) Xiao, X.; Liu, C.; Hu, R.; Zuo, X.; Nan, J.; Li, L.; Wang, L. Oxygen-Rich Bismuth Oxyhalides: Generalized One-Pot Synthesis, Band Structures and Visible-Light Photocatalytic Properties. *J. Mater. Chem.* **2012**, *22* (43), 22840−22843.
(649) Xiong, J.; Di, J.; Li, H. Interface Engineering in Low-Dimensional Bismuth-based Materials for Photoreduction Reactions. *J. Mater. Chem. A* **2021**, *9*, 2662−2677.
(650) Lin, X.; Huang, T.; Huang, F.; Wang, W.; Shi, J. Photocatalytic Activity of A Bi-based Oxychloride Bi_3O_4Cl. *J. Phys. Chem. B* **2006**, *110* (48), 24629−24634.
(651) Li, J.; Zhang, L.; Li, Y.; Yu, Y. Synthesis and Internal Electric Field Dependent Photoreactivity of Bi_3O_4Cl Single-Crystalline Nanosheets with High {001} Facet Exposure Percentages. *Nanoscale* **2014**, *6* (1), 167−171.
(652) Xiao, X.; Jiang, J.; Zhang, L. Selective Oxidation of Benzyl Alcohol into Benzaldehyde over Semiconductors under Visible Light: The Case of $Bi_{12}O_{17}Cl_2$ Nanobelts. *Appl. Catal., B* **2013**, *142*, 487−493.
(653) Zhao, M.; Fu, C.; Wang, K.; Zhang, Y.; Xia, Y.; Zhang, Q.; Li, C.; Liu, M.; Zhang, Z.; Wang, W. Photocatalytic Degradation of Antibacterials using $Bi_xO_yX_z$ with Optimized Morphologies and Adjusted Structures-A Review. *J. Alloys Compd.* **2021**, *852*, 156698.
(654) Prajapati, P. K.; Jain, S. L. Synthesis and Evaluation of CoPc Grafted Bismuth Oxyhalide ($Bi_{24}O_{31}Br_{10}$): A Visible Light-Active Photocatalyst for CO_2 Reduction into Methanol. *Dalton Trans.* **2019**, *48* (15), 4941−4948.
(655) Wang, C.-Y.; Zhang, X.; Qiu, H.-B.; Wang, W.-K.; Huang, G.-X.; Jiang, J.; Yu, H.-Q. Photocatalytic Degradation of Bisphenol A by Oxygen-Rich and Highly Visible-light Responsive $Bi_{12}O_{17}Cl_2$ Nanobelts. *Appl. Catal., B* **2017**, *200*, 659−665.
(656) Zheng, J.; Chang, F.; Jiao, M.; Xu, Q.; Deng, B.; Hu, X. A Visible-Light-Driven Heterojuncted Composite $WO_3/Bi_{12}O_{17}Cl_2$: Synthesis, Characterization, and Improved Photocatalytic Performance. *J. Colloid Interface Sci.* **2018**, *510*, 20−31.
(657) Di, J.; Zhu, C.; Ji, M.; Duan, M.; Long, R.; Yan, C.; Gu, K.; Xiong, J.; She, Y.; Xia, J.; et al. Defect-Rich $Bi_{12}O_{17}Cl_2$ Nanotubes Self-Accelerating Charge Separation for Boosting Photocatalytic CO_2 Reduction. *Angew. Chem., Int. Ed.* **2018**, *57* (45), 14847−14851.
(658) Zhou, C.; Lai, C.; Xu, P.; Zeng, G.; Huang, D.; Zhang, C.; Cheng, M.; Hu, L.; Wan, J.; Liu, Y.; et al. In situ Grown AgI/$Bi_{12}O_{17}Cl_2$ Heterojunction Photocatalysts for Visible Light Degradation of Sulfamethazine: Efficiency, Pathway, and Mechanism. *ACS Sustainable Chem. Eng.* **2018**, *6* (3), 4174−4184.
(659) Wang, L.; Min, X.; Sui, X.; Chen, J.; Wang, Y. Facile Construction of Novel BiOBr/$Bi_{12}O_{17}Cl_2$ Heterojunction Composites with Enhanced Photocatalytic Performance. *J. Colloid Interface Sci.* **2020**, *560*, 21−33.
(660) Huang, H.; Xiao, K.; He, Y.; Zhang, T.; Dong, F.; Du, X.; Zhang, Y. In situ Assembly of BiOI@$Bi_{12}O_{17}Cl_2$ p-n Junction: Charge Induced Unique Front-lateral Surfaces Coupling Heterostructure with High Exposure of BiOI {001} Active Facets for Robust and Nonselective Photocatalysis. *Appl. Catal., B* **2016**, *199*, 75−86.
(661) Jiang, E.; Song, N.; Zhang, X.; Yang, L.; Liu, C.; Dong, H. In-Situ Fabrication of Z-Scheme $Bi_3O_4Cl/Bi_{12}O_{17}Cl_2$ Heterostructure by Facile pH Control Strategy to Boost Removal of Various Pollutants in Water. *Chem. Eng. J.* **2020**, *388*, 123483.
(662) Huo, Y.; Zhang, J.; Wang, Z.; Dai, K.; Pan, C.; Liang, C. Efficient Interfacial Charge Transfer of 2D/2D Porous Carbon Nitride/Bismuth Oxychloride Step-Scheme Heterojunction for Boosted Solar-Driven CO_2 Reduction. *J. Colloid Interface Sci.* **2021**, *585*, 684−693.

https://doi.org/10.1021/acs.chemmater.1c03166
Chem. Mater. 2021, 33, 9012−9092

(663) Che, H.; Che, G.; Dong, H.; Hu, W.; Hu, H.; Liu, C.; Li, C. Fabrication of Z-scheme Bi_3O_4Cl/g-C_3N_4 2D/2D Heterojunctions with Enhanced Interfacial Charge Separation and Photocatalytic Degradation Various Organic Pollutants Activity. *Appl. Surf. Sci.* **2018**, *455*, 705−716.
(664) Shi, L.; Si, W.; Wang, F.; Qi, W. Construction of 2D/2D Layered g-C_3N_4/$Bi_{12}O_{17}Cl_2$ Hybrid Material with Matched Energy Band Structure and Its Improved Photocatalytic Performance. *RSC Adv.* **2018**, *8* (43), 24500−24508.
(665) Ji, M.; Di, J.; Ge, Y.; Xia, J.; Li, H. 2D-2D Stacking of Graphene-like g-C_3N_4/Ultrathin $Bi_4O_5Br_2$ with Matched Energy Band Structure Towards Antibiotic Removal. *Appl. Surf. Sci.* **2017**, *413*, 372−380.
(666) Zhou, C.; Lai, C.; Xu, P.; Zeng, G.; Huang, D.; Li, Z.; Zhang, C.; Cheng, M.; Hu, L.; Wan, J.; et al. Rational Design of Carbon-doped Carbon Nitride/$Bi_{12}O_{17}Cl_2$ Composites: A Promising Candidate Photocatalyst for Boosting Visible-Light-Driven Photocatalytic Degradation of Tetracycline. *ACS Sustainable Chem. Eng.* **2018**, *6* (5), 6941−6949.
(667) Ran, J.; Ma, T. Y.; Gao, G.; Du, X.-W.; Qiao, S. Z. Porous P-doped Graphitic Carbon Nitride Nanosheets for Synergistically Enhanced Visible-Light Photocatalytic H_2 Production. *Energy Environ. Sci.* **2015**, *8* (12), 3708−3717.
(668) Kumar, A.; Kumar, P.; Joshi, C.; Manchanda, M.; Boukherroub, R.; Jain, S. L. Nickel Decorated on Phosphorous-doped Carbon Nitride as An Efficient Photocatalyst for Reduction of Nitrobenzenes. *Nanomaterials* **2016**, *6* (4), 59.
(669) Guo, S.; Deng, Z.; Li, M.; Jiang, B.; Tian, C.; Pan, Q.; Fu, H. Phosphorus-doped Carbon Nitride Tubes with a Layered Micro-Nanostructure for Enhanced Visible-Light Photocatalytic Hydrogen Evolution. *Angew. Chem.* **2016**, *128* (5), 1862−1866.
(670) Kumar, S.; Gawande, M. B.; Kopp, J.; Kment, S.; Varma, R. S.; Zbořil, R. P-and F-co-doped Carbon Nitride Nanocatalysts for Photocatalytic CO_2 Reduction and Thermocatalytic Furanics Synthesis from Sugars. *ChemSusChem* **2020**, *13* (19), 5231−5238.
(671) Zhang, L.; Ding, N.; Hashimoto, M.; Iwasaki, K.; Chikamori, N.; Nakata, K.; Xu, Y.; Shi, J.; Wu, H.; Luo, Y.; et al. Sodium-Doped Carbon Nitride Nanotubes for Efficient Visible Light-Driven Hydrogen Production. *Nano Res.* **2018**, *11* (4), 2295−2309.
(672) Zhang, M.; Bai, X.; Liu, D.; Wang, J.; Zhu, Y. Enhanced Catalytic Activity of Potassium-Doped Graphitic Carbon Nitride Induced by Lower Valence Position. *Appl. Catal., B* **2015**, *164*, 77−81.
(673) Tripathi, A.; Narayanan, S. Potassium Doped Graphitic Carbon Nitride with Extended Optical Absorbance for Solar Light Driven Photocatalysis. *Appl. Surf. Sci.* **2019**, *479*, 1−11.
(674) Tian, J.; Wu, T.; Wang, D.; Pei, Y.; Qiao, M.; Zong, B. One-Pot Synthesis of Potassium and Phosphorus-Doped Carbon Nitride Catalyst Derived from Urea for Highly Efficient Visible Light-driven Hydrogen Peroxide Production. *Catal. Today* **2019**, *330*, 171−178.
(675) Li, C.; Zhao, W.; Wang, A.; Zhu, W.; Shang, D. Multifunctional Carbon Nitride Nano-Homojunction Decorated g-C_3N_4 Nanocomposites for Optoelectronic Performances. *Appl. Surf. Sci.* **2019**, *467*, 1140−1147.
(676) Jiang, L.; Yuan, X.; Zeng, G.; Liang, J.; Wu, Z.; Wang, H.; Zhang, J.; Xiong, T.; Li, H. A Facile Band Alignment of Polymeric Carbon Nitride Isotype Heterojunctions for Enhanced Photocatalytic Tetracycline Degradation. *Environ. Sci.: Nano* **2018**, *5* (11), 2604−2617.
(677) Chen, Y.; Liu, X.; Hou, L.; Guo, X.; Fu, R.; Sun, J. Construction of Covalent Bonding Oxygen-doped Carbon Nitride/Graphitic Carbon Nitride Z-Scheme Heterojunction for Enhanced Visible-Light-Driven H_2 Evolution. *Chem. Eng. J.* **2020**, *383*, 123132.
(678) Jiang, T.; Du, Y.; Dong, M.; Zhao, Q. The Facile Synthesis and Enhanced Photocatalytic Activity of A Graphitic Carbon Nitride Isotype Heterojunction with Ordered Mesopores. *New J. Chem.* **2019**, *43* (27), 10915−10925.
(679) Li, J.; Qi, Y.; Mei, Y.; Ma, S.; Li, Q.; Xin, B.; Yao, T.; Wu, J. Construction of Phosphorus-Doped Carbon Nitride/Phosphorus and Sulfur Co-doped Carbon Nitride Isotype Heterojunction and Their Enhanced Photoactivity. *J. Colloid Interface Sci.* **2020**, *566*, 495−504.
(680) Reshak, A. AA-and ABA-Stacked Carbon Nitride (C_3N_4): Novel Photocatalytic Water Splitting Solar-to-Hydrogen Energy Conversion. *Phys. Chem. Chem. Phys.* **2018**, *20* (35), 22972−22979.
(681) Qiao, Q.; Huang, W.-Q.; Li, Y.-Y.; Li, B.; Hu, W.; Peng, W.; Fan, X.; Huang, G.-F. In-Situ Construction of 2D Direct Z-Scheme g-C_3N_4/g-C_3N_4 Homojunction with High Photocatalytic Activity. *J. Mater. Sci.* **2018**, *53* (23), 15882−15894.
(682) Ye, B.; Han, X.; Yan, M.; Zhang, H.; Xi, F.; Dong, X.; Liu, J. Fabrication of Metal-Free Two Dimensional/Two dimensional Homojunction Photocatalyst using Various Carbon Nitride Nanosheets as Building Blocks. *J. Colloid Interface Sci.* **2017**, *507*, 209−216.
(683) Xu, Q.; Cheng, B.; Yu, J.; Liu, G. Making Co-condensed Amorphous Carbon/g-C_3N_4 Composites with Improved Visible-Light Photocatalytic H_2-Production Performance using Pt as Cocatalyst. *Carbon* **2017**, *118*, 241−249.
(684) Li, X.; Chen, D.; Li, N.; Xu, Q.; Li, H.; He, J.; Lu, J. One-step Synthesis of Honeycomb-like Carbon Nitride Isotype Heterojunction as Low-Cost, High-Performance Photocatalyst for Removal of NO. *ACS Sustainable Chem. Eng.* **2018**, *6* (8), 11063−11070.
(685) Li, Y.; Gong, F.; Zhou, Q.; Feng, X.; Fan, J.; Xiang, Q. Crystalline Isotype Heptazine-/Triazine-based Carbon Nitride Heterojunctions for An Improved Hydrogen Evolution. *Appl. Catal., B* **2020**, *268*, 118381.
(686) Qin, H.; Lv, W.; Bai, J.; Zhou, Y.; Wen, Y.; He, Q.; Tang, J.; Wang, L.; Zhou, Q. Sulfur-Doped Porous Graphitic Carbon Nitride Heterojunction Hybrids for Enhanced Photocatalytic H_2 Evolution. *J. Mater. Sci.* **2019**, *54* (6), 4811−4820.
(687) Dong, F.; Zhao, Z.; Xiong, T.; Ni, Z.; Zhang, W.; Sun, Y.; Ho, W.-K. In Situ Construction of g-C_3N_4/g-C_3N_4 Metal-free Heterojunction for Enhanced Visible-Light Photocatalysis. *ACS Appl. Mater. Interfaces* **2013**, *5* (21), 11392−11401.
(688) Li, H.; Liu, Y.; Gao, X.; Fu, C.; Wang, X. Facile Synthesis and Enhanced Visible-Light Photocatalysis of Graphitic Carbon Nitride Composite Semiconductors. *ChemSusChem* **2015**, *8* (7), 1189−1196.
(689) Zhao, D.; Wang, Y.; Dong, C.-L.; Huang, Y.-C.; Chen, J.; Xue, F.; Shen, S.; Guo, L. Boron-Doped Nitrogen-Deficient Carbon Nitride-based Z-Scheme Heterostructures for Photocatalytic Overall Water Splitting. *Nat. Energy* **2021**, *6* (4), 388−397.
(690) Zeng, F.; Huang, W.-Q.; Xiao, J.-H.; Li, Y.-y.; Peng, W.; Hu, W.; Li, K.; Huang, G.-F. Isotype Heterojunction g-C_3N_4/g-C_3N_4 Nanosheets as 2D Support to Highly Dispersed 0D Metal Oxide Nanoparticles: Generalized Self-Assembly and Its High Photocatalytic Activity. *J. Phys. D: Appl. Phys.* **2019**, *52* (2), 025501.
(691) Wang, J.; Chen, Y.; Shen, Y.; Liu, S.; Zhang, Y. Coupling Polymorphic Nanostructured Carbon Nitrides into An Isotype Heterojunction with Boosted Photocatalytic H_2 Evolution. *Chem. Commun.* **2017**, *53* (20), 2978−2981.
(692) Zhang, J.; Sun, J.; Maeda, K.; Domen, K.; Liu, P.; Antonietti, M.; Fu, X.; Wang, X. Sulfur-Mediated Synthesis of Carbon Nitride: Band-Gap Engineering and Improved Functions for Photocatalysis. *Energy Environ. Sci.* **2011**, *4* (3), 675−678.
(693) Jin, A.; Jia, Y.; Chen, C.; Liu, X.; Jiang, J.; Chen, X.; Zhang, F. Efficient Photocatalytic Hydrogen Evolution on Band Structure Tuned Polytriazine/Heptazine based Carbon Nitride Heterojunctions with Ordered Needle-like Morphology Achieved by An In Situ Molten Salt Method. *J. Phys. Chem. C* **2017**, *121* (39), 21497−21509.
(694) Zeng, Z.; Yu, H.; Quan, X.; Chen, S.; Zhang, S. Structuring Phase Function between Tri-s-Triazine and Triazine Crystalline C_3N_4 for Efficient Photocatalytic Hydrogen Evolution. *Appl. Catal., B* **2018**, *227*, 153−160.
(695) Li, C.; Yu, S.; Zhang, X.; Wang, Y.; Liu, C.; Chen, G.; Dong, H. Insight into Photocatalytic Activity, Universality and Mechanism of Copper/Chlorine Surface Dual-doped Graphitic Carbon Nitride for Degrading Various Organic Pollutants in Water. *J. Colloid Interface Sci.* **2019**, *538*, 462−473.
(696) Yang, Y.; Jin, H.; Zhang, C.; Gan, H.; Yi, F.; Wang, H. Nitrogen-Deficient Modified P-Cl Co-doped Graphitic Carbon

https://doi.org/10.1021/acs.chemmater.1c03166
Chem. Mater. 2021, 33, 9012−9092

Nitride with Enhanced Photocatalytic Performance. *J. Alloys Compd.* **2020**, *821*, 153439.
(697) Cui, W.; Li, J.; Cen, W.; Sun, Y.; Lee, S.; Dong, F. Steering the Interlayer Energy Barrier and Charge Flow via Bioriented Transportation Channels in g-C_3N_4: Enhanced Photocatalysis and Reaction Mechanism. *J. Catal.* **2017**, *352*, 351−360.
(698) Pesci, F. M.; Sokolikova, M. S.; Grotta, C.; Sherrell, P. C.; Reale, F.; Sharda, K.; Ni, N.; Palczynski, P.; Mattevi, C. MoS_2/WS_2 Heterojunction for Photoelectrochemical Water Oxidation. *ACS Catal.* **2017**, *7* (8), 4990−4998.
(699) Chen, L.; Shi, G.; Shen, J.; Peng, B.; Zhang, B.; Wang, Y.; Bian, F.; Wang, J.; Li, D.; Qian, Z.; et al. Ion Sieving in Graphene Oxide Membranes via Cationic Control of Interlayer Spacing. *Nature* **2017**, *550* (7676), 380−383.
(700) Ditto, J.; Merrill, D. R.; Mitchson, G.; Gabriel, J. J.; Mathew, K.; Hennig, R. G.; Medlin, D. L.; Browning, N. D.; Johnson, D. C. Interface-Driven Structural Distortions and Composition Segregation in Two-Dimensional Heterostructures. *Angew. Chem.* **2017**, *129* (46), 14640−14644.
(701) Xiong, T.; Cen, W.; Zhang, Y.; Dong, F. Bridging the g-C_3N_4 Interlayers for Enhanced Photocatalysis. *ACS Catal.* **2016**, *6* (4), 2462−2472.
(702) Li, J.; Zhang, Z.; Cui, W.; Wang, H.; Cen, W.; Johnson, G.; Jiang, G.; Zhang, S.; Dong, F. The Spatially Oriented Charge Flow and Photocatalysis Mechanism on Internal van der Waals Heterostructures Enhanced g-C_3N_4. *ACS Catal.* **2018**, *8* (9), 8376−8385.
(703) Kofuji, Y.; Ohkita, S.; Shiraishi, Y.; Sakamoto, H.; Ichikawa, S.; Tanaka, S.; Hirai, T. Mellitic Triimide-Doped Carbon Nitride as Sunlight-Driven Photocatalysts for Hydrogen Peroxide Production. *ACS Sustainable Chem. Eng.* **2017**, *5* (8), 6478−6485.
(704) Chu, S.; Wang, Y.; Guo, Y.; Feng, J.; Wang, C.; Luo, W.; Fan, X.; Zou, Z. Band Structure Engineering of Carbon Nitride: In Search of A Polymer Photocatalyst with High Photooxidation Property. *ACS Catal.* **2013**, *3* (5), 912−919.
(705) Kofuji, Y.; Ohkita, S.; Shiraishi, Y.; Sakamoto, H.; Tanaka, S.; Ichikawa, S.; Hirai, T. Graphitic Carbon Nitride Doped with Biphenyl Diimide: Efficient Photocatalyst for Hydrogen Peroxide Production from Water and Molecular Oxygen by Sunlight. *ACS Catal.* **2016**, *6* (10), 7021−7029.
(706) Shiraishi, Y.; Kanazawa, S.; Kofuji, Y.; Sakamoto, H.; Ichikawa, S.; Tanaka, S.; Hirai, T. Sunlight-Driven Hydrogen Peroxide Production from Water and Molecular Oxygen by Metal-free Photocatalysts. *Angew. Chem., Int. Ed.* **2014**, *53* (49), 13454−13459.
(707) Kofuji, Y.; Isobe, Y.; Shiraishi, Y.; Sakamoto, H.; Tanaka, S.; Ichikawa, S.; Hirai, T. Carbon Nitride-Aromatic Diimide-Graphene Nanohybrids: Metal-free Photocatalysts for Solar-to-Hydrogen Peroxide Energy Conversion with 0.2% Efficiency. *J. Am. Chem. Soc.* **2016**, *138* (31), 10019−10025.
(708) Kailasam, K.; Mesch, M. B.; Möhlmann, L.; Baar, M.; Blechert, S.; Schwarze, M.; Schröder, M.; Schomäcker, R.; Senker, J.; Thomas, A. Donor-Acceptor-Type Heptazine-based Polymer Networks for Photocatalytic Hydrogen Evolution. *Energy Technol.* **2016**, *4* (6), 744−750.
(709) Chauhan, D. K.; Jain, S.; Battula, V. R.; Kailasam, K. Organic Motif's Functionalization via Covalent Linkage in Carbon Nitride: An Exemplification in Photocatalysis. *Carbon* **2019**, *152*, 40−58.
(710) Karjule, N.; Barrio, J.; Tzadikov, J.; Shalom, M. Electronic Structure Engineering of Carbon Nitride Materials using Polycyclic Aromatic Hydrocarbons. *Chem. - Eur. J.* **2020**, *26*, 6622−6628.
(711) Li, J.; Wu, D.; Iocozzia, J.; Du, H.; Liu, X.; Yuan, Y.; Zhou, W.; Li, Z.; Xue, Z.; Lin, Z. Achieving Efficient Incorporation of Π-electrons into Graphitic Carbon Nitride for Markedly Improved Hydrogen Generation. *Angew. Chem.* **2019**, *131* (7), 2007−2011.
(712) Zhang, P.; Li, X.; Shao, C.; Liu, Y. Hydrothermal Synthesis of Carbon-Rich Graphitic Carbon Nitride Nanosheets for Photoredox Catalysis. *J. Mater. Chem. A* **2015**, *3* (7), 3281−3284.
(713) Che, W.; Cheng, W.; Yao, T.; Tang, F.; Liu, W.; Su, H.; Huang, Y.; Liu, Q.; Liu, J.; Hu, F.; et al. Fast Photoelectron Transfer in (C_{ring})-C_3N_4 Plane Heterostructural Nanosheets for Overall Water Splitting. *J. Am. Chem. Soc.* **2017**, *139* (8), 3021−3026.
(714) Song, T.; Zeng, G.; Zhang, P.; Wang, T.; Huang, S.; Zeng, H. Ultrathin Carbon Nitride with Atomic-level Intraplane Implantation of Graphited Carbon Ring Domain for Superior Photocatalytic Activity in the Visible/Near-Infrared Region. *ACS Sustainable Chem. Eng.* **2019**, *7* (1), 1239−1249.
(715) Cheng, L.; Zhang, H.; Li, X.; Fan, J.; Xiang, Q. Carbon-Graphitic Carbon Nitride Hybrids for Heterogeneous Photocatalysis. *Small* **2021**, *17*, 2005231.
(716) Wang, Y.; Bai, X.; Qin, H.; Wang, F.; Li, Y.; Li, X.; Kang, S.; Zuo, Y.; Cui, L. Facile One-Step Synthesis of Hybrid Graphitic Carbon Nitride and Carbon Composites as High-Performance Catalysts for CO_2 Photocatalytic Conversion. *ACS Appl. Mater. Interfaces* **2016**, *8* (27), 17212−17219.
(717) Lu, X.; Tan, T. H.; Ng, Y. H.; Amal, R. Highly Selective and Stable Reduction of CO_2 to CO by A Graphitic Carbon Nitride/Carbon Nanotube Composite Electrocatalyst. *Chem. - Eur. J.* **2016**, *22* (34), 11991−11996.
(718) Park, J. E.; Kim, M.-J.; Lim, M. S.; Kang, S. Y.; Kim, J. K.; Oh, S.-H.; Her, M.; Cho, Y.-H.; Sung, Y.-E. Graphitic Carbon Nitride-Carbon Nanofiber as Oxygen Catalyst in Anion-Exchange Membrane Water Electrolyzer and Rechargeable Metal-Air Cells. *Appl. Catal., B* **2018**, *237*, 140−148.
(719) Ma, T. Y.; Dai, S.; Jaroniec, M.; Qiao, S. Z. Graphitic Carbon Nitride Nanosheet-Carbon Nanotube Three-dimensional Porous Composites as High-performance Oxygen Evolution Electrocatalysts. *Angew. Chem.* **2014**, *126* (28), 7409−7413.
(720) Zhang, Y.; Zhang, L.; Zhou, C. Review of Chemical Vapor Deposition of Graphene and Related Applications. *Acc. Chem. Res.* **2013**, *46* (10), 2329−2339.
(721) Su, D. S.; Perathoner, S.; Centi, G. Nanocarbons for the Development of Advanced Catalysts. *Chem. Rev.* **2013**, *113* (8), 5782−5816.
(722) Liu, J.; Xu, H.; Xu, Y.; Song, Y.; Lian, J.; Zhao, Y.; Wang, L.; Huang, L.; Ji, H.; Li, H. Graphene Quantum Dots Modified Mesoporous Graphite Carbon Nitride with Significant Enhancement of Photocatalytic Activity. *Appl. Catal., B* **2017**, *207*, 429−437.
(723) Kundu, S.; Bramhaiah, K.; Bhattacharyya, S. Carbon-based Nanomaterials: In the Quest of Alternative Metal-Free Photocatalysts for Solar Water Splitting. *Nanoscale Adv.* **2020**, *2* (11), 5130−5151.
(724) Low, J.; Cheng, B.; Yu, J.; Jaroniec, M. Carbon-based Two-dimensional Layered Materials for Photocatalytic CO_2 Reduction to Solar Fuels. *Energy Storage Mater.* **2016**, *3*, 24−35.
(725) Kandy, M. M. Carbon-based Photocatalysts for Enhanced Photocatalytic Reduction of CO_2 to Solar Fuels. *Sustain. Energy Fuels* **2020**, *4* (2), 469−484.
(726) Xing, W.; Li, C.; Wang, Y.; Han, Z.; Hu, Y.; Chen, D.; Meng, Q.; Chen, G. A Novel 2D/2D Carbonized Poly-(furfural alcohol)/g-C_3N_4 Nanocomposites with Enhanced Charge Carrier Separation for Photocatalytic H_2 Evolution. *Carbon* **2017**, *115*, 486−492.
(727) Kasap, H.; Godin, R.; Jeay-Bizot, C.; Achilleos, D. S.; Fang, X.; Durrant, J. R.; Reisner, E. Interfacial Engineering of a Carbon Nitride-Graphene Oxide-Molecular Ni Catalyst Hybrid for Enhanced Photocatalytic Activity. *ACS Catal.* **2018**, *8* (8), 6914−6926.
(728) Adekoya, D.; Zhang, S.; Hankel, M. 1D-2D C_3N_4/Graphene Composite as a Preferred Anode Material for Lithium-Ion Batteries-Importance of Heterostructure Design via DFT Computation. *ACS Appl. Mater. Interfaces* **2020**, *12* (23), 25875−25883.
(729) Padhiari, S.; Tripathy, M.; Hota, G. Nitrogen-Doped Reduced Graphene Oxide Covalently Coupled with Graphitic Carbon Nitride/Sulfur-Doped Graphitic Carbon Nitride Heterojunction Nanocatalysts for Photoreduction and Degradation of 4-Nitrophenol. *ACS Appl. Nano Mater.* **2021**, *4* (7), 7145−7161.
(730) Loh, K. P.; Bao, Q.; Ang, P. K.; Yang, J. The Chemistry of Graphene. *J. Mater. Chem.* **2010**, *20* (12), 2277−2289.
(731) Allen, M. J.; Tung, V. C.; Kaner, R. B. Honeycomb Carbon: A Review of Graphene. *Chem. Rev.* **2010**, *110* (1), 132−145.

https://doi.org/10.1021/acs.chemmater.1c03166
Chem. Mater. 2021, 33, 9012−9092

(732) Geim, A. K.; Novoselov, K. S. The Rise of Graphene. In *Nanoscience and Technology: A Collection of Reviews from Nature Journals*; World Scientific: 2010; pp 11−19.
(733) Jia, X.; Campos-Delgado, J.; Terrones, M.; Meunier, V.; Dresselhaus, M. S. Graphene Edges: A Review of Their Fabrication and Characterization. *Nanoscale* **2011**, *3* (1), 86−95.
(734) Talirz, L.; Söde, H.; Kawai, S.; Ruffieux, P.; Meyer, E.; Feng, X.; Müllen, K.; Fasel, R.; Pignedoli, C. A.; Passerone, D. Band Gap of Atomically Precise Graphene Nanoribbons as a Function of Ribbon Length and Termination. *ChemPhysChem* **2019**, *20* (18), 2348−2353.
(735) Wu, Y.; Cao, C.; Qiao, C.; Wu, Y.; Yang, L.; Younas, W. Bandgap-Tunable Phosphorus-Doped Monolayer Graphene with Enhanced Visible-Light Photocatalytic H_2-production Activity. *J. Mater. Chem. C* **2019**, *7* (34), 10613−10622.
(736) Kuang, Y.; Shang, J.; Zhu, T. Photoactivated Graphene Oxide to Enhance Photocatalytic Reduction of CO_2. *ACS Appl. Mater. Interfaces* **2020**, *12* (3), 3580−3591.
(737) Yeh, T.-F.; Cihlář, J.; Chang, C.-Y.; Cheng, C.; Teng, H. Roles of Graphene Oxide in Photocatalytic Water Splitting. *Mater. Today* **2013**, *16* (3), 78−84.
(738) Hsu, H.-C.; Shown, I.; Wei, H.-Y.; Chang, Y.-C.; Du, H.-Y.; Lin, Y.-G.; Tseng, C.-A.; Wang, C.-H.; Chen, L.-C.; Lin, Y.-C.; et al. Graphene Oxide as A Promising Photocatalyst for CO_2 to Methanol Conversion. *Nanoscale* **2013**, *5* (1), 262−268.
(739) Putri, L. K.; Tan, L.-L.; Ong, W.-J.; Chang, W. S.; Chai, S.-P. Graphene Oxide: Exploiting its Unique Properties Toward Visible-Light-Driven Photocatalysis. *Appl. Mater. Today* **2016**, *4*, 9−16.
(740) Gao, W. The Chemistry of Graphene Oxide. In *Graphene oxide*; Springer: 2015; pp 61−95.
(741) Du, A.; Sanvito, S.; Li, Z.; Wang, D.; Jiao, Y.; Liao, T.; Sun, Q.; Ng, Y. H.; Zhu, Z.; Amal, R.; et al. Hybrid Graphene and Graphitic Carbon Nitride Nanocomposite: Gap Opening, Electron-Hole Puddle, Interfacial Charge Transfer, and Enhanced Visible Light Response. *J. Am. Chem. Soc.* **2012**, *134* (9), 4393−4397.
(742) Han, Q.; Chen, N.; Zhang, J.; Qu, L. Graphene/Graphitic Carbon Nitride Hybrids for Catalysis. *Mater. Horiz.* **2017**, *4* (5), 832−850.
(743) Bafekry, A.; Akgenc, B.; Shayesteh, S. F.; Mortazavi, B. Tunable Electronic and Magnetic Properties of Graphene/Carbon-Nitride van der Waals Heterostructures. *Appl. Surf. Sci.* **2020**, *505*, 144450.
(744) Ma, J.; Yu, M.; Ye, H.; Song, H.; Wang, D.; Zhao, Y.; Gong, W.; Qiu, H. A 2D/2D Graphitic Carbon Nitride/N-Doped Graphene Hybrid as An Effective Polysulfide Mediator in Lithium-Sulfur Batteries. *Mater. Chem. Frontiers* **2019**, *3* (9), 1807−1815.
(745) Kirtley, J. R.; Mannhart, J. When TTF Met TCNQ. *Nat. Mater.* **2008**, *7* (7), 520−521.
(746) Zhang, Y.; Mori, T.; Niu, L.; Ye, J. Non-Covalent Doping of Graphitic Carbon Nitride Polymer with Graphene: Controlled Electronic Structure and Enhanced Optoelectronic Conversion. *Energy Environ. Sci.* **2011**, *4* (11), 4517−4521.
(747) Prakash, K.; Karuthapandian, S. Construction of Novel Metal-Free Graphene Oxide/Graphitic Carbon Nitride Nanohybrids: A 2D-2D Amalgamation for the Effective Dedyeing of Waste Water. *J. Inorg. Organomet. Polym. Mater.* **2021**, *31*, 716−730.
(748) Pedrosa, M.; Sampaio, M. J.; Horvat, T.; Nunes, O. C.; Dražić, G.; Rodrigues, A. E.; Figueiredo, J. L.; Silva, C. G.; Silva, A. M.; Faria, J. L. Visible-Light-Induced Self-Cleaning Functional Fabrics using Graphene Oxide/Carbon Nitride Materials. *Appl. Surf. Sci.* **2019**, *497*, 143757.
(749) Aleksandrzak, M.; Kukulka, W.; Mijowska, E. Graphitic Carbon Nitride/Graphene Oxide/Reduced Graphene Oxide Nanocomposites for Photoluminescence and Photocatalysis. *Appl. Surf. Sci.* **2017**, *398*, 56−62.
(750) Xie, L.; Ni, J.; Tang, B.; He, G.; Chen, H. A Self-Assembled 2D/2D-Type Protonated Carbon Nitride-Modified Graphene Oxide Nanocomposite with Improved Photocatalytic Activity. *Appl. Surf. Sci.* **2018**, *434*, 456−463.
(751) Sun, L.; Du, T.; Hu, C.; Chen, J.; Lu, J.; Lu, Z.; Han, H. Antibacterial Activity of Graphene Oxide/g-C_3N_4| Composite through Photocatalytic Disinfection under Visible Light. *ACS Sustainable Chem. Eng.* **2017**, *5* (10), 8693−8701.
(752) Song, T.; Long, B.; Yin, S.; Ali, A.; Deng, G.-J. Designed Synthesis of A Porous Ultrathin 2D CN@Graphene@CN Sandwich Structure for Superior Photocatalytic Hydrogen Evolution under Visible Light. *Chem. Eng. J.* **2021**, *404*, 126455.
(753) Gao, X.; Liu, H.; Wang, D.; Zhang, J. Graphdiyne: Synthesis, Properties, and Applications. *Chem. Soc. Rev.* **2019**, *48* (3), 908−936.
(754) Li, Y.; Xu, L.; Liu, H.; Li, Y. Graphdiyne and Graphyne: From Theoretical Predictions to Practical Construction. *Chem. Soc. Rev.* **2014**, *43* (8), 2572−2586.
(755) Huang, C.; Li, Y.; Wang, N.; Xue, Y.; Zuo, Z.; Liu, H.; Li, Y. Progress in Research into 2D Graphdiyne-based Materials. *Chem. Rev.* **2018**, *118* (16), 7744−7803.
(756) Jia, Z.; Li, Y.; Zuo, Z.; Liu, H.; Huang, C.; Li, Y. Synthesis and Properties of 2D Carbon Graphdiyne. *Acc. Chem. Res.* **2017**, *50* (10), 2470−2478.
(757) Long, M.; Tang, L.; Wang, D.; Li, Y.; Shuai, Z. Electronic Structure and Carrier Mobility in Graphdiyne Sheet and Nanoribbons: Theoretical Predictions. *ACS Nano* **2011**, *5* (4), 2593−2600.
(758) Lv, J.-X.; Zhang, Z.-M.; Wang, J.; Lu, X.-L.; Zhang, W.; Lu, T.-B. In Situ Synthesis of CdS/Graphdiyne Heterojunction for Enhanced Photocatalytic Activity of Hydrogen Production. *ACS Appl. Mater. Interfaces* **2019**, *11* (3), 2655−2661.
(759) Yu, H.; Xue, Y.; Li, Y. Graphdiyne and Its Assembly Architectures: Synthesis, Functionalization, and Applications. *Adv. Mater.* **2019**, *31* (42), 1803101.
(760) Thangavel, S.; Krishnamoorthy, K.; Krishnaswamy, V.; Raju, N.; Kim, S. J.; Venugopal, G. Graphdiyne-ZnO Nanohybrids as An Advanced Photocatalytic Material. *J. Phys. Chem. C* **2015**, *119* (38), 22057−22065.
(761) Wu, Y.; Xu, W.; Tang, W.; Wang, Z.; Wang, Y.; Lv, Z.; Zhang, Y.; Zhong, W.; Cai, H.-L.; Yang, R.; et al. In-situ Annealed "M-scheme" MXene-Based Photocatalyst for Enhanced Photoelectric Performance and Highly Selective CO_2 Photoreduction. *Nano Energy* **2021**, *90*, 106532.
(762) Han, Y. Y.; Lu, X. L.; Tang, S. F.; Yin, X. P.; Wei, Z. W.; Lu, T. B. Metal-Free 2D/2D Heterojunction of Graphitic Carbon Nitride/Graphdiyne for Improving the Hole Mobility of Graphitic Carbon Nitride. *Adv. Energy Mater.* **2018**, *8* (16), 1702992.
(763) Xu, Q.; Zhu, B.; Cheng, B.; Yu, J.; Zhou, M.; Ho, W. Photocatalytic H_2 Evolution on Graphdiyne/g-C_3N_4 Hybrid Nanocomposites. *Appl. Catal., B* **2019**, *255*, 117770.
(764) Si, H.; Deng, Q.; Yin, C.; Zhou, J.; Zhang, S.; Zhang, Y.; Liu, Z.; Zhang, J.; Zhang, J.; Kong, J. Gas Exfoliation of Graphitic Carbon Nitride to Improve the Photocatalytic Hydrogen Evolution of Metal-Free 2D/2D g-C_3N_4/Graphdiyne Heterojunction. *J. Alloys Compd.* **2020**, *833*, 155054.
(765) Lim, S. Y.; Shen, W.; Gao, Z. Carbon Quantum Dots and Their Applications. *Chem. Soc. Rev.* **2015**, *44* (1), 362−381.
(766) Li, X.; Rui, M.; Song, J.; Shen, Z.; Zeng, H. Carbon and Graphene Quantum Dots for Optoelectronic and Energy Devices: A Review. *Adv. Funct. Mater.* **2015**, *25* (31), 4929−4947.
(767) Wang, R.; Lu, K.-Q.; Tang, Z.-R.; Xu, Y.-J. Recent Progress in Carbon Quantum Dots: Synthesis, Properties and Applications in Photocatalysis. *J. Mater. Chem. A* **2017**, *5* (8), 3717−3734.
(768) Molaei, M. J. The Optical Properties and Solar Energy Conversion Applications of Carbon Quantum Dots: A Review. *Sol. Energy* **2020**, *196*, 549−566.
(769) Li, M.; Chen, T.; Gooding, J. J.; Liu, J. Review of Carbon and Graphene Quantum Dots for Sensing. *ACS Sensors* **2019**, *4* (7), 1732−1748.
(770) Fernando, K. S.; Sahu, S.; Liu, Y.; Lewis, W. K.; Guliants, E. A.; Jafariyan, A.; Wang, P.; Bunker, C. E.; Sun, Y.-P. Carbon Quantum Dots and Applications in Photocatalytic Energy Conversion. *ACS Appl. Mater. Interfaces* **2015**, *7* (16), 8363−8376.

https://doi.org/10.1021/acs.chemmater.1c03166
Chem. Mater. 2021, 33, 9012−9092

(771) Hoang, V. C.; Dave, K.; Gomes, V. G. Carbon Quantum Dot-based Composites for Energy Storage and Electrocatalysis: Mechanism, Applications and Future Prospects. *Nano Energy* **2019**, *66*, 104093.
(772) Mahala, C.; Sharma, M. D.; Basu, M. ZnO Nanosheets Decorated with Graphite-Like Carbon Nitride Quantum Dots as Photoanodes in Photoelectrochemical Water Splitting. *ACS Appl. Nano Mater.* **2020**, *3* (2), 1999−2007.
(773) Albolkany, M. K.; Wang, Y.; Li, W.; Arooj, S.; Chen, C. H.; Wu, N.; Wang, Y.; Zbořil, R.; Fischer, R. A.; Liu, B. Dual-Function HKUST-1: Templating and Catalyzing Formation of Graphitic Carbon Nitride Quantum Dots Under Mild Conditions. *Angew. Chem.* **2020**, *132* (48), 21683−21688.
(774) Liu, P.; Sun, Y.; Wang, S.; Zhang, H.; Gong, Y.; Li, F.; Shi, Y.; Du, Y.; Li, X.; Guo, S.-s.; et al. Two Dimensional Graphitic Carbon Nitride Quantum Dots Modified Perovskite Solar Cells and Photodetectors with High Performances. *J. Power Sources* **2020**, *451*, 227825.
(775) Qin, J.; Zeng, H. Photocatalysts Fabricated by Depositing Plasmonic Ag Nanoparticles on Carbon Quantum Dots/Graphitic Carbon Nitride for Broad Spectrum Photocatalytic Hydrogen Generation. *Appl. Catal., B* **2017**, *209*, 161−173.
(776) Seng, R. X.; Tan, L.-L.; Lee, W. C.; Ong, W.-J.; Chai, S.-P. Nitrogen-Doped Carbon Quantum Dots-decorated 2D Graphitic Carbon Nitride as A Promising Photocatalyst for Environmental Remediation: A Study on the Importance of Hybridization Approach. *J. Environ. Manage.* **2020**, *255*, 109936.
(777) Wang, X.; Jiang, X.; Sharman, E.; Yang, L.; Li, X.; Zhang, G.; Zhao, J.; Luo, Y.; Jiang, J. Isolating Hydrogen from Oxygen in Photocatalytic Water Splitting with a Carbon-quantum-Dot/Carbon-Nitride Hybrid. *J. Mater. Chem. A* **2019**, *7* (11), 6143−6148.
(778) Zhang, L.; Zhang, J.; Xia, Y.; Xun, M.; Chen, H.; Liu, X.; Yin, X. Metal-Free Carbon Quantum Dots Implant Graphitic Carbon Nitride: Enhanced Photocatalytic Dye Wastewater Purification with Simultaneous Hydrogen Production. *Int. J. Mol. Sci.* **2020**, *21* (3), 1052.
(779) Wang, Y.; Liu, X.; Liu, J.; Han, B.; Hu, X.; Yang, F.; Xu, Z.; Li, Y.; Jia, S.; Li, Z.; et al. Carbon Quantum Dot Implanted Graphite Carbon Nitride Nanotubes: Excellent Charge Separation and Enhanced Photocatalytic Hydrogen Evolution. *Angew. Chem.* **2018**, *130* (20), 5867−5873.
(780) Han, M.; Lu, S.; Qi, F.; Zhu, S.; Sun, H.; Yang, B. Carbon Dots-Implanted Graphitic Carbon Nitride Nanosheets for Photocatalysis: Simultaneously Manipulating Carrier Transport in Inter-and Intralayers. *Solar RRL* **2020**, *4* (4), 1900517.
(781) Liu, H.; Lv, X.; Qian, J.; Li, H.; Qian, Y.; Wang, X.; Meng, X.; Lin, W.; Wang, H. Graphitic Carbon Nitride Quantum Dots Embedded in Carbon Nanosheets for Near-Infrared Imaging-Guided Combined Photo-Chemotherapy. *ACS Nano* **2020**, *14* (10), 13304−13315.
(782) Li, Y.-Y.; Si, Y.; Zhou, B.-X.; Huang, T.; Huang, W.-Q.; Hu, W.; Pan, A.; Fan, X.; Huang, G.-F. Interfacial Charge Modulation: Carbon Quantum Dot Implanted Carbon Nitride Double-Deck Nanoframes for Robust Visible-light Photocatalytic Tetracycline Degradation. *Nanoscale* **2020**, *12* (5), 3135−3145.
(783) Li, B.; Fang, Q.; Si, Y.; Huang, T.; Huang, W.-Q.; Hu, W.; Pan, A.; Fan, X.; Huang, G.-F. Ultra-Thin Tubular Graphitic Carbon Nitride-Carbon Dot Lateral Heterostructures: One-Step Synthesis and Highly Efficient Catalytic Hydrogen Generation. *Chem. Eng. J.* **2020**, *397*, 125470.
(784) Yanagida, S.; Kabumoto, A.; Mizumoto, K.; Pac, C.; Yoshino, K. Poly (p-phenylene)-Catalysed Photoreduction of Water to Hydrogen. *J. Chem. Soc., Chem. Commun.* **1985**, *8*, 474−475.
(785) Bu, Y.; Chen, Z. Role of Polyaniline on the Photocatalytic Degradation and Stability Performance of the Polyaniline/Silver/Silver Phosphate Composite under Visible Light. *ACS Appl. Mater. Interfaces* **2014**, *6* (20), 17589−17598.
(786) Zhang, H.; Zhu, Y. Significant Visible Photoactivity and Antiphotocorrosion Performance of CdS Photocatalysts after Monolayer Polyaniline Hybridization. *J. Phys. Chem. C* **2010**, *114* (13), 5822−5826.
(787) Jiang, W.; Luo, W.; Zong, R.; Yao, W.; Li, Z.; Zhu, Y. Polyaniline/Carbon Nitride Nanosheets Composite Hydrogel: A Separation-Free and High-Efficient Photocatalyst with 3D Hierarchical Structure. *Small* **2016**, *12* (32), 4370−4378.
(788) Xiong, P.; Chen, Q.; He, M.; Sun, X.; Wang, X. Cobalt Ferrite-Polyaniline Heteroarchitecture: A Magnetically Recyclable Photocatalyst with Highly Enhanced Performances. *J. Mater. Chem.* **2012**, *22* (34), 17485−17493.
(789) Li, L.; Hadt, R. G.; Yao, S.; Lo, W.-Y.; Cai, Z.; Wu, Q.; Pandit, B.; Chen, L. X.; Yu, L. Photocatalysts based on Cobalt-Chelating Conjugated Polymers for Hydrogen Evolution from Water. *Chem. Mater.* **2016**, *28* (15), 5394−5399.
(790) An, K.; Yang, D.; Zhao, X.; Ren, H.; Zhao, Z.; Chen, Y.; Zhou, Z.; Wang, W.; Jiang, Z. Biomimetic Synthesis of 2D/2D Mixed Graphitic Carbon Nitride/Carbonized Polydopamine Nanosheets with Excellent Photocatalytic Performance. *Mater. Chem. Phys.* **2020**, *256*, 123621.
(791) Yu, Z.; Li, F.; Yang, Q.; Shi, H.; Chen, Q.; Xu, M. Nature-Mimic Method to Fabricate Polydopamine/Graphitic Carbon Nitride for Enhancing Photocatalytic Degradation Performance. *ACS Sustainable Chem. Eng.* **2017**, *5* (9), 7840−7850.
(792) Xu, Y.; Mao, N.; Zhang, C.; Wang, X.; Zeng, J.; Chen, Y.; Wang, F.; Jiang, J.-X. Rational Design of Donor-π-Acceptor Conjugated Microporous Polymers for Photocatalytic Hydrogen Production. *Appl. Catal., B* **2018**, *228*, 1−9.
(793) Yang, C.; Ma, B. C.; Zhang, L.; Lin, S.; Ghasimi, S.; Landfester, K.; Zhang, K. A.; Wang, X. Molecular Engineering of Conjugated Polybenzothiadiazoles for Enhanced Hydrogen Production by Photosynthesis. *Angew. Chem.* **2016**, *128* (32), 9348−9352.
(794) Sprick, R. S.; Jiang, J.-X.; Bonillo, B.; Ren, S.; Ratvijitvech, T.; Guiglion, P.; Zwijnenburg, M. A.; Adams, D. J.; Cooper, A. I. Tunable Organic Photocatalysts for Visible-Light-Driven Hydrogen Evolution. *J. Am. Chem. Soc.* **2015**, *137* (9), 3265−3270.
(795) Lan, Z.-A.; Ren, W.; Chen, X.; Zhang, Y.; Wang, X. Conjugated Donor-Acceptor Polymer Photocatalysts with Electron-Output "Tentacles" for Efficient Hydrogen Evolution. *Appl. Catal., B* **2019**, *245*, 596−603.
(796) Stegbauer, L.; Schwinghammer, K.; Lotsch, B. V. A Hydrazone-based Covalent Organic Framework for Photocatalytic Hydrogen Production. *Chem. Sci.* **2014**, *5* (7), 2789−2793.
(797) Wang, H.; Wang, H.; Wang, Z.; Tang, L.; Zeng, G.; Xu, P.; Chen, M.; Xiong, T.; Zhou, C.; Li, X.; et al. Covalent Organic Framework Photocatalysts: Structures and Applications. *Chem. Soc. Rev.* **2020**, *49* (12), 4135−4165.
(798) Acharjya, A.; Longworth-Dunbar, L.; Roeser, J. r. m.; Pachfule, P.; Thomas, A. Synthesis of Vinylene-Linked Covalent Organic Frameworks from Acetonitrile: Combining Cyclotrimerization and Aldol Condensation in One Pot. *J. Am. Chem. Soc.* **2020**, *142* (33), 14033−14038.
(799) Wang, Y.; Vogel, A.; Sachs, M.; Sprick, R. S.; Wilbraham, L.; Moniz, S. J.; Godin, R.; Zwijnenburg, M. A.; Durrant, J. R.; Cooper, A. I.; et al. Current Understanding and Challenges of Solar-Driven Hydrogen Generation using Polymeric Photocatalysts. *Nat. Energy* **2019**, *4*, 746−760.
(800) Zhang, G.; Lan, Z. A.; Wang, X. Conjugated Polymers: Catalysts for Photocatalytic Hydrogen Evolution. *Angew. Chem., Int. Ed.* **2016**, *55* (51), 15712−15727.
(801) Krishnaraj, C.; Sekhar Jena, H.; Bourda, L.; Laemont, A.; Pachfule, P.; Roeser, J.; Chandran, C. V.; Borgmans, S.; Rogge, S. M.; Leus, K.; et al. Strongly Reducing (Diarylamino) Benzene-based Covalent Organic Framework for Metal-Free Visible Light Photocatalytic H_2O_2 Generation. *J. Am. Chem. Soc.* **2020**, *142* (47), 20107−20116.
(802) Luo, M.; Yang, Q.; Yang, W.; Wang, J.; He, F.; Liu, K.; Cao, H.; Yan, H. Defects Engineering Leads to Enhanced Photocatalytic H_2 Evolution on Graphitic Carbon Nitride-Covalent Organic Framework Nanosheet Composite. *Small* **2020**, *16* (20), 2001100.

https://doi.org/10.1021/acs.chemmater.1c03166
Chem. Mater. 2021, 33, 9012−9092

(803) Kong, D.; Han, X.; Xie, J.; Ruan, Q.; Windle, C. D.; Gadipelli, S.; Shen, K.; Bai, Z.; Guo, Z.; Tang, J. Tunable Covalent Triazine-based Frameworks (CTF-0) for Visible-Light-Driven Hydrogen and Oxygen Generation from Water Splitting. *ACS Catal.* **2019**, *9* (9), 7697−7707.
(804) Cao, S.; Zhang, Y.; He, N.; Wang, J.; Chen, H.; Jiang, F. Metal-Free 2D/2D Heterojunction of Covalent Triazine-based Frameworks/Graphitic Carbon Nitride with Enhanced Interfacial Charge Separation for Highly Efficient Photocatalytic Elimination of Antibiotic Pollutants. *J. Hazard. Mater.* **2020**, *391*, 122204.
(805) Zhang, G.; Lin, L.; Li, G.; Zhang, Y.; Savateev, A.; Zafeiratos, S.; Wang, X.; Antonietti, M. Ionothermal Synthesis of Triazine-Heptazine-based Copolymers with Apparent Quantum Yields of 60% at 420 nm for Solar Hydrogen Production from "Sea Water. *Angew. Chem., Int. Ed.* **2018**, *57* (30), 9372−9376.
(806) Savateev, A.; Pronkin, S.; Epping, J. D.; Willinger, M. G.; Wolff, C.; Neher, D.; Antonietti, M.; Dontsova, D. Potassium Poly (heptazine imides) from Aminotetrazoles: Shifting Band Gaps of Carbon Nitride-like Materials for More Efficient Solar Hydrogen and Oxygen Evolution. *ChemCatChem* **2017**, *9* (1), 167−174.
(807) Wang, X.; Meng, J.; Yang, X.; Hu, A.; Yang, Y.; Guo, Y. Fabrication of A Perylene Tetracarboxylic Diimide-Graphitic Carbon Nitride Heterojunction Photocatalyst for Efficient Degradation of Aqueous Organic Pollutants. *ACS Appl. Mater. Interfaces* **2019**, *11* (1), 588−602.
(808) Miao, H.; Yang, J.; Sheng, Y.; Li, W.; Zhu, Y. Controlled Synthesis of Higher Interfacial Electron Transfer Graphite-Like Carbon Nitride/Perylenetetracarboxylic Diimide Heterogeneous for Enhanced Photocatalytic Activity. *Solar RRL* **2021**, *5* (2), 2000453.
(809) Zhang, S.; Guo, H.; Hou, W.; Ji, X.; Zhang, H. Synthesis, Structure and Photocatalytic Properties of Benzo [ghi] Perylene-triimide/Graphitic Carbon Nitride Composite. *Mater. Lett.* **2018**, *221*, 38−41.
(810) Feng, J.; Li, M. Large-Scale Synthesis of A New Polymeric Carbon Nitride-C_3N_3 with Good Photoelectrochemical Performance. *Adv. Funct. Mater.* **2020**, *30* (23), 2001502.
(811) Mahmood, J.; Lee, E. K.; Jung, M.; Shin, D.; Choi, H.-J.; Seo, J.-M.; Jung, S.-M.; Kim, D.; Li, F.; Lah, M. S.; et al. Two-Dimensional Polyaniline (C_3N) from Carbonized Organic Single Crystals in Solid State. *Proc. Natl. Acad. Sci. U. S. A.* **2016**, *113* (27), 7414−7419.
(812) Mahmood, J.; Lee, E. K.; Jung, M.; Shin, D.; Jeon, I.-Y.; Jung, S.-M.; Choi, H.-J.; Seo, J.-M.; Bae, S.-Y.; Sohn, S.-D.; et al. Nitrogenated Holey Two-Dimensional Structures. *Nat. Commun.* **2015**, *6* (1), 6486.
(813) Zhou, G.; Shan, Y.; Hu, Y.; Xu, X.; Long, L.; Zhang, J.; Dai, J.; Guo, J.; Shen, J.; Li, S.; et al. Half-Metallic Carbon Nitride Nanosheets with Micro Grid Mode Resonance Structure for Efficient Photocatalytic Hydrogen Evolution. *Nat. Commun.* **2018**, *9* (1), 3366.
(814) Yang, H.; Zhou, Q.; Fang, Z.; Li, W.; Zheng, Y.; Ma, J.; Wang, Z.; Zhao, L.; Liu, S.; Shen, Y.; et al. Carbon Nitride of Five-membered Rings with Low Optical Bandgap for Photoelectrochemical Biosensing. *Chem.* **2021**, *7* (10), 2708−2721.
(815) Kim, I. Y.; Kim, S.; Jin, X.; Premkumar, S.; Chandra, G.; Lee, N. S.; Mane, G. P.; Hwang, S. J.; Umapathy, S.; Vinu, A. Ordered Mesoporous C_3N_5 with a Combined Triazole and Triazine Framework and its Graphene Hybrids for the Oxygen Reduction Reaction (ORR). *Angew. Chem.* **2018**, *130* (52), 17381−17386.
(816) Talapaneni, S. N.; Mane, G. P.; Park, D.-H.; Lakhi, K. S.; Ramadass, K.; Joseph, S.; Skinner, W. M.; Ravon, U.; Al-Bahily, K.; Vinu, A. Diaminotetrazine based Mesoporous C_3N_6 with A Well-Ordered 3D Cubic Structure and Its Excellent Photocatalytic Performance for Hydrogen Evolution. *J. Mater. Chem. A* **2017**, *5* (34), 18183−18192.
(817) Wang, H.; Li, X.; Yang, J. The g-C_3N_4/C_2N Nanocomposite: A g-C_3N_4-based Water-Splitting Photocatalyst with Enhanced Energy Efficiency. *ChemPhysChem* **2016**, *17* (13), 2100−2104.
(818) Sahabudeen, H.; Qi, H.; Glatz, B. A.; Tranca, D.; Dong, R.; Hou, Y.; Zhang, T.; Kuttner, C.; Lehnert, T.; Seifert, G.; et al. Wafer-Sized Multifunctional Polyimine-based Two-Dimensional Conjugated Polymers with High Mechanical Stiffness. *Nat. Commun.* **2016**, *7* (1), 13461.
(819) Qian, Z.; Wang, Z. J.; Zhang, K. A. Covalent Triazine Frameworks as Emerging Heterogeneous Photocatalysts. *Chem. Mater.* **2021**, *33* (6), 1909−1926.
(820) Gong, Y.; Yu, H.; Chen, S.; Quan, X. Constructing Metal-Free Polyimide/g-C_3 N_4 with High Photocatalytic Activity under Visible Light Irradiation. *RSC Adv.* **2015**, *5* (101), 83225−83231.
(821) Hao, Q.; Song, Y.; Mo, Z.; Deng, J.; Yi, J.; El-Alami, W.; Xu, H.; Li, H. Accelerating the Hole Mobility of Graphitic Carbon Nitride for Photocatalytic Hydrogen Evolution via 2D/2D Heterojunction Structural Advantages and $Ni(OH)_2$ Characteristic. *Solar RRL* **2020**, *4*, 1900538.
(822) Gong, S.; Jiang, Z.; Shi, P.; Fan, J.; Xu, Q.; Min, Y. Noble-Metal-Free Heterostructure for Efficient Hydrogen Evolution in Visible Region: Molybdenum Nitride/Ultrathin Graphitic Carbon Nitride. *Appl. Catal., B* **2018**, *238*, 318−327.
(823) Xia, K.; Chen, Z.; Yi, J.; Xu, H.; Yu, Y.; She, X.; Mo, Z.; Chen, H.; Xu, Y.; Li, H. Highly Efficient Visible-Light-Driven Schottky Catalyst MoN/2D g-C_3N_4 for Hydrogen Production and Organic Pollutants Degradation. *Ind. Eng. Chem. Res.* **2018**, *57* (27), 8863−8870.
(824) Tahir, B.; Tahir, M.; Che Yunus, M. A.; Mohamed, A. R.; Siraj, M.; Fatehmulla, A. 2D/2D Mt/m-CN Composite with Enriched Interface Charge Transfer for Boosting Photocatalytic CO_2 Hydrogenation by H_2 to CH_4 under Visible Light. *Appl. Surf. Sci.* **2020**, *520*, 146296.
(825) Wang, X.-j.; Tian, X.; Sun, Y.-j.; Zhu, J.-y.; Li, F.-t.; Mu, H.-y.; Zhao, J. Enhanced Schottky Effect of a 2D-2D CoP/g-C_3N_4 Interface for Boosting Photocatalytic H_2 Evolution. *Nanoscale* **2018**, *10* (26), 12315−12321.
(826) Cao, A.; Zhang, L.; Wang, Y.; Zhao, H.; Deng, H.; Liu, X.; Lin, Z.; Su, X.; Yue, F. 2D-2D Heterostructured Unimof/g-C_3N_4 for Enhanced Photocatalytic H_2 Production under Visible-Light Irradiation. *ACS Sustainable Chem. Eng.* **2019**, *7* (2), 2492−2499.
(827) Shi, J.; Li, S.; Wang, F.; Gao, L.; Li, Y.; Zhang, X.; Lu, J. 2D/2D g-C_3N_4/MgFe MMO Nanosheet Heterojunctions with Enhanced Visible-Light Photocatalytic H_2 Production. *J. Alloys Compd.* **2018**, *769*, 611−619.
(828) Zhang, S.; Xu, D.; Chen, X.; Zhang, S.; An, C. Construction of Ultrathin 2D/2D g-C_3N_4/In_2Se_3 Heterojunctions with High-Speed Charge Transfer Nanochannels for Promoting Photocatalytic Hydrogen Production. *Appl. Surf. Sci.* **2020**, *528*, 146858.
(829) Zhou, Y.; Zhang, C.; Huang, D.; Wang, W.; Zhai, Y.; Liang, Q.; Yang, Y.; Tian, S.; Luo, H.; Qin, D. Structure Defined 2D Mo_2C/2D g-C_3N_4 van der Waals Heterojunction: Oriented Charge Flow In-Plane and Separation within the Interface to Collectively Promote Photocatalytic Degradation of Pharmaceutical and Personal Care Products. *Appl. Catal., B* **2022**, *301*, 120749.
(830) Dong, H.; Hong, S.; Zhang, P.; Yu, S.; Wang, Y.; Yuan, S.; Li, H.; Sun, J.; Chen, G.; Li, C. Metal-Free Z-Scheme 2D/2D VdW Heterojunction for High-Efficiency and Durable Photocatalytic H_2 Production. *Chem. Eng. J.* **2020**, *395*, 125150.
(831) Gu, J.; Yan, J.; Chen, Z.; Ji, H.; Song, Y.; Fan, Y.; Xu, H.; Li, H. Construction and Preparation of Novel 2D Metal-Free Few-Layer BN Modified Graphene-like g-C_3N_4 with Enhanced Photocatalytic Performance. *Dalton Trans.* **2017**, *46* (34), 11250−11258.
(832) Xu, L.; Zeng, J.; Li, Q.; Xia, L.; Luo, X.; Ma, Z.; Peng, B.; Xiong, S.; Li, Z.; Wang, L.-L.; et al. Defect-Engineered 2D/2D hBN/g-C_3N_4 Z-Scheme Heterojunctions with Full Visible-Light Absorption: Efficient Metal-Free Photocatalysts for Hydrogen Evolution. *Appl. Surf. Sci.* **2021**, *547*, 149207.
(833) Kofuji, Y.; Isobe, Y.; Shiraishi, Y.; Sakamoto, H.; Ichikawa, S.; Tanaka, S.; Hirai, T. Hydrogen Peroxide Production on A Carbon Nitride-Boron Nitride-Reduced Graphene Oxide Hybrid Photocatalyst under Visible Light. *ChemCatChem* **2018**, *10* (9), 2070−2077.
(834) Acharya, L.; Pattnaik, S. P.; Behera, A.; Acharya, R.; Parida, K. Exfoliated Boron Nitride (e-BN) Tailored Exfoliated Graphitic Carbon Nitride (e-CN): An Improved Visible Light Mediated

https://doi.org/10.1021/acs.chemmater.1c03166
Chem. Mater. 2021, 33, 9012−9092

Photocatalytic Approach Towards TCH Degradation and H_2 Evolution. *Inorg. Chem.* **2021**, *60* (7), 5021−5033.
(835) Chen, T.; Zhang, Q.; Xie, Z.; Tan, C.; Chen, P.; Zeng, Y.; Wang, F.; Liu, H.; Liu, Y.; Liu, G.; et al. Carbon Nitride Modified Hexagonal Boron Nitride Interface as Highly Efficient Blue LED Light-Driven Photocatalyst. *Appl. Catal., B* **2018**, *238*, 410−421.
(836) Tu, D.; Liao, H.; Deng, Q. Synthesis of BN/g-C_3N_4 as Visible-light-Driven Photocatalysts for Degradation of Different Organic Pollutants. *ChemistrySelect* **2018**, *3* (25), 7170−7177.
(837) Chen, L.; Zhou, M.; Luo, Z.; Wakeel, M.; Asiri, A. M.; Wang, X. Template-Free Synthesis of Carbon-Doped Boron Nitride Nanosheets for Enhanced Photocatalytic Hydrogen Evolution. *Appl. Catal., B* **2019**, *241*, 246−255.
(838) Wang, Y.; Chen, G.; Weng, H.; Wang, L.; Chen, J.; Cheng, S.; Zhang, P.; Wang, M.; Ge, X.; Chen, H.; et al. Carbon-Doped Boron Nitride Nanosheets with Adjustable Band Structure for Efficient Photocatalytic U (VI) Reduction under Visible Light. *Chem. Eng. J.* **2021**, *410*, 128280.
(839) Yang, H.; Wang, Z.; Liu, S.; Shen, Y.; Zhang, Y. Molecular engineering of C_xN_y: Topologies, Electronic Structures and Multi-disciplinary Applications. *Chin. Chem. Lett.* **2020**, *31* (12), 3047−3054.
(840) Bai, Y.; Zheng, Y.; Wang, Z.; Hong, Q.; Liu, S.; Shen, Y.; Zhang, Y. Metal-Doped Carbon Nitrides: Synthesis, Structure and Applications. *New J. Chem.* **2021**, *45*, 11876−11892.
(841) Kim, I. Y.; Kim, S.; Premkumar, S.; Yang, J. H.; Umapathy, S.; Vinu, A. Thermodynamically Stable Mesoporous C_3N_7 and C_3N_6 with Ordered Structure and Their Excellent Performance for Oxygen Reduction Reaction. *Small* **2020**, *16* (12), 1903572.
(842) Vinu, A.; Sathish, C.; Premkumar, S.; Chu, X.; Yu, X.; Breese, M. B.; Al-Abri, M.; Al-Muhtaseb, A. a. H.; Karakoti, A.; Yi, J. Microporous Carbon Nitride ($C_3N_{5.4}$) with New Tetrazine based Molecular Structure for Efficient Adsorption of CO_2 and Water. *Angew. Chem., Int. Ed.* **2021**, *60* (39), 21242−21249.
(843) Schwinghammer, K.; Mesch, M. B.; Duppel, V.; Ziegler, C.; Senker, J. r.; Lotsch, B. V. Crystalline Carbon Nitride Nanosheets for Improved Visible-light Hydrogen Evolution. *J. Am. Chem. Soc.* **2014**, *136* (5), 1730−1733.

https://doi.org/10.1021/acs.chemmater.1c03166
Chem. Mater. 2021, 33, 9012−9092